

ACOUSTIC TRANSDUCTION – MATERIALS AND DEVICES

Period 1 January 2000 to 31 December 2000

Annual Report

VOLUME IV

**OFFICE OF NAVAL RESEARCH
Contract No: N00014-96-1-1173**

**APPROVED FOR PUBLIC RELEASE –
DISTRIBUTION UNLIMITED**

**Reproduction in whole or in part is permitted for any
purpose of the United States Government**

Kenji Uchino

PENNSTATE



**THE MATERIALS RESEARCH LABORATORY
UNIVERSITY PARK, PA**

20010817 077

REPORT DOCUMENTATION PAGE

Form Approved
OMB No. 0704-0188

Public reporting burden for this collection of information is estimated to average 1 hour per response, including the time for reviewing instructions, searching existing data sources, gathering and maintaining the data needed, and completing and reviewing the collection of information. Send comments regarding this burden estimate or any other aspect of this collection of information, including suggestions for reducing this burden, to Washington Headquarters Services, Directorate for Information Operations and Reports, 1215 Jefferson Davis Highway, Suite 1204, Arlington, VA 22202-4302, and to the Office of Management and Budget, Paperwork Reduction Project (0704-0188), Washington, DC 20503.

1. AGENCY USE ONLY (Leave blank)		2. REPORT DATE 7/12/2001	3. REPORT TYPE AND DATES COVERED ANNUAL REPORT 01/01/2000--12/31/2000	
4. TITLE AND SUBTITLE ACOUSTIC TRANSDUCTION -- MATERIALS AND DEVICES			5. FUNDING NUMBERS ONR CONTRACT NO. N00014-96-1-11173	
6. AUTHOR(S) Materials Research Laboratory The Pennsylvania State University University Park, Pa 16802				
7. PERFORMING ORGANIZATION NAME(S) AND ADDRESS(ES)			8. PERFORMING ORGANIZATION REPORT NUMBER	
9. SPONSORING/MONITORING AGENCY NAME(S) AND ADDRESS(ES) Office of Naval Research Office of Naval Research ONR 321SS Regional Office Chicago Ballston Centre Tower One 536 S. Clark Str. RM 208 800 N. Quincy Street Chicago IL 60605-1588 Arlington, VA 2217-5660			10. SPONSORING/MONITORING AGENCY REPORT NUMBER	
11. SUPPLEMENTARY NOTES				
12a. DISTRIBUTION / AVAILABILITY STATEMENT			12b. DISTRIBUTION CODE	
13. ABSTRACT (Maximum 200 words) SEE FOLLOWING PAGE				
14. SUBJECT TERMS			15. NUMBER OF PAGES	
			16. PRICE CODE	
17. SECURITY CLASSIFICATION OF REPORT UNCLASSIFIED	18. SECURITY CLASSIFICATION OF THIS PAGE UNCLASSIFIED	19. SECURITY CLASSIFICATION OF ABSTRACT UNCLASSIFIED	20. LIMITATION OF ABSTRACT	

GENERAL INSTRUCTIONS FOR COMPLETING SF 298

The Report Documentation Page (RDP) is used in announcing and cataloging reports. It is important that this information be consistent with the rest of the report, particularly the cover and title page. Instructions for filling in each block of the form follow. It is important to *stay within the lines* to meet optical scanning requirements.

Block 1. Agency Use Only (Leave blank).

Block 2. Report Date. Full publication date including day, month, and year, if available (e.g. 1 Jan 88). Must cite at least the year.

Block 3. Type of Report and Dates Covered. State whether report is interim, final, etc. If applicable, enter inclusive report dates (e.g. 10 Jun 87 - 30 Jun 88).

Block 4. Title and Subtitle. A title is taken from the part of the report that provides the most meaningful and complete information. When a report is prepared in more than one volume, repeat the primary title, add volume number, and include subtitle for the specific volume. On classified documents enter the title classification in parentheses.

Block 5. Funding Numbers. To include contract and grant numbers; may include program element number(s), project number(s), task number(s), and work unit number(s). Use the following labels:

C - Contract	PR - Project
G - Grant	TA - Task
PE - Program Element	WU - Work Unit Accession No.

Block 6. Author(s). Name(s) of person(s) responsible for writing the report, performing the research, or credited with the content of the report. If editor or compiler, this should follow the name(s).

Block 7. Performing Organization Name(s) and Address(es). Self-explanatory.

Block 8. Performing Organization Report Number. Enter the unique alphanumeric report number(s) assigned by the organization performing the report.

Block 9. Sponsoring/Monitoring Agency Name(s) and Address(es). Self-explanatory.

Block 10. Sponsoring/Monitoring Agency Report Number. (If known)

Block 11. Supplementary Notes. Enter information not included elsewhere such as: Prepared in cooperation with...; Trans. of...; To be published in.... When a report is revised, include a statement whether the new report supersedes or supplements the older report.

Block 12a. Distribution/Availability Statement. Denotes public availability or limitations. Cite any availability to the public. Enter additional limitations or special markings in all capitals (e.g. NOFORN, REL, ITAR).

DOD - See DoDD 5230.24, "Distribution Statements on Technical Documents."

DOE - See authorities.

NASA - See Handbook NHB 2200.2.

NTIS - Leave blank.

Block 12b. Distribution Code.

DOD - Leave blank.

DOE - Enter DOE distribution categories from the Standard Distribution for Unclassified Scientific and Technical Reports.

NASA - Leave blank.

NTIS - Leave blank.

Block 13. Abstract. Include a brief (*Maximum 200 words*) factual summary of the most significant information contained in the report.

Block 14. Subject Terms. Keywords or phrases identifying major subjects in the report.

Block 15. Number of Pages. Enter the total number of pages.

Block 16. Price Code. Enter appropriate price code (*NTIS only*).

Blocks 17. - 19. Security Classifications. Self-explanatory. Enter U.S. Security Classification in accordance with U.S. Security Regulations (i.e., UNCLASSIFIED). If form contains classified information, stamp classification on the top and bottom of the page.

Block 20. Limitation of Abstract. This block must be completed to assign a limitation to the abstract. Enter either UL (unlimited) or SAR (same as report). An entry in this block is necessary if the abstract is to be limited. If blank, the abstract is assumed to be unlimited.

ABSTRACT

This report describes research performed over the period 1st January 2000 to 31st December 2000 on a MURI under Office of Naval Research contract N00014-96-1-1173 on the topic "Acoustic Transduction Materials and Devices". This program brings together researchers from the Materials Research Laboratory (MRL), the Applied Research Laboratory (ARL) and the Center for Acoustics and Vibrations (CAV) at the Pennsylvania State University. As has become customary over many years, research on the program is detailed in the technical appendices of published work, and only a brief narrative description connecting these studies is given in the text.

The program combines a far reaching exploration of the basic phenomena contributing to piezoelectric and electrostrictive response with the highly applied thrusts necessary to produce the "pay-off" in new applications relevant to Navy needs. Polarization vector tilting in the ferroelectric phase of perovskite structure crystals at compositions close to a morphotropic phase boundary (MPB) was first underscored on this program some four years ago, and is now widely accepted as one mode for exploiting the large intrinsic spontaneous strain in the ferroelectric to produce exceedingly strong anhysteretic piezoelectric response and very large electric field controlled elastic strain. New evidence for the importance of both spontaneous (monoclinic) and electric field induced tilting on the properties of both single and polycrystal MPB systems is presented in this report.

The puzzling phenomena associated with relaxor ferroelectric response have long been a topic of study in MRL, where the micro-polar region model and the application of Vogel/Fulcher to the dielectric slowing down were first applied. The current "pay-off" is in the greatly enhanced relaxor ferroelectric electrostrictive response from high electron energy irradiated polyvinylidene difluoride: trifluoroethylene (PVDF: TrFE) co-polymer discussed in this report. This development opens a new field of high strain, high energy density actuators with tremendous practical applicability. Now the possibility of engineering this response by chemical manipulation in the terpolymer systems without irradiation further enhances the exciting possibilities.

In composite structures, the early promise of the flextensional cymbal type actuators is now being fully realized and programs exploring large area cymbal transducer arrays are progressing very well, both at MRL/ARL and at NRL. The connection with CAV at Penn State is particularly important in keeping the MURI faculty aware of problems endemic to water as our host medium and the effects of turbulence in flow and the need for many types of acoustic noise control.

New designs of piezoelectric transformers and motors are demanding materials with lower loss levels under continuous high driving, and important progress is reported in separating and understanding the components of this loss and in designing new doping schemes for ceramics which enhance power capability almost tenfold. New piezoelectric micro-motor designs look particularly attractive and appear to offer significant advantages over electromagnetics for very small-scale applications. Thick and thin film studies for MEMS are progressing well and offering new insights into fatigue and switching behavior in the ferroelectrics.

**ACOUSTIC TRANSDUCTION –
MATERIALS AND DEVICES**

Period 1 January 2000 to 31 December 2000

Annual Report

VOLUME IV

**OFFICE OF NAVAL RESEARCH
Contract No: N00014-96-1-1173**

**APPROVED FOR PUBLIC RELEASE –
DISTRIBUTION UNLIMITED**

**Reproduction in whole or in part is permitted for any
purpose of the United States Government**

Kenji Uchino

APPENDICES

VOLUME I

GENERAL SUMMARY PAPERS

1. Uchino, K., Encyclopedia of Vibration, Partial Charge "Electrostrictive Materials", Academic Press, London (2000). [in press]
2. Uchino, K., and Y. Ito, Encyclopedia Smart Materials, J. Harvey, Edit., Partial Charge "Smart Ceramics: Transducers, Sensors and Actuators", John Wiley & Sons, New York (2000). [in press]
3. Wennu Ma, L.E. Cross, "Observation of the flexoelectric effect in relaxor PB ($\text{Mg}_{1/3}\text{Nb}_{2/3}\text{O}_3$) ceramics", Applied Physics Letters. Volume #8 number 19 pp. 2920
4. R. Hatt and W. Cao, "Landau-Ginzburg Model for Antiferroelectric Phase Transition Based on Microscopic Symmetry", Phys. Rev. B, vol. **62**, pp. 818-823 (2000).

2.0 MATERIALS STUDIES

2.1 Polycrystal Perovskite Ceramics

5. A.S. Bhalla, R. Guo, R. Roy, "The Perovskite Structure - A Review of Its Role in Ceramic Science and Technology, "Mat. Res. Innovat., **4**(1), 3-26, (2000)
6. E.F. Alberta, R. Guo, L.E. Cross, A.S. Bhalla, "Structure-Property Diagrams of Ferroic Solid Solutions. Part I: Perovskite Ferroelectrics with Morphotropic Phase Boundaries," *Ferroelectrics Review*, 3, 1, (2001)
7. B. Noheda, J.A. Gonzalo, L.E. Cross, R. Guo, S-E. Park, D.E. Cox, G. Shirane, "Tetragonal-to-Monoclinic Phase Transition in a Ferroelectric Perovskite: the Structure of $\text{PbZr}_{0.52}\text{Ti}_{0.48}\text{O}_3$ ", *Phys. Rev. B*, **61**(13), 8687-8689, (2000)
8. B. Noheda, D.E. Cox, G. Shirane, R. Guo, B. Jones, L.E. Cross, "Stability of the monoclinic phase in the ferroelectric perovskite $\text{PbZr}_{(1-x)}\text{Ti}_x\text{O}_3$ ", *Los Alamos Natl. Lab., Prepr. Arch., Condens. Matter*, **1-8**, arXiv:cond-mat/0006152, (2000)
9. R. Guo, L.E. Cross, S-E. Park, B. Noheda, D.E. Cox, G. Shirane, "Origin of the high piezoelectric response in $\text{PbZr}_{1-x}\text{Ti}_x\text{O}_3$," *Phys. Rev. Letters*, **84**(23), 5423-5426, (2000)
10. W. Jiang and W. Cao, "Nonlinear Elastic Properties of Lead Zirconate Titanate Ceramics", J. Appl. Phys., vol. **88**: 6684-6689 (2000).
11. Chen, Y. H., D. Viehland and K. Uchino, "Substituent Effects in $0.65\text{Pb}(\text{Mg}_{1/3}\text{Nb}_{2/3})\text{O}_3$ - 0.35PbTiO_3 Piezoelectric Ceramics" J. Electroceramics, **6**, 13-20 (2001). (First Author Supervised by Candidate).
12. W.H. Jiang and W. Cao, "Intrinsic and Coupling-induced Elastic Nonlinearity of Lanthanum-doped Lead Magnesium Niobate-Lead Titanate Electrostrictive Ceramic", Appl. Phys. Lett., vol. **77**, pp. 1387-1389 (2000).

VOLUME II

2.0 MATERIALS STUDIES

2.2 *Single Crystal Systems*

13. L.E. Cross, J. Fousek, "Engineering Multidomain Ferroic Samples", *Ferroelectrics*, 2001, Vol. 252, pp. 171-180.
14. Wada, Satoshi, Takaaki Tsurumi, Miour Osada, Masato Kakihana, Seung Eek Park, L.Eric Cross and Thomas R. Shrout. "Change of Macroscopic and Microscopic Symmetries in Relaxor PZN Single Crystal Under Bias Filed." Transactions of the Material Research Society of Japan, **25** (1). 281-284 (2000).
15. Wada, Satoshi, Takaaki Tsurumi, Miour Osada, Masato Kakihana, Seung Eek Park, L.Eric Cross and Thomas R. Shrout. "Dipolar Behavior in PZN Relaxor Single crystals under Bias Fields." Transactions of the Materials Research Society of Japan **25** (1), 281-284 (2000).
16. Belegundu, U., X. Du and K. Uchino, "Switching Current in $\text{Pb}(\text{Zn}_{1/3}\text{Nb}_{2/3})\text{O}_3$ - PbTiO_3 Single Crystals," Symp. LL Proc., Mater. Res. Soc. Fall Mtg. '99, (LL.1.9, Boston, Nov. 29-Dec.3. 1999), Vol. **604**, 39-44 (2000).
17. Yu Lu, D.-Y. Jeong, Z. Y. Cheng, Q. M. Zhang, H. Luo, Z. Yin, and D. Viehland. Phase Transitional Behavior and Piezoelectric Properties of the orthorhombic Phase of PMN-PT Single Crystals. *Appl. Phys. Lett.* **78**, 3109 (2001).
18. Yu Lu, Z.-Y. Cheng, E. Park, S. F. Liu and Q. M. Zhang. Linear Electro-optic Effect of $0.88\text{Pb}(\text{Zn}_{1/3}\text{Nb}_{2/3})$ - 0.12PbTiO_3 Single Crystal. *Jpn. J. Appl. Phys.* **39**, 141-145 (2000).
19. Y. Barad, Yu Lu, Z. Y. Cheng, S. E. Park, and Q. M. Zhang. Composition, Temperature, and Crystal Orientation Dependence of Linear Electro-optic Properties of PZN-PT Single Crystals. *Appl. Phys. Lett.* **77**, 1247-1249 (2000).
20. Y. Lu, Z.-Y. Cheng, Y. Barad, and Q. M. Zhang. Photoelastic Effects in the Tetragonal PZN-PT Single Crystals near the Morphotropic Phase Boundary. *J. Appl. Phys.* **89**, 5075 (2001).

2.3 *High Strain Polymers*

21. Vivek Bharti, H. S. Xu, G. Shanthi, Q. M. Zhang, and Kuming Liang. Polarization and Structural Properties of High Energy Electron Irradiated P(VDF-TrFE) Copolymer Films. *J. Appl. Phys.* **87**, 452-461 (2000).
22. Haisheng Xu, G. Shanthi, V. Bharti, Q. M. Zhang, and T. Ramatowski. Structural, Conformational, and Polarization Changes of P(VDF-TrFE) Copolymer Induced by High Energy Electron Irradiation. *Macromolecules*, **33**, 4125-4131(2000).
23. Q. M. Zhang, Z. Y. Cheng, and Vivek Bharti. Relaxor Ferroelectric Behavior in High Energy Electron Irradiated P(VDF-TrFE) copolymers. *Appl. Phys.* **A70**, 307-312 (2000).
24. Vivek Bharti and Q. M. Zhang. Dielectric Study of Relaxor Ferroelectric P(VDF-TrFE) Copolymer System. *Phys. Rev. B.* **63**, 184103 (2001).
25. Z.Y. Cheng, Vivek Bharti, T.B. Xu, Hansheng Xu, T. Mai, and Q. M. Zhang. Electrostrictive P(VDF-TrFE) Copolymers. *Sensors and Actuators A-Phys.* **90**, 138-147 (2001)

26. Z. Y. Cheng, V. Bharti, T. Mai, T. B. Xu, Q. M. Zhang, K. Hamilton, T. Ramotowski, K. A. Wright, and R. Ting. Effect of High Energy Electron Irradiation on the Electromechanical Properties of Poly(vinylidene fluoride-trifluoroethylene) 50/50 and 65/35 Copolymers. *IEEE Trans. UFFC* **47**, 1296 (2000).
27. Vivek Bharti, Z.-Y. Cheng, T. Mai, Q. M. Zhang, T. Ramotowski, K. A. Wright. High Electromechanical Coupling Factor and Electrostrictive Strain over a Broad Frequency Range in Electrostrictive Poly(vinylidene fluoride-trifluoroethylene) Copolymer. *Japn. J. Appl. Phys.* **40**, 672 (2001).
28. Vivek Bharti, G. Shanthi, H. Xu, Q. M. Zhang, and K. Liang. Evolution of Transitional Behavior and Structure of Electron Irradiated P(VDF-TrFE) Copolymer Films. *Mater. Lett.* **47**, 107-111 (2001).
29. F. Xia, H. Xu, F. Fang, B. Razivi, Z. Y. Cheng, Yu Lu, Baoming Xu, and Q. M. Zhang. Thickness Dependence Behavior of Ferroelectric Switching in P(VDF-TrFE) Spin Cast Films. *Appl. Phys. Lett.* **78**, 1122 (2001).
30. Q. M. Zhang, H. S. Xu, Fei Fang, Z.-Y. Cheng, Xia Feng, and H. You. Observation of Critical Thickness of Crystallization in Spin Cast Ferroelectric Thin Films. *J. Appl. Phys.* **89**, 2613 (2001).
31. Shizhuo Yin, Q. M. Zhang, K.-W. Chung, R. Yang, Z. Y. Cheng, and Yu Lu. Investigation of the Electro-optic Properties of Electron-irradiated P(VDF-TrFE) Copolymer. *Opt. Eng.* **39**, 670-672 (2000).
32. Hai-Sheng Xu, Z.-Y. Cheng, Vivek Bharti, Shexi Wang, and Q. M. Zhang. All-Polymer Electromechanical Systems Consisting of Electrostrictive Poly(vinylidene fluoride-trifluoroethylene) and Conductive Polyaniline. *J. Appl. Poly. Sci.* **75**, 945-951 (2000).
33. H. Xu, Z.Y. Cheng, D. Olson, T. Mai, Q. M. Zhang, and G. Kavarnos. Ferroelectric and Electromechanical Properties of P(VDF-TrFE-CTFE) Terpolymer. *Appl. Phys. Lett.* **78**, 2360 (2001).

3.0 TRANSDUCER STUDIES

3.1 Composite Structures

34. Uchino, K., "Piezoelectro Composites," Chap.5.24, *Comprehensive Composite Materials*, Elsevier Science, Oxford, UK (2000).
35. Tressler, J. and K. Uchino, "Piezoelectric Composite Sensors," Chap.5.22, *Comprehensive Composite Materials*, Elsevier Science, Oxford, UK (2000).

VOLUME III

36. Meyer, R.J. Jr., A. Dogan, C. Yoon, S. Pilgrim and R.E. Newnham, "Displacement Amplification of Electroactive Materials Using the Cymbal Flexensional Transducer," *Sensors & Actuators A*, vol.87, pp. 157-162 (2001).
37. Dogan, A., K. Uchino and R. E. Newnham, "Flexensional Composite Transducers: Designing, Fabrication and Application," *Proc. NATO- Advanced Research Workshop: Piezoelectric Materials: Advance in Science, Technology and Applications*, (Predeal, Romania, May 24-27, 1999, Kluwer Academic Publ., p.357-374 (2000).

38. Zhang, J., A.C. Hladky-Hennion, W.J. Hughes, and R.E. Newnham, "Modeling and Underwater Characterization of Cymbal Transducers and Arrays," IEEE Transactions on Ultrasonics, Ferroelectrics, and Frequency Control, vol. 48 (2), pp. 560-568 (2001).
39. Zhang, J., W. J. Hughes, R. J. Meyer Jr., K. Uchino and R. E. Newnham, "Cymbal Array: A Broad Band Sound Projector," Ultrasonics 37, 523-529 (2000).
40. Zhang, J., A.C. Hladky-Hennion, W.J. Hughes, and R.E. Newnham, "A Miniature Class V flextensional cymbal transducer with directional beam pattern: The Double-Driver," Ultrasonics, vol. 39, pp. 91-95 (2001).
41. Meyer, R.J. Jr. and R.E. Newnham, "Flextensional transducers with Shape Memory Caps for Tunable Devices," Journal of Intelligent Materials Systems and Structures, vol. 11, pp. 199-205 (2001).
42. Meyer, R.J. Jr., S. Alkoy, J. Cochran, T. Ritter, and R.E. Newnham, "Pre-focused Lead Titanate > 25 MHz Single Element Transducers from Hollow Spheres," IEEE Transactions on Ultrasonics, Ferroelectrics, and Frequency Control, vol. 48 (2), pp. 488-493 (2001).
43. Y. Bai, Z.Y. Cheng, V. Bharti, H. S. Xu, and Q. M. Zhang. High Dielectric Constant Ceramic Powder Polymer Composites. Appl. Phys. Lett. 76, 3804-3806 (2000).
44. M.R. Shen and W. Cao, "Acoustic Bandgap Formation in a Periodic Structure with Multilayer Unit Cells", J. Phys. D: Applied Physics, vol. 33, pp. 1150-1154 (2000).
45. T.B. Xu, Z-Y. Cheng, Q. M. Zhang, R. Baughman, C. Cui, A. Zakhidov, and J. Su. Fabrication and Characterization of 3-Dimensional Periodic Ferroelectric Polymer-Silica Opal Composites and Inverse Opal. J. Appl. Phys. 88(1), 405-409 (2000).

3.2 *Piezoelectric Transformers*

46. Uchino, K., B. Koc, P. Laoratanakul and A. Vazquez Carazo, "Piezoelectric Transformers -New Perspective--," Proc. 3rd Asian Mtg. Ferroelectrics, D1d.1, Hong Kong, Dec. 12-15 (2000).
47. Koc, B., and K. Uchino, "Disk Type Piezoelectric Transformer with Crescent Shape Input Electrodes," Proc. NATO- Advanced Research Workshop: Piezoelectric Materials: Advance in Science, Technology and Applications, (Predeal, Romania, May 24-27, 1999, Kluwer Academic Publ., p.375-382 (2000).

3.3 *High Power Level Materials*

48. Uchino, K. and S. Hirose, "Loss Mechanisms in Piezoelectrics: How to Measure Different Losses Separately," IEEE UFFC Transactions, 48, 307-321 (2001).
49. Uchino, K., and J. Zheng, Y. H. Chen, X. Du and S. Hirose, "Loss Mechanisms in Piezoelectrics and Resonance/ Antiresonance," Proc. 101st Annual Mtg. of Amer. Ceram. Soc., Symp. Electronic Ceramic Materials and Devices, (Indianapolis, April 25 - 28, 1999), p.79-100 (2000).
50. Uchino, K., J. Zheng, Y. H. Chen, X. Du, S. Hirose and S. Takahashi, "Loss Mechanisms in Piezoelectrics -Extrinsic and Intrinsic Losses--," Mater. Res. Soc. Fall Mtg. '99, (LL.1.6, Boston, Nov. 29-Dec.3, 1999), Vol. 604, 25-31 (2000).

51. Chen, Y. H., S. Hirose, D. Viehland and K. Uchino, "Doping Effects in $\text{Pb}(\text{Mg}_{1/3}\text{Nb}_{2/3})\text{O}_3$ - PbTiO_3 Ceramics for High Power Transduction Applications," Mater. Res. Soc. Fall Mtg. '99, (LL.5.8, Boston, Nov. 29-Dec.3, 1999), Vol. **604**, 215-220 (2000).
52. Chen, Y. H., S. Hirose, D. Viehland, S. Takahashi and K. Uchino, " Mn-Modified $\text{Pb}(\text{Mg}_{1/3}\text{Nb}_{2/3})\text{O}_3$ - PbTiO_3 Ceramics: Improved Mechanical Quality Factors for High-Power Transducer Applications," Jpn. J. Appl. Phys. **39**, 4843-4852 (2000).
53. Gao, Y. Y. H. Chen, J. Ryu, K. Uchino and D. Viehland, " Eu and Yb Substituent Effects on the Properties of $\text{Pb}(\text{Zr}_{0.52}\text{Ti}_{0.48})\text{O}_3$ - $\text{Pb}(\text{Mn}_{1/3}\text{Sb}_{2/3})\text{O}_3$ Ceramics: Development of a New High-Power Piezoelectric with Enhanced Vibrational Velocity," Jpn. J. Appl. Phys., **40**, 79-85 (2001).

VOLUME IV

3.4 *Fluid Structure Interactions*

54. Lauchle, G. C., W. A. Kargus IV. Scaling of Turbulent Wall Pressure Fluctuations Downstream of a Rearward Facing Step. *J. Acoust. Soc. Am.* **107**: L1-L6 (2000).
55. Capone, D. E., G. C. Lauchle. Modeling the Unsteady Lift and Drag on a Finite-Length Cylinder in Cross Flow. *J. Fluids and Struct.* **14**: 799-817 (2000).
56. Gavin, J. R., G. C. Lauchle. Modeling the Space-Time Correlations in the Wake Region of a Turbulent Boundary Layer. *Proc. of the ASME Noise Control and Acoustics Division 2000*, NCA-Vol. 27, pp 227-241 (2000).
57. Gavin, J. R., G. C. Lauchle, M. L. Jonson. Prediction of Turbulence Ingestion Forces for Rotors with Arbitrary Rake and Skew. *Proc. of the ASME Noise Control and Acoustics Division 2000*. NCA-Vol. 27, pp 217-226 (2000).
58. Lauchle, G. C, D. K. McLaughlin. Review of: *Acoustics of Fluid Structure Interactions* by M. S. Howe in *Noise Control Eng. J.* **48**: 70-71 (2000).

4.0 ACTUATOR STUDIES

4.1 *Materials and Designs*

59. Koc, B. and K. Uchino, "Piezoelectric Ultrasonic Motors," Chap.6.34, *Comprehensive Composite Materials*, Elsevier Science, Oxford, UK (2000).
60. Uchino, K., "Recent Trend of Piezoelectric Actuator Developments –Material, Design and Drive Technique Related Issues--," *Proc. Actuator 2000 (7th Int'l Conf. New Actuators, June 19-21, 2000)*, p.34-39 (2000).
61. Yao, K., K. Uchino, Y. Xu, S. Dong, and L. C. Lim, "Compact Piezoelectric Stacked Actuators for High Power Applications," *IEEE Trans. UFFC*, **47**, 819-825 (2000).
62. Liu, Rubin, L.e. Cross, Gareth Knowles, Bruce Bower, and Brookd Childers. " A Stackable Bonding-Free Flextensional Piezoelectirc Actuator" *Journal of Electroceramics* **4** (1), 201-206 92000)
63. A. E. Glazounov, Q. M. Zhang, C. Kim. Torsional Actuator Based on Mechanically Amplified Shear Piezoelectric Response. *Sensors and Actuators A* **79**, 22-30 (2000).

4.2 Photostriction

- 64. Poosanaas, P., K. Tonooka and K. Uchino, "Photostrictive Actuators," *J. Mechatronics* **10**, 467-487 (2000).
- 65. Uchino, K., P. Poosanaas and K. Tonooka, "Photostrictive Actuators—New Perspective-," *Proc. 3rd Asian Mtg. Ferroelectrics*, C3p.105, Hong Kong, Dec. 12-15 (2000).
- 66. Uchino, K., P. Poosanaas and K. Tonooka, "Photostrictive Actuators—New Perspective-," *Proc. 5th Euroconf. Appl. Polar Dielectrics*, O-43, Jurmala, Latvia, Aug. 27-30 (2000).
- 67. Poosanaas, P., K. Tonooka, I. R. Abothu, S. Komarneni, and K. Uchino, "Influence of Composition and Dopant on Photostriction in Lanthanum-Modified Lead Zirconate Titanate Ceramics," *J. Intelligent Mater. Systems and Structures* **10**, 439-445 (2000). (
- 68. Poosanaas, P., Dogan, A., Prasadarao, A. V., Komarneni, S. and Uchino, K., "Effect of Ceramic Processing Methods on Photostrictive Ceramics", *J. Advanced Performance Mater.* **6**, 57-69 (1999).

VOLUME V

4.3 High Force Actuators

- 69. A. E. Glazounov, Q. M. Zhang, and C. Kim. Torsional Actuator and Stepper Motor Based on Piezoelectric d_{15} Shear Response. *J. Intel. Mater. Syst. & Struct.* **11**(6), 456-468 (2000).
- 70. Galante, T., J. Frank, J. Bernard, W. Chen, G.A. Lesieutre, and G.H. Koopmann, "A High-Force, High-Displacement Piezoelectric Inchworm Actuator," *Journal of Intelligent Materials Systems and Structures*, Vol. 10, No. 12, December, 2000, pp. 962-972.

4.4 Piezoelectric Motors

- 71. Koc, B. and K. Uchino, "Piezoelectric Ultrasonic Motors," Chap.6.34, *Comprehensive Composite Materials*, Elsevier Science, Oxford, UK (2000).
- 72. Uchino, K., and B. Koc, "Compact Piezoelectric Ultrasonic Motors," *Proc. NATO-Advanced Research Workshop: Piezoelectric Materials: Advance in Science, Technology and Applications*, (Predeal, Romania, May 24-27, 1999, Kluwer Academic Publ., p.309-320 (2000).
- 73. Koc, B., J. F. Tressler and K. Uchino, "A Miniature Piezoelectric Rotary Motor Using Two Orthogonal Bending Modes of a Hollow Cylinder," *Proc. Actuator 2000 (7th Int'l Conf. New Actuators*, June 19-21, 2000), p.242-245 (2000).
- 74. Koc, B., J. F. Tressler and K. Uchino, "A Miniature Piezoelectric Rotary Motor Using Two Orthogonal Bending Modes of a Hollow Cylinder," *Proc. Actuator 2000 (7th Int'l Conf. New Actuators*, June 19-21, 2000), p.242-245 (2000).
- 75. Bouchilloux, P., B. Koc and K. Uchino, "New Concept for Resonant Longitudinal-Shear Ultrasonic Motor," *Symp. LL Proc., Mater. Res. Soc. Fall Mtg. '99*, (LL.2.10, Boston, Nov. 29-Dec.3, 1999), Vol.604, 71-78 (2000).

76. Koc. B., P. Bouchilloux, and K. Uchino, "Piezoelectric Micromotor Using A Metal-Ceramic Composite Structure," IEEE Trans. Ultrasonic, Ferroelectrics, and Frequency Control **47** (4), 836-843 (2000).

4.5 *Acoustic Absorbers*

77. Davis, C.L. and G.A. Lesieutre, "An Actively Tuned Solid State Vibration Absorber Using Capacitive Shunting of Piezoelectric Stiffness," Journal of Sound and Vibration, Vol. 232(3), 4 May 2000, pp. 601-617.
78. Patricia L. Driesch, Hisao Iwata, Gary H. Koopmann, and Jeff Dosch. Nov. 2000. Development and evaluation of a surface acoustic intensity probe. Review of Scientific Instruments, 71 (11), pp. 1-6.
79. W. Huang. G. H. Koopmann, S. J. Sharp, and W. Chen. April 2000. Enhanced Low Frequency Transmission Loss of Lightweight Trim Panels. Journal of Intelligent Material Systems and Structures, Volume 11, No 4.
80. E.W. Constans, A.D. Belegundu, and G.H. Koopmann. 2000. Optimally Designed Shell Enclosures with Tuned Absorbers for Minimizing Sound Power. Optimization and Engineering, 1, 67-86, (an International Journal, Kluwer Publishers)

VOLUME VI

5.0 MODELING AND CHARACTERIZATION

5.1 *Design and Simulation*

81. K. Uchino, "Designing With Piezoelectric Devices" International Center for Actuators and Transducers, Materials Research Institute, The Pennsylvania State University, University Park, PA (2000)
82. W.K. Qi, and W. Cao, "Finite Element Study on 1-D Array Transducer Design", IEEE Transaction, Ultra. Ferro. and Frequency Control, vol. **47**, pp. 949-955 (2000).
83. T.A. Ritter, K. K. Shung, W. Cao and T. R. Shrout, "Electromechanical Properties of Thin Strip Piezoelectric Vibrators at High Frequency", J. Applied Phys, vol. **88**, pp. 394-397 (2000).
84. T.A. Ritter, K. K. Shung, W. Cao and T. R. Shrout, "Electromechanical Properties of Thin Strip Piezoelectric Vibrators at High Frequency", J. Applied Phys, vol. **88**, pp. 394-397 (2000).

5.2 *Thick and Thin Films*

85. Kalpat, S., X. Du, I. R. Abothu, A. Akiba, H. Goto and K. Uchino, "Effect of Crystal Orientation on Dielectric Properties of Lead Zirconate Titanate Thin Films Prepared by Reactive RF-Sputtering," Jpn. J. Appl. Phys., **40**, 158-162 (2001).
86. Kalpat, S., X. Du, I. R. Abothu, A. Akiba, H. Goto, S. Trolier-McKinstry and K. Uchino, "Dielectric Properties of Highly Oriented Lead Zirconate Titanate Thin Films Prepared by Reactive RF-Sputtering," Symp. LL Proc., Mater. Res. Soc. Fall Mtg. '99, (LL.1.3, Boston, Nov. 29-Dec.3, 1999), Vol. **604**, 3-8 (2000).
87. S. Trolier-McKinstry, "Piezoelectric Films for MEMS Applications," J. Ceram. Soc. Jpn. **109** (5) S76-S79 (2001).

88. Jeong Hwan Park, Fei Xu, and Susan Trolier-McKinstry, "Dielectric and Piezoelectric Properties of Sol-Gel Derived Lead Magnesium Niobium Titanate Films with Different Textures," *J. Appl. Phys.* 89(1) 568 - 574 (2001).
89. Q. F. Zhou, E. Hong, R. Wolf, and S. Trolier-McKinstry, "Dielectric and Piezoelectric Properties of PZT 52/48 Thick Films with (100) and Random Crystallographic Orientation," *Ferroelectric Thin Films*, Vol 655 (2000).
90. L.-P. Wang, R. Wolf, Q. F. Zhou, S. Trolier-McKinstry and R. J. Davis, "Wet-etch patterning of lead zirconate titanate (PZT) thick films for microelectromechanical systems (MEMS) application," *Mat. Res. Soc. Symp.* Vol.657 (MEMS)

5.3 Domain Studies

91. Uchino, K., and H. Aburatani, "Field Induced Acoustic Emission in Ferroelectric Ceramics," *Proc. 101st Annual Mtg. of Amer. Ceram. Soc., Symp. Electronic Ceramic Materials and Devices*, SE-56, (Indianapolis, April 25 – 28, 1999), (2000).
92. J. Fousek^{ab}, L.E. Cross^b, "Engineering Multidomain Ferroic Samples, Dept of Physics and International Center for Piezoelectric Research, University of Technology, Liberec, 46117 Czech Republic and^b Materials Research Laboratory, The Pennsylvania State University, University Park, PA 16802, USA. (June 2000)
93. J.H. Yin, and W. Cao, "Domain Configurations in Domain-Engineered 0.955Pb(Zn_{1/3}Nb_{2/3})O₃-0.045PbTiO₃ Single Crystals", *J. Appl. Phys.*, vol. 87, pp. 7438-7441 (2000).
94. Rajeev Ahluwalia, "Computer Simulations of Domain Pattern Formation in Ferroelectrics", *AIP Conference Proceedings Series*, © 2001 American Institute of Physics, *Proceedings of the 2001 Workshop on Fundamental Physics of Ferroelectrics* Williamsburg, Va, 2001
95. R. Ahluwalia and W. Cao, "Influence of Dipolar Defects on Switching Behavior in Ferroelectrics", *Phys. Rev. B*, vol. 63, pp. 012103 (2000)
96. Uchino, K., and H. Aburatani, "Field Induced Acoustic Emission in Ferroelectric Ceramics," *Proc. 101st Annual Mtg. of Amer. Ceram. Soc., Symp. Electronic Ceramic Materials and Devices*, SE-56, (Indianapolis, April 25 – 28, 1999), (2000).

TRANSDUCER STUDIES

Fluid Structure Interactions

APPENDIX 54

Scaling of turbulent wall pressure fluctuations downstream of a rearward facing step

Gerald C. Lauchle

*Penn State University
Graduate Program in Acoustics and Applied Research Laboratory
State College, Pennsylvania 16804
gcl1@psu.edu*

Walter A. Kargus IV

*Johnson Electric Automotive
47660 Halyard Drive, Plymouth, Michigan 48170
wkargus@lear.com*

Abstract: The turbulent boundary layer that forms downstream of a surface discontinuity is locally inhomogeneous. Here, we consider the boundary layer that occurs downstream of a rearward facing step discontinuity on a flat plate that is exposed to a zero incidence, uniform subsonic flow. The wall pressure "point" spectra are measured by small, flush-mounted pressure transducers located at various locations downstream of the step. A new form of the non-dimensional point wall pressure auto-frequency spectrum is proposed that includes the statistical variations of the reattachment location. This form is shown to collapse quite well all of the spectra measured slightly upstream, within, and downstream of the flow reattachment location.

©1999 Acoustical Society of America

PACS numbers: 43.50.Nm, 43.28.Ra, 43.50.Yw

1. Introduction

Flow over a rearward facing step is characterized as a discontinuous boundary-layer flow over a surface in which the elevation of the downstream surface is lower than that of the upstream surface. Lap-joints and cutouts on surfaces exposed to flow are examples. The assumed upstream turbulent boundary layer will separate at the step discontinuity forming a free shear layer and a local recirculation zone immediately downstream of the step. The shear layer eventually reattaches to the downstream surface, and a new highly energized turbulent boundary layer begins to form. This process produces wall pressure fluctuations that are significantly higher than those created by nonseparated, equilibrium turbulent boundary layers. In turn, this increases the direct flow-induced noise radiation and nonrigid surface vibrations that radiate as structural vibration-induced noise.

The scaling of the wall pressure point power spectrum under an equilibrium turbulent boundary layer (TBL) has been subdivided into major regions.¹ Each region conforms to different layers of the flow and has a particular pressure and time scale. The rms pressure fluctuations within the viscous sublayer, for example, scale on the wall shear stress and the viscous time scale. The convecting turbulence in the log-law region causes these pressures to scale on the wall shear stress and a larger time scale that is related to the TBL thickness and shear velocity. The region beyond the log-law region is termed the outer boundary layer. Here, the low-frequency pressure fluctuations scale on the dynamic pressure of the flow, $q = 1/2\rho_0 U_0^2$, and on the time scale δ^*/U_0 , where δ^* is the TBL displacement thickness, ρ_0 is the fluid mean density, and U_0 is the free stream velocity. The higher frequencies scale on viscous variables.

Each region of the TBL influences a different range of frequencies of the point wall

pressure spectrum. The regions beyond the log-law region influence the lower and mid frequencies, whereas the log-law region influences the "overlapping" frequencies between the mid and high frequency range. The region of the viscous sublayer influences the high frequencies. These different scalings are still open to discussion² because of the complexity in modeling a TBL.

In this study, we consider the scaling of the point wall pressure spectrum downstream of a surface step discontinuity, which is more complex than that of a typical nonseparating TBL on a flat plate under zero pressure gradient conditions because of additional length scales, nonhomogeneous flow statistics, and reversed flow patterns. An experiment to characterize the statistics of the wall pressure fluctuations that occur downstream of a rearward facing, 2-D step on a flat plate has been conducted. Presented are scaling relationships that can be used to predict the auto-spectral characteristics of the wall pressure fluctuations for similar situations in which experimental data are unavailable. It is found that the spectra scale on the height of the step, the mean velocity upstream of the separation point, and on the *variance* of the estimated distance from the reattachment point-to-the point of measurement. By incorporating the variance between a fixed measurement location (or point of interest) and the reattachment point, which is known to be chaotic, a useful scaling law is established that has no singularity³ when the measurement location happens to correspond to the reattachment location. This scaling relationship is different from earlier proposals^{4,5} for a similar flow, and provides a better collapse of the experimentally measured spectra.

2. Experimental setup

A special facility was designed and used in a large anechoic chamber to measure the local wall pressure fluctuations and radiated sound from the flow over a rearward-facing step located on an otherwise flat, 2-D plate that supports a TBL on one side only. Figure 1 shows a schematic of the experiment, and the facility is described in complete detail elsewhere.⁶

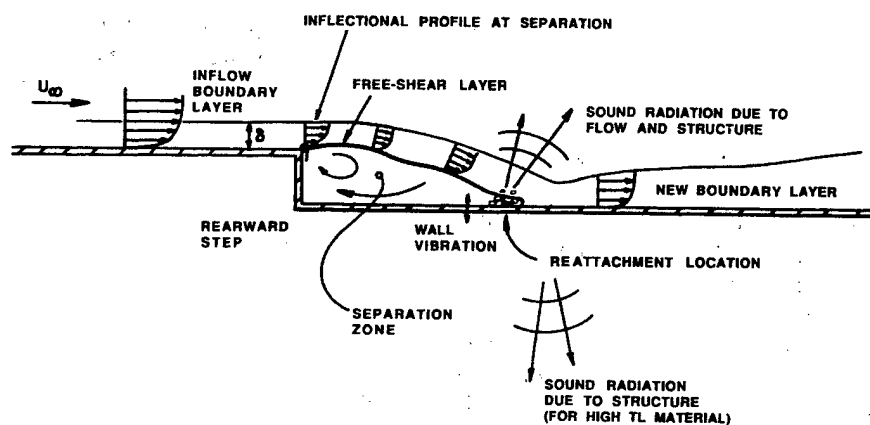


Fig. 1. Schematic of boundary-layer separation over a rearward-facing step. The inflow is from a convergent jet impinging on a 2-D flat plate that supports a TBL.

The flush-mounted pressure transducers are composed of B&K model 4165 (1.27 cm dia) microphones and supporting model 2639 preamplifiers powered by model 2087 power supplies. They are interfaced with the flow surface by a reduced area tube of 1.09 mm inside diameter and 5.7 mm in length. A cavity exists between the diaphragm of the microphone and

the inlet to the tube. It causes a microphone resonant response centered at 1 kHz. The peak response is 12 dB above the nominal free-field response of the microphone, and the half-power bandwidth of the resonance is ~200 Hz.

3. Flow reattachment

It is crucial to understand the fluid mechanics of the flow reattachment region to interpret the measured fluctuating wall pressure statistics. This can be accomplished conveniently by flow visualization. Figure 2 shows the flow pattern in the reattachment zone on the lower plate. This has been determined by photographing fluorescent mini-tufts under black light conditions. The tufts are secured to the plate surface using cyanoacrylate adhesive. The flow direction and "steadiness" is indicated by the orientation and "blurriness," respectively of the individual tufts. One can see tufts aligned with the flow direction downstream of reattachment and regions of reversed flow upstream of the reattachment zone. Of particular interest is the overall width of this zone, identified by the band of tufts that have random orientations. Upon studying many different flow visualizations like this, under various velocity conditions, the reattachment location is clearly identified as a random variable with a mean value, \bar{x}_r , that is weakly dependent on flow speed being proportional to $U_o^{0.1}$. The variation of the reattachment location, σ_{x_r} , is also determined from these data and is found to be proportional to $U_o^{0.5}$.

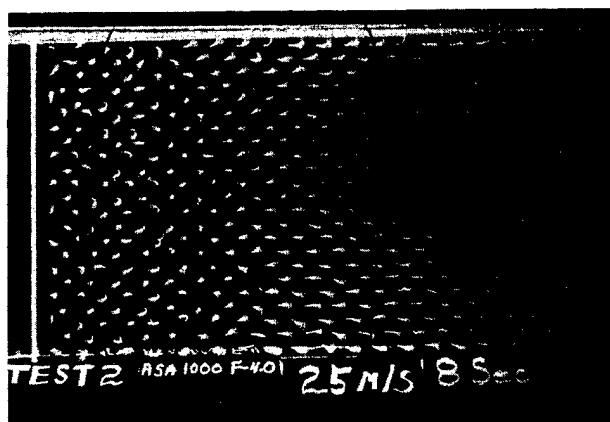


Fig. 2. An 8-s exposure of the mini-tufts exposed to 25 m/s mean flow velocity. The step is the vertical light line seen at the left.

4. Wall pressure fluctuations in reattachment region

The tube microphone was mounted at many streamwise locations along the centerline of the test plate. The signals were collected and analyzed using a Zonic System 7000 digital signal processor that was controlled by a Digital Equipment Corporation VAX Station 3100 m38. The spectral bandwidth is typically 3.125 Hz. Sufficient spectral averages were used to reduce random error to within ± 1 dB. Figure 3 shows the variation of root-mean-square wall pressure through the reattachment region. The peak rms level is high; it is only 24 dB below the dynamic head of the flow. It is seen to occur from 7 to 8 step heights downstream of the step.

The mean position of the flow reattachment region occurs at approximately 6 step heights downstream. Figure 4 shows the details of these variations with flow speed. The location of peak rms wall pressure is a short distance downstream of the mean position of flow reattachment. This difference is possibly due to the short lag time required for the new TBL to form and generate pressure producing velocity fluctuations.

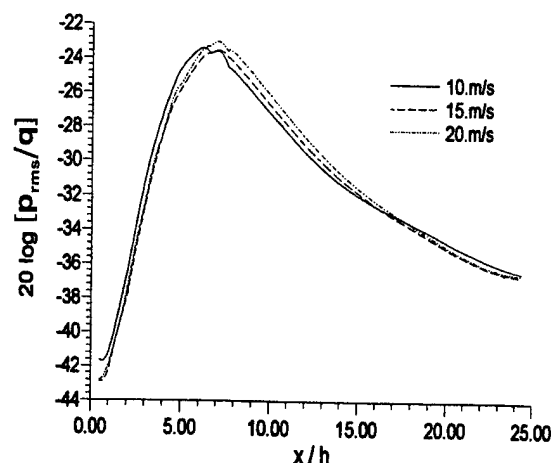


Fig. 3. Variation of rms wall pressure fluctuations with streamwise distance at different speeds.

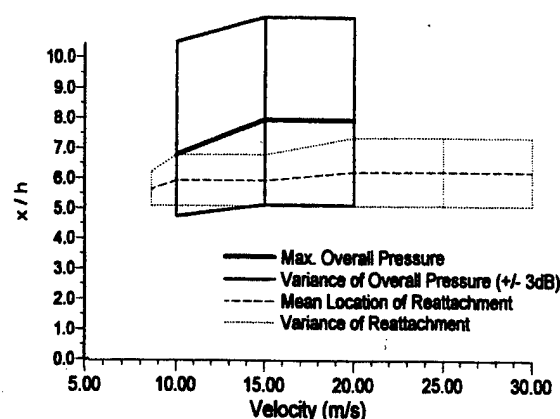


Fig. 4. Position of reattachment compared to the peak value of the rms wall pressure fluctuation.

The wall pressure spectral measurements were performed over extensive ranges of flow velocity ($7.82 \leq U_o \leq 25.1$ m/s) and streamwise location ($3.0 \leq x/h \leq 24.38$). The various types of TBL wall pressure spectrum scaling^{1,4,5} were considered in an unsuccessful attempt to collapse the current spectral data into a single, reasonably well-bounded, universal function. Thus, traditional spectral normalization methods appear to be inappropriate for the pressure fluctuations

occurring downstream of a step discontinuity. As noted previously,³ and also from the data of Fig. 3, we recognize that on both sides of the mean reattachment location, the mean-square wall pressure decreases approximately as $|x - \bar{x}_r|^{-1}$. This means that the spectral amplitude should be weighted by such a factor to compare spectra measured at various locations. The dependence of the spectral magnitude on velocity is found to be satisfied by the outer (inertial) flow scaling typical of TBLs, i.e., spectrum level is proportional to q^2 . The time scale h/U_o appears to be a more appropriate scale than δ^*/U_o . Physically, this means that the time scale of the wall pressure fluctuations is similar to that of the separation-induced vortex.

Now, Figs. 2 and 4 indicate that the reattachment location is chaotic; therefore, it must

be treated as a random variable. To use $|x - \bar{x}_r|^{-1}$ directly in a scaling formula without taking this fact into account will result in a singularity when the measurement point equals \bar{x}_r . To overcome this problem we define:

$$\Psi^2 = E[(x - x_r)^2] = (x - \bar{x}_r)^2 + \sigma_{x_r}^2, \quad (1)$$

where $E[\]$ represents the expected value operation performed over $N \gg 1$ individual records. The mean and variance terms of this expression are shown in Fig. 4. The new scaling formulation for the spectra, $G_{pp}(f)$, of the turbulent wall pressure fluctuations that occur at most locations downstream of a rearward facing step on a flat plate that supports a TBL and at any subsonic velocity is given by:

$$\frac{G_{pp}(f) \Psi U_o}{q^2 h^2} \quad \text{vs.} \quad \frac{fh}{U_o}. \quad (2)$$

Using Eq. (2), point power spectral densities measured at locations slightly upstream, near, and downstream of \bar{x}_r are nondimensionalized and presented for the considered range of velocities in Fig. 5. The collapse of these measured spectra into a single, well defined function is seen to be quite good. The variations for $1.5 < fh/U_o < 3$ are due to the microphone tube resonance. We note that the definition of Ψ assumes that the data shown in Fig. 3 are symmetric about the peak. This is strictly not the case, so the scaling is less valid for locations upstream of reattachment that are in the recirculation region. The spectra of Fig. 5 for $x/h = 3.05$ are measured as far upstream from \bar{x}_r as the scaling appears to apply.⁶ Equation (2) is actually most valid for locations that are within and farther downstream of the reattachment zone where the pressure fluctuations are created by energized boundary layer turbulence. In the recirculation zone, there is essentially no near-wall region of the boundary layer; thus, there would be less high-frequency pressure fluctuations created there. This statement is supported when comparing the spectra of Fig. 5 for $x/h = 3.05$ with those for $x/h = 6.10$ and 12.19 . The spectral levels measured just upstream of \bar{x}_r are some 11 to 15 dB lower than those measured within and downstream of \bar{x}_r for $fh/U_o \geq 1$.

5. Conclusions

The rms wall pressure fluctuations measured downstream of a rearward facing step discontinuity on a flat plate that supports a turbulent boundary layer are found to scale on the dynamic head of the flow, and to peak slightly downstream of the mean position of flow reattachment. The spectra of these fluctuations are found to be proportional to the inertial scales of the separated flow in addition to the statistical parameters describing the location of flow reattachment, which is a random variable. The scaling is most accurate within and downstream of the separation reattachment mean location. Upstream in the recirculation zone, the absence of any substantial near-wall turbulence results in pressure fluctuations that are quite low at high frequencies.

Acknowledgments

The work reported here was supported by Ford Motor Co., and ONR, Code 333.

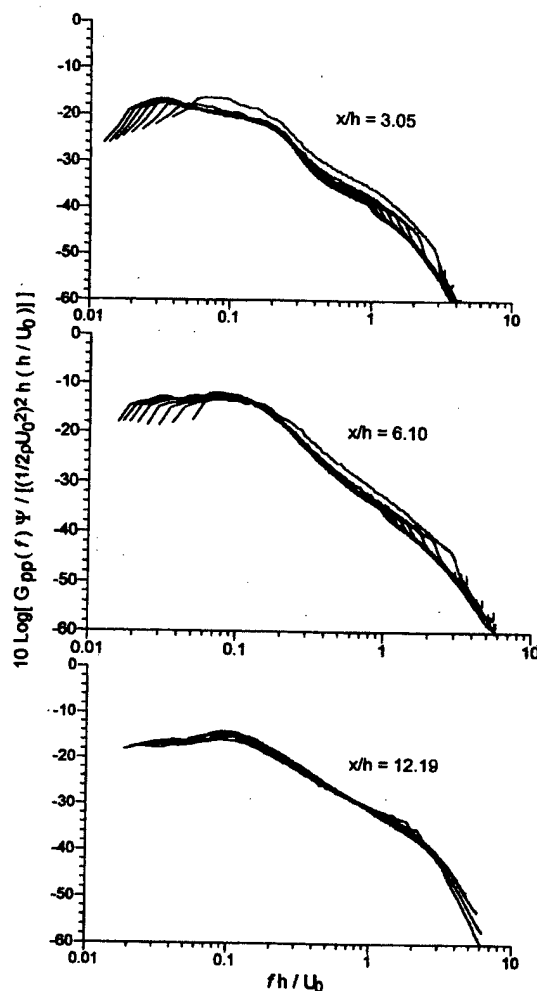


Fig.5. Dimensionless point power spectra of the local wall pressure fluctuations measured upstream ($x/h = 3.05$), near ($x/h = 6.10$), and downstream ($x/h = 12.19$) of the mean position of flow reattachment. The range of velocities for these measurements is from 7.82 to 25.1 m/s, and the step height, $h = 2.5$ cm.

References and links

- ¹ T. M. Farabee and M. J. Casarella, "Spectral Features of Wall Pressure Fluctuations Beneath Turbulent Boundary Layers," *Phys. Fluids A* **3**, 2410-2420 (1991).
- ² W. L. Keith, D. A. Hurdis, and B. M. Abraham, "A Comparison of Turbulent Boundary Layer Wall-Pressure Spectra," *Trans. ASME J. Fluids Eng.* **114**, 338-347 (1992).
- ³ T. A. Brungart, "Boundary Condition Effects on Turbulent Boundary Layer Wall Pressure Fluctuations," Ph.D. thesis, The Pennsylvania State University (1997).
- ⁴ T. M. Farabee, "An experimental Investigation of Wall Pressure Fluctuations Beneath Non-Equilibrium Turbulent Flow," Ph.D. thesis, Catholic University of America (1986).
- ⁵ T. M. Farabee and M. J. Casarella, "Effects of Surface Irregularity on Turbulent Boundary Layer Wall Pressure Fluctuations," *Trans. ASME J. Vib., Acoust., Stress, and Relia. Des.* **106**, 343-350 (1984).
- ⁶ W. A. Kargus IV, "Flow-Induced Sound from Turbulent Boundary Layer Separation Over a Rearward Facing Step," Ph.D. thesis, The Pennsylvania State University (1997).

APPENDIX 55



MODELING THE UNSTEADY LIFT AND DRAG ON A FINITE-LENGTH CIRCULAR CYLINDER IN CROSS-FLOW

D. E. CAPONE

*Pennsylvania State University, Applied Research Laboratory
P. O. Box 30, State College, PA 16804, U.S.A.*

G. C. LAUCHLE

*Pennsylvania State University, Graduate Program in Acoustics and Applied Research
Laboratory, P. O. Box 30, State College, PA 16804, U.S.A.*

(Received 30 July 1999, and in final form 31 March 2000)

Semi-empirical models for unsteady lift and drag are developed to predict the spectral features of the unsteady forces on a finite-length, right circular cylinder in cross-flow. In general, the models consist of two parts; the spatial variation of r.m.s wall pressure on the cylinder, and the correlation lengths which describe the spatial extent of the correlation of the unsteady wall pressures. Experiments were conducted in a low noise wind tunnel as a function of cylinder diameter Reynolds number ($19\,200 < Re < 32\,000$) and the Strouhal number ($0.05 < St < 3.33$), to measure the statistics of the unsteady wall pressures on a model cylinder. These results are incorporated into the theoretical models, and predictions of the spectral characteristics of the lift and drag are made. The r.m.s. wall pressures on the cylindrical surface are found to have the largest amplitude near the cylinder end-cap, and on the rearward portion of the cylinder body. The high levels in these locations are attributed to the separated flow region over the end-cap. The circumferential and axial length-scales decrease exponentially with Strouhal number. Both length-scales exhibit maxima near the Strouhal shedding frequency of $St = 0.21$. The axial length-scales are found to depend on the measurement reference location due to the three-dimensional flow and separated flow region near the end-cap. The unsteady lift and drag predictions using the models developed in this work agree well with previously measured unsteady force data measured on inertial hydrophones exposed to flow. The broadband unsteady lift is found to be greater than the broadband unsteady drag by nominally 3 dB.

© 2000 Academic Press

1. INTRODUCTION

MOORED OR SUSPENDED UNDERWATER ACOUSTIC SENSORS are used in numerous applications for the measurement and localization of underwater sound sources. The performance of these sensors is degraded by the presence of various background noise sources such as, oceanic ambient noise, electronic noise, mechanical suspension-induced noise, and flow noise. Flow noise results from the sensor being located in an environment where fluid flows over the body of the sensor. In the case of sensors configured as bluff bodies, the fluid is disturbed as it passes over the sensor, resulting in turbulence on the surface and in the wake of the body. The turbulence produces time-dependent pressure fluctuations on the surface of the sensor, which result in unsteady lift and drag forces acting on the sensor. Pressure, pressure gradient, and acoustic velocity hydrophones, in addition to acoustic intensity probes, respond to these unsteady body forces, resulting in a spurious signal known as flow noise.

The problem is particularly important for inertial sensors; the outputs of which are proportional to velocity or acceleration. One common shape used for underwater acoustic sensors is that of a finite-length right circular cylinder. Finger *et al.* (1979), and McEachern & Lauchle (1995) have shown that the unsteady forces on such finite-length cylinders can result in flow-induced self-noise being the major component of the transducer output signal. Similar results were identified for spherical-shaped hydrophones by Lauchle & Jones (1998).

Significant research has been performed on the measurement and prediction of unsteady lift and drag on two-dimensional, or "infinite length", cylinders in cross-flow. Ribeiro (1992) provided a comprehensive review of the fluctuating lift and spanwise correlation characteristics determined for 2-D cylinders. Considerably less work has been done on finite-length, or 3-D cylinders, due to the complexity of the problem and due to the limited application of the results.

The work of McEachern (1993), and McEachern and Lauchle (1995) quantified the unsteady lift and drag on finite-length, cylindrical-shaped hydrophones of various aspect ratios and end-cap corner radii. They found that the flow-induced noise on a pressure gradient, or acoustic velocity hydrophone decreases as the aspect ratio and corner radii increases. McEachern & Lauchle (1995) observed that the unsteady force spectra are broadband, and contained considerable energy at frequencies above the predicted vortex-shedding frequency. This observation is consistent with those of Keefe (1961) who noted that the flow over the endcap causes a decorrelation of the vortex-shedding process behind the cylinder, resulting in wake energy which is more broadband in nature. Farivar (1981) measured fluctuating pressures and forces on a cylinder with one end free and the other end mounted to the wall of a wind tunnel. The length-to-diameter ratio (L/D) ranges from 2.78 to 12.5 at a Reynolds number based on free-stream velocity and cylinder diameter of 7.0×10^4 . Definite vortex-shedding frequencies are present on the signals of the pressure sensors for $L/D > 7.5$, but for smaller aspect ratios, no discrete shedding frequency was detected.

Baban *et al.* (1989) measured unsteady forces on both a 2-D cylinder and a 3-D cylinder with one free end. Flow visualization showed an unsteady flow reversal region behind the 3-D cylinder of approximately two cylinder diameters in streamwise length, and of width comparable to the span (L) of the cylinder. A strong correlation between the fluctuating lift and the fluctuating streamwise velocity component was evident for the 2-D case; however, for the 3-D experiment, correlation was essentially nonexistent. The presence of the separated flow over the end of the cylinder inhibits the formation of coherent vortices along the span of the cylinder. Also, the large unsteady recirculation zone behind a finite-length cylinder breaks up the coherent vortices shed by the cylinder. The fluctuating local drag for the 3-D case was found to be larger than the fluctuating local lift measured near the free end of the cylinder.

Due to the complexity of the flow field for any given sensor orientation, no analytical model for the unsteady forces generated on a finite-length circular cylinder in either steady or unsteady flow exists. The objective of this work is to develop semi-empirical models for the statistics of the surface pressure field, in order to predict the spectral features of the unsteady forces on finite-length, right circular cylinders in uniform, steady cross-flow. These models can be used for the prediction of the statistical features of the flow noise signal of acoustic sensors of interest.

2. THEORY

2.1. GENERAL FORMULATION

The coordinate system for the circular cylinder is shown in Figure 1. The total unsteady drag on a cylinder can be found by the integration of the projected surface pressures in the

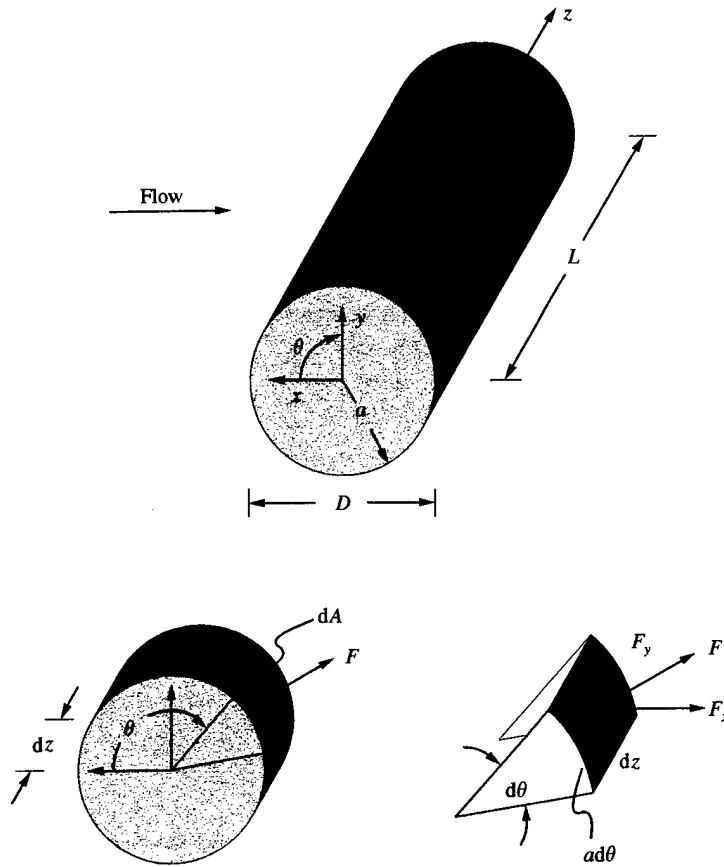


Figure 1. Coordinate system for the right circular cylinder in cross-flow.

x-direction over the surface area of the cylinder:

$$f_x(t) = a \int_0^L \int_0^{2\pi} p(\theta, z, t) \cos \theta \, d\theta \, dz, \quad (1)$$

where $p(\theta, z, t)$ is the unsteady pressure on the surface of the cylinder body. Similarly, the fluctuating lift can be found by replacing the cosine term in equation (1) with a sine term. The autocorrelation of the unsteady drag, using the notation of Bendat & Piersol (1986) for stationary signals, may be represented as

$$R_{xx}(\tau) = E[f_x(t)f_x(t + \tau)], \quad (2)$$

where the variable τ is the time displacement between any two signals and $E[\]$ represents the expected value which is an ensemble average over N records. Substitution of equation (1) into equation (2) yields

$$R_{xx}(\tau) = a^2 \int_0^L \int_0^L \int_0^{2\pi} \int_0^{2\pi} E[p(\theta, z, t)p(\theta', z', t + \tau)] \cos \theta \, d\theta \cos \theta' \, d\theta' \, dz \, dz'. \quad (3)$$

Taking the temporal Fourier cosine transform of equation (3) twice, results in the one-sided autospectrum for the unsteady drag:

$$G_{xx}(f) = a^2 \int_0^L \int_0^{2\pi} \int_0^L \int_0^{2\pi} \Gamma(\theta, \theta', z, z', f) \cos \theta \, d\theta \cos \theta' \, d\theta' \, dz \, dz', \quad f \geq 0. \quad (4)$$

Here $\Gamma(\theta, \theta', z, z', f)$ is the one-sided cross-spectral density function of the unsteady pressures on the cylindrical surface. The autospectrum for the unsteady lift is found by replacing the cosine terms in equation (4) with sine terms.

It can be seen by equation (4) that the unsteady lift and drag forces on the cylinder can be calculated if the wall pressure cross-spectra among all points on the body of the cylinder are known. Due to the number of measurements required for this method, few researchers have adopted this approach. However, such measurements are possible, and easier to perform using modern computer-aided data-acquisition methods. In this research we have adopted the approach described in equation (4), and the results are used to form a model of the cross-spectral densities. In the following section, unsteady lift and drag models will be developed in terms of correlation areas so that future calculations of the unsteady forces on similar cylinders in cross-flow can be performed with only a limited number of experimental measurements.

2.2. MODELS FOR THE UNSTEADY LIFT AND DRAG

A correlation area, Crighton *et al.* (1992) for unsteady drag is defined as

$$S_{cx}(f, \theta, z) \equiv \frac{a \int_0^L \int_0^{2\pi} \Gamma(f, \theta, \theta', z, z') \cos \theta' \, d\theta' \, dz'}{\Gamma(f, \theta, z)}, \quad (5)$$

where $\Gamma(f, \theta, z)$ represents the one-sided autospectrum of the wall pressure fluctuations at locations θ and z . The larger the region over which the pressures are correlated, and hence the larger value for the correlation area, the larger will be the unsteady drag on the cylinder.

If one assumes the circumferential and axial components of the cross-spectral density are separable, similar to the Corcos (1964) theory for turbulent boundary layer wall pressure spectra, the correlation area for unsteady drag can then be represented as

$$S_{cx}(f, \theta, z) \cong a \Lambda_x(f, \theta, z) \Lambda_z(f, \theta, z), \quad (6)$$

where $\Lambda_x(f, \theta, z)$ and $\Lambda_z(f, \theta, z)$ are integral length-scales in the circumferential and axial directions, respectively; see Crighton *et al.* (1992) for a complete description of length-scales. Before defining the integral length-scales for the cylinder, a change of variables will be made in the cross-spectral density representation used in equation (4). In particular, let θ' be replaced by the separation angle $\Delta\theta$, and z' be replaced by the separation distance Δz . The new variables clearly show that the measured cross-spectral densities are a function of both measurement location, and separation distance. With the specified changes in variables, the circumferential correlation length, in radians, for the unsteady drag is defined as

$$\Lambda_x(f, \theta, z) \equiv \int_{-\theta}^{2\pi-\theta} \frac{\Gamma(f, \theta, \Delta\theta)}{\Gamma(f, \theta, z)} \cos(\theta + \Delta\theta) \, d\Delta\theta, \quad (7)$$

and the circumferential correlation length for the unsteady lift is

$$\Lambda_y(f, \theta, z) \equiv \int_{-\theta}^{2\pi-\theta} \frac{\Gamma(f, \theta, \Delta\theta)}{\Gamma(f, \theta, z)} \sin(\theta + \Delta\theta) \, d\Delta\theta, \quad (8)$$

The axial correlation length, in the units of z , is defined as

$$A_z(f, \theta, z) \equiv \int_{-z}^{L-z} \frac{\Gamma(f, z, \Delta z)}{\Gamma(f, \theta, z)} d\Delta z. \quad (9)$$

The last step in the modeling of the unsteady lift and drag forces, is the definition of a simplified representation for the unsteady surface pressures on the cylinder. Let $\Gamma(f, \theta, z)$ be represented by

$$\Gamma(f, \theta, z) = G_{p,p.}(f, \theta_r, z_r) A(\theta, z), \quad (10)$$

where $G_{p,p.}(f, \theta_r, z_r)$ is a reference autospectral density of the wall pressure, p_r , at a specified reference location (θ_r, z_r) , and $A(\theta, z)$ is a deterministic function describing the dependence of the mean-square value of the unsteady pressure on measurement location. For this investigation, $G_{p,p.}$ is taken at the point, $\theta_r = 80^\circ$ and $z_r/D = 1.0$. This chosen value of θ_r coincides with the typical position of boundary layer separation from the surface of a cylinder in the subcritical flow regime.

Substitution of equations (10), (9) and (7) into equation (4) results in the final form of the model for the unsteady drag on the cylinder in cross-flow:

$$G_{xx}(f) = G_{p,p.}(f, \theta_r, z_r) \left\{ a^2 \int_0^L \int_0^{2\pi} A_x(f, \theta, z) A_z(f, \theta, z) A(\theta, z) \cos \theta d\theta dz \right\}. \quad (11)$$

Replacing the cosine term in equation (12) with a sine term, and changing to the circumferential lift correlation length, yields the final form of the model for unsteady lift:

$$G_{yy}(f) = G_{p,p.}(f, \theta_r, z_r) \left\{ a^2 \int_0^L \int_0^{2\pi} A_y(f, \theta, z) A_z(f, \theta, z) A(\theta, z) \sin \theta d\theta dz \right\}. \quad (12)$$

The next section will present the experimental methods used to measure the unsteady pressures on the cylinder body. The experiments involve the measurement of the space-frequency correlations of the fluctuating wall pressures. Analysis of the measurements will determine the length-scales and functional forms of the parameters needed in equations (11) and (12).

3. EXPERIMENTAL SETUP

3.1. WIND TUNNEL

Fluctuating wall pressure measurements were made on a 0.305 m long and 0.153 m diameter aluminum cylinder in a specially designed low-noise wind tunnel located in a hemi-anechoic chamber. The cylinder was rigidly mounted to a stinger attached to the midpoint of the cylinder at the rearward stagnation point. This mounting arrangement provided a finite-length cylinder with two ends which were free of mounting induced flow disturbances. A side-view of the wind tunnel test-section is shown in Figure 2. The contraction section of the wind tunnel, which has an 11:1 contraction ratio, leads to a 0.457 m square test-section, which is 1.50 m long. Downstream, the test-section diffuses at a 7° angle to slow the flow, thereby minimizing acoustic radiation from the trailing edge of the open-ended exit. The cylinder was held by a 0.305 m long sting attached to a vertical steel tube with an aerodynamic cross-section.

Prior to making unsteady pressure measurements on the cylinder, both the mean, U_∞ , and the fluctuating, u' , velocity field in the test section were characterized. Mean velocity profile surveys were conducted over a plane normal to the flow direction and situated at the leading edge of the cylinder. The flow speeds considered were 1.83, 2.44 and 3.06 m/s, which

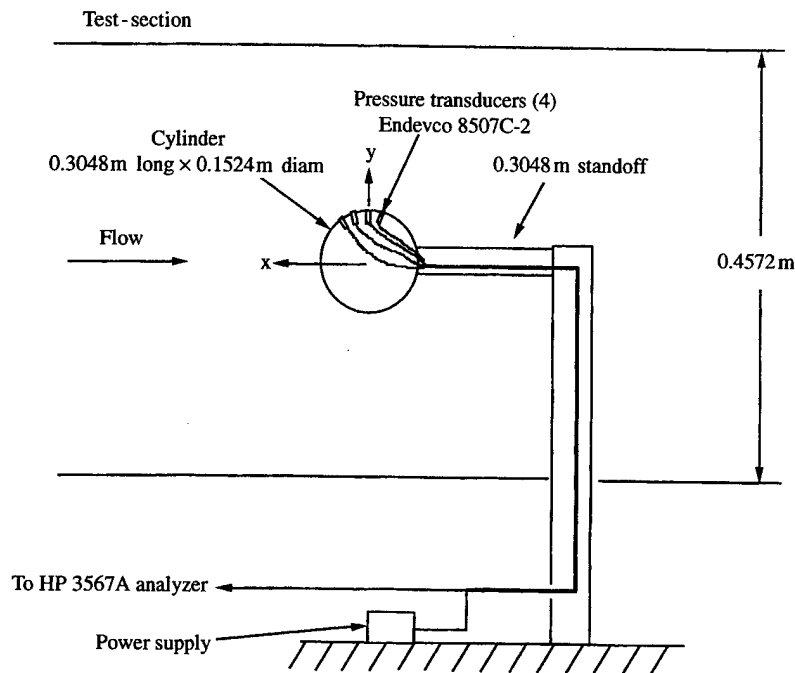


Figure 2. Side view of wind tunnel test-section with cylinder mounted in test position.

correspond to cylinder diameter Reynolds numbers of 19200, 25600, and 32000, respectively. The mean velocity across the test-section was within $\pm 2.0\%$ of that measured at the centerline. The streamwise component of turbulence intensity at the same location was less than 0.5% for all three speeds.

3.2. UNSTEADY WALL PRESSURE MEASUREMENTS

Unsteady wall pressure measurements were made at the Reynolds numbers noted in Section 3.1 and over a frequency range of 1–40 Hz, corresponding to Strouhal numbers, fD/U_∞ , ranging from 0.05 to 3.33. For brevity, detailed results for $Re = 19\,200$ and $32\,000$ will be presented in this paper. Results for $Re = 25\,600$ will be used to formulate conclusions and to verify the scaling relationships developed. For all Reynolds numbers, a detailed map of the unsteady wall pressure field on the body of the cylinder was acquired. Spectral data were obtained using a Hewlett Packard (HP) 3567A dynamic signal analyzer. The analyzer was set up with: 256 averages, Hanning window, 800 lines of resolution, and a 2048 line FFT. The acquired data were corrected to a 1 Hz bandwidth. The wind tunnel background noise measurements were made using a 0.635 cm diameter Brüel and Kjær (B&K) model 4138 microphone, and a B&K model 2633 preamplifier. Prior to mounting the model in the test section, the background noise of the tunnel was measured at all three flow speeds using the B&K microphone mounted in a slit tube. The slit tube allows measurement of the background acoustic noise in a wind stream while discriminating against boundary layer flow noise on the sensor. The unsteady pressures on the surface of the cylinder were measured using four individual Endevco 8507C-2 piezoresistive pressure transducers. These transducers have an active sensing diameter of 0.234 cm.

The cylinder model had a series of 2.67 mm diameter holes drilled in the surface, and the transducers were press-fit into these holes. When the holes were not being used for pressure

measurements, they were filled with modeling clay and faired smooth with the surface of the cylinder. Holes were drilled from $\theta = 80$ to 180° , in 10° increments at eight spanwise locations: $z/D = 0.08, 0.17, 0.33, 0.50, 0.67, 0.83, 1.0$, and 1.91 measured from the end-cap (Figure 1). At the cylinder centerline, $z/D = 1.0$, holes were also drilled from $\theta = 0$ to 80° , in 10° increments. Lastly, at 80 and 90° , a spanwise array of holes were drilled at $z/D = 1.33, 1.50, 1.67, 1.75$, and 1.83 . The hole locations allowed the pressure transducer measurement locations to be systematically varied over the cylinder in both the circumferential and axial directions.

4. RESULTS

4.1. UNSTEADY WALL PRESSURE POWER SPECTRAL DENSITIES

The flow field about the cylinder in the θ -direction is expected to be non homogeneous due to laminar, turbulent, and separated flow regions. Figure 3 shows the circumferential variation of the unsteady wall pressure power spectral densities at axial locations $z/D = 1.0$ and 0.08 . It is evident from Figure 3 that the unsteady wall pressure magnitudes depend on the circumferential measurement location. Although the spectra of the unsteady pressure fluctuations vary with location, the character, or shape, of each curve is consistently the same. The lowest levels are where the boundary layer is laminar and attached to the

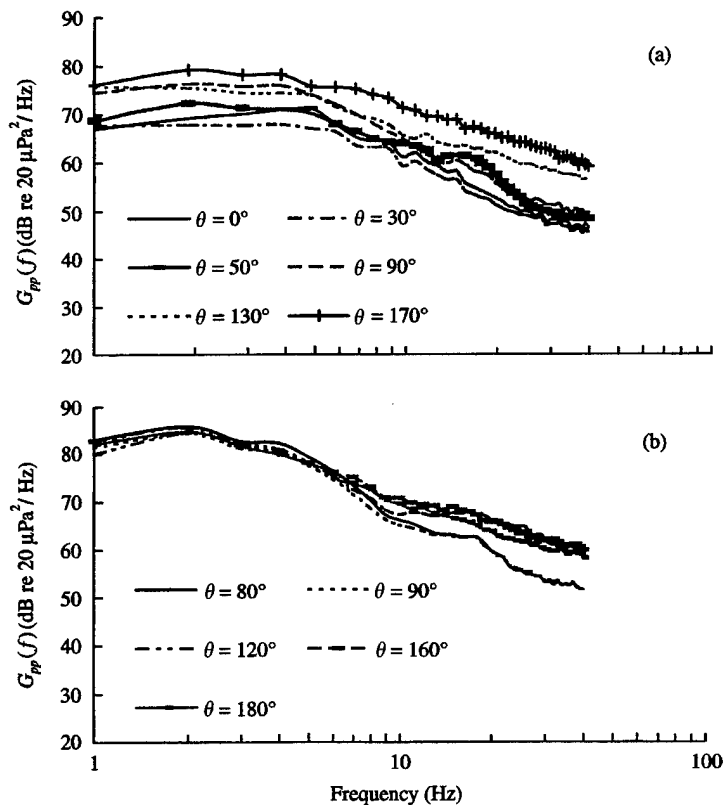


Figure 3. Circumferential variation of the unsteady wall pressure power spectral density for $Re = 32000$. (a) $z/D = 1.0$, (b) $z/D = 0.08$.

surface of the cylinder. They increase towards the rearward portion of the cylinder. Also, as one proceeds from the centerline towards the end-cap of the cylinder ($z/D = 1.0-0.08$) the spectral level increases for a given circumferential location. This result is consistent with the findings of Farivar (1981), who found a maximum in the unsteady wall pressures near the free end of a cantilevered cylinder.

In order to facilitate the modeling of the unsteady forces on the body, a functional form of the root-mean-square (r.m.s.) value of the unsteady wall pressures on the cylinder body was determined using curve-fitting routines. The r.m.s. unsteady wall pressure levels, for $Re = 32000$ and 19200 , are shown in Figure 4. Note that the r.m.s. pressures are normalized by the dynamic head of the free stream, $q = 1/2\rho U_\infty^2$. For $Re = 19200$, an increase in the unsteady pressure level is evident only for spanwise locations $z/D \leq 0.33$, while for the higher Re , the level appears to increase continuously with increases in z/D . The general increase in level as the end-cap is approached is not unexpected because a complicated separated flow field exists there, e.g., see flow visualization photographs in McEachern & Lauchle (1995) or McEachern (1993). In general, the boundary layer separates off the leading edge of the end-cap and eventually mixes with the other separated boundary layer that exists on the cylindrical part of the body. At higher values of the Reynolds number, this mixing occurs downstream, away from the measurement transducers; thus, the levels of Figure 4(a) tend to reach their maximum and stay there. At the lower Reynolds number,

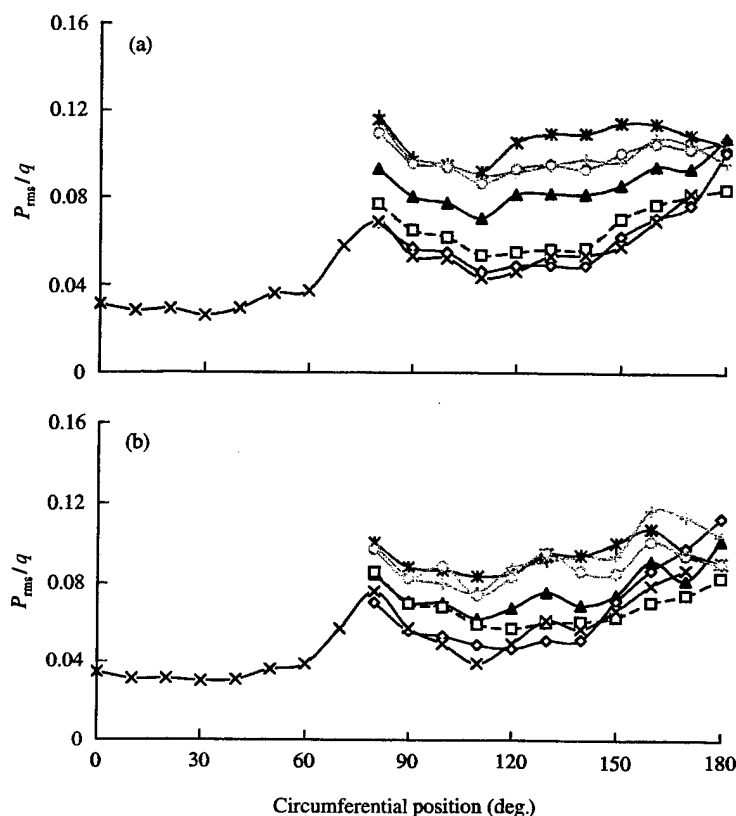


Figure 4. The r.m.s. values of the unsteady wall pressure for all measurement locations on the cylinder body for (a) $Re = 32000$ (b) $Re = 19200$: —*, $z/D = 0.08$; —+, $z/D = 0.17$; —○, $z/D = 0.33$; —▲, $z/D = 0.50$; —□, $z/D = 0.67$; —◇, $z/D = 0.83$; —x, $z/D = 1.00$.

Figure 4(b), the mixing zone of these two separated boundary layers moves further upstream and the pressure transducers respond to the increased turbulent activity. Local reattachment of the shear layer also contributes to the high unsteady pressure levels.

The cylinder centerline separation point ($\theta_r = 80^\circ$, $z_r/D = 1.0$) is used as the reference location for the autospectral density, $G_{p,p}(f, \theta_r, z_r)$, in equation (10). The reference autospectral density captures the frequency dependence of the unsteady pressures at a well-defined point on the surface of the body. The curve fitting allows us to derive an empirical equation, $A(\theta, z/D)$, which describes the variation of the r.m.s wall pressures at any location on the cylinder body relative to that at the reference location.

The r.m.s. unsteady wall pressures were modeled in three ways: a third-order polynomial surface fit, a second-order polynomial surface fit, and a separable model. It was found that the separable model of the unsteady wall pressures overpredicted the measured unsteady force on the cylinder by 10 dB. Clearly, the assumption of separability of the circumferential and axial dependence of the unsteady wall pressures is a weak one. Both the second- and third-order polynomial surface fits result in similar predictions of the unsteady forces on the cylinder; however the second-order polynomial surface fit requires four fewer empirical coefficients, six versus 10. Therefore, results for the second-order polynomial surface fits are presented here. Figure 5 shows a surface plot of the experimental data, and the second-order polynomial surface fit of these data at $Re = 32\,000$. The second-order surface fit is described by

$$A(\theta, z/D) = \frac{p_{rms}}{q} (c_1 z_D^2 + c_2 \theta^2 + c_3 z_D \theta + c_4 z_D + c_5 \theta + c_6),$$

where

$$\begin{aligned} c_1 &= 0.013, \quad c_2 = 0.027, \quad c_3 = 0.018, \quad c_4 = -0.102, \\ c_5 &= -0.125, \quad c_6 = 0.242, \quad \text{and } z_D \equiv z/D. \end{aligned} \quad (13)$$

The quantity p_{rms} is the reference r.m.s. pressure fluctuation value, and the empirical constants c_1 – c_6 are an arithmetic average of the coefficients fit for the data from all three Reynolds numbers tested. The second-order polynomial surface fit captures the gross features of the r.m.s values of the wall pressure fluctuations on the body of the cylinder within the range of Reynolds numbers considered. The fine-scale details are not captured because of the models selected.

4.2. CIRCUMFERENTIAL CROSS-SPECTRAL RESULTS

The circumferential length-scales, equations (7) and (8), are calculated using the measured unsteady pressure cross-spectral data as a function of reference location, axial location, and frequency (or Strouhal number). Cross-spectra were measured at discrete pairs of separation points, but the correlation length calculation requires a continuous representation of the cross-spectra as a function of separation distance. Therefore, a third-order polynomial fit to the measured cross-spectral data is numerically integrated to produce the correlation lengths. This process is repeated for each frequency and given reference location. Significant frequency-to-frequency variation was observed in the calculated correlation lengths. This is due to the finite spatial resolution and narrow frequency resolution of the measurements. A finer spatial resolution would provide correlation lengths which are less sensitive to individual cross-spectral results in the curve fitting procedure.

A least-squares fit to the circumferential lengthscales for unsteady lift and drag at five axial locations and $Re = 32\,000$ are shown in Figure 6. Additional axial locations and greater detail is shown in Capone (1999). In general, the unsteady drag correlation lengths are shorter than those for the unsteady lift. The correlation lengths all tend to peak around

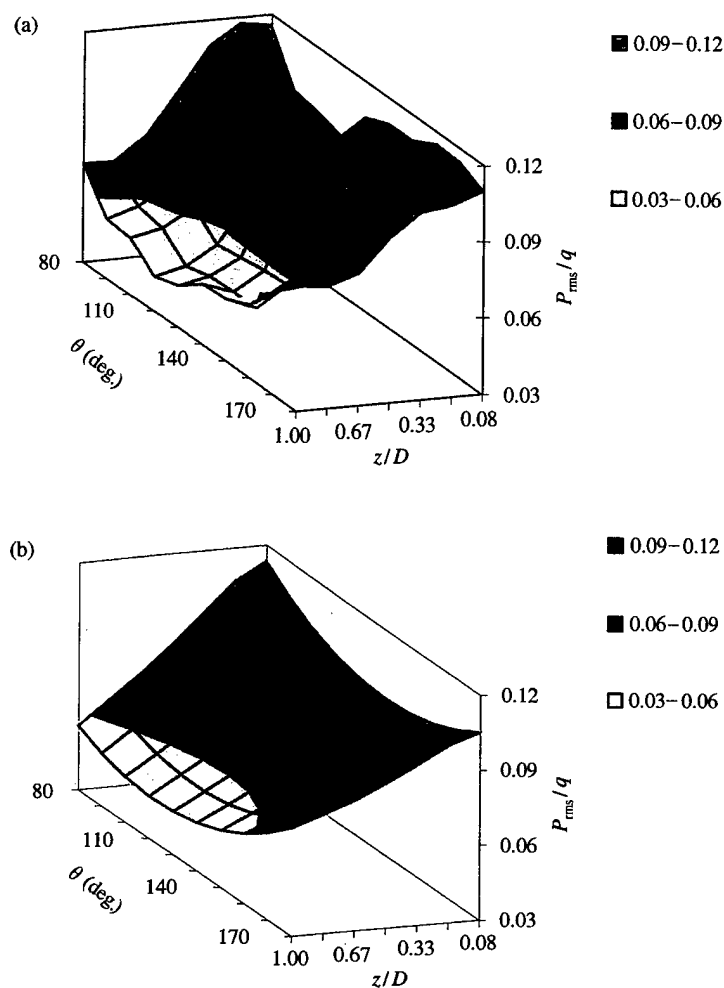


Figure 5. Surface plot and surface fit of the r.m.s. unsteady wall pressures using a second-order polynomial surface fit at $Re = 32\,000$: (a) surface plot; (b) surface fit.

the Strouhal shedding frequency of 0.21. Below $St = 0.21$ the correlation lengths are small, while above $St = 0.21$, the lengthscales decrease mildly with increasing St . The boundary layer thickness affects the wake thickness, and essentially the upper limit of the eddy size that can exist within the flow. Below a certain cut-off frequency, in this case around $St = 0.21$, the flow cannot support structures larger than the largest eddies in the wake; hence, the correlation lengths approach zero very rapidly. Turbulent eddies decorrelate as they convect. The smaller scale, higher frequency eddies decorrelate more rapidly than the larger ones for a given separation distance, resulting in a progressively decreasing correlation length with increasing St .

The Strouhal number dependence of the correlation lengths is modeled using an equation similar to a Rayleigh probability distribution function. Here, the unsteady lift correlation lengths are represented by

$$A_y(St) = 1 + \frac{E_1 St}{E_2^2} \exp\left[\frac{-St}{(2E_2^2)}\right], \quad (14)$$

where E_1 and E_2 are empirical constants.

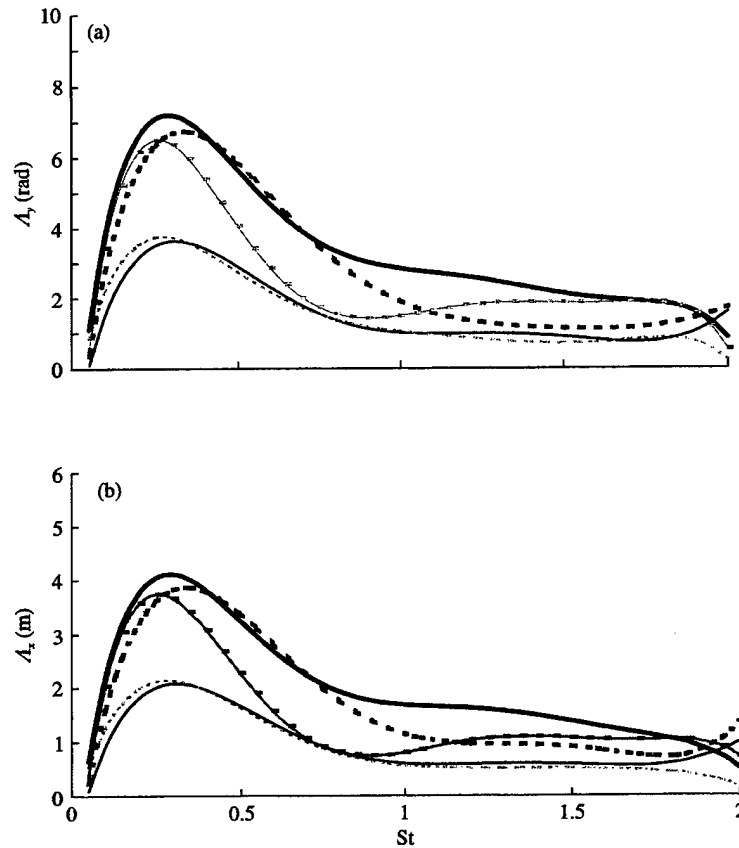


Figure 6. Circumferential correlation lengths for unsteady lift and drag at $Re = 32000$ with a reference location of $\theta = 80^\circ$ for (a) unsteady lift, (b) unsteady drag: —, $z/D = 0.08$; ----, $z/D = 0.33$; — · —, $z/D = 0.50$; — — —, $z/D = 0.83$; - - - -, $z/D = 1.0$.

The variation of the streamwise correlation lengths with axial location are determined from cross-plots of the length-scale data as a function of z/D . Unfortunately, the data points, as shown in Figure 6, show variation from location to location for certain discrete values of the Strouhal number. Approximately, however, the correlation lengths can be modeled assuming they remain essentially independent of z/D for axial locations, $0.5 \leq z/D \leq 1.0$. For axial locations of $z/D < 0.5$, the correlation lengths decrease markedly and are more sensitive to changes in z/D . With these assumptions, the empirical curve fit for the axial variation of the unsteady lift length-scales is given by

$$A_y(z/D) = \exp \left[- \left(\frac{L}{2D} - z/D \right)^2 \right], \quad 0.0 \leq z/D < \leq 2.0. \quad (15)$$

The final step in modeling the correlation lengths for unsteady lift and drag is to account for the variation in length-scale as a function of reference measurement location. This dependence is examined for circumferential reference locations: $\theta_r = 80^\circ, 100^\circ, 120^\circ$, and 140° and axial locations $z/D = 1.00, 0.50$, and 0.08 . Figure 7 shows the least-squares fit to the unsteady lift correlation lengths at $Re = 32000$ for axial locations of $z/D = 0.5$ and 0.08 and for the four circumferential reference locations. It is observed that, for $z/D = 0.5$, the

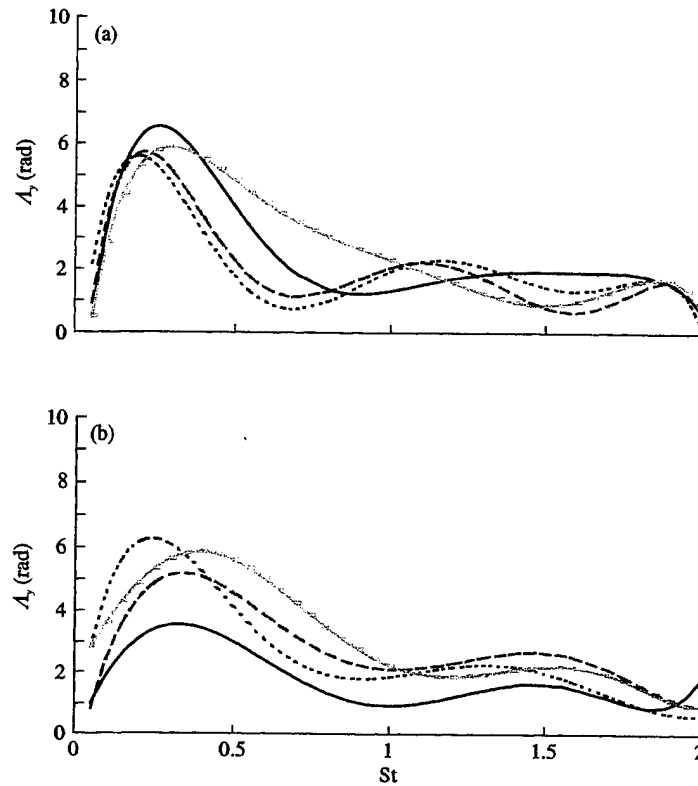


Figure 7. Circumferential correlation lengths for $Re = 32000$ and for circumferential reference locations $\theta_r = 80, 100, 120$, and 140° for (a) $z_r/D = 0.5$ and (b) $z_r/D = 0.8$: —, $\theta = 80^\circ$; ---, $\theta = 100^\circ$; ····, $\theta = 120^\circ$; — · —, $\theta = 140^\circ$.

correlation lengths are essentially the same, independent of the reference location. At $z/D = 0.08$, a more noticeable variation in the correlation lengths is evident with circumferential reference location $\theta_r = 80^\circ$, especially for Strouhal numbers less than 1.0.

Gershfeld (1996) measured pressure cross-spectra in a spatially inhomogeneous turbulent wall pressure field near a blunt trailing edge of a lifting surface. He concluded, as we have, that the inhomogeneous nature of the wall pressure field can be captured primarily by the streamwise variation in the point power spectra. Here, the inhomogeneity seems to be most pronounced as the end-cap is approached. Sectional unsteady lift coefficients measured by Baban, *et al.* & Ottugen (1989) for a cantilevered cylinder, also show a slight decrease as one progresses towards the free end. Baban *et al.* attributed this to the highly three-dimensional flow near the end-cap which obviously contributes to the spanwise inhomogeneity observed for $z/D = 0.08$. Because the increase in lift correlation length is primarily evident only in the $z/D = 0.08$ axial range and for $St < 1.0$, the final form of the model for the circumferential length-scales will assume reference location independence.

Based upon the assumptions discussed above, the final form for the circumferential length-scales for unsteady lift and drag are obtained from equations (14) and (15):

$$A_y(St, z/D) = \left(1 + \frac{E_1 St}{E_2^2} \exp \left[\frac{-St}{(2E_2^2)} \right] \right) \exp \left[- \left(\frac{L}{2D} - z/D \right)^2 \right], \quad (16a)$$

$$A_x(St, z/D) = \left(1 + \frac{E_3 St}{E_2^2} \exp \left[\frac{-St}{(2E_4^2)} \right] \right) \exp \left[- \left(\frac{L}{2D} - z/D \right)^2 \right], \quad (16b)$$

where

$$E_1 = 5.0, \quad E_2 = 0.39 \quad \text{and} \quad E_3 = 5.0.$$

Predictions using equation (16) are compared to the circumferential length-scales at $Re = 32000$ in Figure 8.

4.3. AXIAL CROSS-SPECTRAL RESULTS

The axial length-scales, equation (9), were also calculated from the measured unsteady pressure cross-spectral data. These length-scales are computed as a function of reference location, streamwise location, and frequency, and a suggested model form is derived.

The least-squares fit to the axial length-scales at $Re = 32000$ and 19200 for circumferential locations of $\theta = 80, 120, 140$, and 180° , and a reference location of $z_r/D = 0.08$ are shown in Figure 9. As with the circumferential length-scales, the higher frequency, smaller scale eddies which produce the high-frequency pressure fluctuations decay faster than the lower frequency eddies, which results in a general decrease in Λ_z with increasing frequency.

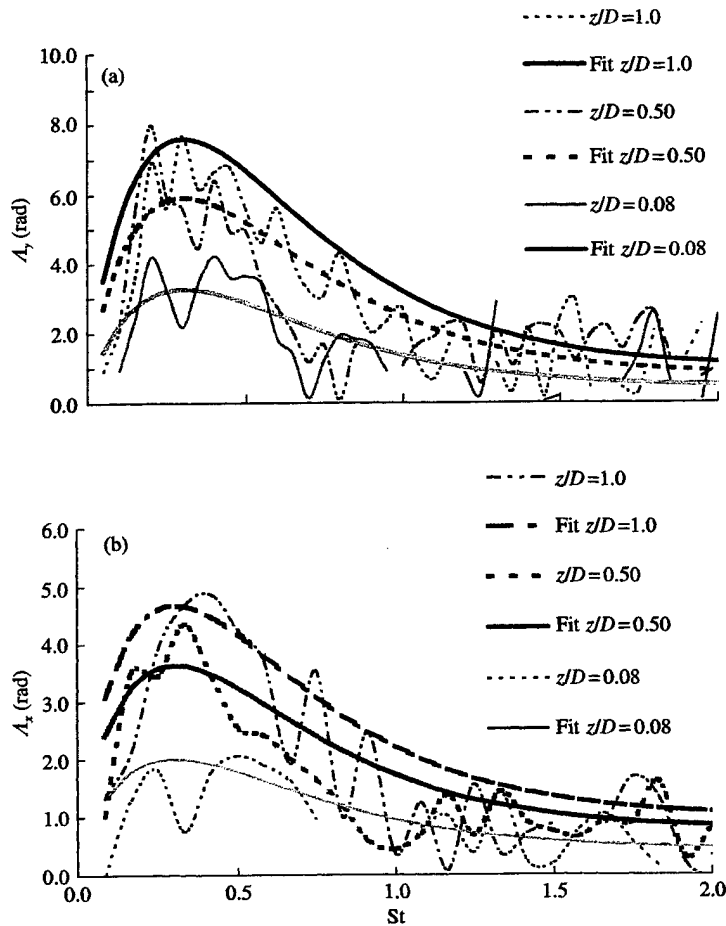


Figure 8. Empirical fit of the correlation lengths for unsteady lift and drag as a function of Strouhal number and axial location compared to measured data with a reference location of $\theta = 80^\circ$ and $Re = 32000$ (a) unsteady lift, (b) unsteady drag.

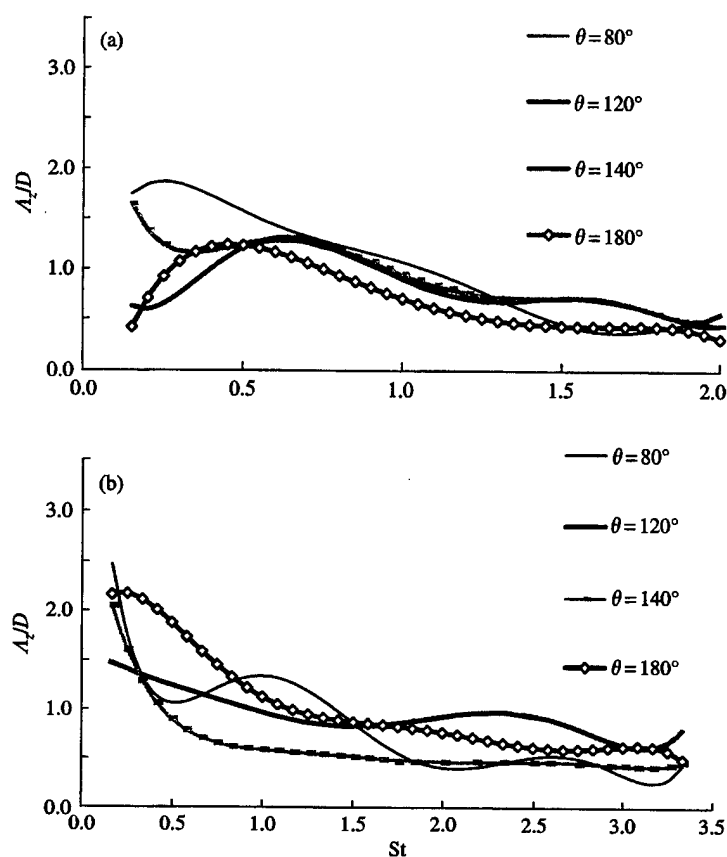


Figure 9. Axial length-scales at $Re = 32\,000$ and $19\,200$ for circumferential locations of $\theta = 80, 100, 120, 140$, and 180° , and a reference location of $z/D = 0.08$ for (a) $Re = 32\,000$, (b) $Re = 19\,200$.

The axial length-scales measured for all three Reynolds numbers are very similar in magnitude and spectral shape, consistent with West & Apelt (1997) who found that the spanwise length-scales on infinite cylinders are independent of Reynolds number over the range 10^4 – 2.1×10^5 . We will further assume that the dependence of A_z on θ is negligible. The Strouhal number dependence of the axial correlation lengths is therefore modeled using the empirical fit of the form

$$\frac{A_z}{D}(St) = E_4 \exp[-St^{0.75}]. \quad (17)$$

The dependence of the axial length-scales on axial reference location is established by examining the data from only two circumferential locations because of the assumption that they are independent of circumferential location at constant z/D . Figure 10 shows the least-squares fit to the spanwise correlation lengths for $\theta_r = 100$ and 140° at $Re = 32\,000$. The correlation lengths increase as the reference location is moved towards the center of the cylinder. This behavior is due to the fact that the flow near the center of the cylinder is less disturbed by 3-D end-cap-flow effects. The flow is more two-dimensional, and a larger axial correlation length is expected.

The variation of the axial correlation length with axial reference location is determined from cross-plots of the data of Figure 10. Similar to the circumferential length-scales, the

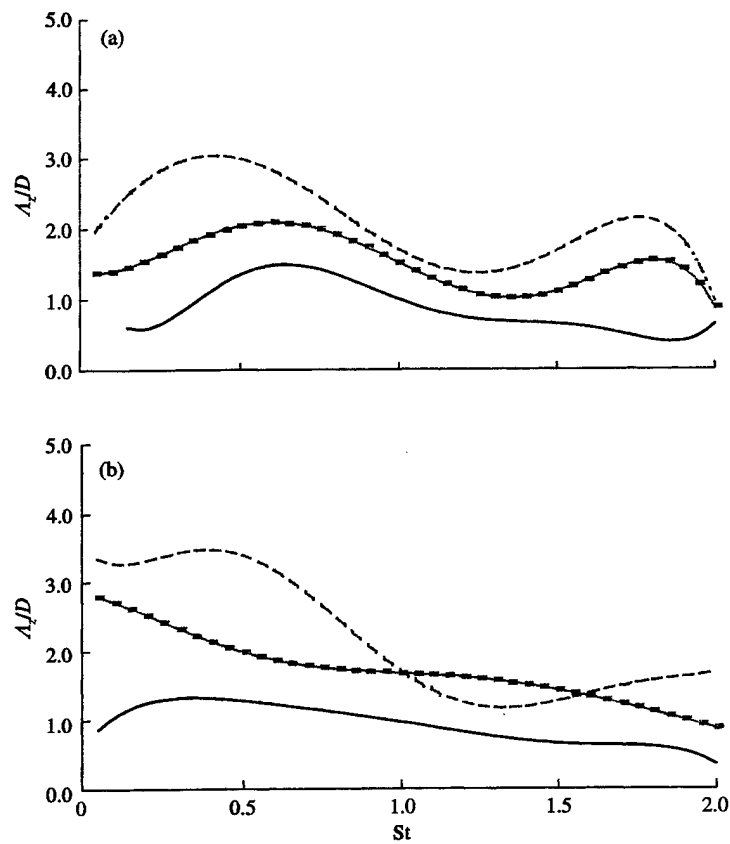


Figure 10. Axial correlation lengths for $Re = 32000$ and for reference locations of $z/D = 0.08, 0.50$, and 1.0 and (a) $\theta_r = 100^\circ$, (b) $\theta_r = 140^\circ$: —, $z/D = 0.08$; ---, $z/D = 0.5$; - - -, $z/D = 1.0$.

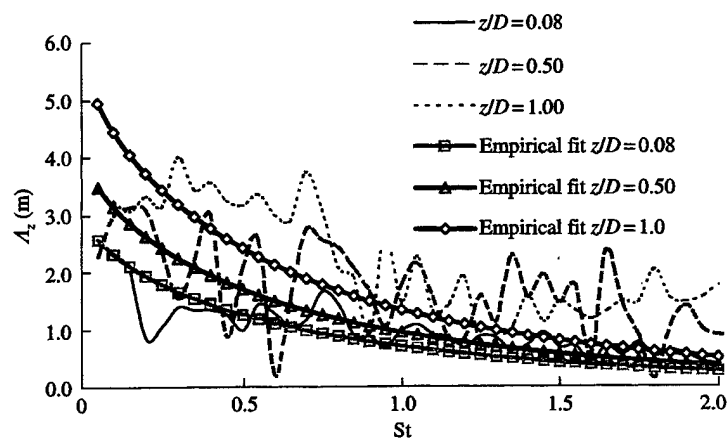


Figure 11. Empirical fit of axial length-scales for various axial locations as a function of Strouhal number for $\theta_r = 140^\circ$ and $Re = 32000$.

axial length-scales show an approximately exponential decrease with decreasing z/D . Combining equation (17) with this exponential function, yields

$$\frac{A_z}{D}(\text{St}, z/D) = E_4 \exp[-\text{St}^{0.75}] E_5 \exp\left[\frac{z/D - L/2D}{E_6}\right], \quad (18)$$

with

$$E_4 = 3.0, \quad E_5 = 1.9, \quad \text{and} \quad E_6 = 1.4.$$

The predictions based on equation (18) are shown compared to axial length-scales at $\theta_r = 140^\circ$ in Figure 11.

5. UNSTEADY FORCE PREDICTIONS

The unsteady lift and drag on the cylinder are calculated using equations (11) and (12) respectively, along with equations (13), (16) and (18). Two validations of the resultant model were performed. The first was a comparison of the r.m.s sectional unsteady lift and drag calculated with the model to sectional unsteady force measurements made on a cylinder with one free end (Baban *et al.* 1989). The Baban *et al.* results, normalized by dynamic head and sectional frontal area, for r.m.s. unsteady lift and drag at a section centered about $z/D = 1.63$ were 0.37 and 0.71, respectively. The values of r.m.s. unsteady lift and drag predicted using the model were 0.33 and 0.65, respectively.

The second portion of the model validation was a comparison of the predicted results for the unsteady lift and drag spectra to unsteady force measurements performed on a cylindrical-shaped inertial hydrophone that was towed in deep water by McEachern & Lauchle (1995). The spectra are presented as a dimensionless fluctuating force spectrum, i.e. for the drag:

$$\left(\frac{G_{xx}(f)}{\rho U_\infty^2 A}\right) \left(\frac{U_\infty}{D}\right) \quad \text{versus} \quad \frac{fD}{U_\infty} \equiv \text{St}. \quad (19)$$

Here, A ($= LD$) is the frontal area for the cylinder body.

Figure 12 shows the non dimensionalized lift and drag spectra predicted for the three Reynolds numbers considered. Note that the use of the reference autospectral density, $G_{p,p}(f, \theta_r, z_r)$, in equation (11) results in a predicted unsteady force with a spectral character similar to that of the measured unsteady pressure data. The data are seen to collapse well using the inertial force and time scales of the flow for nondimensionalization. A comparison of the lift and drag spectra on the cylinder is shown in Figure 13 for $\text{Re} = 19200$. The predicted unsteady lift is typically 3 dB higher than the predicted unsteady drag over the entire range of Strouhal numbers. Measured sectional unsteady lift and drag coefficients on *infinite* cylinders are given by West & Apelt (1997). Their results show unsteady lift values that are 6–10 dB higher than the unsteady drag. In addition, their measured results on *finite-length* cylinders, showed that the sectional unsteady lift and drag coefficients are very similar in magnitude. The larger unsteady drag for the finite-length cylinder is attributed to the 3-D unsteady recirculation zone in the wake of the cylinder near the end-caps.

The spectral results presented by McEachern & Lauchle (1995) are for the combined unsteady lift and drag measured on a 2:1 aspect ratio cylindrical inertial hydrophone exposed to low Reynolds number cross-flow. A power summation (arithmetic addition) of the predicted lift and drag spectra enables a direct comparison to their results. The combined unsteady lift and drag spectrum predicted from the models, is denoted $G(f)$. Its comparison to the experimental results of McEachern & Lauchle (1995), is shown in

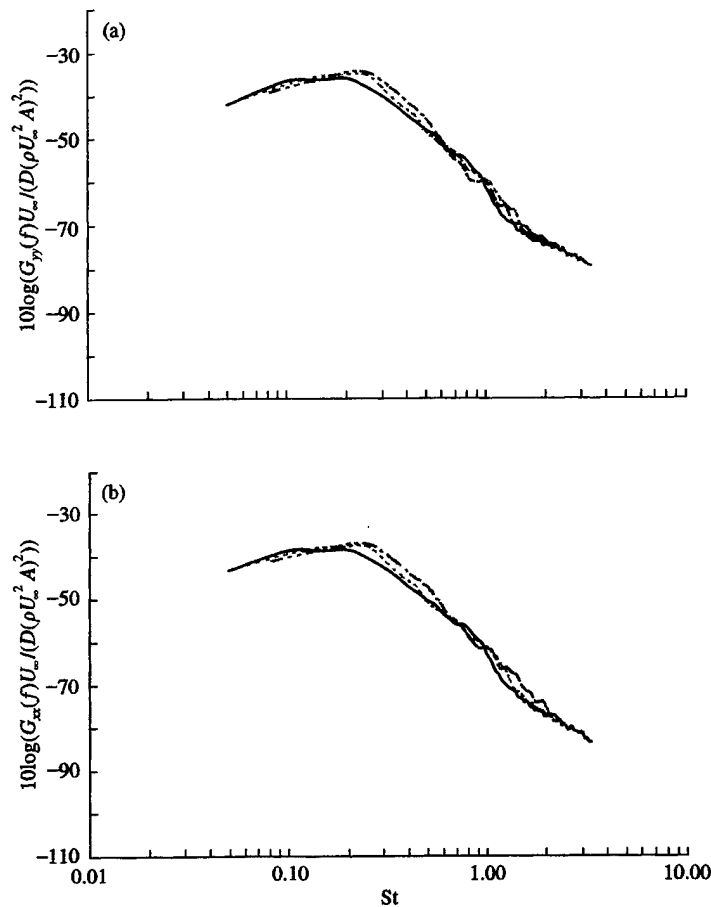


Figure 12. Unsteady lift and drag predictions for (a) unsteady lift and (b) unsteady drag: —, $Re = 32\,000$; ---, $Re = 25\,600$; - · -, $Re = 19\,200$.

Figure 14 for all three speeds. At high values of St , the model results agree to within 2 dB of the measured data.

6. CONCLUSIONS

The highest r.m.s. unsteady pressure levels were measured on the cylindrical surface near the end-caps, and in the rearward portion of the cylinder, aft of 110° . The high unsteady pressures near the end-cap are due to the 3-D separated flow over the cylinder ends. The high unsteady pressures in the rearward portion of the cylinder are due to the presence of a recirculation region behind the cylinder, and a local reattachment of the separated flow over the end-caps. Strong coherent vortex shedding from the cylinder is not present due to this end-induced disturbed flow region behind the cylinder that inhibits the vortex-formation process.

Near the mid-section of the cylinder, the Strouhal number dependence of the circumferential length-scales show a weak maximum near $St = 0.21$. The length-scales decrease as St^{-1} above this value. The decrease in length-scales with increasing Strouhal number is a result of the influence of small-scale, high-frequency, eddies. Below $St = 0.21$, the

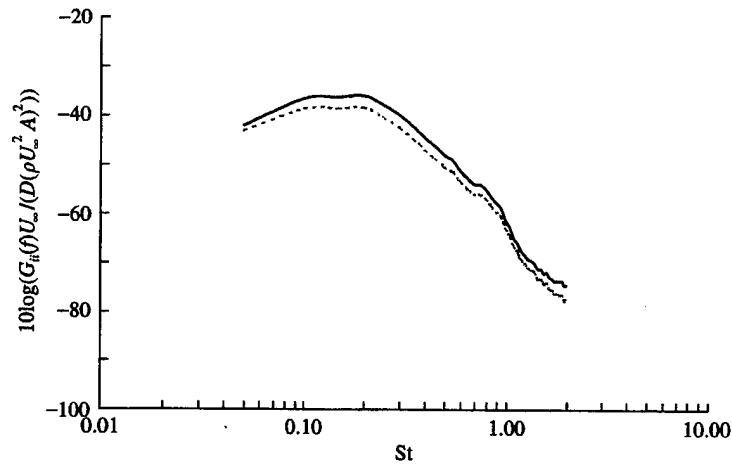


Figure 13. Unsteady lift versus unsteady drag predictions at $Re = 19\,200$: —, unsteady lift, $i = y$; ---, unsteady drag, $i = x$.

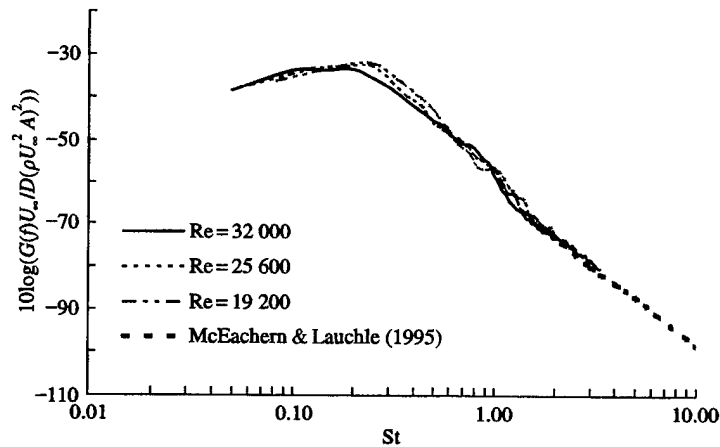


Figure 14. Predicted combination of unsteady lift and drag at $Re = 32\,000$, $25\,600$, and $19\,200$ compared to the experimental data of McEachern & Lauchle (1995) over the range $4000 < Re < 18\,000$.

correlation lengths are also small (or nonexistent), due to the apparent inability of the flow to support large-scale structures. The circumferential length-scales, as a function of axial location, are relatively independent of z/D for $z/D > 0.5$. For locations $z/D < 0.5$, the length-scales are smaller and more sensitive to z/D due to the 3-D chaotic flow field near the end-cap.

The axial length-scales decrease exponentially with increasing Strouhal number. Due to the 3-D flow region near the end-caps, the axial length-scales depend on the reference location; the wall-pressure statistics are inhomogeneous. As the reference location is moved to the mid-sections of the cylinder, the axial length-scales approach values similar to those measured independently on 2-D cylinders.

The unsteady lift spectrum predicted for the cylinder is typically 3 dB higher than the predicted unsteady drag spectrum for the Reynolds numbers and cylinder aspect ratio considered in this study. This difference appears to be much less than it is for a 2-D cylinder which is more in the range of 10–12 dB. The increase in unsteady drag, and the decrease in

unsteady lift on the finite-length cylinder is apparently due to the incoherent recirculation zone created by cylinder end effects.

ACKNOWLEDGMENTS

The work reported here has been supported by ONR Code 321SS, Scott Littlefield, under grant number N00014-96-1-0005.

REFERENCES

- BABAN, F., SO, R. M. C. & OTTUGEN, M. V. 1989 Unsteady forces on circular cylinders in a cross-flow. *Experiments in Fluids* **7**, 293–302.
- BENDAT, J. S. & PIERSON, A. G. 1986 *Random Data Analysis and Measurement Procedures*, 2nd edition. New York: John Wiley and Sons.
- CORCOS, G. M. 1964 The structure of the turbulent pressure field in boundary layer flows. *Journal of Fluid Mechanics*, **18**, 353–378.
- CAPONE, D. E. 1999 Modeling the unsteady forces on a finite-length circular cylinder in cross-flow. Ph. D. thesis, The Pennsylvania State University, University Park, PA, U.S.A.
- CRIGHTON, D. C., DOWLING, A. P., FLOWCS WILLIAMS, J. E., HECKL, M. & LEPPINGTON, F. G. 1994 *Modern Methods in Analytical Acoustics*, Lecture Notes, London: Springer-Verlag.
- FARIVAR, D. J. 1981 Turbulent flow around cylinders of finite length. *AIAA Journal* **19**, 275–281.
- FINGER, R. A., ABBAGNARO, L. A., & BAUER, B. B. 1979 Measurements of low-velocity flow noise on pressure gradient hydrophones. *Journal of the Acoustical Society of America*, **65**(6), 1407–1412.
- GERSHFELD, J. L. 1996 Sound generation from spatially inhomogeneous wall pressure fields. Ph.D. thesis, Catholic University of America, Washington, D. C., U.S.A.
- KEEFE, R. T. 1961 An investigation of the fluctuating forces acting on a stationary circular cylinder in a subsonic stream and of the associated sound field. Institute of Aerophysics, University of Toronto, UTIAS Report No. 76.
- LAUCHLE, G. C. & JONES, A. R. 1998 Unsteady lift force on a towed sphere. *Journal of Fluids and Structures* **12**, 949–958.
- MCEachern, J. F. 1993 The effect of body geometry on the flow noise of cylinders in cross flow. Ph. D. thesis, The Pennsylvania State University, University Park, PA, U.S.A.
- MCEachern, J. F. & LAUCHLE, G. C. 1995 Flow-induced noise on a bluff body. *Journal of the Acoustical Society of America* **97**, 947–953.
- RIBEIRO, J. L. D. 1992 Fluctuating lift and its spanwise correlation on a circular cylinder in a smooth and in a turbulent flow: a critical review. *Journal of Wind Engineering and Industrial Aerodynamics*, **40**, 179–198.
- WEST, G. S. & APELT, C. J. 1997 Fluctuating lift and drag on finite lengths of a circular cylinder in the subcritical Reynolds number range. *Journal of Fluids and Structures*, **11**, 135–158.

APPENDIX 56

PREDICTION OF TURBULENCE INGESTION FORCES FOR ROTORS WITH ARBITRARY RAKE AND SKEW

Joseph R. Gavin
Electric Boat Corporation
Eastern Point Rd.
Groton, Connecticut 06340
860-433-1159 jgavin@ebmail.gdeb.com

Dr. Gerald C. Lauchle
Pennsylvania State University
Graduate Program in Acoustics
P.O. Box 30 State College, Pennsylvania 16804
814-863-7145 gcl1@psu.edu

Dr. Michael L. Jonson
Pennsylvania State University
Applied Research Laboratory
P.O. Box 30, State College, Pennsylvania 16804
814-863-3029 mlj@wt.arl.psu.edu

ABSTRACT

It is well known that turbomachinery rotors produce low frequency forces when subjected to a turbulent inflow. Predictions to date have been based largely upon idealizations of radial blades operating in homogeneous isotropic turbulence. In the present work these models are slightly extended to include the effects of complex blade geometry. The credibility of the method is then tested through comparison to existing experimental data. These comparisons show that the method performs well regarding the shape of the frequency spectrum and the relative effects of complex blade geometries. However, the method tends to sometimes overestimate the absolute levels of the thrust spectra.

geometry are subsequently introduced, and the analysis is applied to predict the available measurements.

NOMENCLATURE

b	- blade number (from 0 to $B-1$)
B	- number of blades
C	- blade chord length
$H_0^{(2)}, H_1^{(2)}$	- Hankel functions
r^α	- Radius to blade strip α
$\partial c_i / \partial \alpha$	- Lift curve slope
X	- Rake (axial offset)
ρ	- Density
ϕ	- blade pitch angle
Λ	- turbulence integral length scale
Ω	- Angular rotor speed (revolutions/sec)
ψ	- Skew (circumferential offset)

OVERVIEW OF THE PREDICTION METHOD

The model is based upon a fixed coordinate system as shown in Figure (1). The mean flow entering the rotor is assumed to be purely axial with a positive sense taken into the page. Rotation is assumed to be counter-clockwise when viewed from forward looking aft. Each blade on the rotor is discretized into an appropriate number of thin spanwise strips. The unsteady lift is determined using 2D airfoil theory and a correlation analysis between all the strips on the rotor.

The turbulent velocity fluctuations entering the rotor are of course random in space and time, and are best expressed as tensors to compactly indicate their location, direction and magnitude.

INTRODUCTION

The database of Jonson [1] clearly demonstrates the benefits of well chosen blade geometry. He showed that rake and skew decorrelated the gusts along the blade span; reducing the net unsteady thrust by as much as 12 dB at the broadband humps (or "haystacks") in the spectrum. However, this data has apparently been neglected as a validation database for testing the accuracy of modern prediction methods.

The data of Sevik [2], and a recent repeat of those measurements by Wojno, Mueller and Blake [3] provide additional data for validation.

Predictions of the above test cases are approached following the original framework of Sevik [2], as modified by Martinez [4] and Jiang et al [5] to account for the effects of blade rotation.

This paper begins by briefly reviewing the prediction method. The description is abbreviated since the material is already well covered by Martinez [4]. The modifications for arbitrary blade

Using the notation of Sevik [2]:

- (1) $u_k^\beta(t)$ = the turbulent velocity fluctuation in direction k , that is encountered by blade strip β at time t .
- (2) $F_{ik}^{\alpha\beta}(t, \tau)$ = the lift force generated by blade strip α in direction i at time t due to a unit amplitude turbulent velocity fluctuation which encounters blade strip β in direction k at time τ .
- (3) $l_i^\alpha(t)$ = total lift force on blade strip α in direction i due to the incident turbulent velocity fluctuations plus the induced effects caused by other blades. This is determined by the following convolution integral:

$$= \int_0^t F_{ik}^{\alpha\beta}(\tau) u_k^\beta(t - \tau) d\tau \quad (1)$$

where $\alpha, \beta = 1, 2, 3, \dots, n$ and $i, k = 1, 2, 3$

The space-time correlation between strips is the expected value of the lift tensors.

$$\Phi_{ij}^{\alpha\beta}(\tau) = E\{l_i^\alpha(t) l_j^\beta(t + \tau)\} \quad (2a)$$

Assuming that the processes are stationary and ergodic then equation (1) can be used to form the space-time correlation function of the unsteady lift:

$$\Phi_{ij}^{\alpha\beta}(\tau) = \lim_{T \rightarrow \infty} \frac{1}{T} \int_0^T \left\{ \int_0^{\tau} F_{ik}^{\alpha\gamma}(\tau_1) u_k^\gamma(t - \tau_1) d\tau_1 \right\} \left\{ \int_0^{\tau + \tau} F_{jr}^{\beta\delta}(\tau_2) u_r^\delta(t - \tau_2 + \tau) d\tau_2 \right\} d\tau$$

Defining the correlation function for the turbulent velocity fluctuations:

$$R_{kr}^{\gamma\delta}(\tau + \tau_1 - \tau_2) = \lim_{T \rightarrow \infty} \frac{1}{T} \int_0^T u_k^\gamma(t - \tau_1) u_r^\delta(t - \tau_2 + \tau) dt \quad (3)$$

Then upon making the necessary substitutions and taking a temporal Fourier transform, the two-sided power spectrum of unsteady lift is given by:

$$\Psi_{l_i l_j}^{\alpha\beta}(\omega) = \frac{1}{2\pi} \left\{ \int_0^{\infty} \int_0^{\infty} F_{ik}^{\alpha\gamma}(\tau_1) F_{jr}^{\beta\delta}(\tau_2) e^{i\omega(\tau_1 - \tau_2)} d\tau_1 d\tau_2 \right\} * \int_{-\infty}^{\infty} R_{kr}^{\gamma\delta}(\tau - \tau_2 + \tau_1) e^{-i\omega(\tau - \tau_2 + \tau_1)} d\tau \quad (4)$$

The term in braces of eq. (4) is now recognized as the Fourier transform of the aerodynamic response functions. These terms are usually named the gust response functions ($H_{ik}^{\alpha\gamma}$), and can be modeled using a variety of approximations from 2D potential flow theory to unsteady computational fluid dynamics. The remaining term in eq. (4) is the two-sided power spectrum of turbulent velocity fluctuations. Most generally this is called the

two-sided cross-power spectral density ($G_{kr}^{\beta\delta}$) of the turbulent velocity fluctuations. The unsteady lift spectrum is thus recast as:

$$\Psi_{l_i l_j}^{\alpha\beta}(\omega) = \{H_{ik}^{\alpha\gamma}\}^* \{H_{jr}^{\beta\delta}\} G_{kr}^{\beta\delta}(\omega) \quad (5)$$

Equation (5) is the fundamental expression which must be evaluated. Most earlier research applies the simplest gust response function available which is that due to Sears [6]. This applies to a flat plate of infinite span, zero thickness, and zero camber. The mean velocity is assumed to be at zero degrees angle of attack to the plate, and the effects of induced velocities are obviously neglected since the blade is assumed to be isolated in space. However, as suggested by Sevik [2], the theoretical value of the lift curve slope is allowed to remain arbitrary to crudely account for cascade effects. The span of the strip (δr) and a direction cosine between the lift vector and axial direction (η) are also included in anticipation of the upcoming integration across strips. Then the gust response functions are given as:

$$H_{ik}^{\alpha\gamma}(\omega) = \frac{\partial c_l}{\partial \alpha} \rho W_{rel} \frac{C}{2} S_{2D} \left(\frac{\omega C}{2W_{rel}} \right) \delta r \eta \quad (6)$$

The Sear's function phased to the blade midchord is given by Blake [7] as a function of the reduced frequency \bar{k} :

$$S_{2D}(\bar{k}) = \frac{H_1^{(2)}(\bar{k})}{H_1^{(2)}(\bar{k}) + iH_0^{(2)}(\bar{k})} \quad \bar{k} = \frac{\omega C}{2W_{rel}} \quad (7)$$

To complete the analysis we must develop a description of the correlation function for gusts normal to the blade, and numerically complete the indicated summations and integrations.

TRANSFORMATION OF VELOCITY FLUCTUATIONS INTO THE FRAME OF THE BLADE The mean velocity entering the rotor is easily described in the stationary frame of Figure (1).

$$\bar{U}^\alpha = U_x^\alpha \hat{e}_x + 0\hat{e}_y + 0\hat{e}_z = U_x^\alpha \hat{e}_x + 0\hat{e}_r + 0\hat{e}_\theta \quad (8)$$

The airfoil sections are assumed to operate at zero angle of attack. Therefore, in the frame of the blade the mean relative velocity is parallel to the blade chord. Defining this direction by a local unit vector \hat{e}_1^α then its companions are taken along the local blade stacking line \hat{e}_2^α and along the normal to the local blade surface \hat{e}_3^α . (These vectors are only orthogonal in a blade with a radial stacking line). Then the mean relative velocity in the frame of the blade can be expressed as:

$$= W_1^\alpha \hat{e}_1^\alpha + 0\hat{e}_2^\alpha + 0\hat{e}_3^\alpha \quad (9)$$

$$\text{where } W_1^\alpha = \sqrt{\left(\frac{U_x^\alpha}{W_{rel}^\alpha}\right)^2 + (2\pi r^\alpha \Omega)^2} \quad (10)$$

The description of gusts normal to the blade is easily accomplished given the orientation of the surface normal vector. This can be found through knowledge of the blade geometry and instantaneous blade position. Figure (2) shows the geometric conventions for this paper. ψ^α is taken as the projected skew angle, and X^α is the axial offset (rake), both measured from the position of the blade reference line.

The vector oriented along the blade chord can be found using the relative velocity triangle (due to the assumption that the mean flow is at zero angle of attack).

$$\begin{aligned} \hat{e}_1^\alpha &= \left(\frac{U_x^\alpha}{W_{rel}^\alpha}\right) \hat{e}_x^\alpha + 0\hat{e}_r^\alpha + \left(\frac{2\pi r^\alpha \Omega}{W_{rel}^\alpha}\right) \hat{e}_\theta^\alpha \\ &= \sin(\phi^\alpha) \hat{e}_x^\alpha + 0\hat{e}_r^\alpha + \cos(\phi^\alpha) \hat{e}_\theta^\alpha \end{aligned} \quad (11)$$

The vector along the blade stacking line can be found from the de geometry. Using the fixed coordinate system, then the J-chord at each strip on the reference blade is defined by a position vector.

$$\bar{y}^\alpha = X^\alpha \hat{e}_x + r^\alpha \hat{e}_r + r^\alpha \psi^\alpha \hat{e}_\theta \quad (12)$$

The location of strips on other blades is similar, but translated through the appropriate angle given by the blade spacing. A central difference about the strip of interest yields the desired vector parallel to the local blade stacking line (\hat{e}_2^α):

$$\begin{aligned} \hat{e}_2^\alpha &= (X^{\alpha+1} - X^{\alpha-1}) \hat{e}_x^\alpha + (r^{\alpha+1} - r^{\alpha-1}) \hat{e}_r^\alpha \\ &\quad + (r^{\alpha+1} \psi^{\alpha+1} - r^{\alpha-1} \psi^{\alpha-1}) \hat{e}_\theta^\alpha \end{aligned} \quad (13)$$

A vector cross-product ($\hat{e}_1^\alpha \times \hat{e}_2^\alpha$) yields the orientation of a vector that is normal to the local blade surface and has the same sense as the lift vector. The result can be cast in terms of direction cosines for compactness of notation:

$$\hat{e}_3^\alpha = \eta_x^\alpha \hat{e}_x^\alpha + \eta_r^\alpha \hat{e}_r^\alpha + \eta_\theta^\alpha \hat{e}_\theta^\alpha \quad (14)$$

$$\text{where: } \eta_x^\alpha = \frac{-\cos(\phi^\alpha) * (r^{\alpha+1} - r^{\alpha-1})}{S^\alpha}$$

$$\eta_r^\alpha = \frac{(\cos(\phi^\alpha) * (X^{\alpha+1} - X^{\alpha-1}) - \sin(\phi^\alpha) * (r^{\alpha+1} \psi^{\alpha+1} - r^{\alpha-1} \psi^{\alpha-1}))}{S^\alpha}$$

$$\eta_\theta^\alpha = \frac{\sin(\phi^\alpha) * (r^{\alpha+1} - r^{\alpha-1})}{S^\alpha} \quad \text{and} \quad S^\alpha = |\hat{e}_1^\alpha \times \hat{e}_2^\alpha|$$

This reveals that rake and skew introduce a new radial component to the lift vector, unless their effects are balanced by the difference noted above.

Finally, we can now project the turbulent velocity fluctuations from the stationary frame onto the local blade unit normal vector. These are the gusts which generate lift in unsteady 2D airfoil theory:

$$u_3^\alpha = \bar{u} \cdot \hat{e}_3^\alpha = u_x^\alpha \eta_x^\alpha + u_r^\alpha \eta_r^\alpha + u_\theta^\alpha \eta_\theta^\alpha \quad (15)$$

The radial and tangential velocity fluctuations can be further resolved into their Cartesian coordinates using the geometry of the fixed frame of reference:

$$\begin{aligned} u_3^\alpha &= u_x^\alpha \eta_x^\alpha + (u_y^\alpha \cos(\theta^\alpha) + u_z^\alpha \sin(\theta^\alpha)) \eta_r^\alpha \\ &\quad + (u_z^\alpha \cos(\theta^\alpha) - u_y^\alpha \sin(\theta^\alpha)) \eta_\theta^\alpha \end{aligned} \quad (16)$$

Then the correlation function between two arbitrary blade strips is given by:

$$\overline{u_3^\alpha u_3^\beta} = \overline{(\eta_x^\alpha u_x^\alpha + \eta_r^\alpha u_r^\alpha + \eta_\theta^\alpha u_\theta^\alpha)(\eta_x^\beta u_x^\beta + \eta_r^\beta u_r^\beta + \eta_\theta^\beta u_\theta^\beta)} \quad (17)$$

Lengthy algebraic manipulations reduce the above to a tensor in terms of the turbulent velocity fluctuations from the stationary frame. The result of these manipulations is summarized in Appendix A for completeness.

The result to this point is completely general. However, it is noteworthy that it includes many correlations that were absent in the original analyses of Jiang et. al [5]. Many of these terms are introduced by coupling to the flow field through blade rake and skew. However, others are simply shown to vanish under the assumptions of homogeneous isotropic turbulence, and thus were of no consequence in their earlier models. In this report these same simplifications can be invoked¹ for the purpose of validating the code against measurements in grid generated turbulence. A complete treatment of the turbulence modeling is given by Hinze [8].

¹ An alternate turbulence model has been proposed by Wojno, Mueller and Blake [3] based upon measurements in grid generated turbulence. They revealed significant local inhomogeneity and anisotropy. This realism is obviously expected to improve the agreement between prediction and measurements. However, this result has not yet been incorporated into the present analysis.

fly, the assumption of homogeneous isotropic turbulence requires that the correlation function is invariant to translations and rotations of the coordinate axis. Assuming further that the streamwise correlation function is characterized by a simple exponential decay with separation distance (as observed experimentally), then

$$R_{xx}^{\alpha\beta} = u_{rms}^2 \exp\left\{-\left|\frac{\Delta x}{\Lambda_x}\right|\right\} \quad (18)$$

Continuity can then be applied to obtain the general form of the correlation function. This result is expressed in tensor notation for compactness where the indices are $i, j = 1, 2, 3$.

$$R_{ij}^{\alpha\beta}(r) = u_{rms}^2 \left[\frac{1}{2r\Lambda} \xi_i \xi_j + \left(1 - \frac{r}{2\Lambda}\right) \delta_{ij} \right] \exp\left\{-\left|\frac{r}{\Lambda}\right|\right\} \quad (19)$$

Here the terms like ξ_i indicate the Cartesian components of the total separation distance. δ_{ij} is the Dirac delta function.

INSTANTANEOUS SEPARATION DISTANCE

BETWEEN BLADE STRIPS In order to evaluate the correlation function we require an estimate of the instantaneous separation distance (ξ_i) between points α and β . Recalling the general formulation for the unsteady lift tensor, repeated here for convenience:

$$\Phi_{ij}^{\alpha\beta} = E\{l_i^\alpha(t)l_j^\beta(t+\tau)\} \quad (20)$$

it is clear that the analysis requires an estimate of the correlation between blade strip α at the reference time, and blade strip β at an arbitrary delay time. Thus, the separation vector must include the effects of forward flight and blade rotation.

If the reference strip α is assumed to exist at $\theta = 0$ at the reference time, then the second strip β is located at an angular offset given by:

$$\Delta\theta = b\left(\frac{2\pi}{B}\right) + (\psi^\beta - \psi^\alpha) + (2\pi\Omega\tau) \quad (21)$$

or by using the law of Cosines, the separation in the plane of the rotor is given by:

$$\Delta s_{in-plane} = \sqrt{(r^\beta)^2 + (r^\alpha)^2 - 2r^\alpha r^\beta \cos(\Delta\theta)} \quad (22)$$

total instantaneous separation must also account for the effects of forward flight and blade rake.

$$\Delta s = \sqrt{(U_x\tau + (X^\beta - X^\alpha))^2 + [(r^\beta)^2 + (r^\alpha)^2 - 2r^\alpha r^\beta \cos(\Delta\theta)]}$$

This separation distance is easily resolved into its Cartesian components in the frame of the body. These distances can then be used to evaluate the correlation function in eq. (19).

COMPARISON OF PREDICTION AND TEST FOR RADIAL BLADES

Comparison data for radial rotors has been acquired by both Sevik [2] and Wojno et. al. [3]. The identical rotor was used in these two experiments: a 10 bladed axial flow design with tip radius of 4 inches and chord of 1 inch.²

In Sevik's [2] experiment the correlation length was not measured directly. However, it can still be estimated using the scaling of Naudascher and Farell [9] (see also Thompson [10] for a treatment of Reynolds number effects). This leads to an estimate of approximately 1.1 inches (about 35% span).

The thrust spectrum for Sevik's test conditions has been estimated using both his broadband theory and the present method. The results are shown in Figure (3). Published measurements are shown for comparison.

It is clear that neither model predicts the published experimental data. However, a minor re-interpretation resolves this discrepancy. Specifically, Sevik's theory predicts a thrust spectrum where frequency has been nondimensionalized by the integral scale and the free stream velocity. Of course, the resultant power spectrum $G(\Gamma)$ must include scaling by the inverse fraction in order to preserve the mean square value of the data in accordance with Parseval's theorem. The desired power spectral density of the unsteady thrust is then obtained as:

$$G(f) = 2\pi \frac{\Lambda}{U_x} G(\Gamma) \quad \text{where} \quad \Gamma = \frac{\omega\Lambda}{U_x} \quad (24)$$

Sevik's data is clearly stated to be normalized to 1 Hz bandwidth. However, it appears that this may have only accounted for the adjustment from circular frequency to Hertz. By rescaling his power spectral density for the remaining terms, the data is now seen to fall within good agreement of both predictions. Further, the character of the data and his broadband theory are now identical to his original publication (albeit 22 dB lower in amplitude). Thus, his conclusions and method remain valid today within the constraints of his

² Wojno et. al. [3] have shown that cascade effects can be significant for reduced frequencies at and below the first haystack. However, no correction for these cascade effects is included in the present calculations.

SUMMARY The correlation method of Martinez [4] has been slightly extended to include rotor geometries with arbitrary rake and skew. The resultant method shows good agreement with measurements for a 10-bladed rotor with radial stacking line. The method also reasonably predicts the trends of the thrust spectra for a 5 bladed rotor with systematic variations in rake and skew. Further improvements are required to predict absolute levels of unsteady thrust. This effort will initially focus on cascade effects for turbomachinery rotors with high solidity.

ACKNOWLEDGEMENTS

This work was supported by General Dynamics Electric Boat Corporation. Dr. Martin Manley and Mr. Gary Cooper are the technical monitors. The work has benefited from conversations with Dr. William Blake and Dr. Rudolf Martinez. Their continued technical guidance and encouragement are greatly appreciated.

REFERENCES

- [1] Jonson, M. L., "The Unsteady Response of Propellers to Ingested, Homogeneous, Isotropic Turbulence", *Pennsylvania State University ARL Review* 1994, pp. 104-108
- [2] Sevik, M. M., "Sound Radiation from a Subsonic Rotor Subjected to Turbulence", *Fluid Mechanics, Acoustics and Design of Turbomachinery Part 2*, NASA SP 304, 1974, pp. 493-511
- [3] Wojno, J. P., Mueller, T. J., and Blake W. K., "Aeroacoustic Response of a Ten-Bladed Rotor to Grid Generated Turbulence", *AIAA-99-1883, 5th AIAA/CAES Aeroacoustics Conference*, Seattle WA, May 10-12, 1999, pp. 567-581
- [4] Martinez, R., "Analysis of the Right Shift of the Blade Rate Hump in Broadband Spectra of Propeller Thrust", *Cambridge Acoustical Associates U-1993-381.9*, 1991,
- [5] Jiang, C. W., Chang, M., and Liu, Y., "The Effect of Turbulence Ingestion on Propeller Broadband Forces", presented at the *19th symposium on Naval Hydrodynamics*, August 24-28, 1992, Seoul, South Korea.
- [6] Sears, W. R., "Some Aspects of Non-Stationary Airfoil Theory and Its Practical Application", *J. Aero. Sci.* 8, 1941 pp. 104-108.
- [7] Blake W., K., "Mechanics of Flow Induced Sound and Vibration, Vol II, Complex Flow Structure Interactions", Academic Press, 1986
- [8] Hinze, O. J., *Turbulence*, McGraw-Hill Inc. 1975
- [9] Naudascher, E. and Farell, C., "Unified Analysis of Grid Turbulence", *J. Engr. Mch Div., Proc. ASCE*, April 1970 pp. 121-141
- [10] Thompson, D. E., "Propeller Time Dependent Forces Due to Nonuniform Flow", Ph.D. Thesis, May 1976, The Pennsylvania State University
- [11] Blake, W. K., *private communications*

APPENDIX A The following equations provide the results of algebraic manipulations from equation (17). The correlation function is given by:

$$\overline{u_3^\alpha u_3^\beta} = (\eta_x^\alpha u_x^\alpha + \eta_r^\alpha u_r^\alpha + \eta_\theta^\alpha u_\theta^\alpha)(\eta_x^\beta u_x^\beta + \eta_r^\beta u_r^\beta + \eta_\theta^\beta u_\theta^\beta)$$

Expanding this result in terms of the direction cosines, and the correlation functions in the frame of the body:

$$\begin{aligned} R_{NN}^{\alpha\beta} = & (\eta_x^\alpha \eta_x^\beta) R_{xx}^{\alpha\beta} \\ & + (-\eta_x^\alpha \eta_\theta^\beta \sin \theta^\beta + \eta_x^\alpha \eta_r^\beta \cos \theta^\beta) R_{xy}^{\alpha\beta} \\ & + (\eta_x^\alpha \eta_\theta^\beta \cos \theta^\beta + \eta_x^\alpha \eta_r^\beta \sin \theta^\beta) R_{xz}^{\alpha\beta} \\ & + (-\eta_\theta^\alpha \eta_x^\beta \sin \theta^\alpha + \eta_r^\alpha \eta_x^\beta \cos \theta^\alpha) R_{yx}^{\alpha\beta} \\ & + \left(\eta_\theta^\alpha \eta_\theta^\beta \sin \theta^\alpha \sin \theta^\beta - \eta_\theta^\alpha \eta_r^\beta \sin \theta^\alpha \cos \theta^\beta \right. \\ & \left. - \eta_r^\alpha \eta_\theta^\beta \cos \theta^\alpha \sin \theta^\beta + \eta_r^\alpha \eta_r^\beta \cos \theta^\alpha \cos \theta^\beta \right) R_{yy}^{\alpha\beta} \\ & + \left(-\eta_\theta^\alpha \eta_\theta^\beta \sin \theta^\alpha \cos \theta^\beta - \eta_\theta^\alpha \eta_r^\beta \sin \theta^\alpha \sin \theta^\beta \right. \\ & \left. + \eta_r^\alpha \eta_\theta^\beta \cos \theta^\alpha \cos \theta^\beta + \eta_r^\alpha \eta_r^\beta \cos \theta^\alpha \sin \theta^\beta \right) R_{yz}^{\alpha\beta} \\ & + (\eta_\theta^\alpha \eta_x^\beta \cos \theta^\alpha + \eta_r^\alpha \eta_x^\beta \sin \theta^\alpha) R_{zx}^{\alpha\beta} \\ & + \left(-\eta_\theta^\alpha \eta_\theta^\beta \cos \theta^\alpha \sin \theta^\beta + \eta_\theta^\alpha \eta_r^\beta \cos \theta^\alpha \cos \theta^\beta \right. \\ & \left. - \eta_r^\alpha \eta_\theta^\beta \sin \theta^\alpha \sin \theta^\beta + \eta_r^\alpha \eta_r^\beta \sin \theta^\alpha \cos \theta^\beta \right) R_{zy}^{\alpha\beta} \\ & + \left(\eta_\theta^\alpha \eta_\theta^\beta \cos \theta^\alpha \cos \theta^\beta + \eta_\theta^\alpha \eta_r^\beta \cos \theta^\alpha \sin \theta^\beta \right. \\ & \left. + \eta_r^\alpha \eta_\theta^\beta \sin \theta^\alpha \cos \theta^\beta + \eta_r^\alpha \eta_r^\beta \sin \theta^\alpha \sin \theta^\beta \right) R_{zz}^{\alpha\beta} \end{aligned}$$

APPENDIX B: The following tables summarize the rotor blade characteristics of Jonson [1]. All three rotors have tip radii of 6 inches. Rotor 4382 is described immediately below. Rotor 4381 is similar except with zero rake and skew.

ptions. We suggest that our reinterpretation is correct. In this adjustment, the present method performs well in predicting the low frequency continuum and the first haystack.

Wojno's [3] measurements were performed in air, and every effort was made to maintain dynamic similarity with the original water tunnel tests of Sevik [2]. The obvious limitations of Wojno's [3] test include a lower Reynolds number and a spatial constraint which placed the rotor somewhat closer to the grid. However, the wind speed and rotor RPM were greatly increased in order to approximate Sevik's advance ratio while achieving a reasonable Reynolds number based upon blade chord.

Wojno et. al. [3] measured the airborne noise (ψ_{pp}) caused by the ingested turbulence. However, at frequencies of interest the rotor was acoustically compact. Therefore, it is possible to infer the unsteady thrust spectra (ψ_{TT}) from simple dipole acoustic theory:

$$\psi_{TT}(f) = \left[\frac{4\pi r_{source}}{\left(\frac{2\pi f}{c_0} \right) \cos \Theta} \right]^2 \psi_{pp}(f) \quad (25)$$

where c_0 is the speed of sound, r_{source} and Θ are the distance and angle from the rotor to the microphone.

This back-calculated thrust spectra can be compared to the direct measurements of Sevik [2] through a suitable normalization. In this comparison the frequencies have been scaled by the blade passing frequency. The power spectral density of unsteady thrust has been scaled as shown in eq (26). The comparison of normalized results is shown in Figure (4).

$$G(f^*) = \frac{G(f) * f_{bpf}}{(\rho U_x^2 R^2) \left(\frac{CB}{R} \frac{u}{U_x} \right)^2} \quad f^* = \frac{f}{f_{bpf}} \quad (26)$$

The haystack in Wojno's data is somewhat less pronounced, and the high frequencies tend to be higher amplitude than Sevik's direct measurements. However, the relative magnitudes and trends are quite similar; giving credibility to Wojno's efforts for achieving dynamic similarity.

In order to directly predict the measurements of Wojno [3] with the current simplified turbulence model it is necessary to choose a single integral length scale. A length of about 2 inches (65% span) represents a rough average between his radial and tangential scales for the energy containing wavenumbers. This integral scale was used as input to the analysis assuming homogeneous isotropic turbulence. The comparison of measurement versus prediction is shown in Figure (5). As

shown, the comparison is quite reasonable. Blake [11] has noted that the prediction at very low frequencies is artificially high due to the lack of cascade effects in the calculation. The actual thrust may actually be low enough to be obscured by background noise from the facility.

In the above cases of radial stacking lines our extended model reduces to the original analysis of Martinez [4], and this performs quite well through at least the first haystack.

COMPARISON OF PREDICTION AND TEST FOR BLADES WITH RAKE AND SKEW

Jonson [1] has measured the unsteady thrust for three rotors operating in grid generated turbulence. The rotors, shown in Figure (6), were designed for similar hydrodynamic performance but included a systematic variation in rake and skew. The objective of these tests was to establish a measured database of turbulent inflow data and unsteady response.

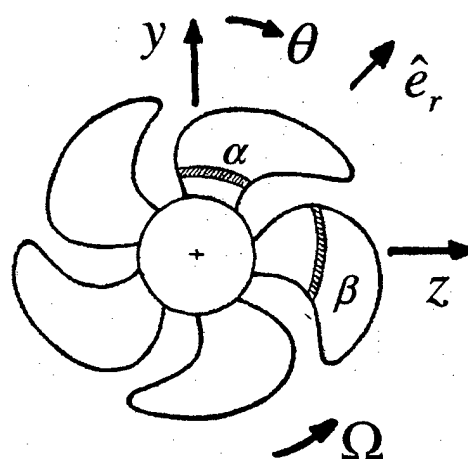
The unsteady thrust and side forces were measured using a downstream dynamometer. The turbulent inflow was measured using a two-component LDV for a point at approximately 70% of the blade span. Reported data includes the spectrum of unsteady thrust and both the intensity and integral scale of streamwise turbulent velocity fluctuations.

The measured thrust spectra are shown in Figure (7). These include a strong haystack near the first blade passing frequency, which is presumably due to the blade-to-blade correlations. The thrust spectra diminish quickly as the frequency approaches the second blade passing frequency.

The unsteady thrust was also calculated for each rotor using the present method. A relative comparison of measurement vs. prediction is shown in Figure (7). It appears that the calculations reasonably capture the shape of the spectra, and the relative effects of rake and skew. However, the calculations significantly overpredict the absolute amplitude of the measurements, and were reduced by 10 dB to facilitate the comparisons that are shown. At least part of this discrepancy is probably due to the retention of an ideal lift curve slope in the calculations (i.e., $\partial c_l / \partial \alpha = 2\pi$). These rotors have solidity at least 50% greater than Sevik's, and yet no correction for cascade effects is included in the method. This is an essential next step in refinement of the method as previously suggested by Blake [11].

It is also clear that the measurements fall off quickly at high frequencies. It is suggested that a dynamometer shaft resonance may have influenced the measurements. This assessment is substantiated in Figure (8), where the present predictions are modified by the magnification factor of a 1 degree-of-freedom resonance just above blade passing frequency.

R/Rtip	Chord/D	Projected Skew degrees	Rake ft
0.200	0.174	0.000	0.000
0.300	0.228	4.620	0.012
0.400	0.275	9.330	0.023
0.500	0.313	13.940	0.035
0.600	0.338	18.380	0.046
0.700	0.348	22.780	0.057
0.800	0.334	27.116	0.068
0.900	0.281	31.600	0.079
0.950	0.219	33.820	0.085
0.960	0.202	34.270	0.086
0.970	0.180	34.730	0.087
0.980	0.152	35.200	0.088
0.990	0.115	35.650	0.089
1.000	0.000	36.140	0.090



Rotor 4542 is described below:

R/Rtip	Chord/D	Projected Skew degrees	Rake ft
0.200	0.177	0.000	0.000
0.300	0.229	4.007	0.010
0.400	0.275	5.956	0.015
0.500	0.312	8.318	0.021
0.600	0.337	13.756	0.034
0.700	0.347	23.972	0.060
0.800	0.334	39.053	0.098
0.900	0.280	59.287	0.148
0.950	0.214	66.453	0.166
0.960	0.194	67.638	0.169
0.970	0.171	68.641	0.172
0.980	0.141	69.568	0.174
0.990	0.100	70.428	0.176
1.000	0.000	71.266	0.178

Figure (1) - Coordinate System and Strip Model for Theoretical Modeling (forward looking aft)

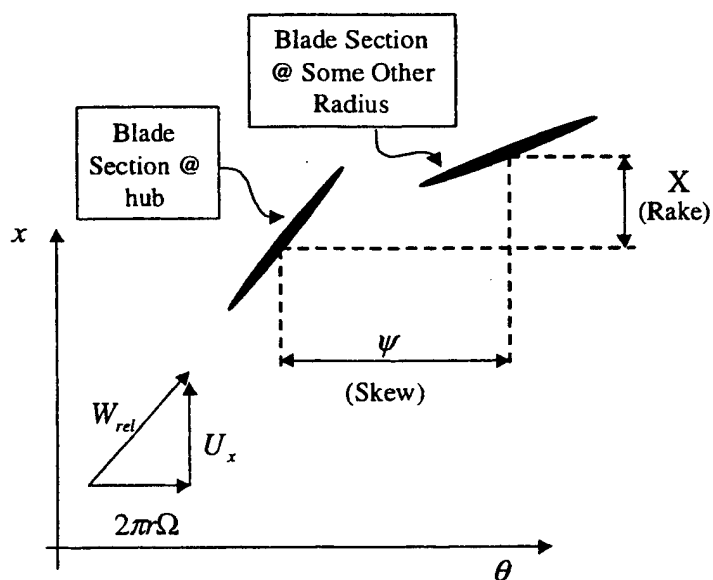


Figure (2) - Geometric Conventions Regarding Blade Rake and Skew

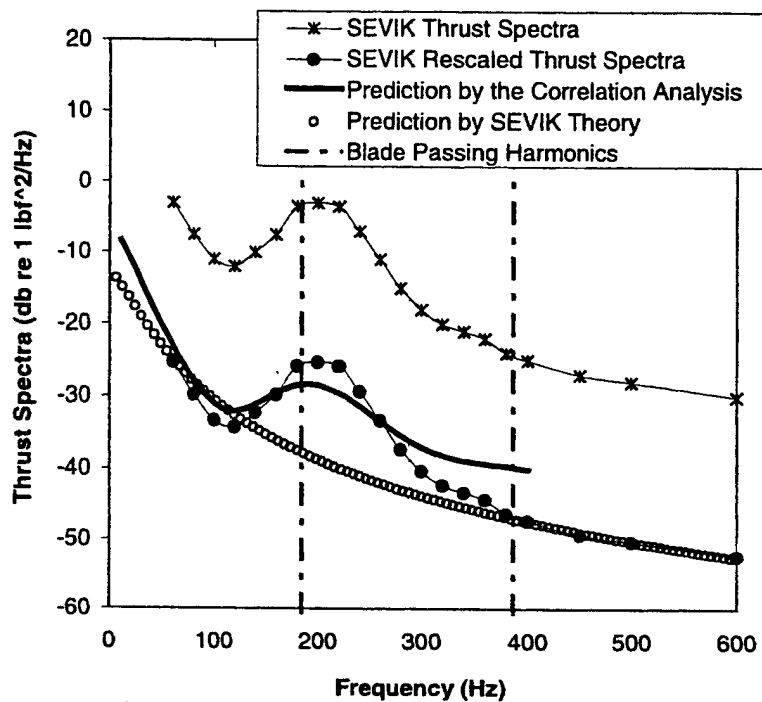


Figure (3) - Comparison of Prediction and Measurement
for the Data of Sevik's 4-Inch Grid

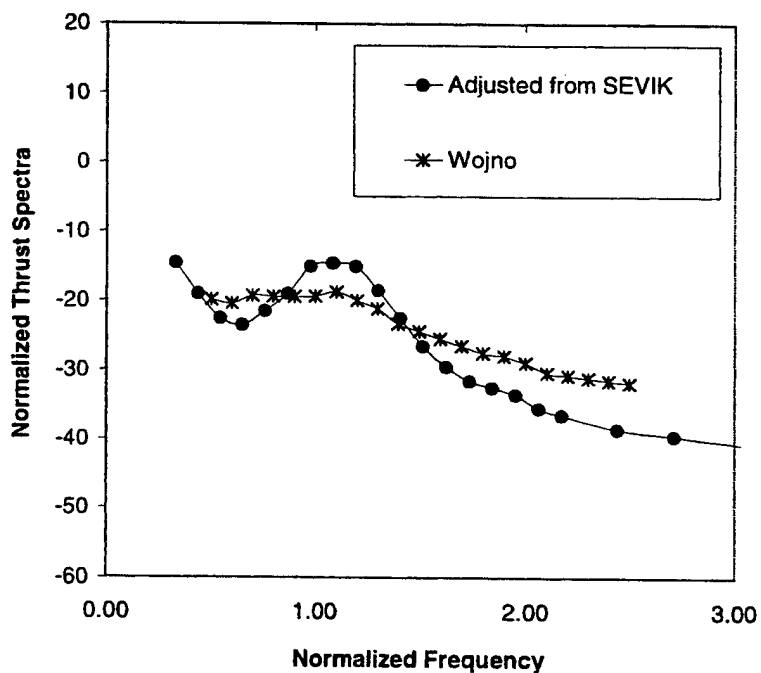


Figure (4) - Comparison of Normalized Measurements
for the 10-Bladed Rotor

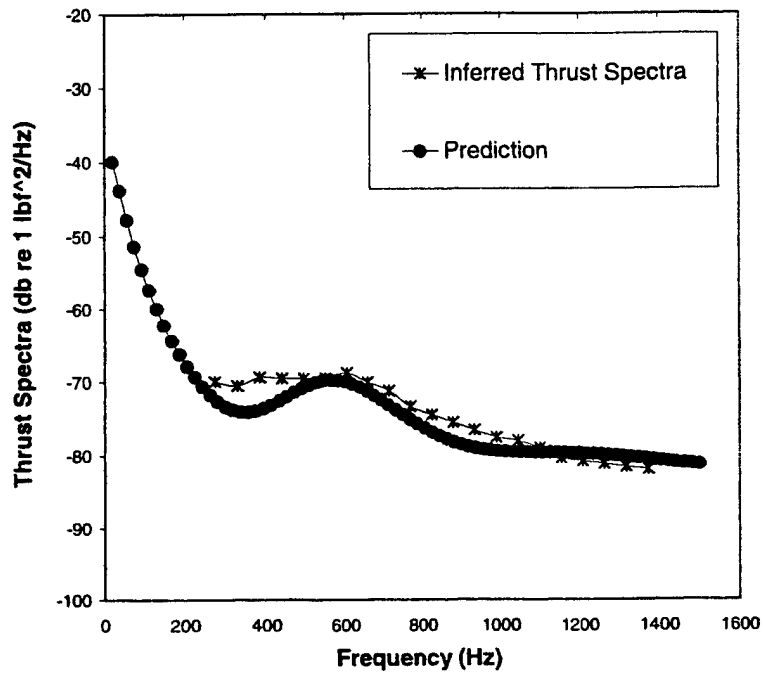


Figure (5) - Comparison of Measurement
versus Prediction for Wojno's Test

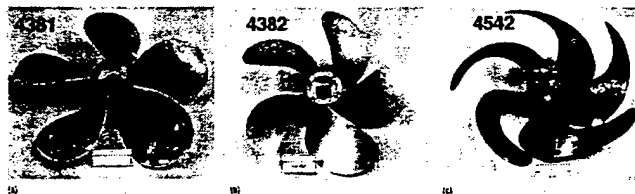


Figure (6) - Rotors Tested by Jonson

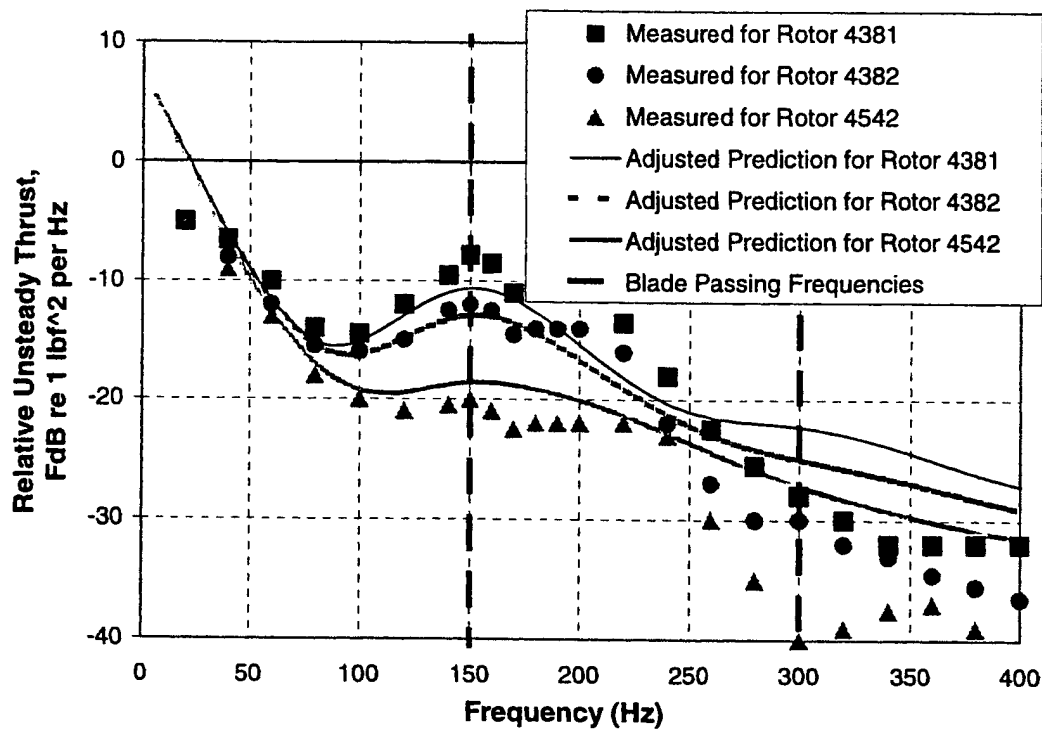


Figure (7) - Comparison of Measurement and Prediction for Jonson's Rotors

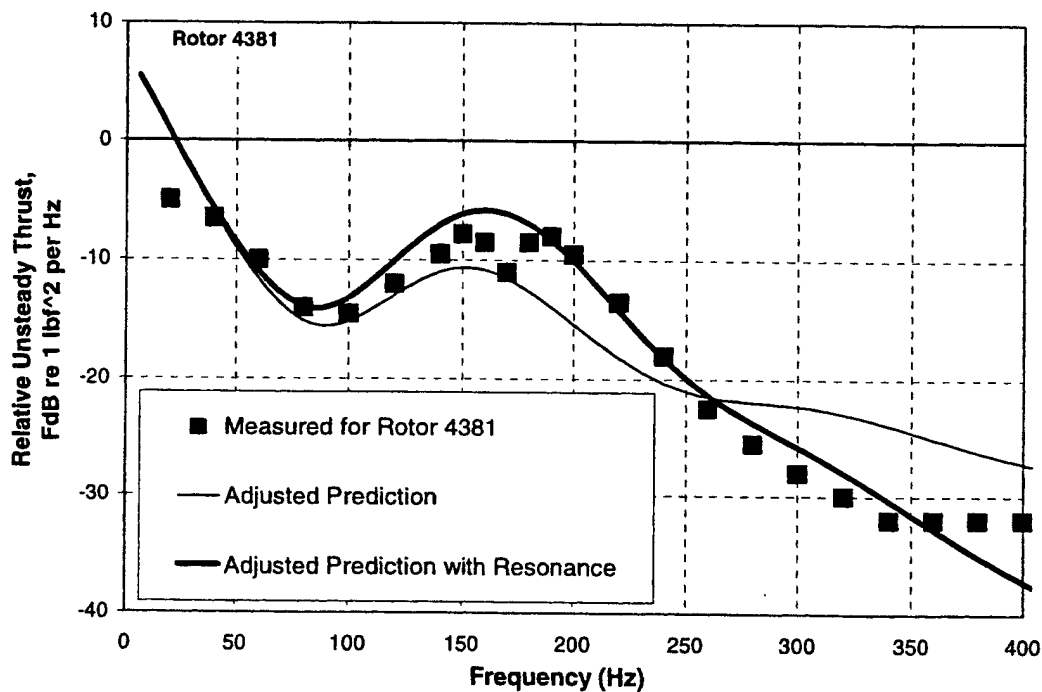


Figure (8) - Typical Effect of a Dynamometer Resonance on the Prediction for Rotor 4381

APPENDIX 57

MODELING THE SPACE-TIME CORRELATIONS IN THE WAKE REGION OF A TURBULENT BOUNDARY LAYER

Joseph R. Gavin
Electric Boat Corporation
Eastern Point Rd.
Groton, Connecticut 06340
860-433-1159 jgavin@ebmail.gdeb.com

Dr. Gerald C. Lauchle
Pennsylvania State University
Graduate Program in Acoustics
P.O. Box 30 State College, Pennsylvania 16804
814-863-7145 gcl1@psu.edu

ABSTRACT An empirical turbulence model has been developed for boundary layer flows. The goal is to simulate the statistical behavior of turbulent velocity fluctuations in both space and time using the two-point correlation field.

The new model is based on physical concepts from earlier measurements and flow visualizations. In particular, it is useful to think of packets of turbulent fluid that are angled to towards the wall and convect with a velocity similar to the local mean. However, the actual behaviors which exist are complicated and sometimes quite subtle (but physically important). For instance, measurements show that the correlation field is only strongly peaked at zero time delay.

This is interpreted in wavenumber space as a rapid decorrelation of the small scale eddies, and is modeled in a way that captures the transition.

The new turbulence model has been calibrated using recent measurements and is now available for general studies. Efforts are underway to refine the model, improve its theoretical basis, and confirm its application to high Reynolds number flows.

INTRODUCTION Blake [1] highlights many situations where turbulence provides an unsteady source term that leads to sound. One classic example is the case where turbulence passes through a turbomachinery rotor; producing a broadband spectrum of forces. Predictions of these forces rely on knowledge of the space-time correlation coefficient (see Sevik [2] and Martinez [3]). However, general models of the correlation coefficient are not readily available so the predictions usually rely on idealizations of homogeneous isotropic turbulence. Manoha [4] overcame this deficiency by measuring the correlation field for gusts normal to the surface of his rotor blade. However, these results cannot be generalized to other flow fields or blade pitch angles.

The present research attempts to find a representative model of the space-time correlations. We specifically want to include the effects of inhomogeneity and anisotropy. A

turbulent boundary layer (TBL) subject to an adverse gradient has been selected as a representative test case.

This paper begins with a brief description of the experimental facility and methods. The measured correlation coefficients are compared to classic observations from the literature (see [5] through [11]). An empirical turbulence model is then proposed based upon the observed physical behaviors. The unknown modeling constants are calibrated using the measured data. Qualitative and quantitative comparisons are provided to measure the model's fidelity. Finally, some comments are provided regarding future efforts that are required to generalize and extend this work.

NOMENCLATURE

$C_{ij}(\bar{x}_s \bar{x}_r, \tau)$	Two point space time correlation coefficient
$G_{uu}(k)$	One-sided wavenumber power spectrum
k	Wavenumber
$R_{ij}(\bar{x}_s \bar{x}_r, \tau)$	Two point space time correlation function
Re_θ	Reynolds number on momentum thickness
s	Distance to each point on the S-plane
u'_i	RMS velocity fluctuation in direction i
u^*	Friction velocity
$\bar{U}(y)$	Mean velocity profile in the TBL
x	Streamwise position relative to the survey plane
\bar{x}_r, \bar{x}_s	Locations of the reference and scanning probes
y	Distance from the wall
y_{ref}	Height of the reference probe
$y^+ = yu^*/\nu$	Normalized distance from the wall
z	Transverse distance from the reference probe
δ	Thickness of the TBL
η	Kolmogorov scale
ν	Kinematic viscosity
τ	Time delay between two probe signals
$\tau_\delta = \delta / \bar{U}(y_{ref})$	Typical time scale at the reference probe

DESCRIPTION OF THE EXPERIMENTAL SETUP

This research was performed using the subsonic wind tunnel at the Applied Research Laboratory of Pennsylvania State University. As shown in Figure (1), a temporary liner was installed along the lower interior surface of the tunnel wall.

A smooth flat plate was also installed horizontally across the span of the tunnel. The leading edge was modified to incorporate a nearly elliptic profile. The flow was tripped there in order to achieve a higher effective Reynolds number (i.e. a thicker boundary layer). All TBL measurements were performed in the shear layer that formed against this flat surface.

The combination of liner and flat plate provided a strong contraction through the inlet nozzle followed by a region with nominally zero pressure gradient. The liner in the aft portion of the tunnel provided a slow expansion of flow area (diffusion angle $\sim 5.3^\circ$); thus decelerating the flow and substantially increasing the TBL thickness.

Velocity surveys were performed using thermal anemometry. The measurements showed that the TBL was fully developed and two-dimensional with an edge thickness of 4 to 10 cm¹ depending on measurement position. The Reynolds number based on momentum thickness was of order 10,000. The free stream turbulence intensity in the test section was 0.3% or less.

Profiles of the mean velocity were all reasonably collapsed onto the standard Law of the Wall with Coles' wake function². In the forward portion of the tunnel these surveys were in good agreement with comparison data for zero pressure gradient TBLs. In the adverse gradient the wake parameter ($\Pi \approx 1.75$) was in agreement with values reported by White [12] for comparable pressure gradients.

The TBL in the region of adverse pressure gradient did not achieve a state of equilibrium between the pressure and viscous forces. However, the estimated Clauser pressure gradient parameter [14] ($\beta_c \approx 1.95$) was only slowly increasing. The increase was less than 10% along the streamwise region (~ 0.75 meters long) where most of the measurements were acquired.

¹ The TBL thickness was a small fraction of the dimensions within the test section. Thus, the various shear layers were independent and did not merge. The TBL thickness represents the approximate distance from the wall where the velocity achieves 99% of that in the free stream.

² The friction velocity was estimated using a variety of techniques. These included fitting the mean velocity profile to the Law of the Wall, using semi-empirical estimates from White [12], and using Moses' [13] suggested closure of the Momentum Integral Equation. All estimates agreed within a tolerance of 3%, which was considered acceptable for the current work.

The uncertainty of the measured correlation coefficients has been estimated at approximately 4%. This was considered acceptable based upon compromises between the selected sampling frequency (10 kHz), integration time (26.4 seconds) and data storage limitations (about 2 GB per event).

MEASUREMENTS OF SPACE TIME CORRELATIONS

The measurements were made with two sensors located at different points within the TBL. The first sensor, designated as the reference probe, was manually pre-positioned at a fixed height from the wall. The scanning probe was then commanded to various grid locations using a three-axis traverse. The measurement grid was densely populated near the reference probe in order to resolve any steep gradients which occurred there. Less refinement was required at other portions of the grid since only "large" scales are expected to be correlated across these distances. The completed measurements defined a transverse/vertical "survey plane" which was normal to the mean flow.

The time history of instantaneous velocities was recorded from both probes for each grid point location. Post-processing quantified the correlation coefficients for the normal stresses and two of the shear stresses ($\overline{u_i u_j}$). The data reduction algorithm assumed that the velocity fluctuations were stationary and ergodic:

$$C_{ij}(\bar{x}_r, \bar{x}_s, \tau) = \frac{R_{ij}(\bar{x}_r, \bar{x}_s, \tau)}{u_i u_j} = \frac{1}{u_i u_j} \lim_{T \rightarrow \infty} \frac{1}{2T} \int_{-T}^{+T} u_i(\bar{x}_r, t) u_j(\bar{x}_s, t + \tau) dt$$

$$\text{where } i, j = 1, 2, 3 \quad (1)$$

This evaluation was performed over a broad range of physical time delays (τ) and scanning probe positions (\bar{x}_s). A subsequent bilinear interpolation [15] mapped the correlation coefficients onto a uniform grid for ease of visualization and analysis. Following testing the reference probe was manually relocated to a new reference height and the entire process was repeated. This was accomplished at four reference probe locations ranging from approximately 20% to 85% of the TBL thickness.

Using computer animations the correlation coefficients were visualized as the time delay marched from an early time (negative time delay) to a late time (positive time delay). Several representative snapshots from this cycle are shown in Figures (2a) through (2c). Transverse symmetry is assumed due to the 2D nature of the flow field and so only one-half of the plane is shown.

In these plots the reference probe is located at approximately 5% of the TBL thickness. Theoretically the correlation coefficient must go to unity at zero spatial separation and zero time delay. However, the two sensors could only be positioned within a minimum finite separation distance that was limited by their size. This minimum separation where data could not be acquired is indicated by the rectangles in Figure (2) where the two point correlation coefficient is zero.

The computer animations highlight behaviors that are generally captured in Figure (2):

- The \overline{uu} and \overline{ww} coefficients are correlated over long time delays but are markedly different in their structure. The \overline{vv} coefficient has a very short correlation time scale.
- At early times the peak of the \overline{uu} coefficient occurs at a height above that of the reference probe. The peak is broad and has gentle curvature. As time marches forward the peak appears to convect towards the wall; actually overlaying the location of the reference probe at zero time delay. At zero time delay the profile is nearly exponential, and the correlated region extends through the thickness of the TBL and across a horizontal span of at least δ . A region of weak negative correlation exists to the side of the reference probe ($z/\delta > 0.4$). At late times the peak has convected to a point below the reference probe, and is again broad with gentle curvature.
- The \overline{vv} coefficient shows a spatial dependence that is similar to the \overline{uu} field (except that it remains positive everywhere). However, the peak of the correlation coefficient remains approximately coincident with the location of the reference probe. The measurements of C_{vv} are suspect at the edge of the TBL where the contour becomes very broad. This may be an artifact caused by the very small amplitude of the signal there. In any event the suspect amplitudes are comparable to the uncertainty.
- The \overline{ww} coefficient is correlated over a region comparable to the \overline{uu} field, but has a region of weak negative correlation along the line of symmetry ($z = 0$). The peak of the \overline{ww} field also appears to convect towards the wall.
- All the correlation coefficients show an essentially exponential vertical and horizontal spatial dependence at zero time delay. Each function has its own integral length scale; but all are on the order of 10% to 30% of the TBL thickness. The cusp of the exponential is only maintained near zero time delay.
- The gentle curvature of the peaks at non-zero time delay can be viewed in wavenumber space by taking a spatial Fourier transform along the vertical line of symmetry.

These results are shown in Figure (3). At zero time delay the spectrum of the data is consistent with the theoretical Fourier transform of a simple exponential function with a single integral length scale. The high wavenumbers have a slope of approximately -5/3. However, after a short time delay ($\approx 0.25 * \delta / \overline{U}(y_{ref})$) the high wavenumbers are strongly attenuated and exhibit a slope of approximately -12/3. In this time delay the low wavenumbers are only weakly attenuated. The resultant change in the shape of the spectrum corresponds to the softening of the peaks in the spatial domain.

These results are consistent with observations from other investigations, as discussed below.

COMPARISONS TO THE LITERATURE Favre [5] and his coworkers performed some of the earliest comprehensive measurements of the \overline{uu} correlation field. Their most relevant work was in a TBL with zero pressure gradient ($Re_\delta \approx 3500$). They found that the contours of constant correlation coefficient were elongated in the streamwise plane. Measurements in a plane normal to the flow revealed correlations which extended vertically through most of the TBL thickness and horizontally across a span of approximately 40% of the TBL thickness. They also found that the peak of the correlation coefficient was only centered over the reference probe at zero time delay.

Kovasnay et al. [8] also worked in a zero pressure gradient wall flow ($Re_\delta \approx 3200$). The reference probe in their work was at approximately 50% of the boundary layer thickness. The scanning probe mapped out a survey plane normal to the flow but located downstream at a distance of almost four TBL heights. They found results similar to Favre [5] with additional regions of weak negative correlation centered at $z/\delta \approx \pm 0.55$. The \overline{vv} field had a comparable spatial extent and remained positive everywhere.

Kovasnay et al [8] also post-processed their data using Taylor's frozen turbulence hypothesis to approximate the contours of the correlation coefficient in the streamwise plane. This showed that the contours of the \overline{uu} field were inclined in the direction of flow, forming an imaginary plane of roughly 15 to 20 degrees to the wall at zero time delay. (A similar treatment of our data is shown in Figure (4), where the line inscribed on the C_{uu} field is at roughly 20 degrees to the wall³.) The contour lines in their data were slightly

³ Our data shows that the C_{vv} field has a similar orientation, but the C_{ww} field shows contours that are oriented normal to the wall.

skewed from a constant angle. At the edge of the boundary layer the contours were slightly ahead of the imaginary plane and towards the wall the contours were slightly behind the imaginary plane. Qualitatively, this suggests a picture where the large eddies are traveling faster at the edge of the TBL than they do near the wall. This implies a stretching and rotation of the correlation field.

Head et al [7] provided further insight through flow visualization ($500 \leq Re_\theta \leq 17500$). They found coherent structures which resembled the horseshoe vortices of Theodorsen [16]. The individual structures were oriented at an angle of nominally 45 degrees to the wall and had transverse dimensions that scaled with inner flow variables. Larger shear layers were also identified associated with "bulges" of low momentum fluid at the edge of the TBL. These bulges had well defined streamwise scales on the order of several times the TBL thickness and were usually oriented at an angle of about 20 degrees to the wall. Head et al [7] postulated that these large zones bounded several coherent hairpin type structures that were traveling as a group.

Robinson [9] performed more detailed investigations of coherent structures using the results from a Direct Numerical Simulation (DNS). He found many structures, but their density was lower than the visualizations of Head et al due to the low Reynolds number ($Re_\theta \approx 670$) of the simulation.

These concepts have been significantly advanced by the recent work of Adrian's group (see [10] and [11]). Their detailed PIV measurements provide realizations of the instantaneous velocities in a vertical/streamwise plane of the TBL ($Re_\theta \leq 7705$). The data are viewed in the frame of arbitrary convection velocities, and this reveals "packets" of coherent vortical structures that are traveling as a group with nearly constant streamwise speeds. The heads of the structures are visualized as regions of compact circulation, and the legs appear as intense shear layers with low streamwise momentum (caused by the pumping action between the vortex legs). These packets can reach up to heights of about 80% of δ and can be as long as 2δ . Finally, the larger (and presumably older) packets are convecting faster than the smaller ones. Careful post-processing showed that the convection velocities of the vortex heads nearly matched the mean velocity profile.

Finally, many of the observed behaviors, such as the regions of positive and negative correlation, are conceptually similar to the patterns of velocities induced about an idealized vortex (see Perry et al. [6]). For example, figure (5) shows how this structure could lead to the region of negative correlation in

the \overline{uu} field⁴. Further exploration of these similarities is ongoing and will be reported in the future.

It is obviously desirable to simulate all the above behaviors in our empirical turbulence model. We start by defining a framework that conceptually represents the observed behaviors. Implementation then relies upon finding the optimum choice of modeling constants.

CONCEPTUAL MODEL OF THE C_{uu} FIELD

Our model is implemented along an imaginary S-plane which is initially oriented as shown in Figure (6). The initial angle to the wall (θ) is nominally 20 degrees, and the S-plane intersects the survey plane at the edge of the boundary layer (i.e., $D_0 \approx 1$).

Functionally, this imagined S-plane represents the loci of the local maximum in the \overline{uu} correlation coefficient found in the streamwise projection of measurements from Kovasnay et al [8]. It can also be interpreted in terms of either (1) the angle of the "bulges" observed in the flow visualization of Head et al. [7], or (2) the imaginary plane enveloping the coherent packets suggested by Adrian's group ([10] and [11]).

In our modeling the physical time delay (τ) is normalized using the TBL thickness (δ) and the local mean velocity at the height of the reference probe ($\overline{U}(y_{ref})$):

$$\tau_{nd} = \tau / \tau_\delta \quad \text{where} \quad \tau_\delta = \delta / \overline{U}(y_{ref}) \quad (2)$$

Points on the S-plane are allowed to convect through the survey plane using the local mean velocity from each point in the TBL. This results in the desired stretching and rotation of the S-plane which would be absent if we had used a single convection velocity for the entire plane. This convection is allowed to begin at an early time ($-\tau_{start}$) such that the S-plane exactly intersects the position of the reference probe at zero time delay.

For completeness, our model computes the mean velocity profile using the standard Law of the Wall ($\kappa = 0.41, C = 5.0$) with Coles' wake function ($\Pi = 1.75$):

⁴ An obvious issue is that the classic hairpin structures are estimated to have widths on the order of 100 wall units (Head et al. [7]). However, the present correlation fields, and those of Favre [5] and Kovasnay [8], are much wider. It is unclear if these two observations can be easily reconciled.

$$\bar{v}(y) = u^* \left[\frac{1}{\kappa} \ln(y^+) + C + \frac{2\Pi}{\kappa} \sin^2 \left(\frac{\pi y}{2\delta} \right) \right] \quad (3)$$

This provided a good fit to the measured velocity profile in the region of the adverse pressure gradient. The initial streamwise position of each point on the S-plane is defined by:

$$x_s(y, -\tau_{start}) = - \left(\frac{D_0 \delta - y}{\tan(\theta)} \right) \quad (4)$$

where $x_s = 0$ is taken to indicate the streamwise position of the survey plane. Then the "start" time for convection can be determined from simple geometry:

$$\tau_{start} = \left(\frac{D_0 \delta - y_{ref}}{\bar{U}(y_{ref}) \tan(\theta)} \right) \quad (5)$$

Assuming parallel flow, then at any later time the streamwise position of points on the S-plane are given by:

$$x_s(y, \tau) = x_s(y, -\tau_{start}) + \bar{U}(y)\tau \quad (6)$$

At any given time a different point on the S-plane physically intersects the transverse survey plane. At early times this intersection is obviously near the edge of the boundary layer, and as time marches forward the intersection point approaches the wall. This behavior will be used to represent the apparent convection of the peak in the correlation coefficient.

The linear distance from the intersection point (x_{int}, y_{int}) to each point on the S-plane will arise as an important term in the turbulence model. This distance is given by:

$$s(x_s, y_s, \tau) = \sqrt{(x_s - x_{int})^2 + (y_s - y_{int})^2} \quad (7)$$

Finally, the correlation coefficient is modeled using spatial and temporal dependencies that are assumed to be separable:

$$C_{uu}(\bar{x}, |\bar{x}_s, \tau) = \Phi_1(\tau) \Phi_2(x) \Phi_3(y) \Phi_4(z) \quad (8)$$

Each function controls a physical behavior of the model. The following sections report on the form of these functions and the subsequent calibration of the modeling constants.

INSTANTANEOUS AMPLITUDE OF C_{uu}

The peak amplitudes from the present measurements have been plotted as a function of the non-dimensional time delay.

The resulting collapse of C_{uu} is shown in Figure (7). The data show a nearly exponential dependence centered at zero time delay; however, the amplitudes at late times are about 5% higher than at corresponding early times. These trends have been modeled using a simple weighting function acting on the exponential:

$$\Phi_1(\tau_{nd}) = \frac{T_0 - \tau_{nd}}{T_0} \exp \left\{ - \left| \frac{\tau_{nd}}{\tau_1} \right| \right\} \quad \tau_{nd} > T_0 \quad (9)$$

where a good match with the data is obtained when the effective integral time scale (τ_1) is allowed to transition as:

$$\tau_1 = m|\tau_{nd}| + b \quad (10)$$

The three modeling constants (T_0, m, b) are chosen to achieve a "best-fit" with the measurements.⁵

It is noted that in the limit of large late times the amplitude of Φ_1 does not decay to zero as it should (in fact, it eventually becomes unbounded). However, animations show that problems from this effect are confined to points that are very close to the wall. These are of little interest for the target application of predicting turbomachinery noise. However, a more general model will clearly be required to ensure acceptable performance in all applications. For example, the current model would be completely unacceptable for modeling the source terms in the Poisson equation for wall pressure fluctuations⁶.

SPATIAL DEPENDENCE OF C_{uu} FOR VERTICAL AND TRANSVERSE SEPARATIONS The spatial dependence in the directions normal to the flow are captured via the generating functions Φ_3 and Φ_4 .

$$\Phi_3(y) = \exp \left\{ - \left| \frac{s}{\Lambda_s} \right|^n \right\} F \left(\frac{y}{\delta} \right) \quad (11)$$

$$\Phi_4(z) = \cos \left(\frac{2\pi z}{\lambda_z} \right) \exp \left\{ - \left| \frac{z}{\Lambda_z} \right|^n \right\} \quad (12)$$

⁵ Values of all calibration constants are reported in Appendix A and B for C_{uu} and C_{vv} respectively.

⁶ We are currently pursuing such a general model in terms of the energy spectrum at low wavenumbers. This work is based upon existing models for homogeneous isotropic turbulence (see Batchelor [17] and Hinze [18]).

where

$$F\left(\frac{y}{\delta}\right) = \begin{cases} 1 & \left(\frac{y}{\delta}\right) < 0.90 \\ \exp\left\{-\frac{y-0.9\delta}{0.15\delta}\right\} & \left(\frac{y}{\delta}\right) > 0.90 \end{cases} \quad (13)$$

$$n = 2 - \exp\left\{-\left|\frac{\tau}{C_2\tau_\delta}\right|^2\right\} \quad (14)$$

$$\Lambda_s = \frac{\delta}{\sin\theta} \left[D_2 - (D_2 - D_1) \exp\left\{-\left|\frac{\tau}{C_2\tau_\delta}\right|\right\} \right] \quad (15)$$

$$\Lambda_z = \delta \left[G_2 - (G_2 - G_1) \exp\left\{-\left|\frac{\tau}{C_2\tau_\delta}\right|\right\} \right] \quad (16)$$

In equation (11) the function $F(y/\delta)$ provides an attenuation for positions that are at the edge of the boundary layer and beyond. The function is unity for all points below 0.9δ . (The form of this term is chosen solely for convenience. A more physical approach might be to base this term on the intermittency distribution.)

In eq. (12) the cosine function provides an envelope that changes the sign of the correlation coefficient along the transverse direction. The result again matches observations from the experimental data; this is again a modeling convenience rather than a physical necessity.

The power n within the generating functions is modeled by equation (14)⁷. It takes on a value of 2 at large time delays, reducing the generating functions to simple Gaussian curve fits. However, at zero time delay the value becomes unity and the generating functions become simple exponentials. This transition modifies the shape of the wavenumber spectrum. This effect is shown in Figure (8), which plots the results of a theoretical Fourier transform for the Gaussian and exponential curve fits. (Note that in this result both functions use the same integral scale and are normalized to have a mean square value of unity.) The spectrum of the Gaussian function indicates a strong preference for the low wavenumbers. This shift is physically meaningful.

The smallest eddies in the TBL are of size η and have a low turbulent Reynolds numbers ($Re_\eta = u'\eta/\nu$). Thus, they are rapidly decorrelated by viscous dissipation. Conversely, the largest scales (which contain most of the energy) have a high Reynolds number and are affected by the comparatively weak

actions of inertial and pressure forces. As a result the low wavenumbers have much longer "lives" than their small scale counterparts. This is manifested in the spectrum mainly as a change in slope at high wavenumbers. At low wavenumbers the spectral shape remains approximately constant. It simply rises and falls as a function of time delay so that its integrated value provides the correct instantaneous peak amplitude of the correlation coefficient.

Thus, the transition governed by equation (14) affects the distribution of energy within the wavenumber spectrum. In order to adjust for this effect it is convenient to also transition the respective integral length scales as indicated by equations (15) and (16). Of course, the integral length scale is just a modeling construct so this does not imply any change in the behavior of the largest scales in the flow. Rather it is used to control the shape of the wavenumber spectrum to match empirical observations. (Although not shown in this paper, the above approach coupled with the Φ_1 amplitude scaling provides a good match to the instantaneous wavenumber spectra of the measurements.)

As shown in Appendix A, the modeling constants which control the shape at zero time delay (i.e., D_1 and G_1) are consistently on the order of 50% of their value from large time delays (D_2 and G_2). This observation could be used to eliminate two calibration constants in the model. In this case equations [14] and [15] would be recast as:

$$\Lambda_s = \frac{D_2\delta}{\sin\theta} \left[1 - \frac{1}{2} \exp\left\{-\left|\frac{\tau}{C_2\tau_\delta}\right|\right\} \right] \quad (17)$$

$$\Lambda_z = G_2\delta \left[1 - \frac{1}{2} \exp\left\{-\left|\frac{\tau}{C_2\tau_\delta}\right|\right\} \right] \quad (18)$$

These simplifications will not be employed for the purposes of this paper. A total of 6 new constants have been added to the model ($\lambda_1, C_2, D_1, D_2, G_1, G_2$).

STREAMWISE DEPENDENCE OF C_{uu} The sensitivity to streamwise separations between points on the S-plane and the survey plane are captured via the function :

$$\Phi_2(x) = \exp\left\{-\left|\frac{x_s}{\overline{U}(y)\tau_2}\right|^n\right\} \quad (19)$$

The ratio of distance to mean velocity within the exponential is essentially the convection time based upon the local mean velocity. The term τ_2 is a new integral time scale given by:

⁷ Knight [19] has suggested an alternate empirical formulation that is more amenable to mathematical analysis. This and other theoretical generalizations are currently being pursued to improve the foundation of the modeling constants, and thus hopefully the scalability to other flow fields.

$$c_2 = \frac{|T_0|\delta}{\overline{U}(y_{ref})} \left\{ C_2 + (C_1 - C_2) \left| \frac{\tau \overline{U}(y_{ref})}{T_0 \delta} \right| \right\} \quad (20)$$

This introduces one new modeling constant (C_1). However, calibration of the modeling constants has shown that the curve fit is optimized when $C_1 = C_2$. Thus, eq. (20) can be recast as:

$$\tau_2 = \frac{C_2 |T_0| \delta}{\overline{U}(y_{ref})} \quad (21)$$

MODELING CONSTANTS FOR C_{uu} The above formulations contain 12 modeling constants (which could be reduced to 9 using the simplifications that are noted). We have calibrated these constants by selecting values which provided the best agreement with measurements across all time delays and reference probe locations.

In general, the results from the calibrations are weakly dependent upon the height of the reference probe. However, acceptable performance has been achieved by using the constants from optimization when the reference probe is at $\leq 5\%$ of the TBL thickness. The values of these constants are reported in Appendix A. As shown in the next section, the discrepancies due to this simplification are most apparent for the measurement location that is closest to the wall.

SUMMARY OF RESULTS

Typical results from the model are shown in Figure (9a-b) for zero time delay and a late time delay respectively.

Typical quantitative comparisons are provided in Figure (10). For this analysis we choose three key metrics: (a) the area (i.e., energy) under the C_{uu} profile for a slice taken along the vertical line of symmetry, (b) the area under the profile for a slice taken horizontally at the elevation of the reference probe, and (c) the span of the elevated region taken along the vertical line of symmetry ($C_{uu} > 0.15$). Results show good agreement with the data in both character and amplitude at all time delays. The average errors between the model and measurements are summarized in Table (1).

EXTENSION TO OTHER CORRELATIONS

We have implemented the above model using a new set of modeling constants in an attempt to also simulate the behavior of the C_{vv} field. The constants from this brief optimization are reported in Appendix B.

Figure (11) shows that the modeled correlation field is in modest agreement with the data at zero time delay. Further, Table 2 shows that the average errors are still acceptable albeit somewhat higher than for the C_{uu} field. These errors are dominated by the disagreement at the broad region of correlation towards the outer edge of the TBL. Of course, we've already noted that this same region of the measurement is suspect and generally comparable to the statistical uncertainty.

The present model forces the peak of the C_{vv} field to convect towards the wall; and this behavior is not observed in the measurements (for example, compare the behavior of the model in Figure (12) vice that of the data in Figure (4)). The correlation time is so short that the behavior is not overwhelming. However, it introduces a shift at small time delays and this is not in agreement with the data.

A simpler and overall more successful model of the C_{vv} field has already been implemented using a plane that is oriented orthogonal to the wall and travels with a constant convection velocity. In this case the relevant modeling constants are similar to those reported here, but the physical behavior and the average errors are both improved.

Finally, the present model has been used to simulate the behavior of the C_{ww} correlation field. Equation (11) was modified in order to capture the spatial dependence for vertical separation distances:

$$\Phi_3(y) = \exp \left\{ - \left| \frac{s}{\Lambda_z} \right|^n \right\} F \left(\frac{y}{\delta} \right) \cos \left(\frac{2\pi y}{\lambda_y} \right) \quad (22)$$

The results are in good qualitative agreement with the measurements, and the average errors are usually less than 10%. A more detailed review of these results will be documented in a future publication.

SUMMARY OF NEEDED RESEARCH

The present turbulence model has several limitations which warrant further development:

1. The model should be recast on firm theoretical ground where possible.
2. The experimental data were acquired at Reynolds numbers that are much lower than many practical applications. Testing at higher Reynolds numbers will be needed to confirm the observed behaviors and make any adjustments to the modeling constants.
3. The present work was limited to reference probe locations in the wake region of the TBL. However, applications such as modeling of wall pressure

fluctuations require knowledge of the correlation fields at points that are much closer to the wall. This work may provide a framework for those experiments.

4. Lastly, it makes sense to further explore the ideas of Perry et al [6] and Adrian's group ([10] and [11]). The objective is to determine the extent to which packets of idealized vortical structures can explain the behaviors that have been observed.

ACKNOWLEDGEMENTS This work was supported by General Dynamics Electric Boat Corporation. Dr. Martin Manley and Mr. Gary Cooper are the technical monitors. The work has benefited from conversations with Dr. Charles Knight and Dr. Phillip Morris. Their insight and suggestions are greatly appreciated.

Mr. Dan Quinlan of Lucent Technologies made the generous donation of hot wire anemometry equipment that made this research possible.

Dr. Steve Deutsch, Dr. Tim Brungart and Mr. David Jenkins provided invaluable assistance with the instrumentation system and the preliminary measurements.

REFERENCES

- [1] Blake W., K., "Mechanics of Flow Induced Sound and Vibration, Vol II, Complex Flow Structure Interactions", Academic Press, 1986
- [2] Sevik, M. M., "Sound Radiation from a Subsonic Rotor Subjected to Turbulence", *Fluid Mechanics, Acoustics and Design of Turbomachinery Part 2*, NASA SP 304, 1974, pp. 493-511
- [3] Martinez, R., "Analysis of the Right Shift of the Blade Rate Hump in Broadband Spectra of Propeller Thrust", U-1993-381.9, 1991, Cambridge Acoustical Associates
- [4] Manoha, E. S., "Broadband Noise from a Propeller in a Turbulent Flow", NCA-Vol. 25 Proc of the ASME Noise Control and Acoustics Division, 1998. pp. 137-148.
- [5] Favre, A. J., "Review on Space Time Correlations in Turbulent Fluids", *J. Applied Mechanics*, June 1965, pp. 241-257
- [6] Perry, A. E., Henbest, S. and Chong, M. S., "A Theoretical and Experimental Study of Wall Turbulence", *J. Fluid Mech.* 165 (1986), pp. 163-199
- [7] Head M.R. and Bandyopadhyay, P., "New Aspects of Turbulent Boundary Layer Structure", *J. Fluid Mech.* 107, pp. 297-338
- [8] Kovasnay, L. S., Kibbens, V. and Blackwelder, R. F., "Large-Scale Motion in the Intermittent Region of a Turbulent Boundary Layer", *J. Fluid Mech.* , 41 part 2 (1970), pp. 283-325
- [9] Robinson, S. K., "The Kinematics of Turbulent Boundary Layer Structure", NASA TM 103859, April 1991
- [10] Tomkins, C. D., Adrian, R. J. and Balachandar, S., "The Structure of Vortex Packets in Wall Turbulence", AIAA Paper No. 98-2962, 29th AIAA Fluid Dynamics Conference, June 15th-18th, 1998. Albuquerque, NM.
- [11] Adrian, R. J., Meinhart, C. D., and Tomkins, C. D., "Vortex Organization in the Outer Region of the Turbulent Boundary Layer", University of Illinois, Theoretical and Applied Mechanics Report No. 924, November 1999.
- [12] White, F. M. (1991), *Viscous Fluid Flow*, McGraw-Hill
- [13] Moses H. L. (1969), "A Strip-Integral Method for Predicting the Behavior of Turbulent Boundary Layers", *Computation of Turbulent Boundary Layers - 1968 Stanford Conference*, edited by S.J. Kline, M.V. Morkovin, G. Sovran and D.J. Cockrell, Stanford University Press
- [14] Clauser F. H., (1954), "Turbulent Boundary Layers in Adverse Pressure Gradients", *Journal of the Aeronautical Sciences*, vol 21, pp 91-108, Feb 1954
- [15] Press, W. H., Teukolsky, S. A., Vetterling, W. T. and Flannery, B. P., "Numerical Recipes in Fortran - Second Edition", Cambridge University Press, 1992
- [16] Theodorsen, T., "Mechanism of Turbulence", Proc. 2nd Midwestern Conference on Fluid Mechanics, Ohio State University, 1952
- [17] Batchelor, G. K., "The Theory of Homogeneous Turbulence", Cambridge University Press, 1953
- [18] Hinze, O. J., *Turbulence*, McGraw-Hill Inc. 1975
- [19] Knight, C. J., private communications

APPENDIX A - MODELING CONSTANTS FOR C_{uu}

The following constants were chosen based upon optimizations when the reference probe was located at approximately 65% of the TBL thickness.

$$\begin{array}{lll}
 \theta = 21^\circ & T_o = -5.5 & C_1 = 0.42 \\
 m = 0.21 & b = 0.35 & C_2 = 0.42 \\
 D_o = 0.95 & D_1 = 0.30 & D_2 = 0.60 \\
 G_1 = 0.22 & G_2 = 0.40 & \lambda_z = 1.05\delta
 \end{array}$$

APPENDIX B - MODELING CONSTANTS FOR C_{vv}

The following constants were chosen based upon optimizations when the reference probe was located at approximately 65% of the TBL thickness.

$\theta = 21^\circ$	$T_o = -5.5$	$C_1 = 0.22$
$i = 0.12$	$b = 0.085$	$C_2 = 0.22$
$D_o = 0.95$	$D_1 = 0.18$	$D_2 = 0.36$
$G_1 = 0.09$	$G_2 = 0.18$	$\lambda_2 = \infty$

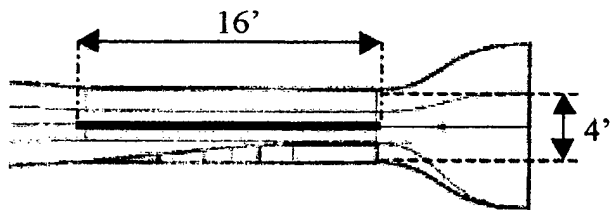


Figure (1) - Wind Tunnel with Liner and Flat Test Plate Installed

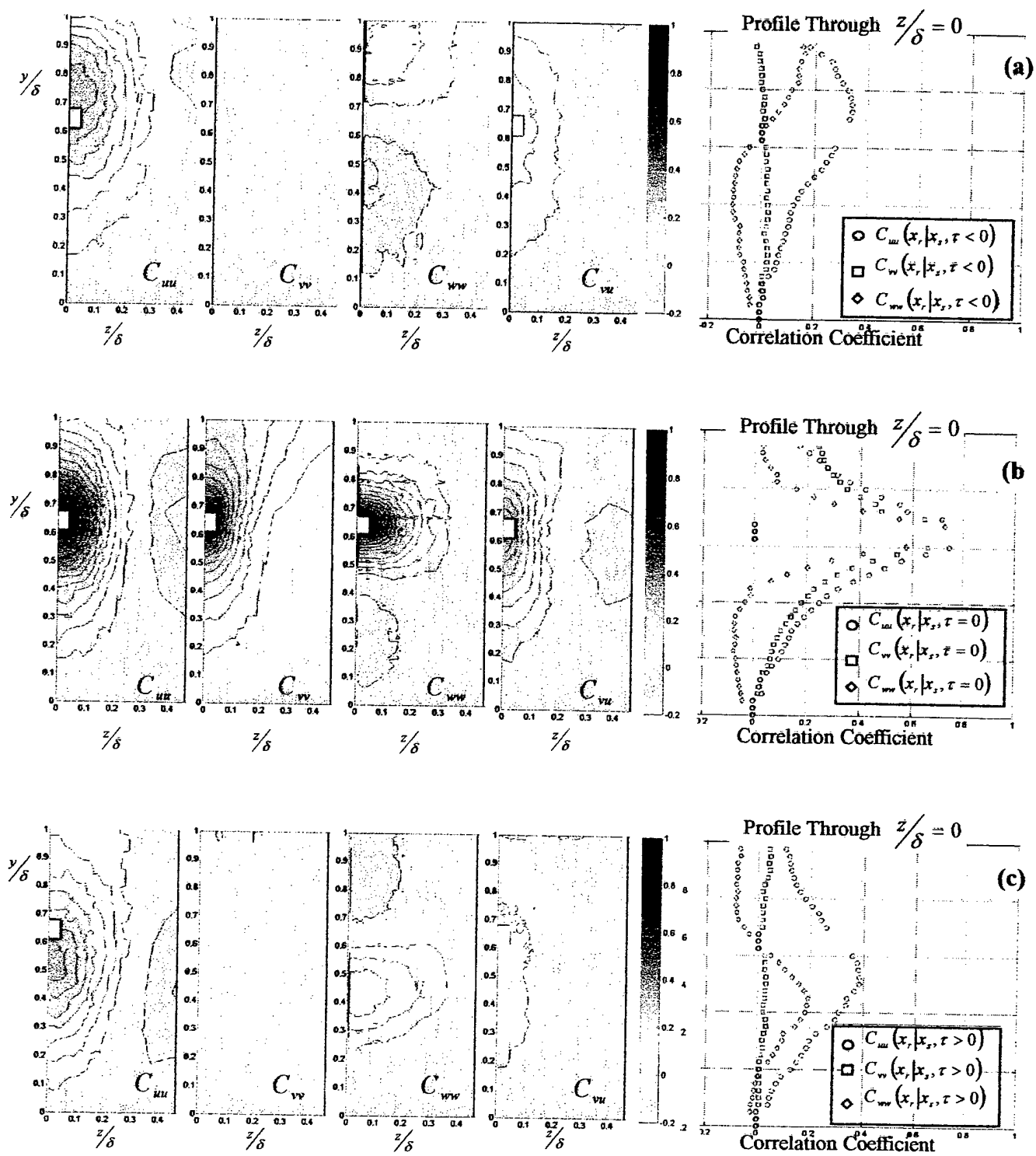


Figure (2) - Summary of Typical Measurements ($y_{ref} = 0.65\delta$) for
(a) an EARLY time ($\tau \sim -\tau_\delta/2$), (b) Zero Time Delay and (c) a LATE time ($\tau \sim +\tau_\delta/2$)

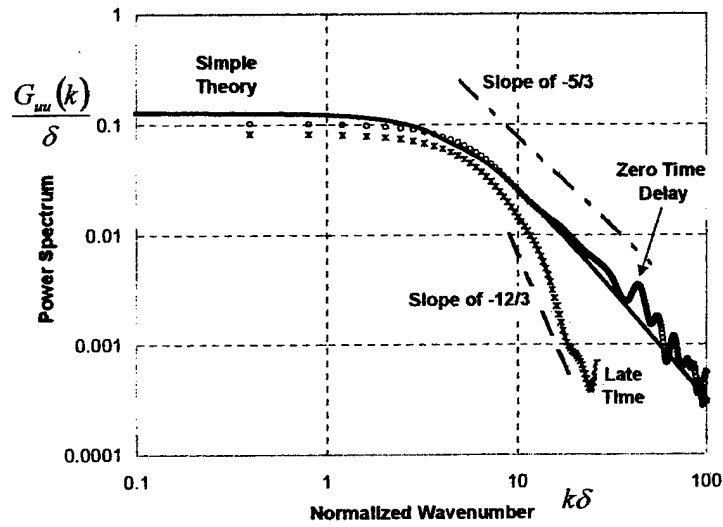


Figure (3) - Wavenumber Spectra Taken along the Vertical Line of Symmetry

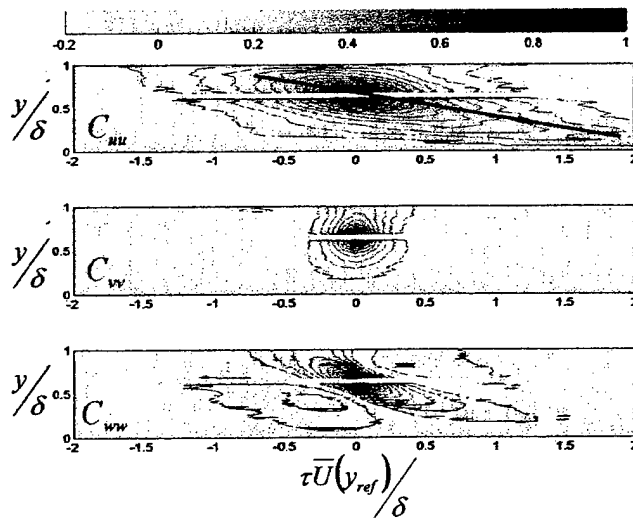


Figure (4) - Projection of the Measured Correlation Coefficient onto the Streamwise Plane using Taylor's Hypothesis ($y_{ref} = 0.65\delta$)

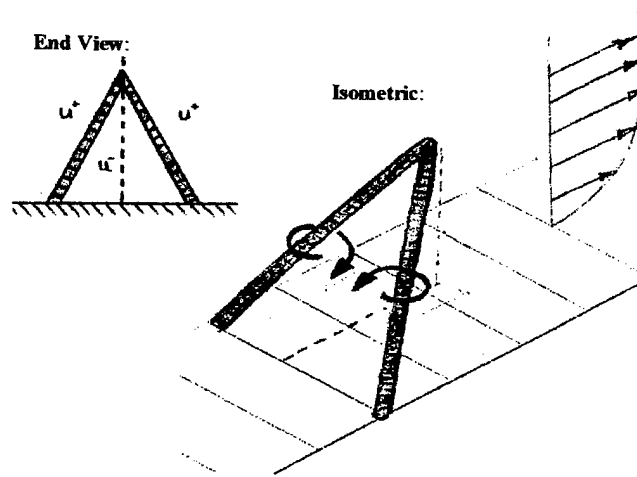


Figure (5) - Induced Velocities about an Idealized Vortex Structure

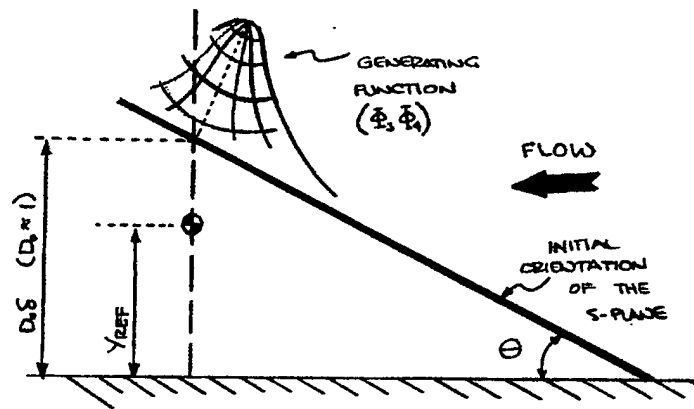


Figure (6) - Framework and Orientation of the Turbulence Model at the Earliest Time

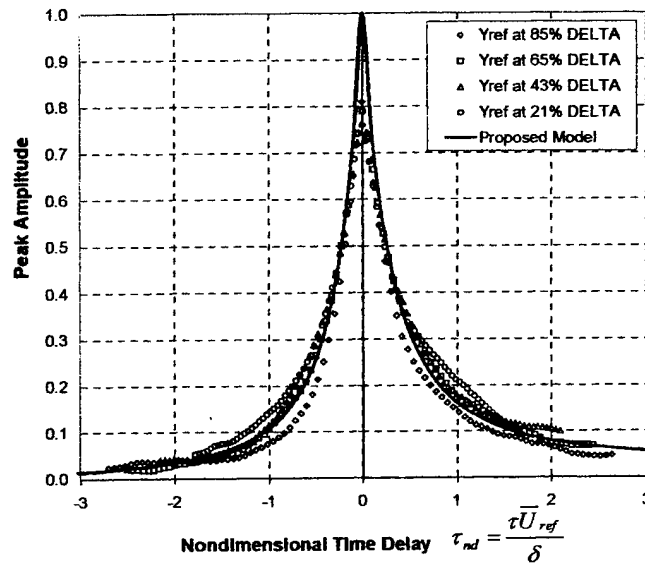


Figure (7) - Modeling the Instantaneous Peak of the Correlation Coefficient

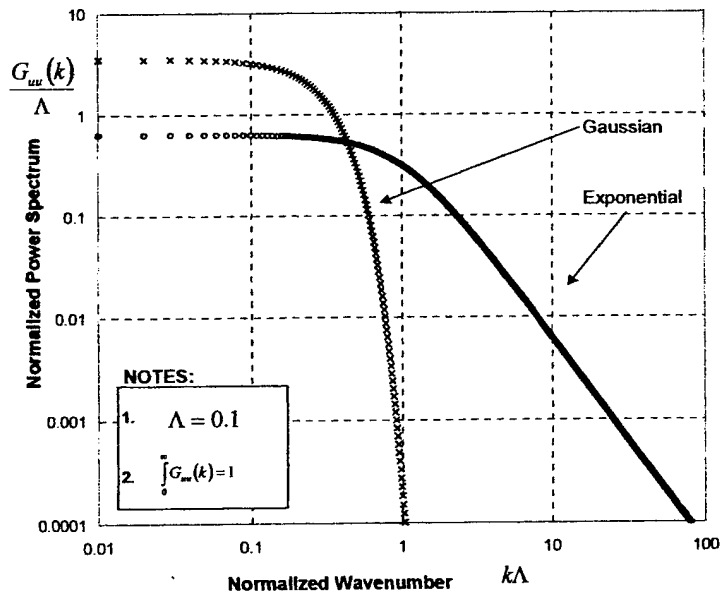


Figure (8) - Theoretical Wavenumber Spectrum for Two Simple Forms of the Correlation Functions

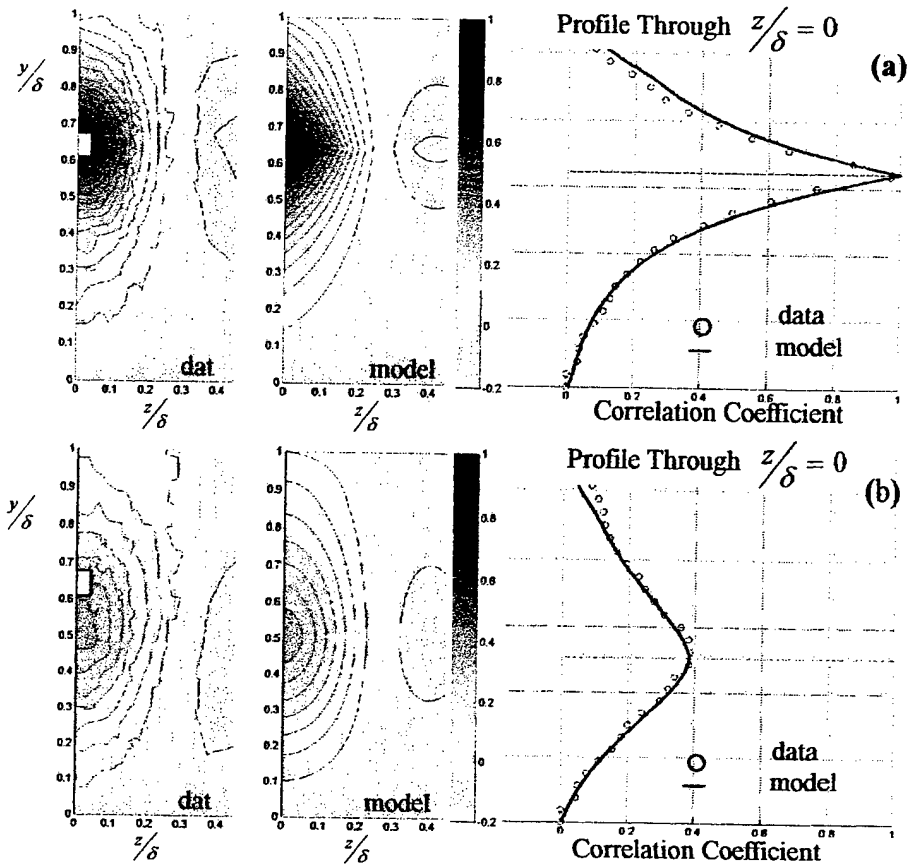


Figure (9) - Typical Comparisons of the Model versus Measurement ($y_{ref} = 0.65\delta$) for C_{uu} at (a) Zero Time Delay, (b) a Late Time

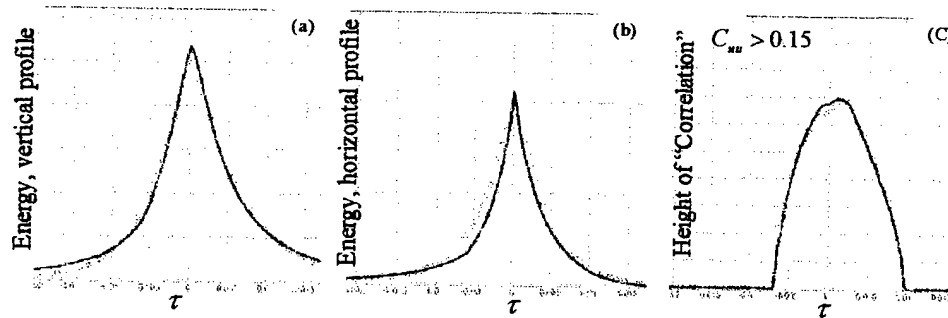


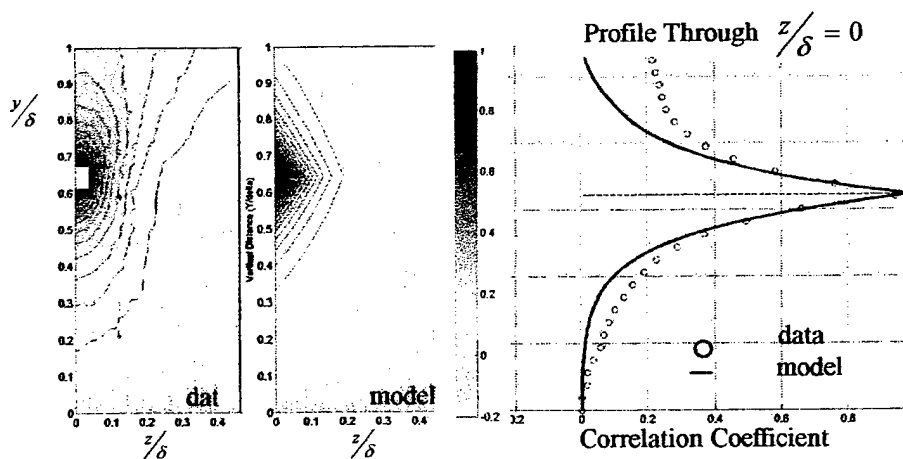
Figure (10) - Comparison of Measurement versus Model ($y_{ref} = 0.65\delta$) for (a) the area under the vertical profile, (b) the area under the horizontal profile, and (c) the span of TBL where $C_{uu} > 0.15$ (circles \rightarrow data, line \rightarrow model)

Table (1)
Summary of Average Errors C_{uu}

Reference Probe Location % of delta	"Energy" Along the Vertical Symmetry Line	"Energy" Along the Horizontal Line @ Ref. Probe	Width of Correlated Region Along Vertical Symmetry Line
85%	4.9%	3.0%	12.5%
65%	2.7%	2.7%	2.5%
43%	4.1%	6.2%	8.2%
21%	7.0%	6.1%	14.8%

Table (2)
Summary of Average Errors for C_{vv}

Reference Probe Location % of delta	"Energy" Along the Vertical Symmetry Line	"Energy" Along the Horizontal Line @ Ref. Probe	Width of Correlated Region Along Vertical Symmetry Line
85%	9.7%	11.6%	14.5%
65%	8.5%	7.1%	12.0%
43%	9.2%	6.7%	11.4%
21%	7.9%	9.3%	12.1%



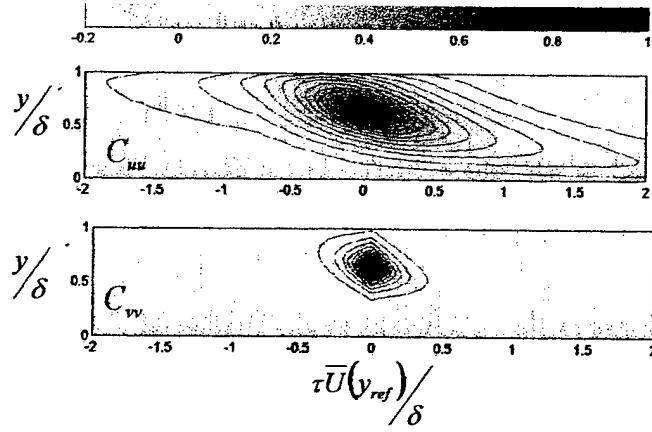


Figure (12) - Projection of the Modeled Correlation Fields onto the Streamwise Plane Using Taylor's Hypothesis ($y_{ref} = 0.65\delta$)

APPENDIX 58

Book Review

Opinions expressed here are not necessarily those of the editors of *Noise Control Engineering Journal* or of the Institute of Noise Control Engineering.

Acoustics of Fluid-Structure Interactions

M. S. Howe

Cambridge Monographs on Mechanics

Cambridge University Press, Cambridge CB2 2RU, UK, 1998
560 pp., ISBN 0521633206, USD 85.00

The acoustics of fluid-structure interactions is a complex subject that deals with the noise created by fluid dynamic sources near solid objects and flexible structures. It is an area of practical concern for the noise control engineer. This book provides an important contribution to this complex field by presenting the equations and solutions for an extremely broad range of fluid-structure interaction problems, and all carefully derived from first principles. Clarity and rigor are the trademarks of each section.

Howe does a marvelous job of setting real-world problems in a mathematical framework. In most cases, he offers concise physical interpretations and insights based on the derived solutions. He does this in a way that allows, in many examples, the incorporation of the *mean* properties of fluid-structure interactions determined from numerical codes. The result is that hydrodynamic calculations for complicated structures can be coupled with the analytical solutions presented here to arrive at accurate predictions of the sound and/or vibration. The first half of the book deals with the radiation and scattering of aerodynamic sources by rigid bodies of various geometrical complexity. The effect of flow-induced structural vibration on the radiation and absorption of sound is then treated rigorously in the second half of the book.

The Introduction covers the fundamental equations of Newtonian fluid mechanics and the structural dynamics of elastic solids, membranes, plates, and shells. The author covers the Green's function method of solution for inhomogeneous wave equations. His treatment of the compact Green's function, which permits the calculation of the leading monopole and dipole terms of the sound produced by low Mach number hydroacoustic sources near solid bodies, is particularly clear. He shows that this function can be computed from elementary potential flow theory. The chapter concludes with the vorticity formulation for aeroacoustic sources, which is useful in the prediction of noise due to, for example, vortex shedding and problems requiring calculation of vortex-induced unsteady forces.

Chapter 2 covers the Lighthill acoustic analogy. Howe emphasizes that the expected quadrupole sources in free-space turbulence can be augmented by additional dipole and monopole "hot spot" sources when density variations are included. This has application to hot jets and emphasizes the role of entropy inhomogeneities in sound production. The Ffowcs Williams-Hawkins equation is discussed in the context of non-stationary flow noise sources on and near solid structures in motion, such as a rotating lifting surface attached to a craft in forward flight. Solutions are valid for either flexible or rigid structures, and with or without fluid aspiration.

Because entropy fluctuations are the dominant sources of low Mach number flow noise, Howe develops an acoustic analogy based on fluctuations of the total enthalpy. He applies the theory to a variety of practical problems including radiation from spinning vortices, laser excited heat sources, and two-phase flow. Damping, absorption, and scattering of sound by turbulence are analyzed, and the chapter concludes with the mechanisms of mixing, screech, and forward flight affected jet noise.

Chapter 3 deals with noise generation by moving rigid surfaces. The compact Green's function is used to compute the radiation from turbulence convecting through nozzles and over semi-infinite planar edges, and wedges. The interaction of free-stream turbulence and vorticity with leading edges is addressed. This has application in turbulence ingestion rotor noise, and in blade-vortex interaction noise. The chapter continues with well-explained noise theories for turbulent boundary layers over smooth and rough surfaces, and for trailing edges of practical shape; rounded, blunt, serrated, and porous. The chapter has examples of noise generated by sources moving at very high-speed. They include rotor blades that support local shocks, or have cross-sectional profiles that result in thickness noise. The time-dependent pressure pulse created in a tunnel due to the entering of a high-speed train is also discussed. The analysis is detailed enough to show the effect of tunnel portal shape on the magnitude of the induced pressure pulse.

Chapter 4 provides analysis of sound sources in the vicinity of an elastic plate. The presentation includes the excitation of a plate—with and without a coating—by the evanescent (subsonic) pressure components of a grazing turbulent flow. Structural energy flow within the plate is considered, and the effects of structural discontinuities on the scattering of this internal, as well as the external, acoustic energy is detailed with rigor. Howe solves the flexible trailing edge noise problem in the concluding sections of this chapter.

Chapter 5 provides analysis of fluid-structure interactions in which the compliance of the surface contributes to the damping of the radiated noise. This is followed by a thorough discussion of attenuation of sound by vorticity production at edges and by normal or grazing flow interactions with perforated screens. This applies to acoustic liners installed in a duct with flow. Discussion continues with jetting flow in rigid and elastic tube banks, along with the various kinds of nonlinear interactions that occur in ducts with acoustic streaming, or within the vena contracta that occurs in normal flows through apertures.

Chapter 6 covers the analysis of several resonant and unstable systems including cavity resonances and edge tones. Expressions are derived for the frequencies of instability, the vorticity fluctuations, the radiated sound, or the absorption of sound due to flow excited cavities situated in walls or pipes (side branches). The theory of edge tones is given equal treatment. Howe uses a vortex model of the jet, and then derives

the interactions of these vortices with the edge geometry of interest. Applications include devices like the hole whistle, flue organ pipe, and flute. The final topics of the book are flame and combustion instabilities, and thermoacoustic engines and heat pumps. The reference section of the book is very complete, having 486 entries.

The book, in general, is quite theoretical and the mathematics challenge the reader. But because a well-posed model can be used to identify the parameters of a physical

system that are important from the noise production point of view, the formulations found in this book may be very valuable in the interpretation and scaling of experimental flow noise data collected by the noise control engineer. The models can also be used to help plan a test matrix involving many types of noise sources of fluid dynamic origin.

*Gerald C. Lauchle
Dennis K. McLaughlin
Penn State University*

ACTUATOR STUDIES

Materials And Designs

APPENDIX 63

Torsional actuator based on mechanically amplified shear piezoelectric response

A.E. Glazounov^a, Q.M. Zhang^{a,*}, C. Kim^b

^a Materials Research Laboratory, The Pennsylvania State University, University Park, PA 16802, USA

^b Naval Research Laboratory, Washington, DC 20375, USA

Received 7 October 1998; received in revised form 15 June 1999; accepted 1 July 1999

Abstract

A torsional actuator, based on the concept of mechanical amplification of piezoelectric shear strain and capable of generating large angular displacement, was proposed and studied experimentally. The actuator is a tube consisting of an even number of the segments poled along the length, which are adhesively bonded together, and the joints act as electrodes to apply the driving voltage. The experimental data measured on the prototype actuators (i) prove the proposed concept of mechanical amplification of small piezoelectric shear strain to generate large torsional motion, (ii) show that the actuator functions well both without load and under the torque load and (iii) demonstrate that the actuator can operate continuously for a long period of time without drop in its performance. Also, the results demonstrated that the proposed torsional actuator is capable of producing both large torque and large angular displacement in a compact package, sufficient to meet many smart structures requirements, and can be tailored for a variety of application requirements. Finally, one of the obvious advantages of the present design of the actuator is its simplicity: the piezoelectric shear strain is transformed directly into the angular displacement, whereas in the previously reported actuators, the conversion mechanism into the torsional motion was rather complicated which thus required a sophisticated design of the whole system. © 2000 Elsevier Science S.A. All rights reserved.

Keywords: Torsional actuator; Shear strain; Piezoelectric ceramics; Nonlinearity; Reliability

1. Introduction

Piezoelectric ceramic materials, such as lead zirconate titanate (PZT) are now widely used in solid-state actuators and sensors which were designed for numerous applications, such as precision positioning, noise and vibration sensing and cancellation, linear motors, and many others [1,2]. In many of those applications, a large torsional displacement is required, for example, in robotics to achieve the micropositioning [3,4], in CD drivers [5], in helicopters to control the trailing edge flaps (TEF) of rotor blades [6–8], etc. To meet this demands, many works have recently been devoted to the development of actuators capable of generating a large angular displacement with a large torque output [3–9] from the piezoelectric strain.

Recently, a novel type of torsional actuator has been proposed [10]. Its concept is to use shear piezoelectric effect and tubular geometry in order to generate the angular displacement. The advantages of this design include (i) the possibility to obtain large angular displacement by using the geometrical amplification, L/R (where L and R are the length and the radius of the tube, respectively). Also, (ii) in most piezoelectric ceramic materials, the shear piezoelectric coefficient, d_{15} , has the highest value among piezoelectric coefficients, which also contributes to developing large values of torsional angle and torque output. Finally, (iii) the design is simple, because the piezoelectric shear strain is transformed directly into the angular displacement (whereas in the previously reported actuators, the conversion mechanism into the torsional motion was rather complicated, including the use of hinges, which thus required a sophisticated design of the whole system [4–9]).

It is the purpose of this paper to continue the study of the proposed torsional actuator and report the results of the

* Corresponding author. Tel.: +1-814-863-7846; fax: +1-814-863-7846; E-mail: qxz1@psu.edu

detailed tests of its performance, which addresses both the device and material issues. The former include operation of the actuator in different conditions, such as without load, under the torque load, and at electromechanical resonance. Material issues are related with the utilization in this actuator of piezoelectric shear response of PZT ceramics, which has not yet received a broad use in the actuator applications. They include fatigue behavior, mechanical strength and nonlinear shear piezoelectric response of PZT ceramics.

2. Actuator design

An idea of the torsional actuator proposed recently [10] and studied in this work is to use the shear piezoelectric effect, where the external electric field is applied perpendicular to the direction of the remanent polarization, P_r (Fig. 1(a)), in order to produce the angular displacement. A schematic view of the actuator is shown in Fig. 1(b). The actuator is a tube consisting of an even number of piezoelectric ceramic segments which are adhesively bonded together using a conductive epoxy, which acts as electrodes to apply the driving field, E . The segments are poled along the length, where the polarization direction alternates between adjacent segments. Since the segments are electrically connected in parallel, they will exhibit a coherent shear deformation under the applied electric field. The cylindrical symmetry of the actuator will directly transform the shear strain, $S_5 = d_{15}E$, induced in each segment into the angular displacement, β , of the top of the tube with respect to its bottom (Fig. 1(b)) which is equal to:

$$\beta = \frac{L}{R_{\text{out}}} d_{15} E, \quad (1)$$

where L is the length of the tube and R_{out} is its outer radius. This equation shows that even though the shear

strain is usually quite small in the piezoelectric materials, a large torsional displacement β can be achieved by using a tubular structure with a large ratio of L/R_{out} . Using elastic properties of tube-shaped samples [11], the torque, T_{dev} , developed by the actuator can be found as:

$$T_{\text{dev}} = \frac{\pi(R_{\text{out}}^4 - R_{\text{in}}^4)}{2s_{44}R_{\text{out}}} d_{15} E, \quad (2)$$

where s_{44} is the shear elastic compliance of the material and R_{in} is the inner radius of the tube. According to Eq. (2), the torque T_{dev} is independent of the length of the tube, even though the angular displacement β increases linearly with L , Eq. (1).

3. Experimental

Prototype torsional actuators were fabricated from the commercial piezoelectric ceramic tubes of composition PZT-5A ("EDO", USA). Each tube was first cut into eight segments, which then were poled along the length using a continuous poling technique [12]. Finally, the segments were bonded together using a silver-filled epoxy adhesive MB-10HT/S ("Master Bond", USA), which was selected because it has both high shear strength, and is easy to process. This adhesive compound was coated on both surfaces of the segments, which were then assembled into the tubular actuator according to the design shown in Fig. 1(b), and cured at 125°C for 1 h using a vacuum bagging process. Consolidation of the joints by vacuum bagging lead to joints typically 25 μm in thickness and very uniform along their length [12]. The assembled single-tube prototype actuator had the following dimensions: $R_{\text{in}} = 0.96$ cm, $R_{\text{out}} = 1.27$ cm, and $L = 6.35$ cm, so that the aspect ratio in Eq. (1) was equal to $L/R_{\text{out}} = 5$.

According to Eq. (1), in the proposed design of torsional actuator, the angle β increases linearly with the

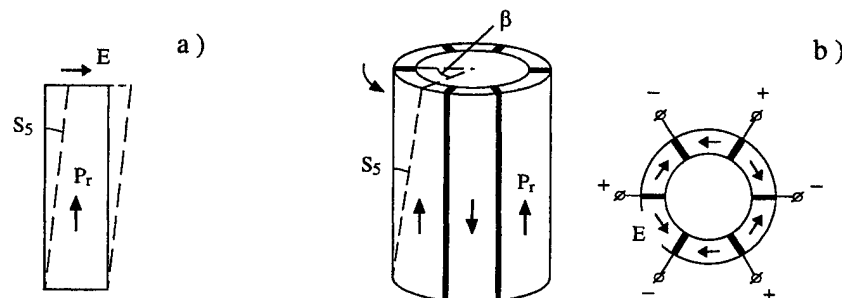


Fig. 1. (a) In piezoelectric shear effect, electric field, E , is applied perpendicular to the direction of the remanent polarization, P_r , thus, producing the shear strain, $S_5 = d_{15}E$, in the sample. Solid and dashed lines show the sample before and after deformation, respectively. (b) The proposed torsional actuator is a tube consisting of an even number of the segments of piezoelectric ceramics which are poled along the length and bonded together using a conductive epoxy. The polarization direction alternates between adjacent segments, as shown with arrows on the left. The electric field, E , is applied perpendicular to P_r , and also has opposite directions in neighboring segments (as shown with arrows on the right). Therefore, depending upon the polarity of applied voltage, the top of the tube will twist by angle β either clockwise or counterclockwise with respect to its bottom.

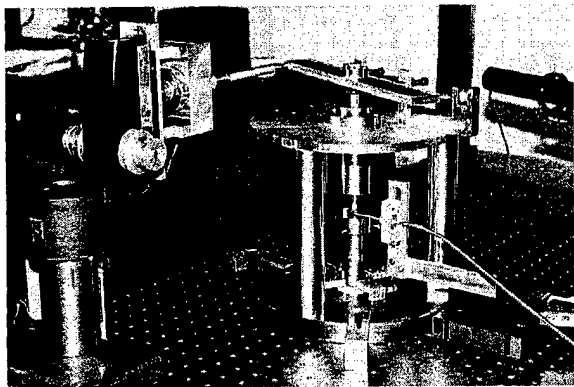


Fig. 2. A photograph of the set-up used for the study of the effect of external static torque on the response of the torsional actuator.

length L of the actuator. To test this hypothesis, two identical tubes with the dimensions described above were joint together lengthwise. The test included the characterization of the tubes before and after the joining them together.

To characterize the actuator, the torsional angle produced by the applied electric field was measured in the following experiments. In the load-free conditions, β was measured as a function of the amplitude and frequency of the ac driving field. Also, electrical fatigue test was performed, where the ac field with a fixed amplitude and frequency was applied to the actuator, and β was monitored as a function of time. Under the torque load, T , the torsional angle was measured as a function of dc and ac electric driving field at different values of T .

In all experiments, the actuator was tightly clamped with its bottom to the optical table, and its top was free to twist due to the applied electric field. In order to measure β , a small mirror was attached on the top of the tube and the distance change between the mirror and the optical fiber probe of a MTI-2000 fonic sensor was measured. The electrical output signal from the MTI-2000 was monitored using an oscilloscope or SR-830 lock-in amplifier.

The effect of the torque load on the actuator performance was studied using a special set-up (Fig. 2) which was developed in Materials Research Laboratory [13]. Although, there are commercial torque load test machines available, they are not suitable for the torque load test of torsional actuators. The main reason is that these machines were mainly designed to test the properties of the metals, and therefore deal with the magnitudes of torque and twisting angle which are much larger than those expected for the piezoelectric actuators. Additionally, the commercial machines are very expensive, which does not justify their purchase and the following modification to meet the requirements of experiments with actuators. In the developed set-up (Fig. 2), the external torque was produced by applying a force to the lever using springs with different elastic constants.

4. Characteristics of prototype actuator

4.1. Proof of the concept of the torsional actuator

Fig. 3 summarizes the data which verify the concept of the proposed torsional actuator. In Fig. 3(a), the torsional angle measured at 10 Hz is plotted as a function of the amplitude of the ac driving voltage for two separate tube (open circles), and for the same tubes joint lengthwise (closed circles). For separate tubes, the actuation behavior is almost identical and angular displacement is doubled when the length of the actuator is increased by joining these two tubes. This behavior agrees with predictions of Eq. (1).

The further proof of the concept of the proposed torsional actuator is illustrated in Fig. 3(b). The plot compares the data for the piezoelectric coefficient d_{15} of

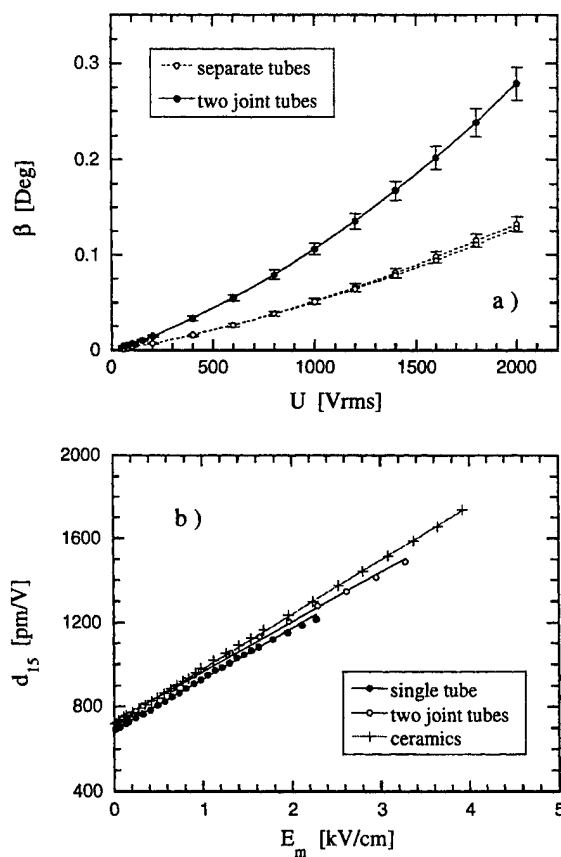


Fig. 3. (a) Angular displacement of torsional actuator as a function of the ac driving voltage for two separate tubes and two tubes joint as one assembly. (b) Piezoelectric shear coefficient d_{15} as a function of the amplitude of the ac driving field, E_m . Circles correspond to the data calculated from the torsional angle of the actuator, consisting of a single tube (closed circles) and two joint tubes (open circles), using Eq. (1). Plus signs show the data measured directly from the cubic ceramic sample of the same composition, PZT-5A. Symbols show the experimental data and the lines correspond to the fit of the data to the linear function, Eq. (7). In (a) and (b), the frequency of the ac voltage is 10 Hz.

PZT-5A ceramics derived from the experimentally measured data for $\beta(E_m)$ of a single tube (closed circles) and two tubes joint lengthwise (open circles) using Eq. (1), where the amplitude E_m of the driving field was substituted for E , with d_{15} values measured directly from the cubic ceramic samples of the same composition, PZT-5A ("EDO", USA). As one can see, the values of the d_{15} derived from the actuators are nearly the same as those measured on the cubic sample. The small, less than 5%, difference could be attributed to the difference in the aging states of ceramics in segments and cubic samples. To summarize, the results presented in Fig. 3(a) and (b) prove the concept of the proposed torsional actuator, Eq. (1), that is, to use the shear piezoelectric effect, d_{15} , and the geometrical amplification, L/R_{out} , to generate a large angular displacement, β .

4.2. Evaluation of torsional angle and torque output

The results reported in Section 4.1 demonstrate that knowing the material properties, d_{15} , the magnitude of driving electric field, E , and the tube dimensions, L and R_{out} , the torsional angle produced by the actuator (Fig. 1(b)) can be calculated using Eq. (1).

In order to evaluate the torque output, T_{dev} , developed by the actuator, we studied the effect of the torque load on static response of the prototypes. In these experiments, a static torque, T , was first applied to the actuator, thus, producing its initial twisting, β_0 . Afterwards, a dc field was turned on, with the polarity to induce a twisting of the actuator in the direction opposite to β_0 . In Fig. 4, the torsional angle β measured on the two joint tubes is plotted as a function of the driving field at different torque loads. The blocking torque of the actuator can be evaluated from the intersection of the curve $\beta(E)$ measured at a fixed torque load, with the dashed line corresponding to $\beta = 0$. The zero torsional angle means that at that value of the electric driving field the absolute value of the torque, T_{dev} , developed by the actuator is equal to the external

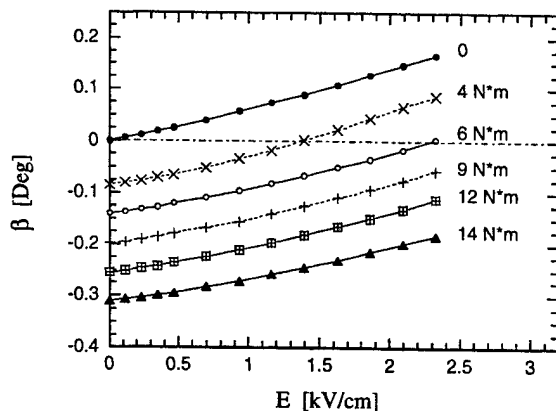


Fig. 4. Torsional angle of the two-tube actuator is plotted as a function of applied dc field at different external static torque.

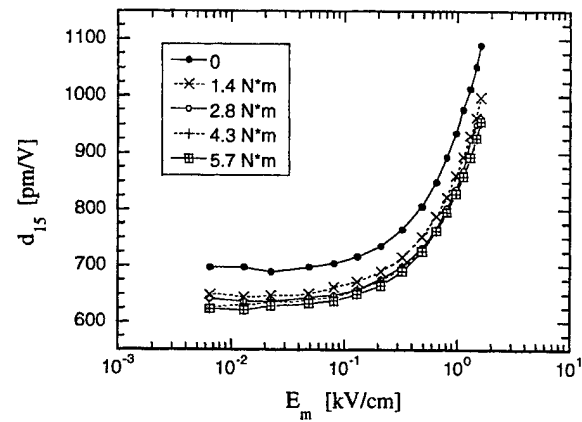


Fig. 5. The effect of the static torque on the dynamic response of the torsional actuator. The values of the piezoelectric coefficient d_{15} calculated from the data on the torsional angle are plotted as a function of the amplitude of the ac driving field. The frequency of the field is 10 Hz. The values of applied torque are given in the legend.

static torque, T . For example, at $E = 2.5$ kV/cm, the torque output is approximately equal to $T_{dev} \approx 6$ N m, as can be concluded from the curve measured under external torque of 6 N m, Fig. 4.

4.3. Effect of the torque load on actuator performance

The effect of the torque load on the static response of the prototype actuator is illustrated in Fig. 4 for the two-tube assembly. This data clearly demonstrates that the torque load almost does not change the response of the actuator to the dc field, because the initial twisting, β_0 , can be completely nullified by the appropriate choice of the magnitude of the electric field, and because the slope of $\beta(E)$ curve, which according to Eq. (1) gives the shear piezoelectric coefficient, $d_{15}(E)$, does not show marked change with increasing T (cf. Fig. 4). Similar result was obtained for the single tube actuator.

In the experiment of investigating the effect of external torque on the dynamic response of the prototype actuator, an ac driving field of 10 Hz was applied to the actuator and the torsional angle was measured as a function of the ac field amplitude and the torque load. Fig. 5 shows the plot of the ac field dependence of piezoelectric coefficient d_{15} derived from the data on $\beta(E_m)$ using Eq. (1). Similar to the static response, the external torque does not affect significantly the actuator response to the ac field. Application of the torque results only in a small, less than 10%, change in d_{15} from its value measured under load-free condition, $T = 0$ N m. With the further increase in T , the d_{15} remains nearly constant (Fig. 5).

4.4. Frequency dependence of torsional angle

The frequency dependence of the torsional angle was measured within the frequency range 3–600 Hz under a

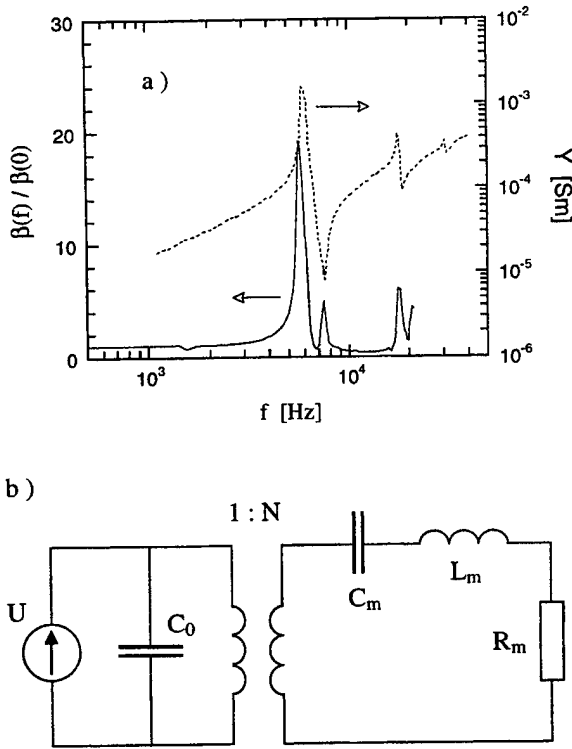


Fig. 6. (a) Frequency dependence of the torsional angle normalized over its static value (solid line) and of the electrical admittance of the torsional actuator (dashed line). (b) Equivalent circuit corresponding to the torsional actuator around its resonance frequency, $f_r = 6$ kHz.

relatively large electric fields, $E_m \approx 2$ kV/cm. Only a minor decrease in β , equal to 3% per decade, with increasing frequency was observed.

For small electric fields, $E_m = 50$ V/cm, the frequency dependence of β was measured over a broad frequency range from 100 Hz to 20 kHz. In Fig. 6(a), the solid line shows the frequency dependence of the ratio $\beta(f)/\beta(0)$, where $\beta(0)$ corresponds to the low-frequency value of the torsional angle, given by Eq. (1). A series of the peaks are seen in this curve. A comparison of $\beta(f)$ with the frequency dependence of the electrical admittance of the actuator (dashed line in Fig. 6(a)) shows that the peaks occur at resonance and antiresonance frequencies of the tube, which correspond to the maximum and minimum admittance, respectively.

In order to understand the origin of these peaks, we performed a theoretical analysis of the acoustic modes propagating in the tube. The analysis showed that the resonance peaks are related with the shear mode propagating along the axis z of the tube, i.e., along its length. When the bottom, $z = 0$, of the tube is mechanically clamped, and the top, $z = L$, is free, the angular displacement at the top of the tube can be written as:

$$\beta = d_{15} E \frac{L}{R_{out}} \frac{\tan \alpha L}{\alpha L}, \quad (3)$$

and the electrical admittance of the actuator is given by:

$$Y = j2\pi f C_0^T \left(1 - k_{15}^2 + k_{15}^2 \frac{\tan \alpha L}{\alpha L} \right), \quad (4)$$

where $\alpha = 2\pi f \sqrt{\rho s_{44}}$ (ρ is the density of PZT), k_{15} is shear electromechanical coupling coefficient, and C_0^T is the electrical capacitance of the tube in stress-free condition. The resonances occur when $\alpha L = n\pi/2$ (n is the odd value), which gives the resonance frequency equal to: $f_r = n/4L \sqrt{\rho s_{44}}$. Using Eq. (4), around the first resonance frequency f_r with $n = 1$, we can substitute the tube with the equivalent circuit which is shown in Fig. 6(b). In this circuit, $C_0 = C_0^T(1 - k_{15}^2)$, $N = d_{15}(R_{out} - R_{in})/s_{44}$, $C_m = 8Ls_{44}/\pi^3(R_{out}^2 - R_{in}^2)$, $L_m = 1/(2\pi f_r)^2 C_m$, and we took into account mechanical losses in the actuator by introducing $R_m^{-1} = 2\pi f C_m Q_m$, where Q_m is the mechanical quality factor. Using the equivalent circuit, one can show that at resonance frequency, f_r , the time dependence of the torsional angle is given by:

$$\beta = \frac{8Q_m}{\pi^2} \frac{d_{15} E_m L}{R_{out}} \sin(2\pi f_r t - 90^\circ), \quad (5)$$

when the electric driving field changes with time as: $E(t) = E_m \sin(2\pi f_r t)$. Eq. (5) shows that at resonance there is a phase shift of -90° between the torsional angle and the driving field, and that the amplitude of the torsional angle should be amplified by the factor of $8Q_m/\pi^2$ compared to the low-frequency value given by Eq. (1).

Inspection of the experimental data showed that the model can fit the data nicely. Using actuator dimensions and material datasheet from "EDO", the resonance frequencies corresponding to $n = 1, 3, 5$ were estimated as: 6.2, 18.6, and 31 kHz, respectively, and were in a good agreement with the positions of the maxima in electrical admittance in Fig. 6(a). Also, from the peak in $\beta(f)/\beta(0)$ corresponding to the first resonance in Fig. 6(a), the mechanical quality factor of the actuator can be determined as $Q_m = 22$. This value closely compares with that determined from the half-width of the electrical conductance of the tube, which gave $Q_m \approx 20$. Finally, in direct measurements of the torsional angle, at resonance, $f_r = 6$ kHz, we observed the phase shift between $\beta(t)$ and driving field $E(t)$ very close to -90° . All these data indicate that the torsional actuator performed well also in resonance conditions.

The additional angular amplification of the torsional angle by a factor of $8Q_m/\pi^2$ at resonance frequency is very important for possible application of the torsional actuator in the piezoelectric motors, where the actuators usually operate in a resonance mode. To make the stator of the motor, the tube shown in Fig. 1(b) may be combined with another piezoelectric actuator generating longitudinal displacement. The combination of torsional and longitudinal displacements will produce an elliptical motion of the contact surface between the stator and rotor, which may be necessary to spin the rotor [14].

4.5. Reliability test of prototype actuator

At present, most commercially available solid state actuators are fabricated of the ferroelectric ceramics PZT. A common feature of ferroelectric materials is a fatigue, or a degradation of their properties caused by cycling them with the electrical field of large magnitude. In addition, in the tubular assembly of the actuator (Fig. 1(b)), there is also a possibility of the fatigue caused by bonding layer between segments. Therefore, the reliability test of the actuator should include the study of time variation of actuator performance related with its fatigue under required operation conditions.

In present work, the actuator was driven by an ac field of amplitude $E_m = 1.5$ kV/cm and frequency 20 Hz. The change in the torsional angle with time was monitored using a MTI-2000 fonic sensor and lock-in amplifier. Fig. 7 shows β as a function of the number of the fatigue cycles, N . As one can see, the torsional angle remains nearly constant with N up to $3 \cdot 10^6$ cycles (which corresponds to 2 days of continuous operation). This result indicates that there is no degradation of torsional actuator caused by large ac driving field.

The absence of the fatigue shown in Fig. 7 agrees with the results of other studies of the fatigue in ferroelectric ceramics. For example, it was shown [15] that the fatigue in PZT ceramics was observed only when the amplitude of the ac driving field exceeded the coercive field, and, thus, caused the switching of the spontaneous polarization. The fatigue occurred already after 10^4 cycles. At the same time, when the driving field was smaller than the coercive field (even being very close to it), no fatigue was observed, up to 10^6 cycles [15]. Based on this result, one should not expect electrical fatigue in the case of the torsional actuator studied in this work. This is because in this actuator one uses the shear piezoelectric effect, where the electric field is applied in the direction perpendicular to the spontaneous polarization, and drives the material with

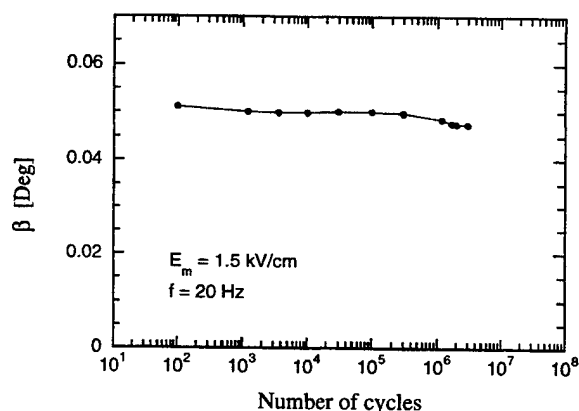


Fig. 7. Torsional angle is plotted as a function of the number of fatigue cycles.

field lower than the coercive field, in order not to switch the polarization in the direction along the field.

For torsional actuators studied in this work, the experiments were limited to the use of the driving field of $E_m = 2\text{--}3$ kV/cm. This limit was mostly determined by the desire to avoid a possible damage to the actuator due to the electrical short circuit related with the discharge over the surface of the segments, which was observed above approximately 3–3.5 kV/cm. If special precautions, related with an electrical insulation of the contacts are made, the electric driving field can be significantly higher. Special test was performed on a cubic sample of PZT-5A immersed into silicone oil, where electric field was applied in the direction perpendicular to the spontaneous polarization, and the shear strain, $S_5(E)$, was measured using MTI-2000 fonic sensor. With electric fields as high as $E_m = 9$ kV/cm, no evidence for the polarization switching into direction along the electric field was observed: the field dependence of induced strain, $S_5(E)$, had a cigar-like shape and remained fully reversible upon increase and decrease of the field amplitude, E_m . If the polarization switching occurred, the strain would change from shear to longitudinal one and its field dependence would have a shape of the “butterfly loop”, which characterizes the strain related with the polarization reversal in ferroelectric materials [16].

Another reliability test included the measurements of the mechanical strength of the torsional actuator. The results of this study will be published separately. Here, we mention only that the mechanical fracture strength of the actuator was determined by the mechanical strength of PZT ceramics, and not by the joints between ceramic segments. This conclusion was suggested by the inspection of the fragments of the broken prototype actuator, and was supported by the fact that the fracture shear stress of the tube, $\sigma_{fr} = 13$ MPa, almost coincided with that of PZT ceramics of the same composition, $\sigma_{fr} \approx 14$ MPa, which was measured for the cubic ceramic sample [17].

5. Tailoring of the characteristics of the torsional actuator for different applications

The specific values of torsional angle and torque output can be different for each particular application. Using the results obtained in this work, we can evaluate the proposed torsional actuator to its application in helicopter rotor blades in TEF, where the actuation should reduce the vibration and improve the lifting power [6–8]. The eight seat commercial helicopter [12] requires the following values: $\beta = \pm 4^\circ$ and $T_{dev} = 5 \pm 3$ N m. The prototype torsional actuators made of PZT-5A ceramics has $d_{15} = 1800$ pm/V at $E = 4$ kV/cm (Fig. 3(b)), which yields the angular displacement $\beta = \pm 0.4^\circ$ (for $L/R_{out} = 10$), and the torque output $T_{dev} = 40$ N m. Even though the angular displacement is smaller than the required values, it can be

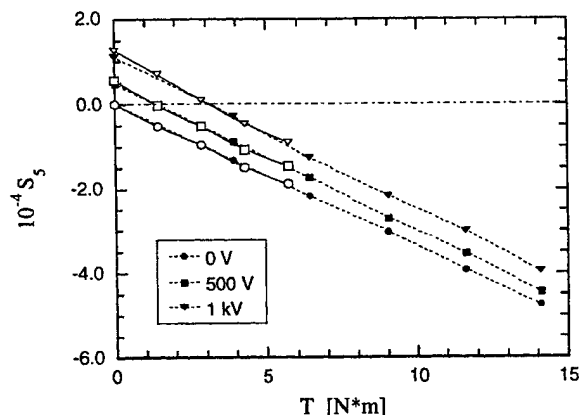


Fig. 8. Shear strain calculated from the experimentally measured values of the torsional angle is plotted as a function of the external static torque at different values of the dc driving voltage. Closed symbols correspond to the actuator consisting of two joint tubes and open circles show the data for the single tube.

increased by using an additional amplification mechanisms. Possible solutions include either hinges (in this case, some excess torque output can be traded off, since T_{dev} is much larger than the value required for TEF application) or an accumulation of displacement over many periods of the ac driving voltage. The latter approach is employed in linear “inchworm” actuators or ultrasonic motors. Based on tubular actuator described in this work, a torsional “inchworm” motor was developed. As will be shown in a separate publication [18], the motor produces a smooth stepwise motion within 360° interval with a precise control over angular positioning. These features make the motor useful for various applications, not only the active control of TEF.

Each particular application will set the requirements not only for the absolute values of the torsional angle and/or torque developed, but also will limit the actuator dimensions. Based on the result of this study, we can suggest the following ways to improve the characteristics of the proposed torsional actuator. The increase in the magnitude of induced shear strain, $S_s = d_{15}E$, will result in the increase of both β and T_{dev} , as predicted by Eqs. (1) and (2). This implies the use of larger values of driving electric field and the development the new piezoelectric materials with higher values of shear piezoelectric coefficient, d_{15} (see Section 6). From the engineering point of view, the increase in the torque output of the actuator, Eq. (2), can be achieved by using the tube with a larger outer radius, R_{out} (which gives an increase proportional to R_{out}^3), and with a smaller ratio R_{in}/R_{out} .

At this point, we would like to stress one important advantage of the present tubular design of the torsional actuator. As predicted by Eq. (1), the tube with a larger length L will produce larger torsional angle, whereas the torque output will remain the same, Eq. (2). We can prove this statement using the experimental results for the single tube and for the two tubes joint lengthwise. Fig. 3(a)

already showed that the joining two identical tubes doubles the torsional angle. To demonstrate that the torque output remains the same, for the same tubes we compare the data for the torsional angle, β , measured as a function of static torque load, T , at different magnitudes of the dc driving voltage. Using Eq. (1), we calculate the shear strain as: $S_s = \beta R_{out}/L$, and plot the data for $S_s(T)$ in Fig. 8. As one can see, for the same value of the driving field, the data for single tube and two joint tubes agree well. Since according to Eq. (2), the shear strain produces the torque T_{dev} , this result indicates that for tubular actuator, the torque output is independent of the length of the tube.

The last feature represents an important advantage of the present design of torsional actuator over another design based on piezoelectric bimorphs where the displacement of the tip of the bimorph due to its bending under the driving electric field is converted into the torsional motion using the system of levers [6]. In the bimorph system, the produced torsional angle depends upon the displacement of the tip of the bimorph, η . Since η changes with the length, L_b , of the bimorph, as [19] $\eta \propto L_b^2$, the longer the bimorph, the larger should be the torsional angle β . However, the increase in L_b will result simultaneously in the decrease of the force, F , developed by the bimorph, since the force is inversely proportional to the length of the bimorph: [19] $F \propto L_b^{-1}$. In contrast, the tubular actuator (Fig. 1(b)) is free of this drawback, because, as we showed before, its torque output is independent of the length, L , of the tube. Therefore, by increasing L , one can achieve larger torsional angle, Eq. (1): $\beta \propto L/R_{out}$, without drop in the produced torque.

Finally, we suggest that instead of increasing the length of the tube, larger values of the torsional angle can be achieved by a slight modification of the actuator geometry. One alternative to the tubular assembly (Fig. 1(b)) is a conical actuator which is schematically drawn in Fig. 9. The advantage of this configuration is that the radius of the end 1 can be made much larger than that of the end 2. If end 1 is fixed at a support and end 2 generates the twisting, this design is quite desirable. For conical geometry, the length, L , of the ceramic segments becomes longer

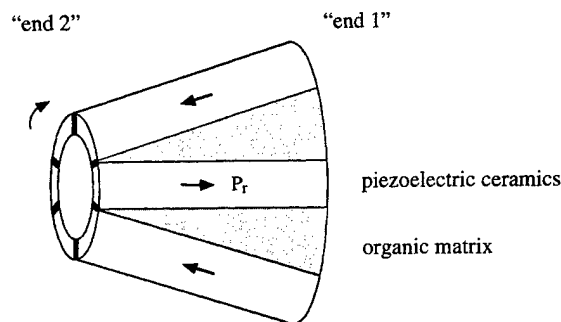


Fig. 9. Schematic drawing of the torsional actuator fabricated in the form of the cone. It is expected, that in the real application, the end 1 is fixed at a support, while the torsional displacement is produced at the end 2.

than that in the tubular structure (Fig. 1(b)), and the effective outer radius of the actuator, R_{out} , becomes smaller, since now it is the radius of the actuator at the end 2. The combined effect will be the increase in the amplification factor, L/R_{out} , in Eq. (1) and, therefore, in the produced torsional angle.

6. Nonlinear piezoelectric effect

In actuator and transducer applications, the piezoelectric ceramics is often subjected to high electric fields where the electric field dependence of induced strain is strongly nonlinear [2]. It is believed that the nonlinearity of the piezoelectric response of PZT ceramics is controlled by the irreversible displacement of domain walls [20–22] which separate regions of the material with different orientation of spontaneous polarization. The domain wall motion may be affected by many factors, including the crystal structure and microstructure of ceramics, the presence of impurities, dopants, defects, and a local variation in the composition of ceramics [2,21]. Possible mechanisms of domain wall motions have recently been discussed in detail in Refs. [21,22].

Shear piezoelectric response of PZT-5A strongly depends upon the magnitude of the driving electric field. This is evident from Fig. 3(b), where one can see that at $E = 3 \text{ kV/cm}$, the magnitude of piezoelectric shear coefficient, d_{15} , of PZT-5A is doubled compared to the low field value, which is usually reported in manufacturer datasheets. Also, one can see that within the studied range of the ac field amplitude, the data corresponding to both ceramic sample and tubular actuators can be fit to the linear function:

$$d_{15} = d_{15}(0) + aE_m, \quad (6)$$

where $d_{15}(0)$ is the low-field limit of piezoelectric shear coefficient and a is the parameter. The fit of the data to Eq. (6) is shown in Fig. 3(b) with the lines.

This result suggests two conclusions which are important for practical application of PZT. First, the knowledge of how the material response changes with the amplitude of the driving field and its proper mathematical description are important for the modeling of the device performance. The data shown in Fig. 3(b) contradicts to a conventional description of strain response of ferroelectrics, where the field induced strain is expressed in terms of the Taylor series expansion in terms of electric field. Using symmetry arguments, one would expect to have the following expression for $d_{15}(E)$ [22]:

$$d_{15} = d_{15}(0) + b_1 E_m^2 + b_2 E_m^4 + \dots \quad (7)$$

Thus, for the device modeling, Eqs. (1) and (2), one should use the experimentally derived linear dependence of $d_{15}(E)$, Eq. (6), rather than the polynomial expansion, Eq. (7). The second conclusion is important for the materials

development for their application in torsional actuator. The strong change in the piezoelectric shear coefficient with electric driving field indicates that one should optimize the entire characteristic $d_{15}(E)$ in order to achieve the highest value of the piezoelectric coefficient, $d_{15}(E)$, as a function of the driving field. The higher the d_{15} , the larger will be the values of the torsional angle and the torque output, according to Eqs. (1) and (2).

7. Summary

In this work, we performed a detailed experimental study of a novel type of the piezoelectric torsional actuator. The data obtained prove the proposed concept of the torsional actuator, show that the actuator functions well both without load and under the torque load, and demonstrate that the actuator can operate continuously for a long period of time without drop in its performance. Comparison of the experimental data obtained on the tube and ceramic samples, such as piezoelectric shear coefficient, d_{15} , and mechanical fracture stress, σ_{fr} , indicates that the material properties determine the performance of the torsional actuator. Also, the experimental results demonstrated that the proposed torsional actuator is capable of producing both large torque and large angular displacement in a compact package, sufficient to meet many smart structures requirements, and can be tailored for a variety of application requirements. Finally, one of the obvious advantages of the present design of the actuator is its simplicity: the piezoelectric shear strain is transformed directly into the angular displacement.

Acknowledgements

The authors wish to thank Dr. W. Chen (PSU) for his help in designing the torque load set-up, and DARPA for the financial support of this work.

References

- [1] K. Uchino, Electrostrictive actuators: materials and application, Bull. Am. Ceram. Soc. 65 (1986) 647.
- [2] L.E. Cross, Ferroelectric ceramics: materials and application issues, Ceram. Trans. 68 (1996) 15.
- [3] Y. Fuda, T. Yoshida, Piezoelectric torsional actuator, Ferroelectrics 160 (1994) 323.
- [4] J. Satonobu, N. Torii, K. Nakamura, S. Ueha, Construction of megatorque hybrid transducer type ultrasonic motor, Jpn. J. Appl. Phys. 35 (1996) 5038.
- [5] A. Yabuki, M. Aoyagi, Y. Tomikawa, T. Takano, Piezoelectric linear motors for driving head element of CD-ROM, Jpn. J. Appl. Phys. 33 (1994) 5365.
- [6] D.K. Samak, I. Chopra, A feasibility to build a smart rotor: trailing edge flap actuation, Proc. of the 1993 SPIE's North American Symposium on Smart Structures and Materials, Albuquerque, NM, 1993.

- [7] I. Chopra, Status of application of smart structures technology to rotocraft systems, Presented at the Innovation in rotocraft technology, Royal Aeronautical Society, London, June 1997.
- [8] E.F. Prechtel, S.R. Hall, Design of a high efficiency discrete servo-flap actuator for helicopter rotor control, SPIE Conference on Smart Structures and Materials, SPIE 3041 (1997) 158.
- [9] M. Aoyagi, S. Tsuchiya, Y. Tomikawa, Trial production of an ultrasonic motor using longitudinal and torsional vibrations of a rod vibrator driven by piezoceramic plates inserted in its axial direction, *Jpn. J. Appl. Phys.* 36 (1997) 6106.
- [10] A.E. Glazounov, Q.M. Zhang, C. Kim, Piezoelectric actuator generating torsional displacement from piezoelectric d_{15} shear response, *Appl. Phys. Lett.* 72 (1998) 2526.
- [11] P.Ch. Chou, N.J. Pagano, *Elasticity: tensor, dyadic, and engineering approaches*, Dover Publications, New York, 1992, pp. 115–144.
- [12] C. Kim, D. Lewis III, C.Cm. Wu, A.E. Glazounov, Q.M. Zhang, High authority piezoelectric torsional actuators, Presented at ISAF-98, Montreux, Switzerland, August 1998.
- [13] A.E. Glazounov, Q.M. Zhang, C. Kim, A new torsional actuator based on shear piezoelectric response, SPIE Conference on Smart Structures and Materials, SPIE 3324 (1998) 82.
- [14] S. Ueha, Y. Tomikawa, *Ultrasonic Motors*, Clarendon Press, Oxford, 1993.
- [15] D. Wang, E. Fotinich, G. Carman, Influence of temperature on the electromechanical and fatigue behavior of piezoelectric ceramics, *J. Appl. Phys.* 83 (1998) 5342.
- [16] B. Jaffe, W. Cook, H. Jaffe, *Piezoelectric Ceramics*, Academic Press, London, 1971.
- [17] A.E. Glazounov, Q.M. Zhang, C.Cm. Wu, C. Kim, to be published.
- [18] A.E. Glazounov, S. Wang, Q.M. Zhang, C. Kim, High efficiency piezoelectric motor combining continuous rotation with precise control over angular positioning, submitted to *Appl. Phys. Lett.*
- [19] V.D. Kugel, S. Chadran, L.E. Cross, Caterpillar-type piezoelectric d_{33} bimorph transducer, *Appl. Phys. Lett.* 69 (1996) 2021.
- [20] Q.M. Zhang, W.Y. Pan, S.J. Jang, L.E. Cross, Domain wall excitations and their contributions to the weak-signal response of doped lead zirconate titanate ceramics, *J. Appl. Phys.* 64 (1988) 6445.
- [21] D. Damjanovic, Stress and frequency dependence of the direct piezoelectric effect in ferroelectric ceramics, *J. Appl. Phys.* 82 (1997) 1788.
- [22] V. Mueller, Q.M. Zhang, Shear response of lead zirconate titanate piezoceramics, *J. Appl. Phys.* 83 (1998) 3754.

APPENDIX 59

6.35

Ceramic Actuators

KENJI UCHINO

Pennsylvania State University, University Park, PA, USA

6.35.1 INTRODUCTION	663
6.35.2 TRENDS IN CERAMIC ACTUATORS	663
6.35.3 COMPOSITE STRUCTURES	664
6.35.4 ACTUATOR MATERIALS	665
6.35.5 RELIABILITY OF MULTILAYER ACTUATORS	666
6.35.6 APPLICATIONS OF MULTILAYER ACTUATORS	667
6.35.6.1 USA	668
6.35.6.2 Japan	668
6.35.6.3 Europe	669
6.35.7 CONCLUSIONS	669
6.35.8 REFERENCES	670

6.35.1 INTRODUCTION

Piezoelectric and electrostrictive ceramic materials have become key components in smart actuator/sensor systems for use as precision positioners, miniature ultrasonic motors, and adaptive mechanical dampers. In particular, composite structures such as multilayers, multimorphs, and moonies/cymbals have been intensively investigated in order to improve their reliability and to expand their applications. Recent developments in USA, Japan, and Europe will be compared.

6.35.2 TRENDS IN CERAMIC ACTUATORS

Piezoelectric actuators are forming a new field midway between electronic and structural ceramics (Uchino, 1993, 1994, 1995c, 1996). Application fields are classified into three categories: positioners, motors, and vibration suppressors. The manufacturing precision of

optical instruments such as lasers and cameras, and the positioning accuracy for fabricating semiconductor chips, which are adjusted using solid-state actuators, is of the order of 0.1 μm . Regarding conventional electromagnetic motors, tiny motors smaller than 1 cm are often required in office or factory automation equipment, and are rather difficult to produce with sufficient energy efficiency. Ultrasonic motors whose efficiency is insensitive to size are superior in the minimotor area. Vibration suppression in space structures and military vehicles using piezoelectric actuators is also a promising technology.

Composite structures, in particular, multilayer structures (2-2 composites, in which each phase connects two-dimensionally), are mainly used for practical applications because of their low drive voltage, high energy density, quick response, and long lifetime (Yoshikawa and Shrout, 1993; Uchino, 1995b). Figure 1 illustrates multilayer, multimorph, and multilayer-moonie structures, which will be covered

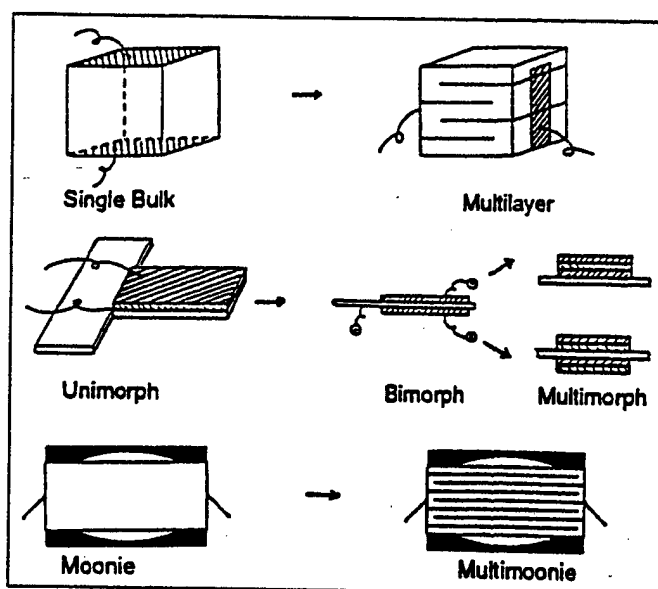


Figure 1 Examples of multilayer, multimorph, and multilayer-moonie structures.

in this chapter. Recent investigations have focused on the improvement of reliability and durability in multilayer actuators.

This chapter reviews the investigations of device structures, reliability issues, and recent applications of composite actuators, comparing the developments in USA, Japan, and Europe.

6.35.3 COMPOSITE STRUCTURES

Two preparation processes are possible for multilayer ceramic devices: one is a cut-and-bond method and the other is a tape-casting method. The tape-casting method requires expensive fabrication facilities and sophisticated techniques, but is suitable for the mass-production of thousands of pieces per day. Tape-casting also provides thin dielectric layers, leading to low drive voltages of 40–100 V (Dibbern, 1995; Takada *et al.*, 1994).

A multilayer actuator with interdigital internal electrodes has been developed by Tokin (Ohashi *et al.*, 1993a, 1993b). In contrast to the conventional electrode configuration in Figure 1, line electrodes are printed on piezoelectric ceramic green sheets, and are stacked in such a way that alternating electrode lines are displaced by one-half pitch (see Figure 2). This actuator generates motions at right angles to the stacking direction using the longitudinal piezoelectric effect. Long ceramic actuators up to 74 mm in length are manufactured.

A three-dimensional positioning actuator with a stacked structure has been proposed by PI Ceramic (Figure 3), in which shear strain is utilized to generate x and y displacements (Bauer and Moller, 1995). Notice that by adding another parameter, that is, the polarization

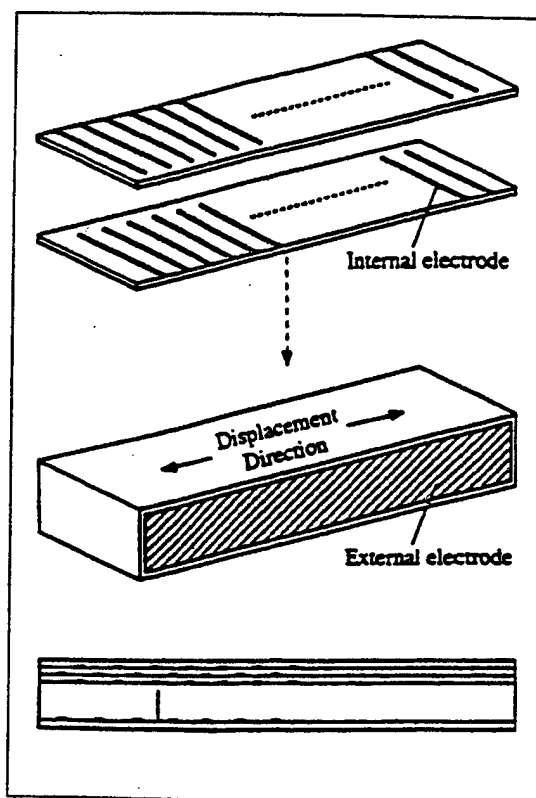


Figure 2 Structure of an internal interdigital electrode actuator.

direction to a 2–2 composite configuration, a new function such as the displacement to a different direction can be supplemented.

Composite actuator structures called “moonies” and “cymbals” have been developed at Pennsylvania State University to provide characteristics intermediate between the multilayer and bimorph actuators. These transducers

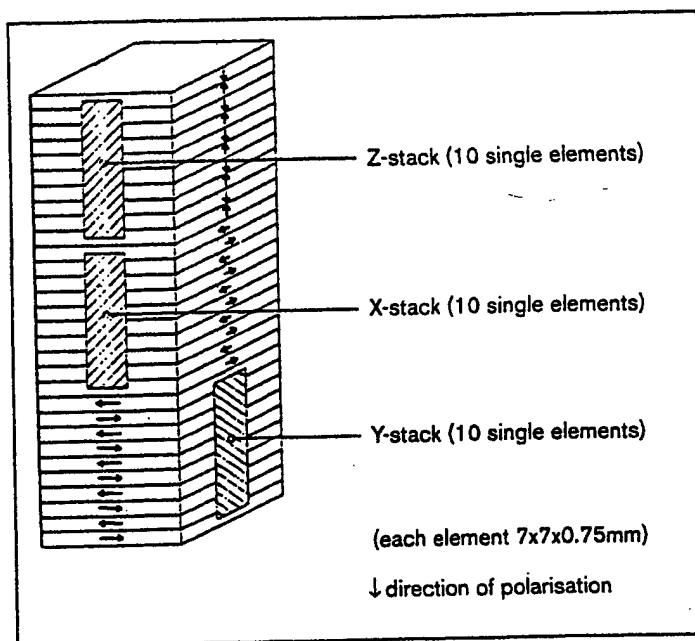


Figure 3 3-D controllable multilayer piezoelectric actuator.

exhibit an order of magnitude larger displacement than the multilayer, and much larger generative force with quicker response than the bimorph (Sugawara *et al.*, 1992; Onitsuka *et al.*, 1995). The device consists of a thin multilayer piezoelectric element and two metal plates with narrow moon-shaped cavities bonded together as shown in Figure 1. A moonie $5 \times 5 \times 2.5 \text{ mm}^3$ in size can generate a $20 \mu\text{m}$ displacement under 60 V, eight times as large as the displacement of a multilayer of the same size (Goto *et al.*, 1992). This new compact actuator has been used to make a miniaturized laser beam scanner (Goto *et al.*, 1992). Moonie/cymbal characteristics have been investigated for various constituent materials and sizes (Tressler *et al.*, 1994; Dogan *et al.*, 1994).

6.35.4 ACTUATOR MATERIALS

Actuator materials are classified into three categories: piezoelectric, electrostrictive, and phase-change materials. Modified lead zirconate titanate [PZT, $\text{Pb}(\text{Zr,Ti})\text{O}_3$] ceramics are currently the leading materials for piezoelectric applications. The PLZT [$(\text{Pb,Lu})(\text{Zr,Ti})\text{O}_3$] 7/62/38 (Lu, 7 at.%; Zr, 62 at.%; Ti, 38 at.%) compound is one such composition (Furuta and Uchino, 1986). The strain curve is shown Figure in 4(a), left. When the applied field is small, the induced strain x is nearly proportional to the field E ($x = dE$, where d is the piezoelectric constant). As the field becomes larger (i.e., greater than about 1 kV cm^{-1}), however, the strain curve deviates from this linear trend and significant hysteresis is exhib-

ited due to polarization reorientation. This sometimes limits the usage of such materials in actuator applications that require nonhysteretic response.

An interesting new family of actuators has been fabricated in Germany from a barium stannate titanate system $[\text{Ba}(\text{Sn,Ti})\text{O}_3]$ (Cieminski and Beige, 1991). The useful property of $\text{Ba}(\text{Sn}_{0.15}\text{Ti}_{0.85})\text{O}_3$ is its unusual strain curve, in which the domain reorientation occurs only at low fields, and there is then a long linear range at higher fields (Figure 4(a), right); i.e., the coercive field is unusually small. Moreover, this system is particularly intriguing since it contains no Pb ions, an essential feature as ecological concerns grow in the future.

The second category of actuators is based on electrostriction as in PMN [$\text{Pb}(\text{Mg}_{1/3}\text{Nb}_{2/3})\text{O}_3$] based ceramics, developed in the USA. Although a second-order phenomenon of electromechanical coupling ($x = ME^2$, where M is called the electrostrictive constant), it can be extraordinarily large (more than 0.1%) (Cross *et al.*, 1980). An attractive feature of these materials is the near absence of hysteresis (Figure 4(b)). The superiority of PMN to PZT was demonstrated in a scanning tunneling microscope (STM) (Uchino, 1988). The PMN actuator could provide extremely small distortion of the image even when the probe was scanned in the opposite direction.

The third category is based on phase-change-related strains, i.e., polarization-induced by switching from an antiferroelectric to a ferroelectric state, as systematically investigated by our group (Uchino and Nomura, 1983). Figure 4(c) shows the field-induced

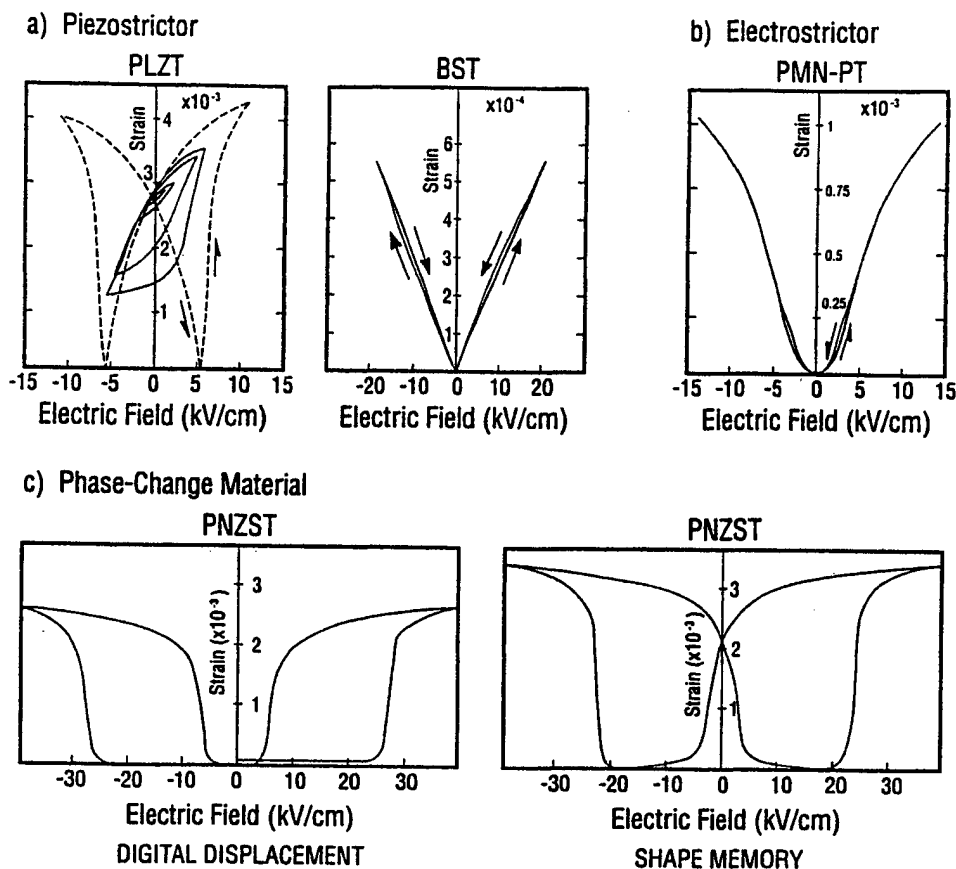


Figure 4 Electric field-induced strains in ceramics. (a) Piezoelectric $(\text{Pb},\text{La})(\text{Zr},\text{Ti})\text{O}_3$ and $\text{Ba}(\text{Sn},\text{Ti})\text{O}_3$. (b) Electrostrictive $\text{Pb}(\text{Mg}_{1/3}\text{Nb}_{2/3},\text{Ti})\text{O}_3$. (c) Phase-change material $\text{Pb}(\text{Zr},\text{Sn},\text{Ti})\text{O}_3$.

strain curves taken for the lead zirconate stannate based system $[\text{Pb}_{0.99}\text{Nb}_{0.02}(\text{Zr}_x\text{Sn}_{1-x})_{1-y}\text{Ti}_y]_{0.98}\text{O}_3$. The longitudinally induced strain reaches more than 0.3%, which is much larger than that expected in normal piezoelectric actuators or electrostrictors. A rectangular-shape hysteresis in Figure 4(c), left, referred to as a "digital displacement transducer" because of the two on/off strain states, is interesting. Moreover, this field-induced transition exhibits a shape memory effect in appropriate compositions (Figure 4(c), right). Once the ferroelectric phase has been induced, the material "memorizes" its ferroelectric state even under zero-field conditions, although it can be erased with the application of a small reverse bias field (Furuta *et al.*, 1992). This shape memory ceramic is used in energy saving actuators.

6.35.5 RELIABILITY OF MULTILAYER ACTUATORS

As the application fields expand, the reliability and durability issues of multilayer actuators become increasingly important. The reliability of ceramic actuators depends on a number of complex factors, which can be divided into three major categories: reliability of the ceramic

itself, reliability of the device design, and drive technique.

Compositional changes of actuator ceramics and the effect of doping are primary issues used in stabilizing the temperature and stress dependence of the induced strains. A multilayer piezoactuator for use at high temperatures (150°C) has been developed by Hitachi Metal, using Sb_2O_3 doped $(\text{Pb},\text{Sr})(\text{Zr},\text{Ti})\text{O}_3$ ceramics (Watanabe *et al.*, 1993). Systematic data on uniaxial stress dependence of piezoelectric characteristics have been collected on various Navy PZT materials (Zhang *et al.*, 1996). Grain size and porosity control of the ceramics are also important in controlling the reproducibility of actuators (Okada *et al.*, 1993). Aging phenomena, especially the degradation of strain response, are, in general, strongly dependent on the applied electric field as well as on temperature, humidity, and mechanical bias stress (Sakai *et al.*, 1992).

The device design strongly affects its durability and lifetime. Silver electrode metal tends to migrate into the piezoceramic under a high electric field in high humidity. Silver-palladium alloys suppress this behavior effectively. Resistive coatings of the device should also be taken into account (Takada, 1992). To overcome electrode delamination, improved adhesion can be

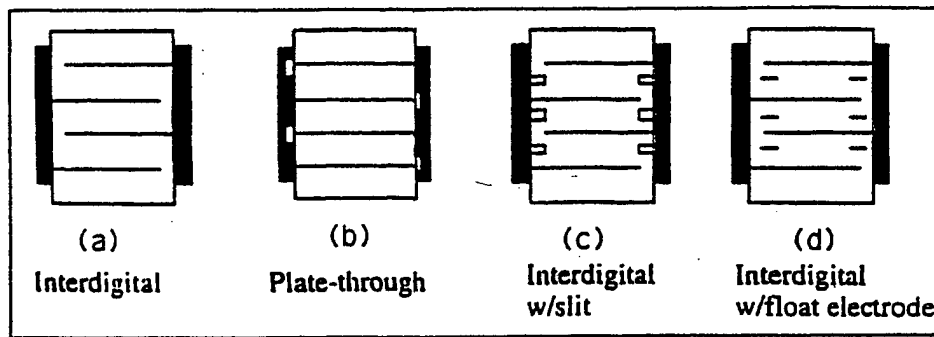


Figure 5 Various internal electrode configurations in multilayer actuators. (a) Interdigital, (b) plate-through, (c) slit-insert, and (d) float electrode.

realized by using a mesh-type electrode or an electrode material with mixed metal and ceramic powders. Pure ceramic electrode materials have also been developed using semiconductive perovskite oxides (barium titanate-based PTCR ceramics) (Abe *et al.*, 1986). The lifetime characteristics of a multilayer actuator with applied d.c. or unipolar a.c. voltage at various temperatures (Nagata and Kinoshita, 1994, 1995a) and at various humidities (Nagata and Kinoshita, 1995b) have been investigated. The relationship between the logarithm of the lifetime and the reciprocal of absolute temperature showed linear characteristics similar to Arrhenius type. Nevertheless, the degradation mechanism remains a critical problem.

In multilayer actuators, reduction of the tensile stress concentration around the internal electrode edge of the conventional interdigital configuration is the central problem. Regarding the destruction mechanism of multilayer ceramic actuators, systematic data collection and analysis have led to considerable progress (Furuta and Uchino, 1993, 1994; Aburatani *et al.*, 1994; Wang and Singh, 1995; Cao and Evans, 1994; Schneider *et al.*, 1994; Suo, 1993; Hao *et al.*, 1996). Two typical crack patterns are generated in a conventional interdigital multilayer device: one is a Y-shaped crack located on the edge of an internal electrode, and the other is a vertical crack located in a layer adjacent to the top or bottom inactive layer, connecting a pair of internal electrodes.

To overcome this crack problem, three electrode configurations have been proposed as illustrated in Figure 5: plate-through, interdigital and slit, and interdigital and float electrode types. The "float electrode" type is an especially promising design which can be fabricated using almost the same process as the conventional multilayer actuator, and lead to much longer lifetimes (Aburatani *et al.*, 1995). An empirical rule, "the thinner the layer, the tougher the device" (Aburatani *et al.*, 1994; Furuta and Uchino, 1994) is also very intriguing, and will

be more theoretically investigated in the near future.

Failure detection or lifetime prediction methods are expected to remarkably increase the reliability of multilayer actuators. Acoustic emission and surface potential monitoring are promising methods (Uchino and Aburatani, 1994). Penn State has developed a modified multilayer actuator containing a strain gauge as an internal electrode. This internal strain gauge electrode can detect the crack initiation sensitively and monitor the field-induced strain (Aburatani and Uchino, 1996).

Regarding drive techniques for ceramic actuators, pulse drive and a.c. drive require special attention; the vibration overshoot associated with a sharp-rise step/pulse voltage causes a large tensile force, leading to delamination of the multistacked structure, while long-term application of a.c. voltage generates considerable heat. A special pulse drive technique using a mechanical bias stress is required in the first case, and heat generation can be suppressed by changing the device design. An analytical approach to the heat generation mechanism in multilayer actuators has been reported, indicating the importance of larger surface area (Zheng *et al.*, 1996). Heat generation in piezoelectric ceramics is mainly attributed to the P - E hysteresis loss under large electric field drive (Hirose *et al.*, 1995b; Takahashi *et al.*, 1995). For ultrasonic motors, anti-resonance drive is preferable to resonance drive because of higher efficiency and lower heat generation for the same vibration level (Hirose *et al.*, 1995a).

6.35.6 APPLICATIONS OF MULTILAYER ACTUATORS

Table 1 compares a variety of ceramic actuator developments in the USA, Japan, and Europe. Additional details will be described in this section.

Table 1 Ceramic actuator developments in the USA, Japan, and Europe.

	USA	Japan	Europe
Target Category	Military-oriented products Vibration Suppressors	Mass-consumer products Positioner Minimotor	Laboratory equipment Minimotor Positioner Vibration suppressor
Application field	Space structures Military vehicles	Office equipment Cameras Precision machines Automobiles	Lab stage-steppers Airplanes Automobiles
Actuator size	Upsizing (30 cm)	Downsizing (1 cm)	Hydraulic systems Intermediate size (10 cm)
Major manufacturer	AVX/Kyocera Morgan Matroc Itek Opt. Systems Burleigh AlliedSignal	Tokin Corp. NEC Hitachi Metal Mitsui Chemical Canon Seiko Instruments	Philips Siemens Hoechst Ceram Tec. Ferroparm Physik Instrumente

6.35.6.1 USA

The principal target is military-oriented applications such as vibration suppression in space structures and military vehicles. Substantial upsizing of the actuators is required for these purposes.

A typical example is found in the aircraft wing proposed by NASA (Heeg, 1993). A piezoelectric actuator was installed near the support of the wing, allowing immediate suppression of unwanted mechanical vibrations. Several papers have reported on damper and noise cancellation applications (Mather and Tran, 1993; Agrawal and Bang, 1993).

Passive dampers constitute another important application of piezoelectrics, where mechanical noise vibration is radically suppressed by the converted electric energy dissipation through Joule heat when a suitable resistance, equal to an impedance of the piezoelectric element $1/\omega C$, is connected to the piezoelement (Uchino and Ishii, 1988). A widely publicized application took place with the image correction mechanism of the Hubble telescope launched by the Space Shuttle. Multilayer PMN electrostrictive actuators corrected the image by adjusting the phase of the incident light wave (Figure 6) (Wada, 1993). PMN electrostrictors provided superior adjustment of the telescope image because of negligible strain hysteresis.

6.35.6.2 Japan

Japanese industries seek to develop mass-consumer products, especially minimotors and micropositioners, aimed at applications such as office equipment and cameras/video cameras.

Tiny actuators smaller than 1 cm^3 are the main focus in these products.

A dot matrix printer was the first widely commercialized product using multilayer ceramic actuators (Yano *et al.*, 1984). Each character formed by such a printer was composed of a 24×24 dot matrix in which a printing ribbon was impacted by a multiwire array. The printing element was composed of a multilayer piezoelectric device with a sophisticated hinge lever magnification mechanism. The magnification by a factor of 30 resulted in an amplified displacement of 0.5 mm and an energy transfer efficiency greater than 50%. A modified impact printer head has been developed by Tokin, using new interdigital internal electrode type actuators, which have lowered production cost (Ono and Fuda, 1994). A color ink-jet printer has also been commercialized by Seiko Epson, using multilayer piezoactuators (Yonekubo, 1995). Automotive applications by Toyota Motor have been accelerated recently. Multilayer actuators have been introduced to an electronically controlled suspension (Fukami *et al.*, 1994) and a fuel injection system for diesel engines (Abe *et al.*, 1994).

Efforts have been made to develop high-power ultrasonic vibrators as replacements for conventional electromagnetic motors. The ultrasonic motor is characterized by "low speed and high torque," which is contrasted with the "high speed and low torque" of the electromagnetic motors. After invention of the π -shaped linear motors (Tohda *et al.*, 1989), various modifications have been reported (Funakubo *et al.*, 1995; Saigoh *et al.*, 1995). The Mitsui Petrochemical model is of particular interest because the motor body is composed of only one component prepared by a co-firing method as illustrated in Figure 7 (Saigoh *et al.*, 1995). A

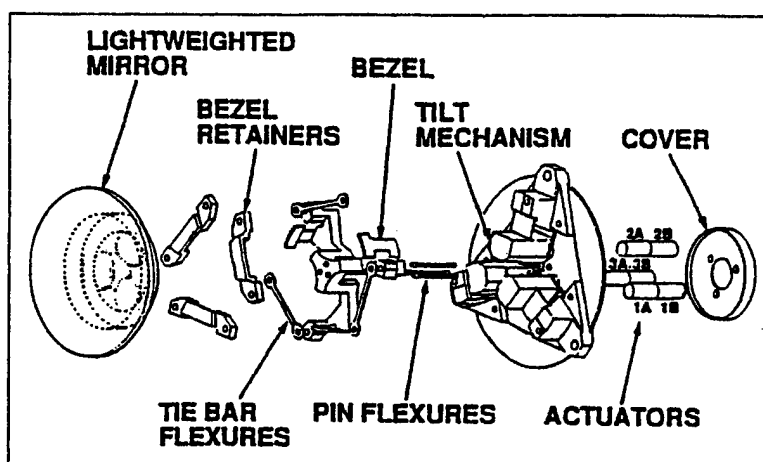


Figure 6 Articulating fold mirror using PMN multilayer actuators.

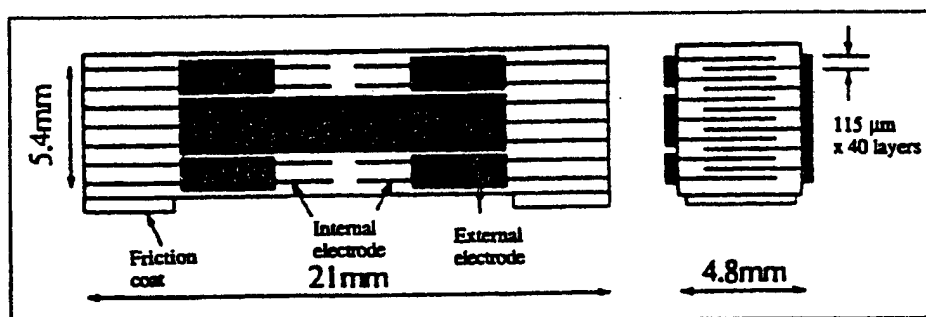


Figure 7 Monolithic multilayer piezoelectric linear motor.

maximum speed of 200 mm s^{-1} and a maximum thrust of 0.6 N were reported for this motor.

Camera motors utilize a traveling elastic wave induced by a thin piezoelectric ring. A ring-type slider in contact with the "rippled" surface of the elastic body bonded onto the piezoelectric can be driven in both directions by exchanging the sine and cosine voltage inputs. Another advantage is its thin design, making it suitable for installation in cameras as an automatic focusing device. Nearly 80% of the exchange lenses in Canon's "EOS" camera series have ultrasonic motor mechanisms installed (Uchino, 1995a).

Intriguing research programs are underway in Japan on the vibration damping of earthquakes using piezoelectric actuators (Shimoda *et al.*, 1992; Fujita, 1994). Active damping of a multilayer piezoactuator was tested using an actual size H-type steel girder, and was verified to be effective during earthquakes.

6.35.6.3 Europe

Ceramic actuator development has begun relatively recently in Europe with a wide range

of research topics (minimotors, positioners, and vibration suppressors). A current focus of several major manufacturers is on laboratory equipment products such as laboratory stages and steppers with rather sophisticated structures.

Figure 8 shows a walking piezomotor with four multilayer actuators by Philips (Koster, 1994). Two short actuators function as claspers while the two longer actuators provide a proceeding distance in an inchworm mechanism. Physik Instrumente has developed more complicated two-leg type walkers (Gross, 1994).

6.35.7 CONCLUSIONS

Twenty-five years have passed since the intensive development of piezoelectric actuators began in Japan, then spread worldwide. Presently, the focus has been shifted to practical device applications. This chapter has reviewed several reliability issues of composite ceramic actuators such as multilayers, bimorphs, and other new actuator structures, and compared the developments of recent applications among USA, Japan, and Europe.

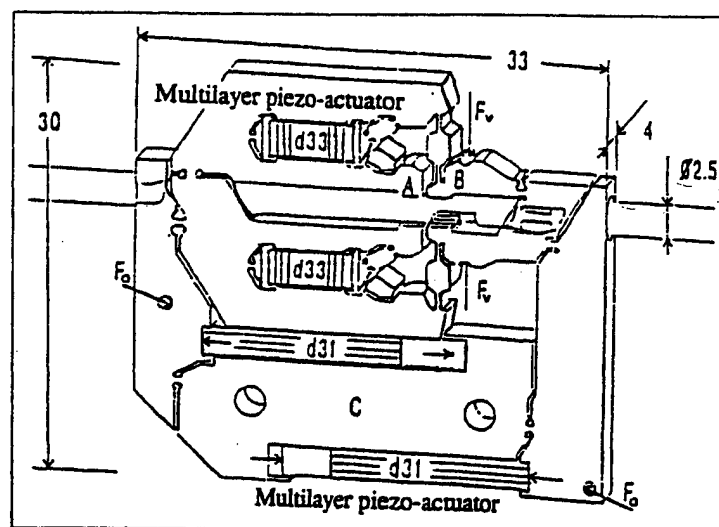


Figure 8 An inchworm using multilayer piezoelectric actuators.

The markets in USA are chiefly limited to military and defense applications, and it is difficult to estimate the amount of sales. The current Navy needs include smart submarine skins, hydrophone actuators, and prop noise cancellation. Smart aircraft skins are an Air Force objective, while Army requires helicopter rotor twisting, aeroservoelastic control, and cabin noise/seat vibration cancellation.

Meanwhile in Japan, piezoelectric shutters (Minolta Camera) and automatic focusing mechanisms in cameras (Canon), dot-matrix printers (NEC), and part-feeders (Sanki) are now commercialized and mass-produced by tens of thousands of pieces per month. During the commercialization, new composite designs which can amplify the displacement levels, and drive-control techniques with high efficiency using simple and cheap power supplies, have been mainly developed over the past few years. A number of patent disclosures have been generated by NEC, TOTO Corporation, Matsushita Electric, Brother Industry, Toyota Motors, Tokin, Hitachi Metal, and Toshiba.

If we estimate the annual sales in 2005 (expecting economical recovery in Japan), ceramic actuator units, camera-related devices, and ultrasonic motors are expected to reach \$500 million, \$300 million, and \$150 million, respectively. Regarding the final actuator-related products, \$10 billion is a realistic goal (Uchino, 1995a).

Future research trends can be divided in two ways: upsizing in space structures and downsizing in office equipment. Further downsizing will also be required in medical diagnostic applications such as blood test kits and surgical catheters.

Key words for the future of ceramic actuators are "miniaturization" and "hybridization."

Layers thinner than $10\text{ }\mu\text{m}$, corresponding to current multilayer capacitor technology, will also be introduced in actuator devices replacing the present $100\text{ }\mu\text{m}$ sheets. Piezoelectric thin films compatible with silicon technology are a focus in microelectromechanical systems. Ultrasonic rotary motors as small as 2 mm in diameter (Flynn *et al.*, 1992) and two-dimensional micro-optical scanners (Goto, 1994), both of which were fabricated on a silicon membrane, are good examples.

Nonuniform configurations or heterostructures of different materials, layer thickness, or electrode patterns will be adopted for practical devices. Functionally gradient piezoelectric actuators now being prototyped indicate a new trend (Kim *et al.*, 1992).

Developments of sophisticated composite actuator structures will be definitely required.

6.35.8 REFERENCES

- K. Abe, K. Uchino and S. Nomura, *Ferroelectrics*, 1986, 68, 215-223.
- S. Abe, T. Igashira, Y. Sakakibara and F. Kobayashi, *Soc. Automot. Eng. Jpn.*, 1994, 15, 201-208.
- H. Aburatani, S. Harada, K. Uchino, A. Furuta and Y. Fuda, *Jpn. J. Appl. Phys.*, 1994, 33, 3091-3094.
- H. Aburatani and K. Uchino, in 'Stress and Fatigue Estimation in Multilayer Ceramic Actuators Using an Internal Strain Gauge, Abstract Annual Meeting & Exposition of the American Ceramic Society International Symposium on Solid-State Sensors and Actuators 7-96', American Ceramic Society, OH, 1996, pp. 191.
- H. Aburatani, K. Uchino, A. Furuta and Y. Fuda, in 'Proc. 9th Int Symp. Appl. Ferroelectrics', 1995, pp. 750-752.
- B. N. Agrawal and H. Bang, *Am. Soc. Mech. Eng. Des. Eng. Div.*, 1993, 61, 169-179.
- A. Bauer and F. Moller, in 'Proc. 4th Intl. Conf. New Actuators (Actuator 94)', Germany, 1995, pp. 128-132.
- H. C. Cao and A. G. Evans, *J. Am. Ceram. Soc.*, 1994, 77, 1783-1786.

- J. von Cieminski and H. Beige, *J. Phys. D*, 1991, **24**, 1182-1186.
- L. E. Cross, S. J. Jang, R. E. Newnham, S. Nomura and K. Uchino, *Ferroelectrics*, 1980, **23**(3), 187.
- U. Dibbern, in 'Proc. 4th Int. Conf. New Actuators (Actuator '94)', AXON, Bremen, Germany, 1995, pp. 114-118.
- A. Dogan, J. F. Fernandez, K. Uchino and R. E. Newnham, in 'Proc. 4th Euro Ceramics', 1994, pp. 127-132.
- A. M. Flynn, L. S. Tavrow, S. F. Bart, R. A. Brooks, D. J. Ehrlich, K. R. Udayakumar and L. E. Cross, *IEEE J. Microelectromechanical Systems*, 1992, **1**, 44-51.
- T. Fujita, *New Ceramics*, 1994, **7**(12), 52-55.
- A. Fukami, M. Yano, H. Tokuda, M. Ohki and R. Kizu, *Int. J. Veh. Des.*, 1994, **15**, 348-357.
- T. Funakubo, T. Tsubata, Y. Taniguchi, K. Kumei, T. Fujimura and C. Abe, *Jpn. J. Appl. Phys.*, 1995, **34**, 2756-2759.
- A. Furuta, K. Y. Oh and K. Uchino, *Sensors and Mater.*, 1992, **3**(4), 205-215.
- A. Furuta and K. Uchino, *J. Am. Ceram. Soc.*, 1993, **76**, 1615-1617.
- A. Furuta and K. Uchino, *Ferroelectrics*, 1994, **160**, 277-285.
- A. Furuta and K. Uchino, *Adv. Ceram. Mater.*, 1986, **1**, 61-63.
- H. Goto, *J. Opt. Tech. Contact*, 1994, **32**, 322-330.
- H. Goto, K. Imanaka and K. Uchino, *Ultrasonic Technol.*, 1992, **5**, 48-51.
- R. Gross, in 'Proc. 4th Int. Conf. New Actuators', AXON, Bremen, Germany, 1994, pp. 190-192.
- T. H. Hao, X. Gong and Z. Suo, *J. Mech. Phys. Solids*, 1996, **44**(1), 23-48.
- J. Heeg, Analytical and Experimental Investigation of Flutter Suppression by Piezoelectric Actuation, NASA Tech. Pap., NASA-TP-3241, 1993, p. 47.
- S. Hirose, M. Aoyagi, Y. Tomikawa, S. Takahashi and K. Uchino, in 'Proc. Ultrasonic Int.', 1995a, pp. 1-4.
- S. Hirose, S. Takahashi, K. Uchino, M. Aoyagi and Y. Tomikawa, *Proc. Mater. Res. Soc.*, 1995b, **360**, 15-20.
- H. S. Kim, S. C. Choi, J. K. Lee and H. J. Jung, *J. Korean Ceram. Soc.*, 1992, **29**, 695-704.
- M. P. Koster, in 'Proc. 4th Int. Conf. New Actuators', AXON, Bremen, Germany, 1994, pp. 144-148.
- G. P. Mather and B. N. Tran, Aircraft Cabin Noise Reduction Tests Using Active Structural Acoustic Control, Paper American Institute of Aeronautics and Astronautics AIAA-93-4437, 1993, p. 7.
- K. Nagata and S. Kinoshita, *J. Powder Metallurgy*, 1994, **41**, 975-979.
- K. Nagata and S. Kinoshita, *Jpn. J. Appl. Phys.*, 1995a, **34**, 5266-5269.
- K. Nagata and S. Kinoshita, *J. Powder Metallurgy*, 1995b, **42**, 623-627.
- J. Ohashi, Y. Fuda and T. Ohno, *Jpn. J. Appl. Phys.*, 1993a, **32**, 2412-2414.
- J. Ohashi, Y. Fuda and T. Ohno, *Tekin Tech. Rev.*, 1993b, **19**, 55-60.
- N. Okada, K. Ishikawa, K. Murakami, T. Nomura and M. Ogino, Improving Hysteresis of Piezoelectric PZT Actuator, Bull. Shizuoka Univ. Electron. Sci. Grad. School, 1993, vol. 14, pp. 7-13.
- K. Onitsuka, A. Dogan, J. F. Tressler Q. C. Xu, S. Yoshikawa and R. E. Newnham, *J. Intelligent Mater. Systems and Struct.*, 1995, **6**, 447-455.
- Y. Ono and Y. Fuda, in 'Proc. 6th Symp. on Electro-Magnetic Related Dynamics', 1994, pp. 135-138.
- H. Saigoh, M. Kawasaki, N. Maruko and K. Kanayama, *Jpn. J. Appl. Phys.*, 1995, **34**, 2760-2764.
- T. Sakai, M. Ishikiriya, Y. Terai and R. Shimazaki, *Toyota Tech. Rev.*, 1992, **42**, 52-59.
- M. Sano, K. Ohya, K. Hamada, Y. Inoue and Y. Kajino, *NEC Giho*, 1993, **46**(10), 100-103.
- G. A. Schneider, A. Rostek, B. Zickgraf and F. Aldinger, in 'Proc. 4th Int. Conf. Electronic Ceram. and Appl.', Germany, Augustinus, Buchhandlung, Germany, 1994, pp. 1211-1216.
- H. Shimoda, J. Ohmata and F. Okamoto, *J. Precision Eng. Jpn.*, 1992, **58**, 2111-2117.
- Y. Sugawara, K. Onitsuka, S. Yoshikawa, Q. C. Xu, R. E. Newnham and K. Uchino, *J. Am. Ceram. Soc.*, 1992, **75**, 996-998.
- Z. Suo, *J. Mech. Phys. Solids*, 1993, **41**, 1155-1176.
- S. Takada, *NEC Giho*, 1992, **45**, 109-113.
- S. Takada, Y. Inoue, K. Oya and M. Inagawa, *NEC Giho*, 1994, **47**, 98-102.
- S. Takahashi, Y. Sakaki, S. Hirose and K. Uchino, *Jpn. J. Appl. Phys.*, 1995, **34**, 5328-5331.
- M. Tohda, S. Ichikawa, K. Uchino and K. Kato, in 'Ultrasonic Linear Motor Using a Multilayered Piezoelectric Actuator, Ferroelectrics (Proc. ECAPD-1/ISAF 88) 93', Gordon and Breach, Amsterdam, 1989, pp. 287-294.
- J. F. Tressler, Q. C. Xu, S. Yoshikawa, K. Uchino and R. E. Newnham RE, in 'Composite Flexensional Transducers for Sensing and Actuating, Ferroelectrics 156 (Proc. 8th Int. Mtg. Ferroelectricity)', Gordon and Breach, Amsterdam, 1994, pp. 67-72.
- K. Uchino, 'Ceramic Data Book 88', Institute of Industrial Manufacturing Technology, Tokyo, 1988.
- K. Uchino, *MRS Bull.*, 1993, **18**, 42-48.
- K. Uchino, in 'Proc. 4th Int. Conf. Electronic Ceramics & Appl.', Augustinus, Buchhandlung, Germany, 1994, pp. 179-191.
- K. Uchino, in 'Piezoelectric Actuators/Ultrasonic Motors—Their Developments and Markets Proc. 9th Int'l Symp. Appl. Ferroelectrics', eds. R. K. Pandey, M. Liu and A. Sayari, IEEE Service Center, Piscataway, NJ, 1995, pp. 319-324.
- K. Uchino, in 'Manufacturing Technology of Multilayered Transducers Proc. Amer. Ceram. Soc., Manufacture of Ceramic Components', 1995, pp. 81-93.
- K. Uchino, *Mater. Lett.*, 1995c, **22**, 1-4.
- K. Uchino, 'Piezoelectric Actuators/Ultrasonic Motors', Kluwer, Boston, MA, 1996.
- K. Uchino and H. Aburatani, in 'Proc. 2nd Int. Conf. Intelligent Materials', Technomic, Lancaster, PA, 1994, pp. 1248-1256.
- K. Uchino and T. Ishii, *J. Jpn. Ceram. Soc.*, 1988, **96**, 863-867.
- K. Uchino and S. Nomura, *Ferroelectrics*, 1983, **50**(1), 191-196.
- B. Wada, Summary of Precision Actuators for Space Application, JPL Document D-10 659, 1993.
- H. Wang and R. N. Singh, *Ferroelectrics*, 1995, **168**, 281-291.
- J. Watanabe, T. Sometsugu, Y. Watanabe, S. Johmura, K. Kurihara and K. Kazama, *Hitachi Metal Giho*, 1993, **9**, 59-64.
- T. Yano, I. Fukui, E. Sato, O. Inui and Y. Miyazaki, in 'Proc. Electr. & Commun. Soc. (Spring, 1984)', 1984, p. 156.
- S. Yonekubo, *J. Electron. Photo Soc.*, 1995, **34**, 226-228.
- S. Yoshikawa and T. ShROUT, in 'Multilayer Piezoelectric Actuators—Structures and Reliability AIAA/ASME/ASCE/AHS/ASC Struct. Struct. Dyn. Mater. Conf.', 1993, pp. 3581-3586.
- Q. M. Zhang, J. Z. Zhao, K. Uchino and J. H. Zheng, *J. Mater. Res.*, 1996, **12**, 226-234.
- J. H. Zheng, S. Takahashi, S. Yoshikawa, K. Uchino and J. W. C. de Vries, *J. Am. Ceram. Soc.*, 1996, **79**, 3193-3198.

APPENDIX 60

RECENT TREND OF PIEZOELECTRIC ACTUATOR DEVELOPMENTS

-- Material, Design and Drive Technique Related Issues --

Kenji Uchino

International Center for Actuators and Transducers

Materials Research Laboratory, The Pennsylvania State University
University Park, PA 16802, USA

Abstract:

In these several years, piezoelectric materials have become key components in smart actuator/sensor systems such as precision positioners, miniature ultrasonic motors and adaptive mechanical dampers. This paper reviews recent developments of piezoelectric and related ceramic actuators with particular focus on the improvement of actuator materials, device designs, and control techniques.

INTRODUCTION

Piezoelectric actuators are forming a new field between electronic and structural ceramics [1-4]. Application fields are classified into three categories: positioners, motors and vibration suppressors. The manufacturing precision of optical instruments such as lasers and cameras, and the positioning accuracy for fabricating semiconductor chips, which must be adjusted using solid-state actuators, is of the order of 0.1 μm . Regarding conventional electromagnetic motors, tiny motors smaller than 1 cm are often required in office or factory automation equipment and are rather difficult to produce with sufficient energy efficiency. Ultrasonic motors whose efficiency is insensitive to size are superior in the mini-motor area. Vibration suppression in space structures and military vehicles using piezoelectric actuators is also a promising technology.

This article reviews recent developments of piezoelectric and related ceramics to smart actuator/sensor systems, including the improvement of actuator materials, and design and drive/control issues of the devices.

CERAMIC ACTUATOR MATERIALS

The research focus is still put on the enhancement of induced strain magnitude (real part). However, the research trend is gradually shifting to the improvement of strain hysteresis or loss (imaginary part) of the piezoelectric materials, which is more important for the actual commercialization of the piezoelectric actuators. Also optomechanical coupling devices are a new trend, targeting the coming optical information age. Recent six topics are reviewed here: single crystals, thin/thick films, phase-change materials, polymers, high-power piezoelectrics and photostrictive materials.

Relaxor Single Crystal Transducers

Since the enhancement of the induced strain level is a primary target, single crystals with a high capability for generating larger strains are tried to be used in these days.

In 1981, we firstly reported an enormously large electromechanical coupling factor $k_{33} = 92\%$ and piezoelectric constant $d_{33} = 1500 \text{ pC/N}$ in solid solution single crystals between relaxor and non-ferroelectrics, $\text{Pb}(\text{Zn}_{1/3}\text{Nb}_{2/3})\text{O}_3\text{-PbTiO}_3$ [5]. This discovery has not been marked practically more than 10 years until high k materials have been paid attention in medical acoustics recently. The data have been reconfirmed, and much more improved data were obtained recently, aiming at medical acoustic applications [7,8]. The strains as large as 1.7% can be induced practically for morphotropic phase boundary composition of PZN-PT solid solution single crystals. It is noted that the highest values are observed for rhombohedral composition only when the single crystal is poled along the perovskite [001] axis, along the [111] spontaneous polarization axis.

Epitaxial PZT Films

A series of theoretical calculations made for perovskite type ferroelectric crystals suggests that large d and k values in similar magnitudes to PZN-PT can also be expected in PZT. Crystal orientation dependence of piezoelectric properties is phenomenologically calculated for composition around the morphotropic phase boundary of PZT [9]. The maximum longitudinal piezoelectric constant d_{33} (4 - 5 times enhancement) and electromechanical coupling factor k_{33} (more than 50%) in the rhombohedral composition were found to be at 57° and 51° angles, respectively, canted from the spontaneous polarization direction [111], which correspond roughly to the perovskite [100] axis.

Figure 1 shows the principle of the enhancement in electromechanical couplings. Because the shear coupling d_{15}

is the highest in perovskite piezoelectric crystals, the applied field should be canted from the spontaneous polarization direction to obtain the maximum strain.

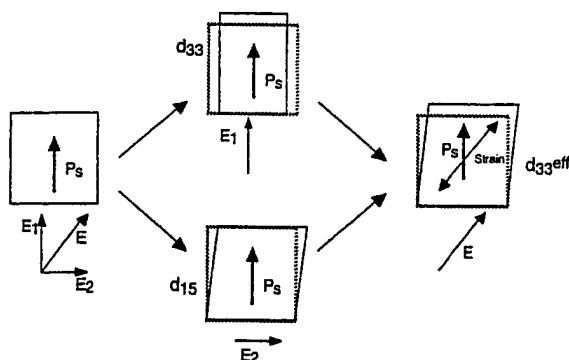


Fig.1 Principle of the enhancement in electromechanical couplings in a perovskite piezoelectric.

Some research groups including us are demonstrating [001] oriented epitaxially grown thin/thick films using a rhombohedral PZT composition, which are expected to enhance the effective piezoelectric constant by 4-5 times [10].

Phase-Change Materials

Concerning the phase-change-related strains, polarization induction by switching from an antiferroelectric to a ferroelectric state has been proposed [11].

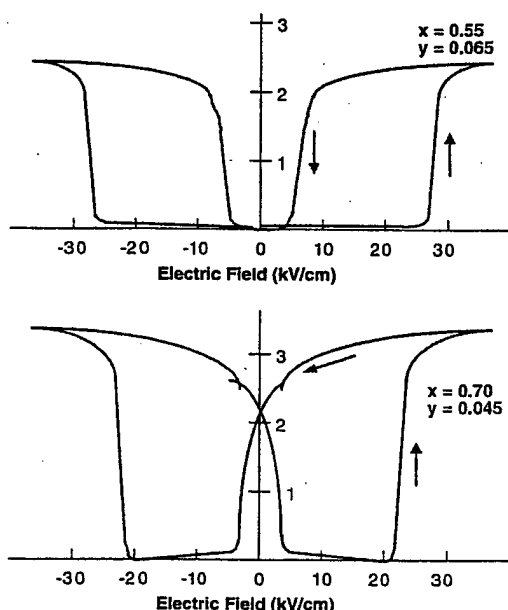


Fig.2 Field-induced strain curves for the lead zirconate stannate system $Pb_{0.99}Nb_{0.02}((Zr_xSn_{1-x})_{1-y}Ti_y)_{0.98}O_3$. Top: $x=0.55$, $y=0.065$, and bottom: $x=0.70$, $y=0.045$.

Figure 2 shows the field-induced strain curves taken for the lead zirconate stannate based $Pb_{0.99}Nb_{0.02}((Zr_xSn_{1-x})_{1-y}Ti_y)_{0.98}O_3$ system (top: $x=0.55$, $y=0.065$; and bottom: $x=0.70$, $y=0.045$). The longitudinally induced strain reaches up to 0.4%, which is larger than that expected in normal piezoelectrics or electrostrictors. A rectangular-shape hysteresis in Fig.2 top, referred to as a "digital displacement transducer" because of the two on/off strain states, is interesting. Moreover, this field-induced transition exhibits a shape memory effect in appropriate compositions (Fig.2 bottom). Once the ferroelectric phase has been induced, the material will "memorize" its ferroelectric state even under zero-field conditions, although it can be erased with the application of a small reverse bias field [12]. This shape memory ceramic is used in energy saving actuators. A latching relay is composed of a shape memory ceramic unimorph and a mechanical snap action switch, which is driven by a pulse voltage of 4ms. Compared with the conventional electromagnetic relays, the new relay is much simple and compact in structure with almost the same response time.

Polymer Actuators

Polyvinylidene difluoride-trifluoroethylene (PVDF-TrFE) copolymer is a well-known piezoelectric which has been popularly used in sensor applications such as keyboards. Recently, Q. M. Zhang's group at Penn State reported that the field induced strain level can be significantly enhanced up to 5 % by using a high-energy electron irradiation onto the PVDF films [13].

Dielectric elastomer actuators are based on the deformation of a soft polymer which acts as a dielectric between highly compliant electrodes. This effect is dominated by the Maxwell's stresses imposed by the compliant electrodes. Extremely high strains at low frequencies have been reported by Pelrine et al. [14]. In-plane strains of more than 100% and 200% were observed in silicone and acrylic elastomers, respectively.

High-Power Piezoelectrics

In order to obtain a large output mechanical power, the piezoelectric materials are driven under a high vibration level, namely under a relatively large AC electric field. This causes heat generation as well as a significant degradation in piezoelectric properties. Therefore, the high-power device such as an ultrasonic motor requires a very "hard" piezoelectric with a high mechanical quality factor Q_M , to suppress heat generation. The Q_M is defined as an inverse value of the loss factor, $\tan\delta_m$. It is also notable that the actual mechanical vibrational amplitude at the resonance frequency is directly

proportional to this Q_M value. Recent research efforts by S. Hirose, S. Takahashi and us are introduced below.

The vibration velocity dependence of the piezoelectric constant, permittivity, elastic compliance and electro-mechanical coupling factor was obtained for PZT based samples [15]. Figure 3 shows the mechanical quality factor Q_M and the actual temperature rise plotted as a function of the average vibration velocity. Notice a significant decrease in Q above a certain critical vibration level, which is the limit of the output vibration energy. Even if the input electrical energy is increased further, the additional energy will be converted only into heat.

Figure 4 shows the temperature rise versus vibration velocity for undoped, Nb-doped and Fe-doped PZT samples. The suppression of heat generation is remarkable in the Fe-doped (acceptor-doped) ceramic.

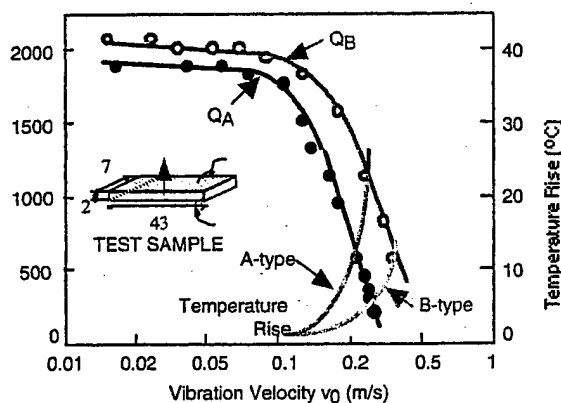


Fig.3 Vibration velocity dependence of the quality factor Q_M and temperature rise for both A (resonance) and B (antiresonance) type resonances of a longitudinally vibrating PZT ceramic transducer through d_{31} .

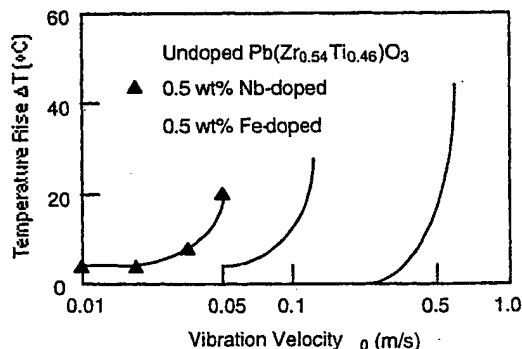


Fig.4 Temperature rise ΔT vs. effective vibration velocity v for PZT k_{31} plate samples.

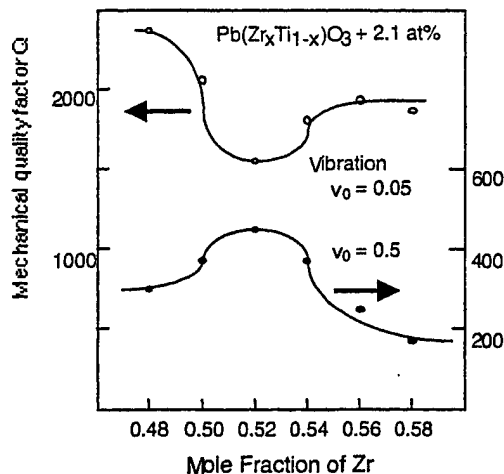


Fig.5 Mechanical quality factor Q_M vs. mole fraction of Zr (x) effective vibration velocities $v_0 = 0.05$ and 0.5 m/s for $Pb(Zr_xTi_{1-x})O_3 + 2.1$ at% Fe^{3+} ceramics.

Figure 5 shows mechanical Q_M versus mole fraction of Zr (x) at effective vibration velocities $v_0 = 0$ m/s and 0.5 m/s for $Pb(Zr_xTi_{1-x})O_3$ doped with 2.1 at% of Fe^{3+} [16]. The decrease in mechanical with increase in vibration level is minimum around the rhombohedral-tetragonal morphotropic phase boundary (52/48). In other words, the weak material at a small vibration level becomes the best at a large vibration level, and data obtained from conventional impedance analyzer are not relevant for high power materials.

At present, the highest value 0.62 m/s of maximum vibration velocity (defined at $20^\circ C$ rise from room temperature) can be obtained in $(z)Pb(Zr_xTi_{1-x})O_3 - zPb(Mn_{1/3}Sb_{2/3})O_3$ at $x = 0.48$ and $y = 0.05$ [17].

Figure 6 highlights the key material-related factors affecting heat generation in the piezoelectric material. The resistances R_d and R_m in the equivalent electrical circuit are separately plotted as a function of vibration velocity [18]. Note that R_m is mainly related to the mechanical loss, is insensitive to the average vibration velocity, while R_d , related to the dielectric loss, changes significantly around a certain critical vibration velocity. Thus, the resonance loss Q_M^{-1} at a small vibration velocity is mainly determined by the extensive mechanical loss, and with increasing vibration velocity, the extensive dielectric loss contribution significantly increases. We can conclude that heat generation is caused primarily by dielectric loss (approximated by the E hysteresis loss). Refer to Ref. [19] for the detailed discussion on the loss mechanisms in piezoelectric materials.

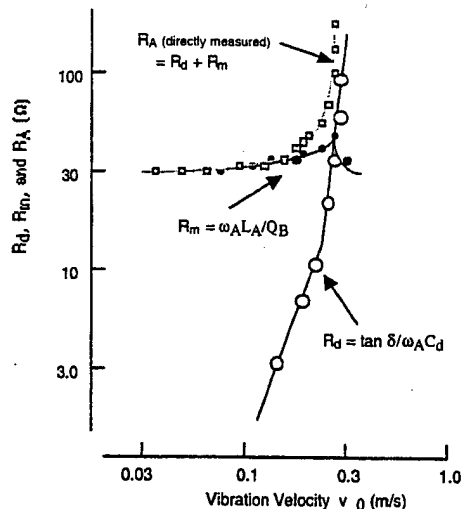


Fig.6 Vibration velocity dependence of the resistances R_d and R_m in the equivalent electric circuit for a piezoelectric component.

Photostrictive Actuators

A photostrictive actuator is a fine example of an intelligent material, incorporating "illumination sensing" and self production of "drive/control voltage" together with final "actuation." In certain ferroelectrics, a constant electromotive force is generated with exposure of light, and a photostrictive strain results from the coupling of this bulk photovoltaic effect to inverse piezoelectricity. A bimorph unit has been made from PLZT 3/52/48 ceramic doped with slight addition of tungsten [20]. The remnant polarization of one PLZT layer is parallel to the plate and in the direction opposite to that of the other plate. When a violet light is irradiated to one side of the PLZT bimorph, a photovoltage of 1 kV/mm is generated, causing a bending motion. The tip displacement of a 20mm bimorph 0.4mm in thickness was 150 μ m, with a response time of 1 sec.

A photo-driven micro walking device, designed to begin moving by light illumination, has been developed [21]. It is simple in structure, having neither lead wires nor electric circuitry, with two bimorph legs fixed to a plastic board. When the legs are irradiated alternately with light, the device moves like an inchworm with a speed of 100 μ m/min.

In pursuit of thick film type photostrictive actuators for space structure applications, in collaboration with researchers at Jet Propulsion Laboratory we investigated the optimal range of sample thickness and surface roughness dependence of photostriction. We have found that 30 μ m thick PLZT films exhibit the maximum photovoltaic phenomenon [22].

ACTUATOR DESIGNS

Two of the most popular actuator designs are multilayers and bimorphs. The multilayer, in which roughly 100 thin piezoelectric/electrostrictive ceramic sheets are stacked together, has advantage in low driving voltage (100V), quick response (10 μ sec), high generative force (100kgf) and high electromechanical coupling. But the displacement in the range of 10 μ m is not sufficient for some applications. This contrasts with the bimorph consisting of multiple piezoelectric and elastic plates bonded together to generate a large bending displacement of several hundred μ m, but the response (1msec) and the generative force (100gf) are low.

A multilayer actuator with interdigital internal electrodes has been developed by Tokin [23]. In contrast to the conventional electrode configuration, line electrodes are printed on piezoelectric green sheets, and are stacked so that alternating electrode lines are displaced by one-half pitch. This actuator generates motions at right angles to the stacking direction using the longitudinal piezoelectric effect. Long ceramic actuators up to 74 mm in length were manufactured, which could generate the displacement up to 55 μ m.

A three-dimensional positioning actuators with stacked structure has been proposed by PI Ceramics in which shear strain is utilized to generate x and y displacements [24].

A monomorph device has been developed to replace the conventional bimorphs, with simpler structure and manufacturing process. The principle is superposed effect of piezoelectricity and semiconductivity [25]. The contact between semiconductor and a metal (Schottky barrier) causes non-uniform distribution of the electric field, even in a compositionally uniform ceramic. Suppose the ceramic possesses also piezoelectricity, only one side of a ceramic plate tends to contract, leading to bending deformation in total. A monomorph plate with 30mm in length and 0.5 mm in thickness can generate 200 μ m tip displacement, in equivalent magnitude of that of the conventional bimorph. The "rainbow" actuator by Aura Ceramics [26] is a modification of the above-mentioned semiconductive piezoelectric monomorphs, where half of the piezoelectric plate is reduced so as to make a thick semiconductive electrode to cause bend.

A composite actuator structure called the "moon" has been developed at Penn State to provide characteristics intermediate between the multilayer and bimorph actuators; this transducer exhibits an order of magnitude larger displacement than the

multilayer, and much larger generative force with quicker response than the bimorph [27,28]. Figure 7 shows the structures for a Moonie and a modified Cymbal. A Cymbal with a thickness 2 mm and a diameter 12 mm can generate a displacement up to 100 μm . The Cymbal has been applied to make a miniaturized laser beam scanner.

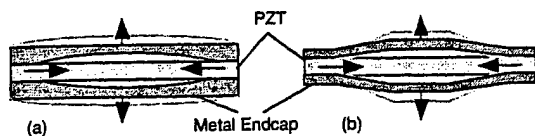


Fig.7 Comparison of the structures for a Moonie (a) and a Cymbal (b).

DRIVE TECHNIQUES

One of the problems in wide commercialization of piezoelectric actuators and ultrasonic motors includes rather bulky and expensive drive circuitry inevitably required. Noticing that the largest components in the drive circuit are electromagnetic transformers, we have been working on replacing these conventional transformers with piezoelectric transformers. The piezotransformer has input and output terminals fabricated on a piezo-device, and the input/output voltage is changed through the vibration energy transfer.

Historically, piezoelectric transformers were used in color TV's because of their compact size in comparison with the conventional electromagnetic coil-type transformers. Since serious problems were found initially in the mechanical strength (collapse happened at the nodal line!) and in heat generation, the original Rosen-type failed to be commercialized.

However, recent lap-top computers with a liquid crystal display require a very thin, no electromagnetic-noise transformer with a high efficiency as an inverter of a fluorescent backlight. This application has accelerated the development of the piezo-transformer recently. NEC recently commercialized a multilayer rectangular type transformer in order to increase the voltage step-up ratio, using a third-order longitudinal mode, which is one method to distribute the stress concentration [29].

We proposed a new disk type transformer which has a higher voltage step-up ratio and a wider application area than the rectangular types. Our disk type with an asymmetrical electrode pattern utilizes a coupled vibration mode between k_p and k_{15} , different from k_{31} of the conventional types. Since k_p and k_{15} are larger than k_{31} in most of PZT based piezoelectrics, our design provides a higher step-up ratio and a higher efficiency than the rectangular types. Moreover, stress concentration in the device

under driving is remarkably released, leading to longer lifetime [30].

We propose a new application of these pie transformers, that is, power supplies piezoelectric actuators and ultrasonic motors schematically illustrated in Fig. 8. The pie transformers can reduce the total system volume & weight significantly.

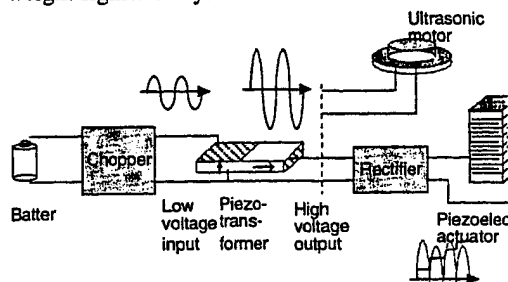


Fig.8 Piezoactuator drive system using a piezo-transformer

FUTURE RESEARCH TREND

Future research trends will be divided into two ways: up-sizing in space structures and down-sizing in office equipment. Further down-sizing will also be required in medical diagnostic applications such as blood test kits and surgical catheters.

Piezoelectric thin films compatible with silicon technology will be much focused in microelectromechanical systems. An ultrasonic rotary motor as tiny as 2 mm in diameter fabricated on silicon membrane is a good example [31].

One ceramic multilayer component actuator proposed by Mitsui Chemical is very suggestive for predicting the future trend [32]. Only by the external connection, a combined vibration of the longitudinal L_1 and bending B_2 modes can be excited. The Penn State University has developed compact ultrasonic rotary motor as tiny as 3 mm diameter. The stator consists basically of two piezoelectric rings and a metal ring with "windmill shaped fingers bonded together, so as to generate coupled vibration of radial and bending types on finger [33]. Since the component number and the fabrication process were minimized, the fabrication price would be decreased remarkably, and it would be adaptive to the disposable usage. When driven 160 kHz, the maximum revolution 2000rpm and the maximum torque 0.8mN·m were obtained for a 1 mm motor. Notice that even the drive of the motor is intermittent, the output rotation becomes very smooth because of the inertia of the rotor.

Miniaturization and integration of the drive circuit will be also an important research area for the actuators.

wide commercialization of piezoactuators and ultrasonic motors. Piezoelectric transformers may cause a breakthrough for this application.

With expanding the application field of ceramic actuators, the durability/reliability issue becomes more important. The final goal is, of course, to develop much tougher actuator ceramics mechanically and electrically. However, the reliability can be improved significantly if the destruction symptom of the actuator is monitored.

Safety systems or health monitoring systems have been proposed with two feedback mechanisms: position feedback which can compensate the position drift and the hysteresis, and breakdown detection feedback which can stop the actuator system safely without causing any serious damages onto the work, e.g. in a lathe machine [34]. Acoustic emission and internal potential measurements, and resistance monitoring of a strain-gauge type internal electrode embedded in a piezo-actuator under a cyclic electric field drive are good predictors for the lifetime [35,36].

Future research and development should focus on superior systems ecologically (i.e. fit for human!) as well as technologically. Material-wise, Pb (lead)-free piezoceramics have started to be developed partly due to the governmental regulation expected in the near future. Single crystals such as barium titanate and potassium niobate/tantalate based are the primary targets [37]. Safety systems, which can monitor the fatigue or the destruction symptom of materials/devices, and stop the equipment safely without causing serious problems, will be desired.

REFERENCES

- [1] K.Uchino, *Piezoelectric Actuators and Ultrasonic Motors*, Kluwer Academic Publ. (1996)
- [2] K.Uchino, *Bull.Am.Ceram.Soc.*, **65**(4), 647 (1986)
- [3] K.Uchino, *MRS Bull.*, **18**(4), 42 (1993)
- [4] K.Uchino, *Proc. 4th Int'l Conf. Electronic Ceramics & Appl.*, p.179(1994)
- [5] J.Kuwata, K.Uchino and S.Nomura, *Ferroelectrics*, **37**, 579 (1981)
- [6] J.Kuwata, K.Uchino and S.Nomura, *Jpn.J.Appl.Phys.*, **21**, 1298 (1982)
- [7] K.Yanagiwawa, H.Kanai and Y.Yamashita, *Jpn.J.Appl. Phys.*, **34**, 536 (1995)
- [8] S.E.Park and T.R.ShROUT, *Mat.Res.Innovt.*, **1**, 20 (1997)
- [9] X.H.Du, J.Zheng, U.Belegundu and K.Uchino, *J.Appl. Phys.Lett.*, **72**, 2421 (1998)
- [10] D.Damjanovic, D.V.Taylor and N.Setter, *Proc. Mater. Res. Soc., Symp. VIII* (1999) [in press]
- [11] K.Uchino and S.Nomura, *Ferroelectrics*, **50**(1), 191 (1983)
- [12] A.Furuta, K.Y.Oh and K.Uchino, *Sensors and Mater.*, **3**(4), 205 (1992)
- [13] V.Bharti, H.S.Xu, G.Shanti, Q.M.Zhang and K.Liang, *J.Appl.Phys.* **87**, 452 (2000)
- [14] Pelrine et al., *Science* (2000) [in press]
- [15] S.Takahashi and S.Hirose, *Jpn.J.Appl.Phys.*, **32** Pt.1, No.5B, 2422 (1993).
- [16] K.Uchino, J.Zheng, A.Joshi, Y.H.Chen, S.Yoshikawa, S.Hirose, S.Takahashi and J.W.C deVries, *J. Electro-ceramics*, **2**, 33 (1998).
- [17] S.Takahashi, Y.Sasaki, S.Hirose and K.Uchino, *Proc. Mater.Res.Soc.Symp.Vol.360*, p.305 (1995)
- [18] S.Hirose, M.Aoyagi, Y.Tomikawa, S.Takahashi and K. Uchino, *Proc. Ultrasonics Int'l. '95*, Edinburgh, p.184 (1995).
- [19] K.Uchino and S.Hirose, *IEEE-UFFC Trans.* (2000) [accepted]
- [20] K.Uchino, *Mat.Res.Innovat.*, **1**, 163 (1997)
- [21] K.Uchino, *J.Rob.Mech.*, **1**(2), 124 (1989)
- [22] P.Poosanaas, K.Tonooka and K.Uchino, *J.Mechatronics* (2000) [in press]
- [23] J.Ohashi, Y.Fuda and T.Ohno, *Jpn.J.Appl.Phys.*, **32**, 2412 (1993)
- [24] A.Banner and F.Moller, *Proc. 4th. Int'l Conf. New Actuators*, AXON Tech.Consult.GmbH, p.128 (1995)
- [25] K.Uchino, M.Yoshizaki, K.Kasai, H.Yamamura, N. Sakai and H.Asakura, *Jpn.J.Appl.Phys.*, **26**(7), 1046 (1987)
- [26] Aura Ceramics, Inc., Catalogue "Rainbow"
- [27] Y.Sugawara, K.Onitsuka, S.Yoshikawa, Q.C.Xu, R.E.Newnham and K.Uchino, *J.Am.Ceram.Soc.*, **75**(4), 996 (1992)
- [28] A.Dogan, K.Uchino and R.E.Newnham, *IEEE Trans. UFFC*, **44**,597 (1997)
- [29] S.Kawashima, O.Ohnishi, H.Hakamata, S.Tagami, A. Fukuoka, T.Inoue and S.Hirose, *Proc. IEEE Int'l Ultrasonic Symp. '94*, France (1994)
- [30] B.Koc, S.Alkoy and K.Uchino, *Proc. IEEE Ultrasonic Symp., Nevada* (1999)
- [31] A.M.Flyn, L.S.Tavrow, S.F.Bart, R.A.Brooks, D.J. Ehrlich, K.R.Udayakumar and L.E.Cross, *J. Microelectro-mechanical Systems*, **1**, 44 (1992)
- [32] H.Saigo, *15th.Symp.Ultrasonic Electronics*, No.PB-46, p.253 (Nov.1994)
- [33] B.Koc and K.Uchino, *IEEE int'l. Ultrasonic Symp.*, YY-6, Sendai, Japan (Oct.1998)
- [34] K.Uchino, *J.Industrial Education Soc. Jpn.*, **40** 28 (1992)
- [35] H.Aburatani, K.Uchino, A.Furuta and Y.Fuda, *Proc. 9th Int'l Symp.Appl.Ferroelectrics*, p.75C (1995)
- [36] H.Aburatani and K.Uchino, *Jpn.J.Appl.Phys.*, **37**, part 1, No.1, 204 (1998)
- [37] X.H.Du, Q.M.Wang, U.Belegundu, A.Bhalla and K. Uchino, *Mater.Lett.* **40**, 109 (1999)

APPENDIX 61

Compact Piezoelectric Stacked Actuators for High Power Applications

Kui Yao, *Member, IEEE*, Kenji Uchino, *Member, IEEE*, Yuan Xu, Shuxiang Dong, and Leong Chew Lim

Abstract—Small, hollow, multilayer actuators with a diameter of 3 mm were fabricated by the stacking method from piezoelectric hard lead zirconate titanate (PZT) ceramics. Langevin vibrators were also constructed with the hollow multilayer actuators. The performance capabilities of the actuator and Langevin vibrator samples were examined under high-power conditions. The high-power vibration level at a given sinusoidal drive voltage was significantly enhanced by using a multilayer structure under either a nonresonance or resonance condition. A maximum vibration velocity of 0.17 m/sec was obtained for the 9-layer actuator sample under nonresonance conditions. The vibration velocity was further improved with the Langevin vibrator driven at the resonance frequency. The temperature rise due to heat generation under high-power conditions was the immediate limitation on the maximum accessible vibration velocity for the stacked actuators.

I. INTRODUCTION

HIGH-POWER piezoelectric devices, such as ultrasonic motors and piezoelectric transformers, are being intensively investigated [1]. Because piezoelectric devices often have significant advantages over conventional electromagnetic devices at smaller sizes, miniaturization of piezoelectric devices is attractive. Multilayer structures offer better generative force, electromechanical coupling, and energy density properties than other configurations such as bimorph [2], [3] and moonie structures [4], [5]; thus they are promising designs for compact devices [6], [7]. Commercialized multilayer actuators have been designed and specified as devices to provide pseudo-static or pulse displacements. These actuators have been used for optical modulations, such as optical interferometers [8], [9] and deformable mirrors [10], [11]; vibration suppression and active damping [12]; fluid control [13]; and printer heads [14], [15]. The use of such multilayer actuators also has been attempted for high-power piezoelectric devices [16]–[20]. However, their applicability when driven at their ultrasonic resonance frequency under large electric field is in question due to the losses associated with the piezoelectric soft materials, which may produce considerable heat generation [18], [21]. Therefore, to meet the present need for compact piezoelectric actuators suitable for high power ap-

plications, we developed stacked multilayer actuators with diameters as small as 3 mm and with hollow structures from a hard lead zirconate titanate (PZT) material. The use of hard piezoelectric material and the hollow structure favor the suppression of a temperature increase, even under high-power conditions.

In the literature, theoretical analyses were conducted to clarify the electromechanical dynamic response, power transfer and consumption, and thermal effects of the stacked piezoelectric structures under dynamic driving condition [22]–[25]. However, it is difficult to quantitatively predict the actual electromechanical and thermal behaviors for the stacked actuators under high power conditions due to their composite structures and complicated materials related mechanisms. Experimental studies on the dynamic properties of the co-fired multilayer actuators [26]–[28] and disc-stacked actuators [29] under dynamic driving conditions also are being conducted. The actuators under these investigations were prepared from soft piezoelectric ceramic. The disc-stacked actuators in the previous dynamic study have a large size, and the reported experimental results on their high frequency dynamic response and thermal behaviors are very few.

This paper reports the development of the miniaturized, hollow, stacked multilayer actuator samples from hard PZT ceramic, and their electromechanical and heat generation characteristics. Considering the important applications of the metal-ceramic composite vibrators [30]–[32], Langevin vibrators also were fabricated with the stacked actuators, and the effects of the stacked actuators on their performance also were examined.

II. FABRICATION AND EXPERIMENTAL MEASUREMENTS

Ceramic tubes with an outside diameter of 3 mm were first prepared from commercialized hard PZT powders (PZT-841, APC International Ltd.) by a molding and sintering process. The tubes were subsequently cut into thin annular disks with a 1 mm hole at the center. The ceramic disks were polished to a thickness of 0.25 mm and electroded with fired on silver. This was followed by a poling process done at 150°C for 10 min. with an electric field of 2.5 kV/mm to get piezoelectrically active ceramic rings.

Hollow 3 mm multilayer samples were fabricated by bonding multiple piezoelectric rings and copper electrode shims alternately with epoxy. On an average, the thickness of each epoxy layer was 5 μm . An exploded view for the assembly of the multiple PZT ceramic and copper layers

Manuscript received March 1, 1999; accepted September 21, 1999.

K. Yao, S. Dong, and L. C. Lim are with the Institute of Materials Research and Engineering, 3 Research Link, Singapore 117602 (e-mail: k-yao@imre.org.sg).

K. Uchino, Y. Xu are with the International Center for Actuators and Transducers, Materials Research Laboratory, The Pennsylvania State University, University Park, PA 16802.

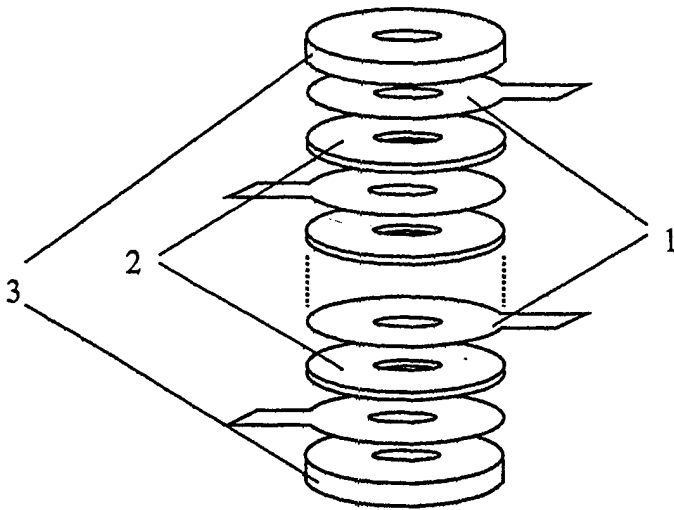


Fig. 1. An exploded view for the stacked, hollow, multilayer actuator. (1) Copper shims, (2) PZT ceramic rings, (3) copper caps.

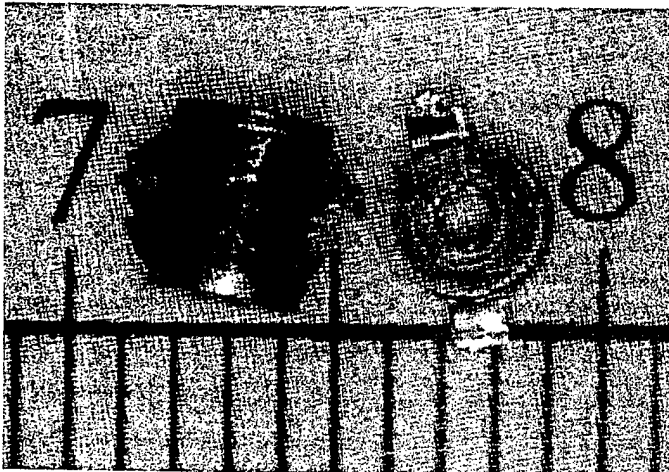


Fig. 2. An axial and side view of the 3 mm stacked hollow multilayer actuator samples. The metric ruler in the photo indicates the scale.

is shown in Fig. 1. Note that the polarization direction between the adjacent PZT disks was opposite. The copper shims, each with a thickness of $25\ \mu\text{m}$, were sandwiched between the PZT rings as the electrode. The electrode configuration is referred to as a plate-through type [1]. Extended fingers of the copper shims were exposed for external electrical connection with silver paste. Two hollow copper cylinder caps were attached to the two terminals. A photo of the 3 mm multilayer samples is shown in Fig. 2. The 3 mm Langevin vibrators were constructed with the actuators by substituting two long and hollow brass cylinders for the short caps to increase the total length and enhance the vibration magnitude near the longitudinal resonance frequency [33].

The mechanical quality factor, Q_m , for the adopted PZT material was 1400, which is favorable for suppressing heat generation. The hollow structure is not only advantageous for heat dissipation, but it is also compatible with a structural design for ultrasonic motor applications.

The dielectric properties of the samples were examined with a Stanford LCR Meter (SR715) and the impedance spectra were measured with an HP Impedance/Gain Phase Analyzer (HP4194A). The dielectric loss under high-drive electric field was characterized by examining the hysteresis between the electric polarization and the drive field with a Sawyer-Tower circuit. The d_{33} value of the ceramic ring was measured by an acoustic method with a Piezo d_{33} Meter. The pseudo-static displacement of the samples was measured using a linear variable differential transformer (LVDT). The displacement in a frequency range of 0.1 Hz–200 kHz, including the displacement at the resonance frequency of the Langevin vibrator, was measured with an MTI Fotonics Sensor (MTI2000) with the sample clamped at the center of its length. The measured displacement from the Fotonics Sensor was doubled to represent the total displacement in the longitudinal direction. The vibration velocity was calculated based on the displacement of one terminal surface versus the clamping point (i.e., half of the total displacement) to represent the actual velocity of one of the terminals of the actuator. To examine the temperature rise of the samples at a high power driving condition, a thermocouple with a diameter of $25\ \mu\text{m}$ was fixed with an adhesive agent at the center of the lateral surface.

III. RESULTS AND DISCUSSION

A. Dielectric Properties

A single piezoelectric ceramic ring showed a dielectric constant, $\epsilon_{33}^T/\epsilon_0$, of about 1300 and a dielectric loss of 0.35% at 1 kHz under low field conditions. This compares well to the specified values of 1380 and 0.35%, respectively, indicating the sample was well sintered. Low dielectric loss was preferred because loss is a major source of heat generation. The dielectric loss of the laminated multilayer sample under low field conditions, measured with the impedance analyzer at 1 kHz, which was far below the resonance frequency, varied from 0.4 to 0.5%, depending upon the samples.

The hysteresis of polarization as a function of alternating electric field at 10 Hz for a 9-layer sample is given in Fig. 3. The loop area was calculated to be $0.34\ \mu\text{J}/\text{mm}^3$, which stands for the dielectric loss per AC drive cycle under a voltage of 220 V peak-to-peak.

B. Impedance Spectra and Q_m

Fig. 4 shows the impedance spectra of a single ring and a multilayer 3 mm piezoelectric actuator. The first impedance peak at 547 kHz for the single ring was attributed to the first radial resonance mode and the peak near 4.75 MHz attributed to the thickness mode. After the lamination and assembly for a 9-layer sample with two copper caps, the thickness-mode resonance peak of the single ring disappeared, and a new resonance peak appeared

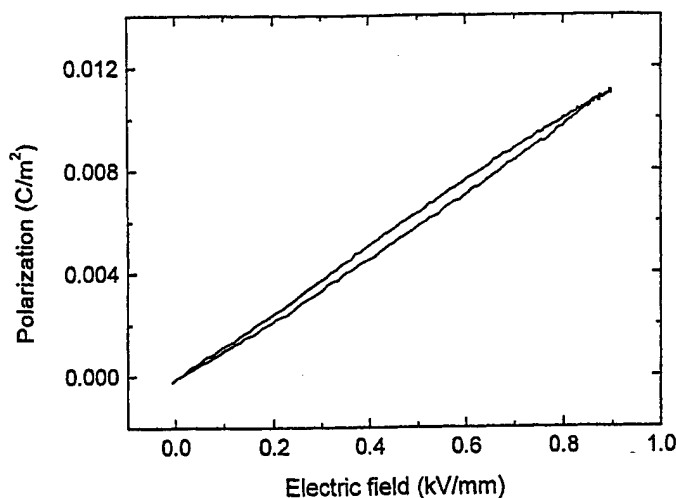


Fig. 3. P-E hysteresis loop for a 9-layer hollow actuator sample.

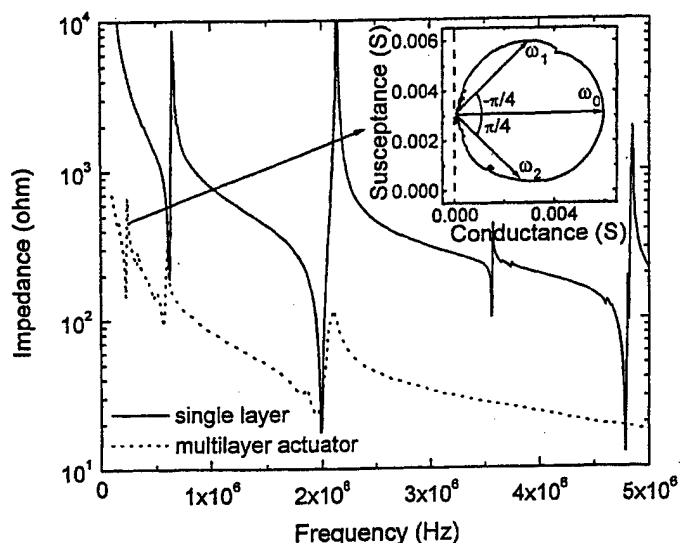


Fig. 4. Impedance spectra of a single ceramic ring and a 9-layer actuator. The admittance circle near the thickness-mode resonance and antiresonance frequencies of the 9-layer actuator is presented.

near 223 kHz. This was interpreted as the longitudinal resonance of the laminated body. The first radial mode resonance peak shifted slightly to 565 kHz in the multilayer sample.

To characterize the apparent mechanical quality factor, Q_m , the admittance circles near the resonance-antiresonance peaks were measured. Q_m was then determined by:

$$Q_m^{-1} = (\omega_2 - \omega_1)/\omega_0 \quad (1)$$

where ω_0 is the resonance angular frequency and ω_1 and ω_2 are the first and second quadrantal angular frequencies, respectively [34]. For the 9-layer actuator samples, the admittance circle near the thickness-mode resonance and antiresonance frequencies was not ideal, and some spurious signals were revealed. A typical admittance circle is presented in Fig. 4 with ω_0 , ω_1 , and ω_2 designated. The

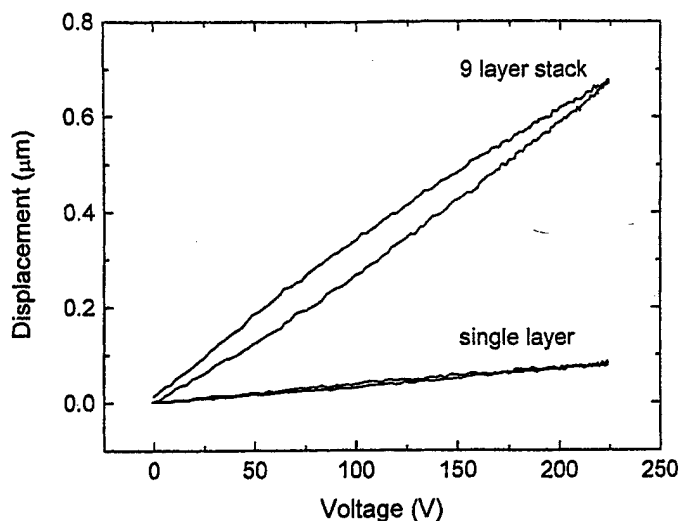


Fig. 5. Displacement of a single ceramic ring and a 9-layer actuator sample under a sine wave drive voltage of 220 V peak-to-peak at 0.2 Hz.

measured Q_m 's for the single ring were 280 and 240 for the radial mode and thickness mode resonance, respectively. Q_m 's for the 9-layer actuator sample were 45 and 35, respectively. Thus, the Q_m of the ceramic ring measured by the admittance circle method was significantly lower than the specified Q_m value of the materials and was further decreased for the multilayer stacks. The small size and annular shape of the composite structure, along with the epoxy in the actuator, led to complicated clamping effects, complicated boundary and interface conditions, and multi-mode coupling effects. Consequently, lower Q_m values were measured. As Q_m further decreases under high-power conditions [35]–[37], the apparent Q_m of the actuator measured by the admittance circle method at low-drive voltages could not be used to analyze the performance under high-power conditions.

C. Displacement

The measured d_{33} value of the ceramic ring was about 300×10^{-12} C/N, which was close to the specified data of 323×10^{-12} C/N. Fig. 5 shows the pseudo-static displacement of a single ceramic ring and a 9-layer stacked actuator under a peak-to-peak drive voltage of 220 V at a frequency of 0.2 Hz. A displacement of $0.67 \mu\text{m}$ was produced with a hysteresis of 10.2% under the applied voltage in the 9-layer sample, which was approximately 9 times that of the single ring. The hysteresis, 10.2%, was larger than the hysteresis of the single ring, 6.6%. The frequency dependence of the displacement from 0.1 Hz to 100 kHz of the 9-layer actuator showed that the displacement decreased slightly with increasing frequency. Fig. 6 gives the dynamic displacement response when the sample was driven under 220 V peak-to-peak at 100 kHz, well below the resonance frequency. The displacement was $0.55 \mu\text{m}$.

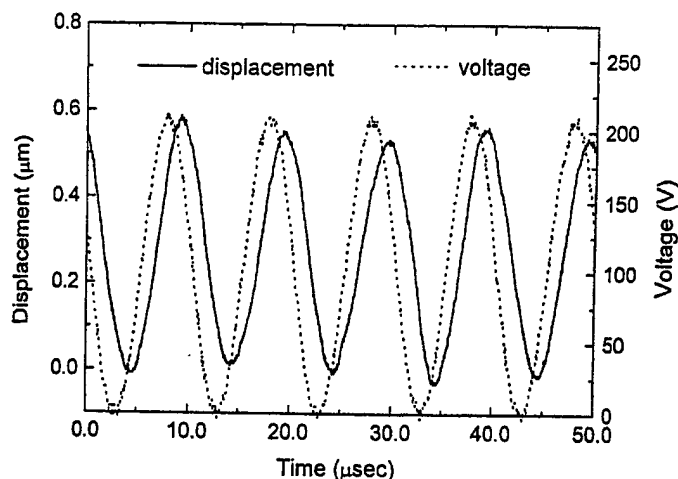


Fig. 6. Dynamic displacement response of a 9-layer actuator sample under a sine wave driving voltage of 220 V peak-to-peak at 100 kHz.

D. Vibration Velocity and Temperature Rise

The temperature rise of a 9-layer stacked actuator due to heat generation driven off-resonance at 100 kHz with different voltages is shown in Fig. 7. The temperature rise was significant when the drive voltage exceeded 200 V at 100 kHz. A temperature rise of more than 50°C was observed when it was driven at 220 V. The corresponding maximum vibration velocity of one terminal of the sample defined by (2):

$$v_{\max} = 2\pi f \times \delta/2 \quad (2)$$

was about 0.17 m/sec, where f and δ are the drive frequency and total displacement between the two terminals of the sample, respectively. The maximum sample temperature under a drive voltage of 220 V was close to 80°C. This was the highest temperature observed that was not accompanied by a significant degradation in the performance of the sample. Thus in the present investigation, the resulting temperature rise was the most immediate limitation on the maximum accessible vibration velocity for the stacked actuators. The vibration velocity corresponding to the temperature rise of 20°C, which is sometimes defined as the maximum vibration velocity for a device, was about 0.15 m/sec.

A theoretical analysis carried out by the authors indicates that, if the conduction heat transfer rate through the lead wires of an actuator is negligible compared to the rate of heat flow by radiation and convection, the temperature rise of the actuator $T - T_0$ can be approximately expressed as [28]:

$$T - T_0 = \delta T(1 - e^{-\frac{t}{\tau}}). \quad (3)$$

The ratio of the total temperature rise at the final thermal balance condition, δT , to the time constant, τ , is equivalent to the initial rate of temperature rise and is expressed as:

$$\frac{\delta T}{\tau} = \frac{ufv_e}{\rho cv} \quad (4)$$

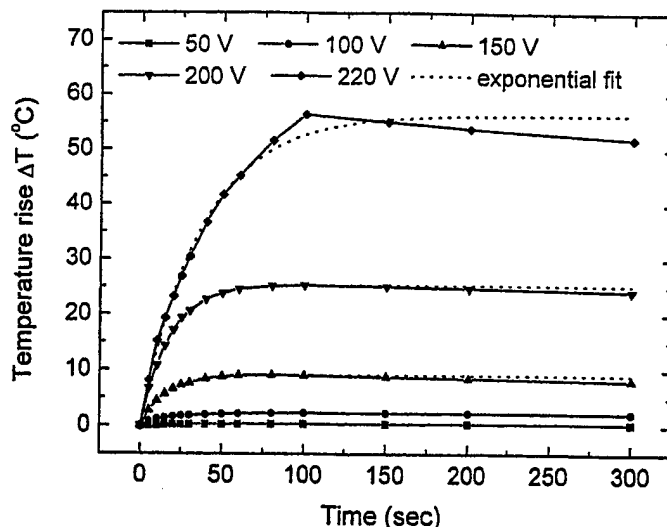


Fig. 7. Temperature rise of a hollow 9-layer actuator sample due to heat generation when driven under various peak-to-peak sine wave voltages at 100 kHz.

where u is the loss of the sample per driving cycle per unit volume; v is the total volume of the sample; v_e is the piezoelectric active volume; and ρ , c , and f are the density, specific heat, and driving frequency, respectively.

Exponential curves calculated according to (3) also are plotted in Fig. 7 with the dotted lines, which match the experimental data well. However, all the experimental curves in Fig. 7 showed that the temperature dropped slightly after it rapidly rose to a maximum value. This may be attributed to the heat sink of the metal end caps and the outward extended internal electrode shims. The heat sink effect became stronger at higher temperatures, resulting in larger deviations of the experimental data from the exponential curves.

According to (4), u was calculated as $0.08 \mu\text{J}/\text{mm}^3$ under 220 V based on the values of τ and δT derived from the exponential fit results. This was only about 1/4 of the P-E loss per drive cycle at 10 Hz, which we measured in Section A. The main reason for this difference could be the smaller P-E loss at 100 kHz at an elevated temperature than that at 10 Hz at room temperature. The dielectric measurements at a low electric field showed that the dielectric loss of the sample at 100 kHz was only about 30% of that at 10 Hz at room temperature. The dielectric loss at 100 kHz at a temperature of 75°C was about 88% of that at room temperature. Additionally, the heat sink effects of the end-caps and the outward extended internal electrode shims enhanced the heat dissipation, leading to a lower temperature rise than that expected from theoretical analysis. If a similar frequency and temperature dependence of the dielectric loss under 220 V are assumed, the above thermal analysis appears to be reasonable. This may also indicate that the dielectric loss was the main contribution to the total loss and heat generation when the actuators were driven off resonance.

Although a high apparent Q_m value was not achieved in the tiny, hollow stacked-actuator sample comprised of

hard PZT ceramic and copper layers bonded by epoxy, the observed temperature rise seemed to be much smaller than that in soft PZT ceramics [28]. The reason was believed to be that the low dielectric loss in the hard ceramic played a more essential role to suppress heat generation than the mechanical loss when the samples were driven under non-resonance conditions. (Note that the Q_m is derived under the resonance condition, and the mechanical loss plays a dominant role on the Q_m value when the dielectric loss is relatively low). In addition, the small size, hollow structure, metal end caps and outward extended internal electrode were preferred features to enhance heat dissipation. The Q_m value was not very adequate for a reasonable judgement of the actual thermal effect of the actuator. Directly monitoring the temperature rise of the actuator was a more reliable method to finally determine the limitation of the highest driving power.

The organic epoxy in the stack structure was not favorable due to its low thermal conductivity, low Q_m value, and low maximum operating temperature. Tape-casting and co-firing multilayer actuators avoid these unfavorable features brought about by the organic binder. However, more efforts must be made to minimize the problems of delamination and crack formation occurring in the co-fired multilayer actuators in order to achieve the desired long-term reliability under high-power driving conditions [38].

E. Application for Langevin Vibrators

The longitudinal displacement of the 3 mm Langevin vibrators activated by 10-layer and 2-layer PZT stacks in the frequency range of 0.1 Hz to 200 kHz under 100 V is shown in Fig. 8. The total length for both of the two Langevin vibrators was 23 mm. Two major displacement resonance peaks were observed for each Langevin vibrator. The vibration magnitudes of the Langevin vibrator with a 10-layer stack were 2.6 and 1.2 μm at the first and second resonance frequencies, respectively, compared to only 0.4 and 0.34 μm for the vibrator with a 2-layer stack. The maximum vibration velocity was 0.62 m/sec at the second resonance frequency for the Langevin vibrator activated by the 10-layer stack under 100 V, whereas it was about 0.18 m/sec for that activated by the 2-layer stack. The vibration velocity 0.62 m/sec of the Langevin vibrator activated by the 10-layer stack was about 11 times that of the 10-layer stack under the same drive voltage and frequency. The actual displacement responses of the two Langevin vibrators at their respective second resonance frequency also are presented in Fig. 8. These results confirmed that much larger displacements and vibration velocities could be achieved even at the resonance frequency if the number of the piezoelectric ceramic layers for the Langevin vibrator was increased.

F. Discussion

The performance of the developed multilayer actuator showed that it could be used for high-power condi-

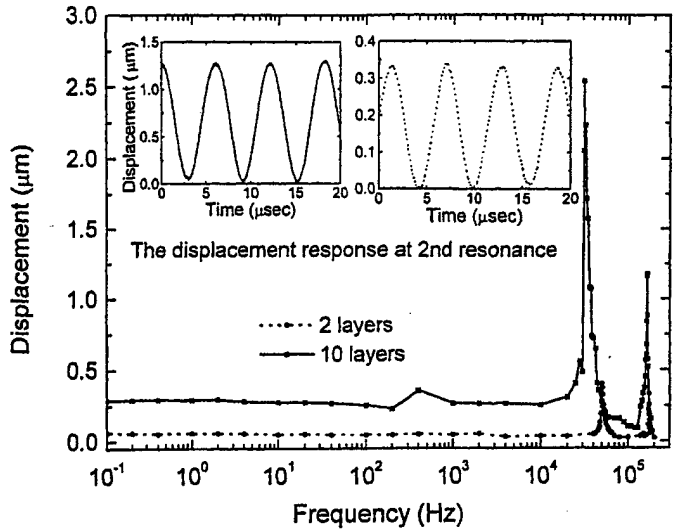


Fig. 8. Frequency dependence of the longitudinal displacement of the two Langevin vibrators, one with a 10-layer and the other with a 2-layer stacked actuator. Both are 3 mm in diameter and driven by a sine wave voltage of 100 V peak-to-peak. The dynamic displacement response curves at their respective second resonance conditions of the two vibrators are also shown.

tions even under nonresonance conditions. A maximum vibration velocity of 0.17 m/sec under a stress-free condition was realized with a 9-layer stacked actuator sample under 220 V at 100 kHz, which was below the resonance frequency. Generally, high power operation of the piezoelectric actuators is conducted at the resonance frequency to reduce the drive voltage. However, the resonance only occurs in a very narrow frequency range, particularly for high Q_m materials, and the resonance frequency strongly depends on the drive voltage, vibration velocity [35], load, and temperature. Such high-power devices cannot work stably without accessory feedback systems to control their driving frequencies. Using the multilayer actuators provides an alternative way to reduce the input impedance and drive voltage in high-power devices off-resonance, leading to large vibration magnitude as well as high stability.

Typically, a Langevin vibrator is activated with a 2- or 4-layer piezoelectric stack [30]–[32]. The application of the 10-layer stacked actuator for the Langevin vibrator in the present work was to examine the effect of the number of the stack layers on the vibration level under resonance conditions. The above-stated significant enhancement of the vibration magnitude and velocity by increasing the number of the piezoelectric stack layers confirmed the advantage of the multilayer stack for high-power applications under resonance conditions. With multilayer Langevin vibrators formed with more active layers, much larger vibration amplitudes were achieved.

IV. SUMMARY

Compact multilayer actuators as small as 3 mm in diameter and characterized by a hollow structure were fabricated by a stacking method using hard PZT ceramic. Several 3 mm Langevin vibrators also were constructed with the developed multilayer actuators. The low dielectric loss of the hard PZT ceramic, the hollow structure, and the metal end caps and outward extended internal electrodes were favorable for suppressing the temperature rise accompanying high-level vibrations. A maximum vibration velocity of 0.17 m/sec was achieved under nonresonance conditions at each terminal of the 9-layer actuator. The vibration velocity was greatly improved with the Langevin vibrator driven at the resonance frequency. By increasing the number of stacked layers, the vibration level at the resonance of the Langevin vibrator with a constant total length was significantly enhanced. The capability and advantage of the multilayer actuators for high-power piezoelectric applications were demonstrated at both nonresonance and resonance conditions by our experimental results. Heat generation under high-power drive was the immediate limitation on the maximum accessible vibration velocity for the stacked actuators.

ACKNOWLEDGMENT

The authors gratefully acknowledge discussions with Mr. Hideaki Aburatani, Ms. Yun-Han Chen, and Ms. Jiehui Zheng at the International Center for Actuators and Transducers, The Pennsylvania State University.

REFERENCES

- [1] K. Uchino, *Piezoelectric Actuators/Ultrasonic Motors*, Boston: Kluwer, 1996.
- [2] E. G. Thurston, "The theoretical sensitivity of three types of rectangular bimorph transducers," *J. Acoust. Soc. Amer.*, vol. 25, pp. 870-872, 1953.
- [3] J. G. Smits, S. I. Dalke, and T. K. Cooney, "The constituent equations of piezoelectric bimorph," *Sens. Actuators A*, vol. 28, pp. 41-61, 1991.
- [4] Y. Sugawara, K. Onitsuka, S. Yoshikawa, Q. Xu, R. E. Newnham, and K. Uchino, "Metal-ceramic composite actuators," *J. Amer. Ceram. Soc.*, vol. 75, pp. 996-998, 1992.
- [5] A. Dogan, K. Uchino, and R. E. Newnham, "Composite piezoelectric transducer with truncated conical endcaps cymbal," *IEEE Trans. Ultrason., Ferroelect., Freq. Contr.*, vol. 44, pp. 597-605, 1997.
- [6] S. Takahashi, "Longitudinal mode multilayer piezoelectric actuators," *Ceram. Bull.*, vol. 65, pp. 1156-1157, 1986.
- [7] K. Yao, W. Zhu, K. Uchino, Z. Zhang, and L. C. Lim, "Design and fabrication of a high performance multilayer piezoelectric actuator with bending deformation," *IEEE Trans. Ultrason., Ferroelect., Freq. Contr.*, vol. 46, pp. 1020-1027, 1999.
- [8] M. J. Smeeth and J. F. James, "An electrically controlled Fabry-Perot spectrometer," *J. Phys. E: Sci. Instrum.*, vol. 4, pp. 429-434, 1971.
- [9] R. W. Basedow and T. D. Cocks, "Piezoelectric ceramic displacement at low frequencies and their consequences in Fabry-Perot interferometry," *J. Phys. E: Sci. Instrum.*, vol. 13, pp. 840-844, 1980.
- [10] R. E. Aldrich, "Requirements for piezoelectric materials for deformable mirrors," *Ferroelectrics*, vol. 27, pp. 19-25, 1980.
- [11] M. A. Ealey and J. F. Washeba, "Continuous facesheet low voltage deformable mirrors," *Opt. Eng.*, vol. 29, pp. 1191-1198, 1990.
- [12] D. R. Browning and W. D. Wynn, "Vibration damping system using active negative capacitance shunt circuit with piezoelectric reaction mass actuator," U.S. Patent 5558477, 1996.
- [13] T. Shimizu, K. Tujimura, and M. Iwamoto, "Fluid control device," U.S. Patent 4695034, 1987.
- [14] T. Kitahara, "Ink jet head with multilayer piezoelectric actuator," in *Proc. IS&T's 11th Int. Congr. on Advances in Non-Impact Printing Technol.*, 1995, pp. 346-349.
- [15] T. Yano and S. Takahashi, "Utilization of piezoelectric stiffened effects on impact printer heads," *Electron. Commun. Jpn, Part 2: Electronics*, vol. 72, pp. 19-32, 1989.
- [16] K. Uchino, K. Kato, and M. Tohda, "Ultrasonic linear motors using a multilayered piezoelectric actuator," *Ferroelectrics*, vol. 87, pp. 331-334, 1988.
- [17] H. Saigoh, M. Kawasaki, N. Maruko, and K. Kanayama, "Multilayer piezoelectric motor using the first longitudinal and the second bending vibrations," *Jpn. J. Appl. Phys.*, vol. 34, pp. 2760-2764, 1995.
- [18] T. Funakubo, T. Tsubata, Y. Taniguchi, K. Kumei, T. Fujimura, and C. Abe, "Ultrasonic linear motor using multilayer piezoelectric actuators," *Jpn. J. Appl. Phys.*, vol. 34, pp. 2756-2759, 1995.
- [19] J. W. C. de Vries, P. Jedeloo, and R. Porath, "Co-fired piezoelectric multilayer transformers," in *Proc. 10th IEEE International Symp. Appl. Ferroelect., ISAF'96*, 1996, vol. I, pp. 173-176.
- [20] T. Inoue, M. Yamamoto, S. Kawashima, and S. Hirose, "Third order longitudinal mode piezoelectric ceramic transformer for high voltage power inverter," *IEICE Trans. on Electron.*, vol. E81-C, pp. 1128-1135, 1998.
- [21] K. Uchino, "Materials issues in design and performance of piezoelectric actuators: An overview," *Acta Mater.*, vol. 46, pp. 3745-3753, 1998.
- [22] X. Wang, C. Ehlers, and M. Neitzel, "Electro-mechanical dynamic analysis of the piezoelectric stack," *Smart Mater. Struct.*, vol. 5, pp. 492-500, 1996.
- [23] R. A. Lomenzo, H. Sumali, and H. H. Cudney, "Maximizing mechanical power transfer from piezoelectric stacked actuators to structures," *Adapt. Struct. Mater. Syst., ASME'93*, 1993, vol. 35, pp. 229-235.
- [24] E. Flint, C. Liang, and C. A. Rogers, "Electromechanical analysis of piezoelectric stack active member power consumption," *J. Intell. Mater. Syst. Struct.*, vol. 6, pp. 117-124, 1995.
- [25] D. Ye and J. Q. Sun, "Dynamic analysis of piezoelectric stack actuators including thermal and pyroelectric effects," in *Proc. of SPIE, Smart Structures and Materials: Mathematics and Control in Smart Structures*, 1997, vol. 3039, pp. 619-629.
- [26] E. Wehrsdorfer, G. Borchhardt, and W. Karthe, "Large signal measurements on piezoelectric stacks," *Ferroelectrics*, vol. 174, pp. 259-275, 1995.
- [27] A. Wolff, D. Cramer, H. Hellebrand, C. Schuh, T. Steinkopff, and K. Lubitz, "Energy considerations of PZT multilayer actuators under dynamic driving conditions," in *Proc. of the 10th IEEE International Symp. Appl. Ferroelec., ISAF'96*, 1996, vol. I, pp. 317-320.
- [28] J. Zheng, S. Takahashi, S. Yoshikawa, K. Uchino, and J. W. C. de Vries, "Heat generation in multilayer piezoelectric actuators," *J. Amer. Ceram. Soc.*, vol. 79, pp. 3193-3198, 1996.
- [29] T. Sakai and H. Kawamoto, "Durability properties of piezoelectric stack actuator," *Jpn. J. Appl. Phys.*, vol. 37, pp. 5338-5341, 1998.
- [30] J. Van Randerat and R. E. Settrington, *Piezoelectric Ceramics*, Eindhoven, The Netherlands: Philips' Gloeilampenfabrieken, 1974, ch. 8, pp. 123-145.
- [31] Y. Koike, M. Kihara, J. Satonobu, K. Nakamura, and S. Ueha, "A peripherally bolted torsional Langevin vibrator with large diameter," *J. Acoust. Soc. Jpn. (E)*, vol. 18, pp. 239-246, 1997.
- [32] S. Chen and J. H. Jeng, "The characteristics of a high power ultrasonic transducer determined by the experimental technique," in *Proc. Ultrason. International Conf*, London: Butterworth-Heinemann, 1993, pp. 193-196.
- [33] T. Sashida and T. Kenjo, *An Introduction to Ultrasonic Motors*. Oxford: Clarendon, 1993, pp. 62-63.

[34] T. Ikeda, *Fundamentals of Piezoelectricity*. Oxford: Oxford Sci. Pub., 1990, pp. 138-142.

[35] S. Takahashi, S. Hirose, and K. Uchino, "Stability of PZT piezoelectric ceramics under vibration level change," *J. Amer. Ceram. Soc.*, vol. 77, pp. 2429-2432, 1994.

[36] S. Tashiro, M. Ikehiro, and H. Igarashi, "Influence of temperature rise and vibration level on electromechanical properties of high-power piezoelectric ceramics," *Jpn. J. Appl. Phys.*, vol. 36, pp. 3004-3009, 1997.

[37] S. Takahashi, Y. Sasaki, S. Hirose, and K. Uchino, "Stability of $\text{PbZrO}_3\text{-PbTiO}_3\text{-Pb}(\text{Mn}_{1/3}\text{Sb}_{2/3})\text{O}_3$ piezoelectric ceramics under vibration-level change," *Jpn. J. Appl. Phys.*, vol. 34, pp. 5328-5331, 1995.

[38] A. Furuta and K. Uchino, "Dynamic observation of crack propagation in piezoelectric multilayer actuators," *J. Amer. Ceram. Soc.*, vol. 76, pp. 1615-1617, 1993.



Kui Yao (M'99) was born in China on October 14, 1967. He received the B.S. degree in E.E. and the Ph.D in electronics materials and devices, both from Xi'an Jiaotong University, China, in 1989 and 1995, respectively, and the M.S. degree in technical physics from Xidian University, China, in 1992.

He is a research fellow of the Institute of Materials Research and Engineering (IMRE), Singapore. From 1998-1999, he worked as an adjunct research associate in the Materials Research Laboratory, The Pennsylvania State

University, PA.

His research interests are in functional materials and devices, sensors, and actuators.



Kenji Uchino (M'89) was born on April 3, 1950, in Tokyo, Japan. He received the B.S. degree in physics in 1973, the M.S. and Ph.D. degrees in physical electronics in 1975 and 1981, respectively, from Tokyo Institute of Technology, Tokyo, Japan.

He is presently director of the International Center for Actuators and Transducers and a professor of electrical engineering at the Pennsylvania State University, University Park, PA, and vice-president of NF Electronic Instruments, Inc., State College, PA. Previously, he was a faculty member at Tokyo Institute of Technology and Sophia University, Tokyo, Japan.

His research interests are in dielectrics, ferroelectrics, and piezoelectrics, including basic research on materials, device design, and fabrication processes, as well as applicational development of solid state actuators to precision positioners, ultrasonic motors, etc.



Yuan Xu got his Ph.D. degree from the University of Manchester, Institute of Science and Technology, UK. Afterward he worked in Beijing University of Science and Technology, Beijing, China; Ames National Laboratory; The Pennsylvania State University, in the fields of materials science and engineering.

Dr. Xu is now a senior research fellow and project manager of the Singapore Institute of Materials Research and Engineering, working in the field of MEMS.



Shuxiang Dong was born in Hubei, China, in 1957. He received the B.S. degree in semiconductor physics from Wuhan University, Wuhan, China, in 1982, and the M.S. and Ph.D. degrees in acoustical physics and piezoelectric ceramic materials and devices from Tsinghua University, Beijing, China, in 1989 and 1993, respectively.

He worked as a lecturer, associate professor at State Key Laboratory of New Ceramics and Fine Processing, Department of Materials Science and Engineering in Tsinghua University from 1993 to 1997. He is currently a research associate in the Institute of Materials Research and Engineering in Singapore.

His research interests include piezoelectric ultrasonic motors, micromotors, sensors, and actuators.



Leong Chew Lim obtained his B.Sc., M.Sc. (with distinction), and Ph.D. degrees from the Nanyang University (Singapore), the University of Leeds (U.K.), and Cornell University (U.S.A.), in 1976, 1978, and 1985, respectively.

He is currently an associate professor in the Department of Mechanical and Production Engineering, National University of Singapore (NUS). Previously, he was the programme director of the Advanced Engineering Materials Programme of the Institute of Materials Research and Engineering from 1997-1999. His areas of research cover novel processing of functional ceramics, optical crystal growth, grain boundary phenomena in materials, and weld and braze repair of aeroengine materials and components.

APPENDIX 62



A Stackable Bonding-Free Flextensional Piezoelectric Actuator

RUIBIN LIU & L.E. CROSS

187 Materials Research Laboratory, The Pennsylvania State University, University Park, PA 16802, USA

GARETH KNOWLES & BRUCE BOWER

Qor TeK, Inc., 4121 Jacks Hollow Road, Williamsport, PA 17701, USA

BROOKS CHILDERS

MS 231 NDE Branch, NASA Langley Research Center Hampton, VA 23665, USA

Submitted March 25, 1999; Revised July 13, 1999; Accepted July 28, 1999

Abstract. A flextensional actuator was designed using commercial multilayer stacked actuator so as to produce large displacements at intermediate force levels. The simple design chosen eliminated the need for bonding the actuators into the frame and permitted easy series connection of multiple units. To satisfy the need for a fiber grating tuning device to interrogate an array of Bragg grating fiber optic stress sensors, a tuning device using four series connected units was constructed. The unit performs well, but the actual measured amplification is less than theoretical expectation. The problem was traced to unwanted flexing of the simple original frame and a hinged more robust flexing beam construction was shown to eliminate the problem.

Keywords: piezoelectric actuator, flextensional amplifier, optical fiber grating system

1. Introduction

The use of precisely tuned fiber optic grating system to permit the monitoring of local strain at a number of locations along a long glass fiber stress sensor has important applications in specialized space structure. To interrogate such gratings sequentially, it is desirable to have an agile sensor which can be tuned over a range of optical frequencies. Such an agile filter can be envisaged using a fiber optic grating system whose period is varied by mechanically stretching the fiber. For this type of application, typical requirements are a gauge length of 45 mm with a tuning range of $\pm 100 \mu\text{m}$ which for a conventional fiber would require a generative force at order 10 N. Clearly, the strain required $\pm 0.22\%$ is beyond the range of a simple piezoelectric material driven through d_{31} or d_{33} [1] and some amplification is necessary if a piezoelectric device is to be used [2]. In this realization, a simple flextensional device is demonstrated in a design that can use commercial multilayer co-fired

stacked actuators and eliminates the need for glue bonds. The design also permits easy series connection of the flextensionals and four such series connected device (named Dual Opposing Actuator, U.S. patent applied for) are shown to satisfy the current tuning need.

2. Experimental Procedure

The single-cell flextensional actuator is shown in Fig. 1. The metal frame is made by EDM (Electric Discharge Machining) from a whole piece of brass for both single cell and array. The piezoelectric multilayer actuator used is a commercial Tokin actuator, the dimension of the single cell is $5 \times 5 \times 18 \text{ mm}$, with the displacement capability of $15 \mu\text{m}/100 \text{ V}$ and blocking force of $87 \text{ kg}/100 \text{ V}$. Two single actuators were bonded to a steel substrate by J.B. Weld epoxy. Both metal frame and the steel substrate base have a hole at the center position in order to let the fiber pass

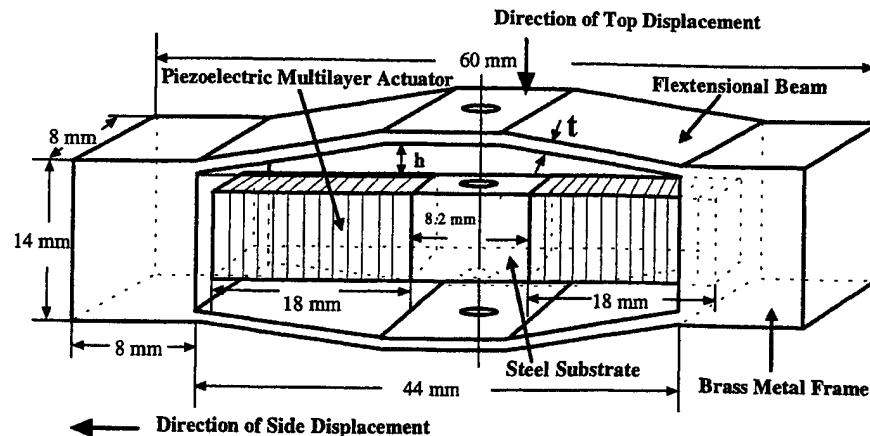


Fig. 1. Configuration of bonding-free flextensional piezoelectric actuator with rectangular shape.

through. The total length of the actuator plus substrate is 0.2 mm longer than the inside wall distance of the metal frame, so the actuator can be loaded into the metal frame by deforming the frame and is fixed in position by the resulting prestress. The stretching function can be realized by arrangement of single-cell actuators in an array. The configuration view of such an array is shown in Fig. 2. The displacement and the generative force for single-cell actuator are measured by a Fontonic sensor MTI 2000 (MTI Instrument) and a load cell ELF-TC (Entran, Inc.). The schematic view of experimental set-up for displacement and generative-force measurement is shown in Fig. 3. Brass is used as the metal frame material. The amplification factor of the frame will be determined by the height h (Fig. 1) if the length of the actuator is fixed. The height is set as 3.6 mm for current metal frame. Therefore, the theoretical amplification factor should be 5 for each side. The rigidity and the capability to generate force for the frame are strongly dependent on the stiffness of the flextensional beam in the frame.

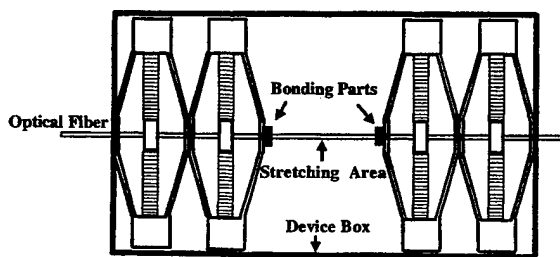


Fig. 2. Schematic view of array system for optical fiber stretching.

3. Experimental Results and Discussions

3.1. Simple Metal Frame

The metal frame with a flat-flextensional-beam with a thickness of 1 mm was first studied. The single cell actuator was characterized first under unloaded dc conditions. The side displacement of the metal frame and the axial displacement of the flextensional beam were measured at different driving voltage levels. The results are listed in Table 1, from which we can calculate the amplification factor of the metal frame. The displacement and the amplification factor listed in Table 1 are the sum for the two actuators and the two sides of the metal frame. There is a difference between the designed and measured amplification factor for this simple-metal-frame. The reason for this difference will be discussed later.

The loaded capability of the single cell actuator is usually represented by the term blocking force. The blocking force is defined as the external force needed to completely restrain to zero displacement the actuator at some driving voltage. The blocking force of the actuator was derived in the following procedure. The load cell was mounted on a movable station, which provides the possibility to apply an external force to pull back the actuator in a direction opposite to the one driven by the applied electric field. Theoretically speaking, we could read the blocking force directly by pulling the actuator to its original position. This concept leads to the present approach to measure the blocking force. We can drive the actuator to the unloaded displacement state at some set

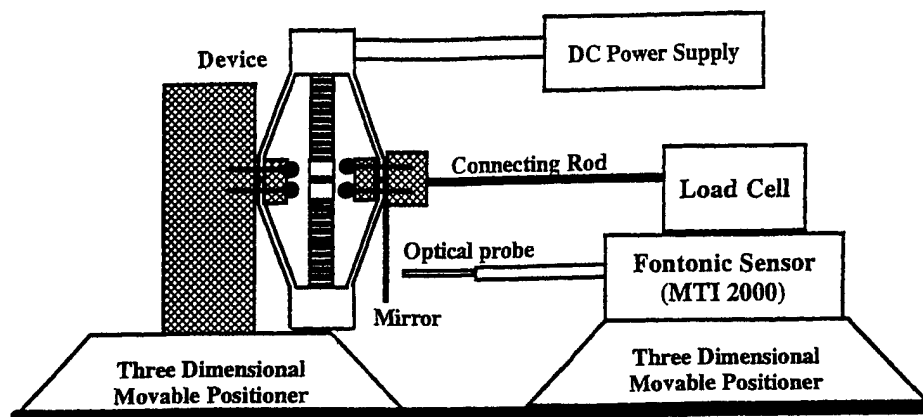


Fig. 3. Experimental set-up for measurement of displacement and generative force.

voltage, pull the actuator back to its original position. For every displaced position, the required pulling force is measured establishing the load line for the actuator. In order to avoid the nonlinear response and possible breakage of the actuator, the external pulling force is restricted to below 12 N. By curve fitting from linear line based on the measured points, as shown in Fig. 4. We can simply extrapolate the curve to the pulling force axis where the displacement is zero. The corresponding pulling force is also equivalent to the blocking force. The blocking force measured by this method for the single-cell actuator driven at 50 V voltage is 15.1 N.

The experimental results show that the generative force from the simple metal frame can satisfy the requirement. Unfortunately, the single cell actuator can not provide enough displacement for the optical fiber stretching. Thus, a four-cell array was fabricated in order to achieve the required displacement. The picture of the prototype device is shown in Fig. 5. A special designed energy recovery circuit for piezoelectric device was developed to operate it at very low-power consumption (2 W) [3]. It was shown that the design has excellent performance in stretching a erbium doped Bragg grating fiber and the detail will be discussed in a later paper.

3.2. Hinged Metal Frame

From actual measurement, it was found that the amplification factor of simple-metal-frame is approximately only half of the value designed (as shown in Table 1). The most probable reason is that the rigidity of the simple flat-flextensional-beam is not enough to transfer the displacement without deformation. That is the flextensional beam deforms before transferring the motion. A simple analysis shows that the rigidity of the flextensional beam is proportional to the thickness of the beam if the width of the beam is constant. However, it is required that the metal frame should be too rigid to limit the flextensional function of the structure. Flexure hinges are usually used to connect the flextensional beam with a combination of stiffness and appropriate elastic compliance [4]. In the present study, the flat-flextensional-beam of the simple metal-frame was modified to the hinged-metal-frame. For the hinged frame, the thickness of the flextensional beam was increased from 1 mm to 3 mm in order to increase the rigidity of the metal frame. Flexure hinges were introduced to each beam in order to increase the flextensional function of the frame. The thinnest part of the hinge was 1 mm. A schematic diagram of hinged-metal-frame is shown in Fig. 6.

Table 1. The unloaded and dc properties of the simple-metal-frame

Driving voltage (V)	Side displacement μm	Top displacement μm	Amplification factor	Unloaded actuator displacement μm
40	9.21	51.42	5.58	12
50	11.56	64.19	5.61	15

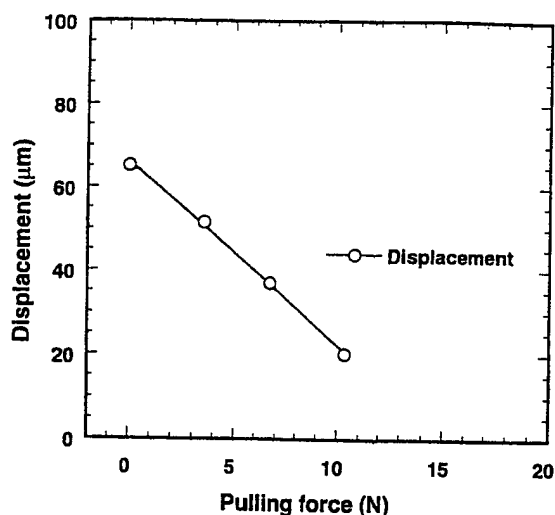


Fig. 4. Capability of displacement as a function of opposite pulling force.

Fig. 6. The other dimensions are identical to the simple-metal-frame. The same actuator was used to drive the hinged-metal-frame. Firstly, the unloaded and dc properties of hinged-metal-frame were characterized at different driving voltages. The results are listed in Table 2.

As previously, the actuator was fixed inside the metal frame by a prestress from the metal frame. The side displacements of the Table 1 and 2 are actually

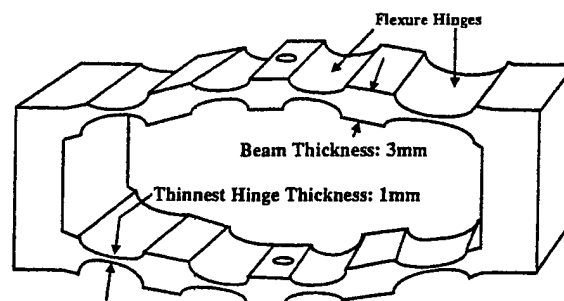


Fig. 6. Schematic diagram of hinged-metal-frame.

the sum of the clamped displacement of the actuator. The clamped displacements are controlled by the rigidity of the metal frame. In the simple-metal-frame, the clamped displacement of the actuator is 76% of the unloaded condition. However, the clamped displacement of the hinged-metal-frame is only 30% of the unloaded condition. Therefore, there is a dramatically enhancement in the rigidity of the metal frame by increasing the thickness of the beam from 1 mm to 3 mm.

The amplification factor of the hinged-metal-frame, however, reaches to 9.5, which is very close to the designed value. That means the rigidity of the structure is a critical point to acquire the designed amplification ability. However, the increasing of the rigidity of the metal frame will increase the clamping

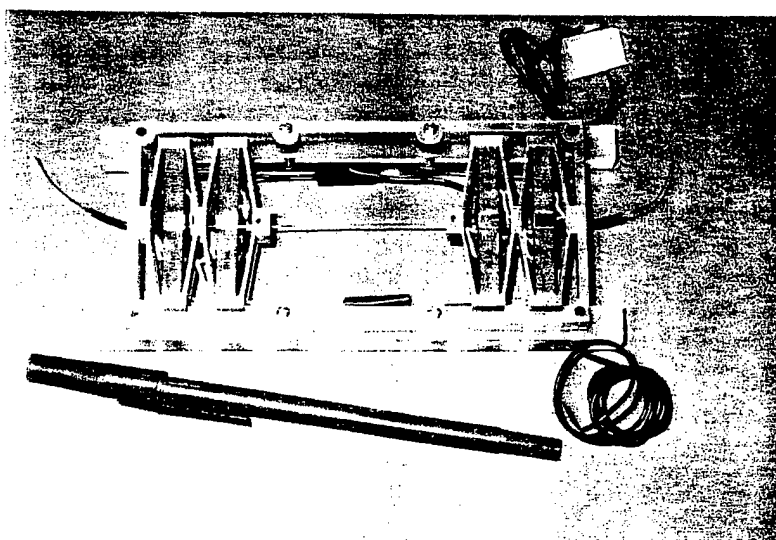


Fig. 5. Picture of the four-cell array prototype device.

Table 2. The unloaded and dc properties of the hinged-metal-frame

Driving voltage (V)	Side displacement μm	Top displacement μm	Amplification factor	Unloaded actuator displacement μm
40	3.58	34.18	9.55	12
50	4.96	46.81	9.43	15

effect on the actuator. In the current case, the final top displacement of the hinged-metal-frame is lower as compared to the simple-metal-frame driven at the same voltage. Therefore, the current hinged-metal-frame is just an example to demonstrate the effect of introducing the flexure hinges to the flextensional beam and is far from the idea design. For certain

displacement and ideal generative force combinations, there will be an optimum dimension of the hinged-metal-frame. Finite element analysis will be employed to generate accurate models of the hinged-metal-frame designs in the future work.

The loaded properties as a function of driving voltage of both simple-metal-frame and hinged-metal-frame were measured, as shown in Fig. 7. The derived blocking forces as a function of driving voltages are shown in Fig. 8. The blocking forces show very good linear relationship with the driving voltage.

Acknowledgment

This work was supported in part by NASA under contract NAS1-97147 and NAS8-98109. The authors would like to thank Dr. Richard Barday of NASA GSFC, Electromechanical Branch and Dr. Weicheng Chen of Center for the Acoustics and Vibration of Penn State University for helpful discussions.

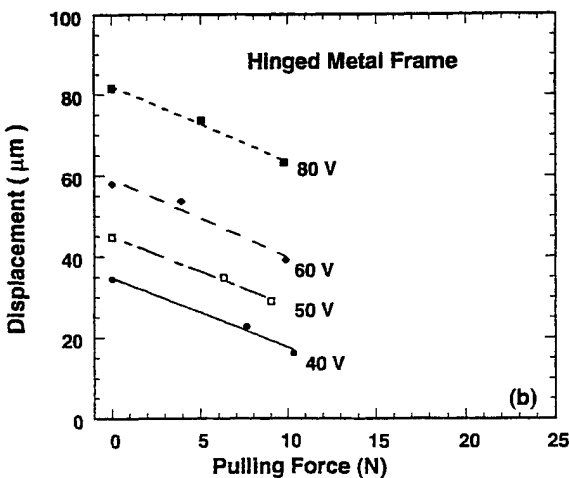
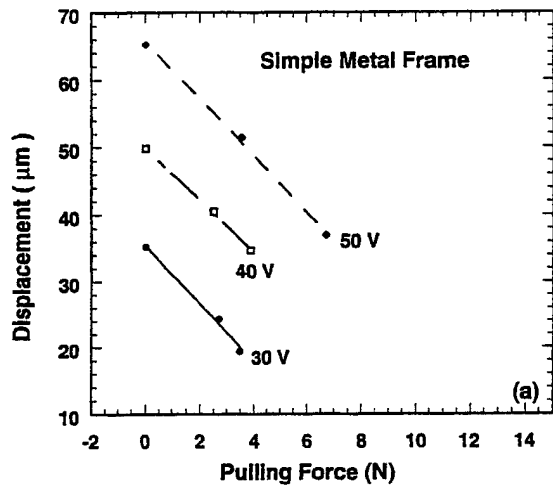


Fig. 7. Measured curves for derivation of the blocking forces at different driving voltage; (a) simple-metal-frame, (b) hinged-metal-frame.

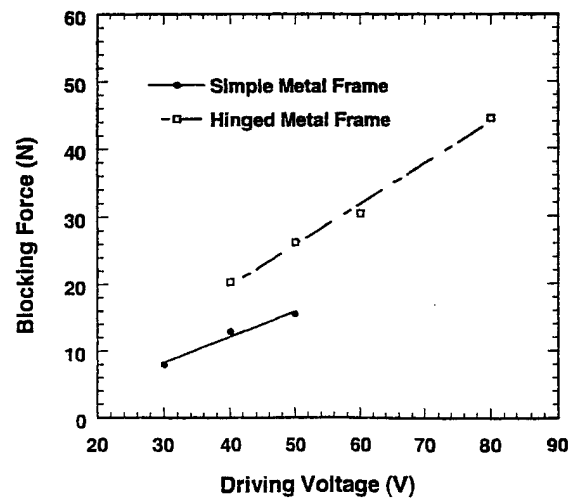


Fig. 8. Comparison of blocking forces between simple and hinged metal frames as a function of driving voltage.

References

1. K. Uchino, *MRS Bulletin*, **18**(4), 42 (1993).
2. A. Dogan, K. Uchino, and R.E. Newnham, *IEEE Transaction on Ultrasonic, Ferroelectrics, and Frequency Control*, **44**(3), (1997).
3. G.J. Knowles, *Final report NAS1-97147*, (1998).
4. J.M. Paros and L. Weisbord, *Machine Design*, **37**, 151 (1965).

ACTUATOR STUDIES

Photostriction

APPENDIX 64



PERGAMON

Mechatronics 10 (2000) 467–487

MECHATRONICS

Photostrictive actuators

Patcharin Poosanaas^a, Kazuhiko Tonooka^b, Kenji Uchino^{a,*}

^a*International Center for Actuators and Transducers, Materials Research Laboratory, The Pennsylvania State University, University Park, PA 16802, USA*

^b*Materials Division, Hokkaido National Industrial Research Institute, Sapporo, Japan*

Abstract

Photostrictive materials, exhibiting light induced strain, are of interest for future generation wireless remote control photo-actuators, micro-actuators, and micro-sensors applications. (Pb, La)(Zr, Ti) O₃ (PLZT) ceramics doped with WO₃ exhibit large photostriction under uniform illumination of near-ultraviolet light. Using a bimorph configuration, a photo-driven relay and a micro walking device have been demonstrated. However, for the fabrication of these devices, materials exhibiting higher photovoltaic effect and higher response speed must be developed. The present paper reviews a new theoretical model for photovoltaic effect first, then enhanced performance photostrictive materials through sample surface characteristics, finally its potential future applications. © 2000 Elsevier Science Ltd. All rights reserved.

Keywords: Photovoltaic effect; Photostriction; Photostrictive actuators; Surface characteristics; PLZT ceramics

1. Introduction

The continuing thrust towards greater miniaturization and integration of microrobotics and microelectronics has resulted in significant work towards the development of ceramic actuators, utilizing their wavelength-dependent optical actuation mechanisms. In recent times, *Photostrictive actuators* — which directly

* Corresponding author. Tel.: +1-814-863-8035; fax: +1-814-865-2326.
E-mail address: kxul@alpha.mrl.psu.edu (K. Uchino).

convert photonic energy to mechanical motion — have drawn significant attention for their potential usage in microactuation and microsensing applications.

Photostrictive materials have the ability to convert light directly to physical motion. The mechanism of photostriction can be described as the superposition of the photovoltaic and converse piezoelectric effects. When noncentrosymmetric materials, such as ferroelectric single crystals or polarized ferroelectric ceramics, are uniformly illuminated, a high voltage, considerably exceeding the band gap energy, is generated. In certain ferroelectric materials this photovoltage is of the order of kV/cm (10^5 V/m). Along with this photovoltage, mechanical strain is also induced due to the converse piezoelectric effect. The fortuitous combination of these two effects makes these ferroelectrics suitable for wireless actuator applications, activated and driven by incident light. These optical actuators have received considerable attention for applications in areas related to micromechanics, ultrahigh vacuum and space technologies. Optical actuators are also anticipated to be used as the driving component in optically controlled “electromagnetic-noise free” systems. The photostrictive effect has also recently been used in fabricating a photophonic device, where light was transformed directly into sound from the mechanical vibration induced by intermittent illumination.

The photostrictive effect has been studied mainly in ferroelectric polycrystalline materials for potential commercial applications. Lanthanum-modified lead zirconate titanate (PLZT) ceramic is one of the most promising photostrictive materials due to its relatively high piezoelectric coefficient and ease of fabrication. However, previous studies have shown that for commercial applications, improvements in the photovoltaic efficiency and response speed of the PLZT ceramics are essential. The improvement in photostrictive properties require consideration of several parameters, such as:

- material parameters (e.g. composition and stoichiometry, dopant type and concentration)
- processing condition (e.g. processing route and parameters) and microstructure, and
- sample configuration and performance testing conditions (e.g. surface characteristics and illumination).

The photostrictive response of a material can be considerably increased and controlled by understanding the influence of these parameters and by optimizing these parameters. This paper reviews a new model to explain the photovoltaic effect first, then the fundamentals of photostrictive effect in PLZT ceramics, and finally describes some of the potential applications. The influence of sample geometry has also been illustrated.

2. Photostrictive effect

Photostriction is a phenomenon in which strain is induced in the sample by

incident light. In principle, this effect arises from a superposition of the photovoltaic effect, i.e. the generation of large voltage from the irradiation of light, and the converse-piezoelectric effect, i.e. expansion or contraction under the voltage applied [1]. It must be noted that the photostrictive effect is different from thermal dilatation and pyroelectricity, where strain is produced due to the temperature rise from the light illumination.

The photostrictive phenomenon has been observed in certain ferroelectric materials. The figure of merit of photostriction is generally expressed as the product of photovoltage, E_{ph} , and the piezoelectric constant, d_{33} . Therefore, for application purposes, enhancement and/or optimization of photostrictive properties requires consideration of both terms in the figure of merit. Recently, PLZT ceramics have gained considerable attention due to their excellent photostrictive properties, high d_{33} and ease of fabrication.

2.1. Mechanism of photovoltaic effect

When a noncentrosymmetric ferroelectric material is illuminated with uniform light having a wavelength corresponding to the absorption edge of the material, a steady photovoltage/photocurrent is generated [2]. In some materials, the photovoltage generated is greater than the band-gap energy, and can be of the order of several kV/cm. This phenomenon, referred to as the anomalous photovoltaic effect (APV), is different from the corresponding phenomenon in the p-n junction of semiconductors (e.g. solar battery) [3,4]. The APV effect is observed only in the direction of the spontaneous polarization (P_s) in the ferroelectric material. The generated photovoltage is proportional to the sample length along the P_s direction. The APV effect has been observed to disappear in the paraelectric phases.

The origin of the photovoltaic effect is not yet clear, even though several models have been proposed on the mechanism of photovoltaic effect. The key issue in understanding the APV mechanism is the importance of both impurity doping as well as crystal asymmetry. Fig. 1 illustrates one of the proposed models, the

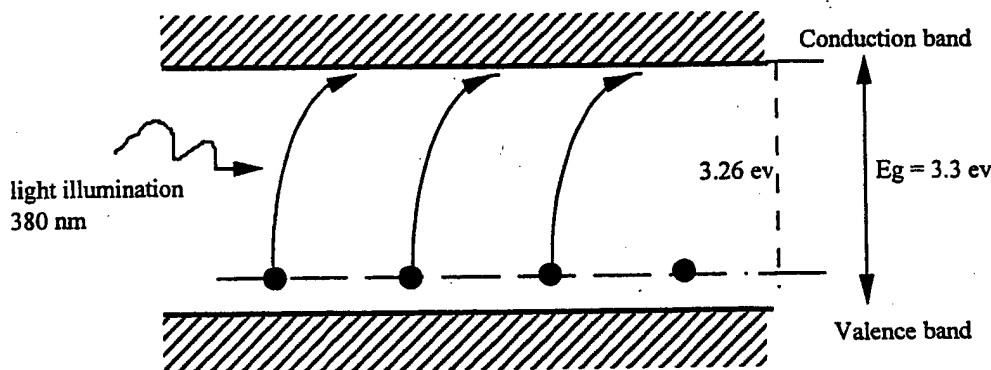


Fig. 1. Energy band gap model of excited transition from impurity level in PLZT [5].

electron energy band model proposed for PLZT ceramics by one of the authors [5]. The energy band is basically generated by the hybridized orbit of p-orbital of oxygen and d-orbit of Ti/Zr. The donor impurity levels induced in accordance with La doping (or other dopants) are present slightly above the valence band. The transition from these levels with an asymmetric potential due to the crystallographic anisotropy may provide the “preferred” momentum to the electron. Electromotive force is generated when electrons excited by light move in a certain direction of the ferroelectric crystal, which may arise along the spontaneous polarization direction. The asymmetric crystal exhibiting a photovoltaic response is also piezoelectric in principle, and therefore, a photostriction effect is expected as a coupling of the bulk photovoltaic voltage with the piezoelectric constant.

Recently the mechanism of APV has also been proposed based on the voltage source model. The possibility of generating an effective dc field has been explained on the basis of nonlinear properties of a ferroelectric material having noncentric symmetry [6]. The details of the model are explained in the following section.

2.1.1. Voltage source model

The photovoltaic properties are attributed to the photocarriers and internal electric fields generated by short-wavelength illumination. The optical nonlinearity of the second order has been proposed as the origin of photo-induced dc field generation. The expression for the polarization of dielectrics, considering the nonlinear effect up to the second order is given by [7]:

$$P = \epsilon_0(\chi_1 E_{op} + \chi_2 E_{op}^2) \quad (1)$$

where ϵ_0 is the permittivity of vacuum, χ_1 is the linear susceptibility, χ_2 is the nonlinear susceptibility of the second order, and E_{op} is the electric field at an optical frequency.

In ferroelectric ceramics, nonlinearity is expected to appear due to the poling. To the first approximation, the susceptibilities (χ_1) and (χ_2) can be assumed to be constant. The illuminating light — being an electromagnetic wave — will provide an electric field for charges in dielectrics. When an alternating electric field with amplitude E_{op} , and optical frequency ω_{op} , is applied to a dielectric material having a nonlinear response, the polarization as a function of time, t , can be written as

$$P = \epsilon_0\{\chi_1 E_{op} \cos(\omega_{op}t) + \chi_2 E_{op}^2 \cos^2(\omega_{op}t)\} \quad (2)$$

In a linear material, χ_2 will be zero and the induced polarization will be proportional to the applied electric field at any moment. As a result, in the linear material, the polarization oscillates at an optical frequency of ω_{op} . However, in a nonlinear material, an asymmetric polarization wave is produced due to the nonlinear dielectric response which suggests that the induced polarization contains the higher order components as well as the fundamental wave. The Fourier

analysis of the second harmonic wave shows that it contains the second harmonic component and also has a nonzero average. This average term of the induced polarization can result in a dc electric field for carriers.

In dielectrics, the value of the local electric field is different from the value of the macroscopic electric field. An additional field due to the polarization charges appears in polarized dielectrics. For simplicity, the local field in dielectrics has been approximated using the Lorentz relation for a ferroelectric material as [8]:

$$E_{\text{local}} = E + \frac{\gamma P}{3\epsilon_0} \quad (3)$$

where E is the macroscopic electric field and γ is the Lorentz factor.

When an alternating electric field at an optical frequency is applied, the local field in a dielectric material having second-order nonlinearity can be given as:

$$E_{\text{local}} = E_{\text{op}} \cos(\omega_{\text{op}} t) + \frac{\gamma}{3} \{ \chi_1 E_{\text{op}} \cos(\omega_{\text{op}} t) + \chi_2 E_{\text{op}}^2 \cos^2(\omega_{\text{op}} t) \} \quad (4)$$

The average of the local electric field E_{local} in Eq. (4) will be:

$$\overline{E_{\text{local}}} = \frac{1}{6} \gamma \chi_2 E_{\text{op}}^2 \quad (5)$$

It must be noted that Eq. (5) has been derived for nonlinear dielectrics under a coherent propagation of the light wave at a single frequency. However, the condition of coherent illumination may not be satisfied in the experimental conditions described in this work, where a mercury lamp is used as a light source. The nonlinear effect will be affected by to the degree of coherence. Therefore, considering the depression of nonlinear effect due to the incoherence, the expression for the effective dc field induced by incoherent light source may be modified as:

$$\overline{E_{\text{local}}} = c_1 \gamma \chi_2 (E_{\text{op}}^2)^\beta \quad (6)$$

where c_1 is a constant and β is a parameter expressing the depression effect.

Replacing the variable E_{op}^2 with the intensity (I_{op}) [7], the following expression for the average induced (dc) field due to the incoherent light can be obtained:

$$E_{\text{dc}} = \overline{E_{\text{local}}} = c_2 \gamma \chi_2 (I_{\text{op}})^\beta \quad (7)$$

where c_2 is a constant and E_{dc} is the effective dc field for photoinduced carriers. Note that the induced field, E_{dc} , is proportional to the nonlinear susceptibility as well as the Lorentz factor, γ .

The concentration of carriers excited by optical irradiation is governed by the following rate equation,

$$\frac{dn_c}{dt} = g - Rn_c^2 - \frac{n_c}{\tau_c} \quad (8)$$

where n_c is the carrier density, g is the generation rate of the carrier, R is the recombination rate of the carrier, and τ_c is the intrinsic lifetime of the carrier. When the excitation is adequately strong, the recombination process dominates, and the carrier density becomes:

$$n_c = \sqrt{\frac{g}{R}} \quad (9)$$

The generation rate (g) being proportional to the light intensity (I_{op}), the carrier density can be written as:

$$n_c = c_3 \sqrt{\frac{I_{op}}{R}} \quad (10)$$

where c_3 is a constant. Introducing the carrier mobility (μ), the electric conductivity due to the photoinduced carriers will then become [2]

$$\sigma_{op} = q n_c \mu \quad (11)$$

where, q is the charge of the photocarrier. Combining Eqs. 10 and 11, the photoconductivity can be obtained as a function of light intensity,

$$\sigma_{op} = c_3 q \mu \sqrt{\frac{I_{op}}{R}} \quad (12)$$

The photocurrent will be the product of the photoconductivity and the photoinduced dc field:

$$J_{ph} = \sigma_{op} E_{dc} \quad (13)$$

Substituting Eqs. (7) and (12) into (13), the expression for the photocurrent can finally be obtained:

$$J_{ph} = c_4 q \mu \gamma \chi_2 \sqrt{\frac{1}{R}} (I_{op})^{\beta + \frac{1}{2}} \quad (14)$$

where, c_4 is a constant. Eqs. (12) and (14) provide a correlation for the photovoltaic response of ferroelectrics on the basis of optical nonlinearity.

2.1.2. Model validation and analysis

The predictions for the proposed model were validated against experimental measurements of photoconductivity and photocurrent. PLZT (3/52/48) ceramics samples were cut into the standard sizes of $5 \times 5 \text{ mm}^2$ and polished to 1 mm thickness. The samples were poled along the length (5 mm) under a field of 2 kV/mm at 120°C for 10 min. The present model was validated by comparing the experimental results with the prediction based on Eq. (12) for photoconductivity and Eq. (14) for photocurrent.

Fig. 2 shows the plot of photoconductivity (σ_{op}) as a function of light intensity (I_{op}). The exponent relating the photoconductivity and the light intensity was calculated to be 0.54. This is in good agreement with the value of 0.5 derived for the recombination process of the carriers, Eq. (12).

Fig. 3 shows the experimental results of short-circuit photocurrent (J_{ph}) as a function of light intensity. The parameter β based on Eq. (14) was calculated to be 0.46. The value of parameter β is expected to lie between 0 and 1. The depression in β value can be attributed to the incoherent illumination of the mercury lamp.

Fig. 4 shows the experimental results of the open-circuit photovoltage (E_{ph}) as a function of light intensity. The photovoltage was found to be proportional to the square root of the light intensity.

The experimental data was further analyzed to investigate the effects of incoherent illumination. Since a partial coherence of illuminating light can be achieved in a very small area, an increase in β value is expected in thinner photovoltaic samples. In order to reconfirm this effect, the photocurrent was measured as a function of light intensity (Fig. 5) in a very thin (140 μm) PLZT sample. The parameter β based on Eq. (14) was recalculated and was found to be 0.80, which is higher than the β value of 0.46 in the thicker sample (1 mm thickness). These results suggest that the parameter β increases with a decrease in the thickness of the photovoltaic sample, due to a higher coherency of illumination in the thinner samples. This suggests that an enhancement in the photovoltaic properties may be achieved in a very thin sample or by using coherent illumination.

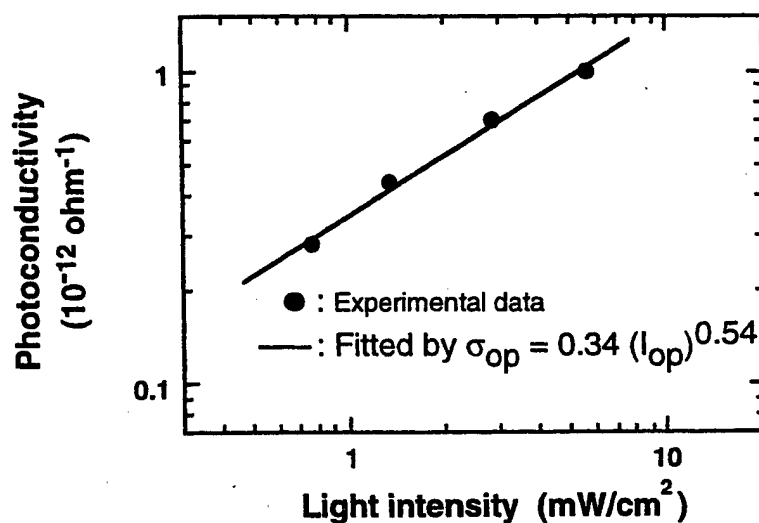


Fig. 2. Dependence of photoconductivity on illumination intensity in PLZT (3/52/48) ceramics. The exponent of the curve was found to be 0.54 which is close to the model.

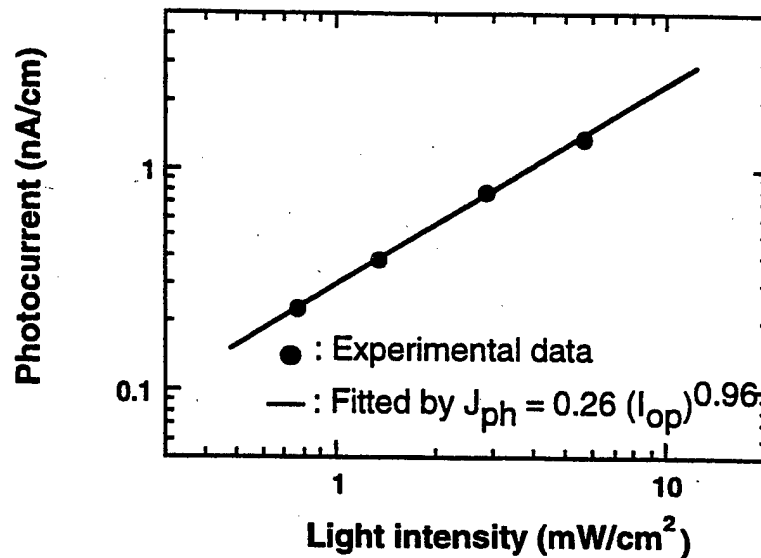


Fig. 3. Dependence of photocurrent on illumination intensity for 1 mm thick sample of PLZT (3/52/48) ceramics. The parameter β was estimated to be 0.46.

2.2. Experimental setup for photovoltaic and photostrictive measurements

Fig. 6 shows the experimental setup. Photovoltaic measurements were done using a high-input-impedance electrometer (Keithley 617), while the photostriction was measured by a displacement sensor (LVDT, Millitron model 1301). The

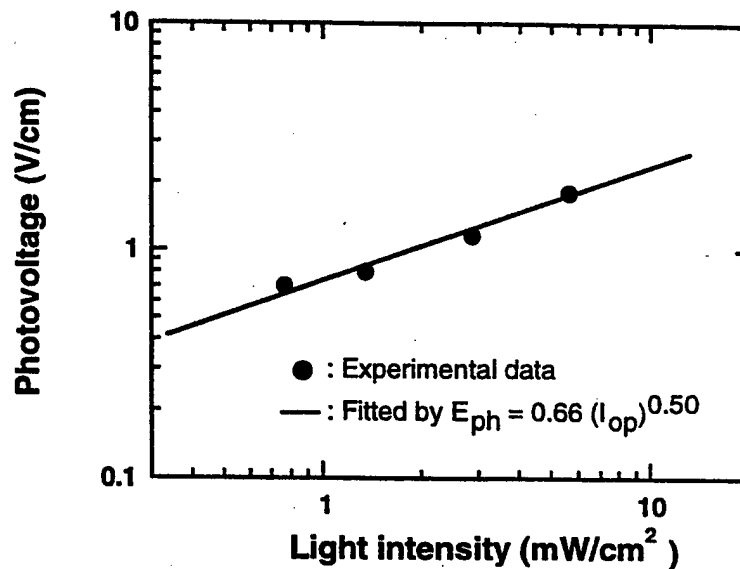


Fig. 4. Dependence of photovoltage on illumination intensity in PLZT (3/52/48) ceramics. Photovoltage was found to be proportional to the square root of the light intensity.

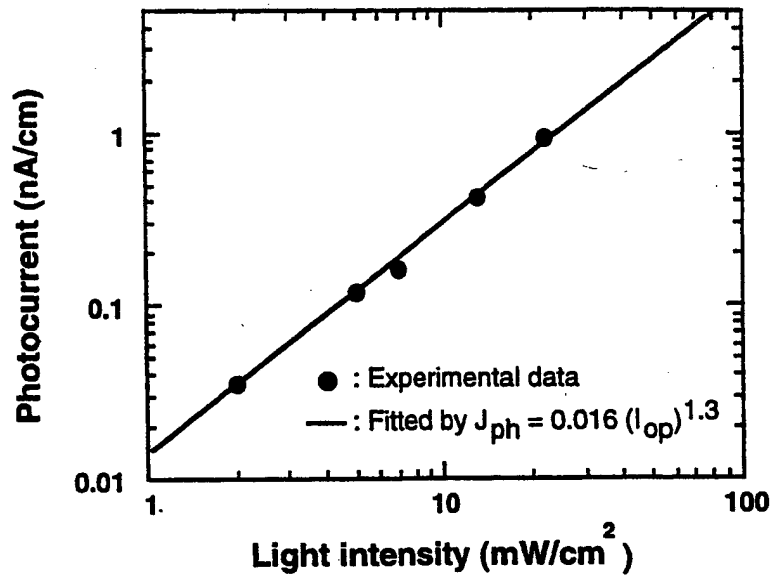


Fig. 5. Dependence of photocurrent in thin sample (140 μm) of PLZT (3/52/48) ceramics on illumination intensity. The parameter β was estimated to be 0.80 by the curve fitting.

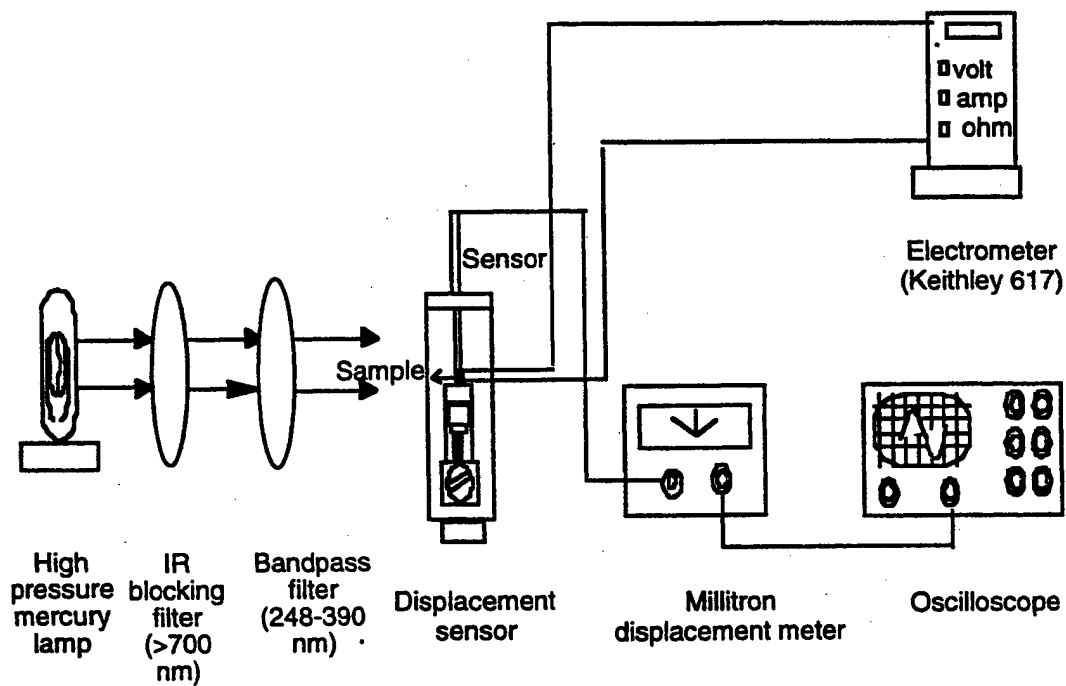


Fig. 6. Experimental set up for photovoltaic and photostrictive measurements.

photovoltage and photocurrent were determined from the current–voltage relation by applying voltage between -100 and $+100$ V, while illuminating the samples as described in the following. The photovoltage was determined in an open circuit state from the intercept of the horizontal applied voltage axis, while the photocurrent was obtained for the short circuit state from the intercept of the vertical current axis.

A short arc mercury lamp (Ushio Electric USH-500D) was used as a light source. The original lamp radiation was passed through an Infrared (IR) blocking filter and Ultraviolet (UV) bandpass filter to obtain a monochromatic beam with a maximum strength around 366 nm wavelength. Light with this wavelength has been reported to yield the maximum photovoltaic properties in the PLZT samples [9,10].

3. Sample geometry dependence

Since the photostrictive effect is excited by the absorption of illumination in the surface layer of ceramics, it is apparent that the surface geometry of the photostrictive material will have a strong bearing on the generation of photocurrent and photovoltage. These surface characteristics are further reinforced by the absorption occurring at the surface layer of the piezoelectric material facing the illumination. Using a sample thickness closer to the penetration depth will ensure that the entire film will be active and efficiently utilized. Therefore, investigation of photovoltaic response as a function of sample thickness is desired in determining the optimal thickness range with maximum photovoltaic effect. In addition, studying the effect of surface roughness on the photovoltaic effect will provide an insight on the absorption dependence of photostriction.

3.1. Thickness dependence

In order to determine the optimum sample thickness, dependence of photovoltaic effect on sample thickness of PLZT (3/52/48) ceramics doped with 0.5 at.% WO_3 was examined. Photovoltaic response was found to increase with a decrease in sample thickness in PLZT ceramics. A model has been proposed to explain and quantify the observed influence of sample thickness on photovoltaic response [11] as shown in Fig. 7, where the absorption coefficient is assumed to be independent of light intensity and the photocurrent density is taken to be proportional to light intensity. The sample is assumed to comprise of thin slices along the thickness direction of the sample. A circuit diagram representing these layers is also shown in Fig. 7.

Fig. 8 shows the plot between the normalized photocurrent (i_m) and sample thickness calculated for the external resistance ($R_m = 200 \text{ T}\Omega$). The computed results shows good agreement with the experimental data. With increase in sample thickness, i_m increases, reaches a maxima, and subsequently decreases with the

sample thickness. The decrease in i_m can mainly be attributed to the dark conductivity (σ_d). The optimum thickness (for the present set of samples) which yields maximum photocurrent is found at 33 μm . The extremely low value of optimum thickness implies that the lower sample thickness will be expected to give better photovoltaic response.

3.2. Surface roughness dependence

The effect of surface roughness on photovoltaic and photostrictive properties was examined in the PLZT ceramics, the sample as used in Section 3.1, with different surface roughness obtained by polishing to different surface finishes. The surface roughness was measured by a profilometer (Tencor, Alpha-Step 200) and

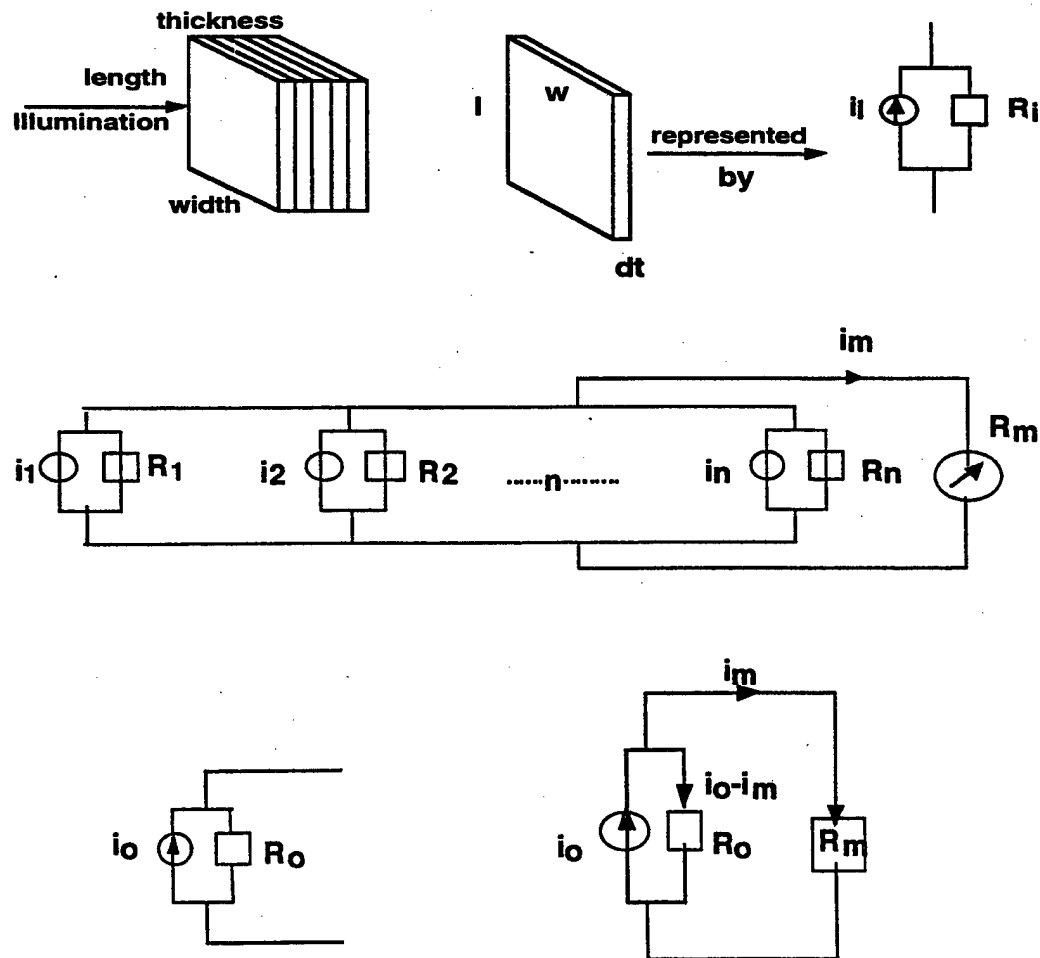


Fig. 7. Schematic of the model to compute the dependence of photocurrent on sample thickness. The sample has been modeled as thin slices along the thickness direction and the corresponding circuit diagrams are also shown.

the average surface roughness was determined using the graphical center line method.

The variation of photovoltaic (photovoltage and photocurrent) and photostrictive properties with surface roughness are plotted in Fig. 9 (a)–(c). The photovoltaic and photostrictive responses increase exponentially with decreasing surface roughness. This is due to the fact that, with increase in surface roughness the penetration depth of the illumination decreases, while contributions from multiple reflections increase.

A model has been proposed to explain and quantify the influence of surface roughness. The effect of multireflection has not been considered in the following formulation. Two different shapes, a sine profile and a “V” profile roughness (Fig. 10 (a)), were assumed for simplicity. In both these shapes, the amplitude was taken as a center line roughness (r) and the wavelength as (g). The detail will be made only for a “V” profile.

The corresponding equations for the unit cell of the “V” profile rough surface (Fig. 10 (b) and (c)) are:

$$y = r \left(\frac{4x}{g} + 1 \right) \quad \text{where} \quad \frac{-g}{4} \leq x \leq \frac{g}{4}, \quad (15)$$

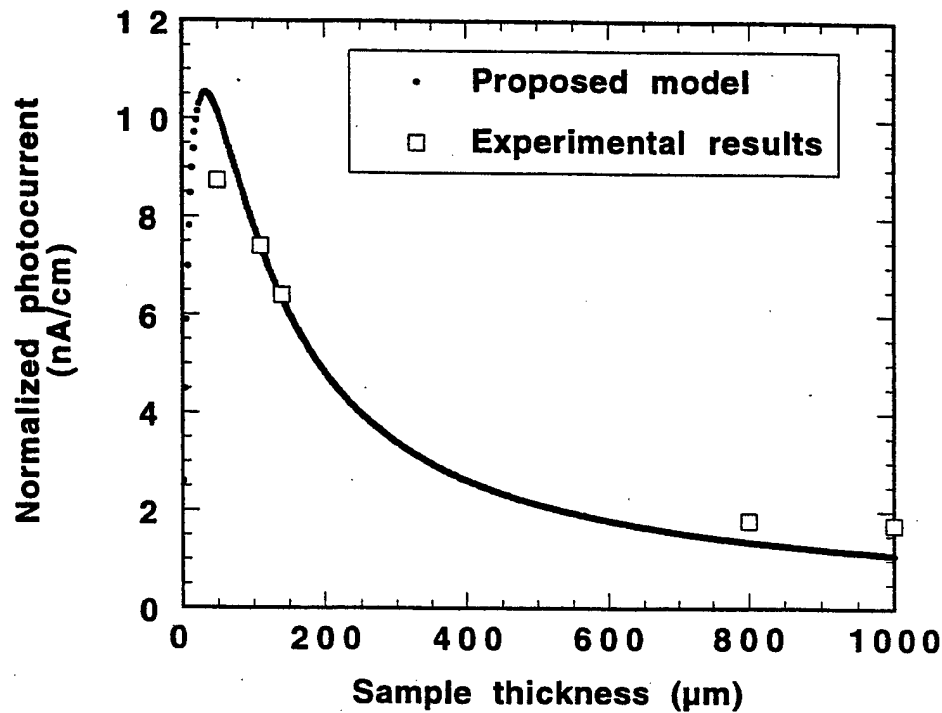


Fig. 8. Comparison of measured and computed normalized photocurrent in 0.5 at.% WO_3 doped PLZT (3/52/48) ceramics. The optimum thickness was found at 33 μm .

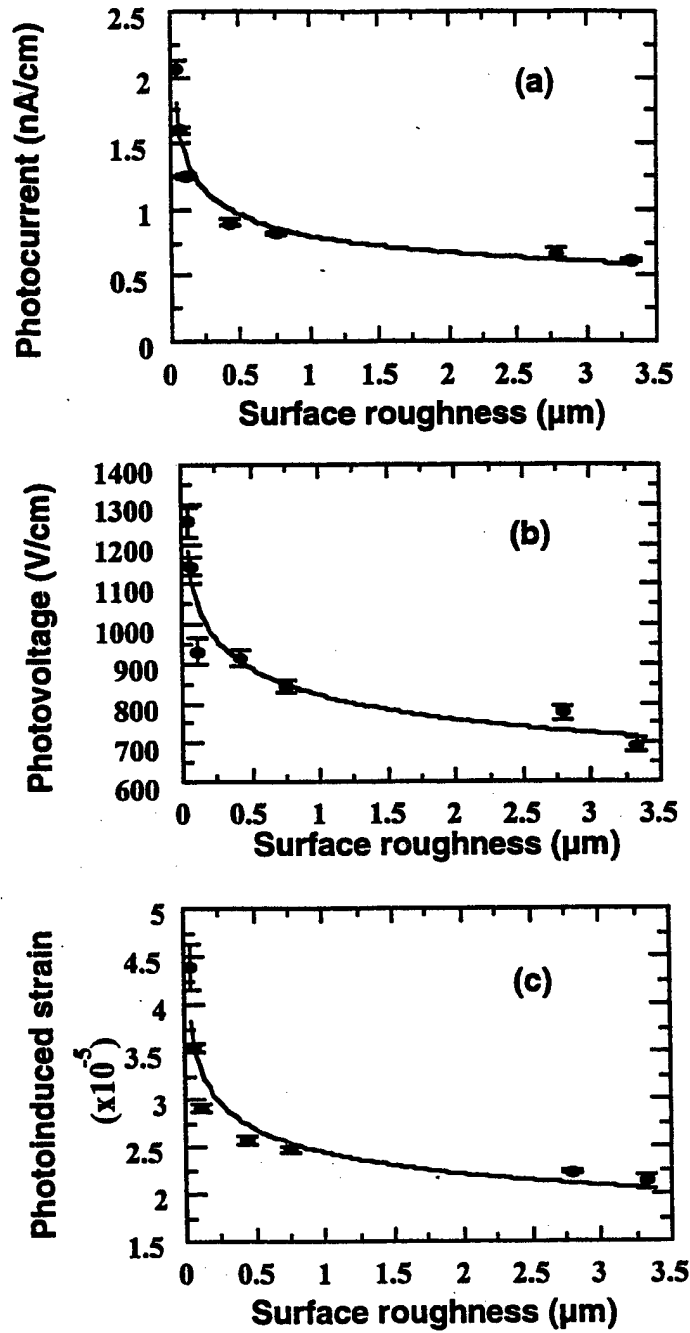


Fig. 9. Variation of (a) photocurrent, (b) photovoltage, and (c) photo-induced strain with surface roughness of 0.5 at.% WO_3 doped PLZT ceramics.

$$\tan \theta_i = \frac{dy}{dx} = \frac{4r}{g} \quad (16)$$

where θ_i is an angle with the vertical incident beam. By means of Snell's law [7],

$$n_i \sin \theta_i = n_t \sin \theta_t \quad (17)$$

where θ_t is the transmitted angle, n_i and n_t are the refractive indexes of air and

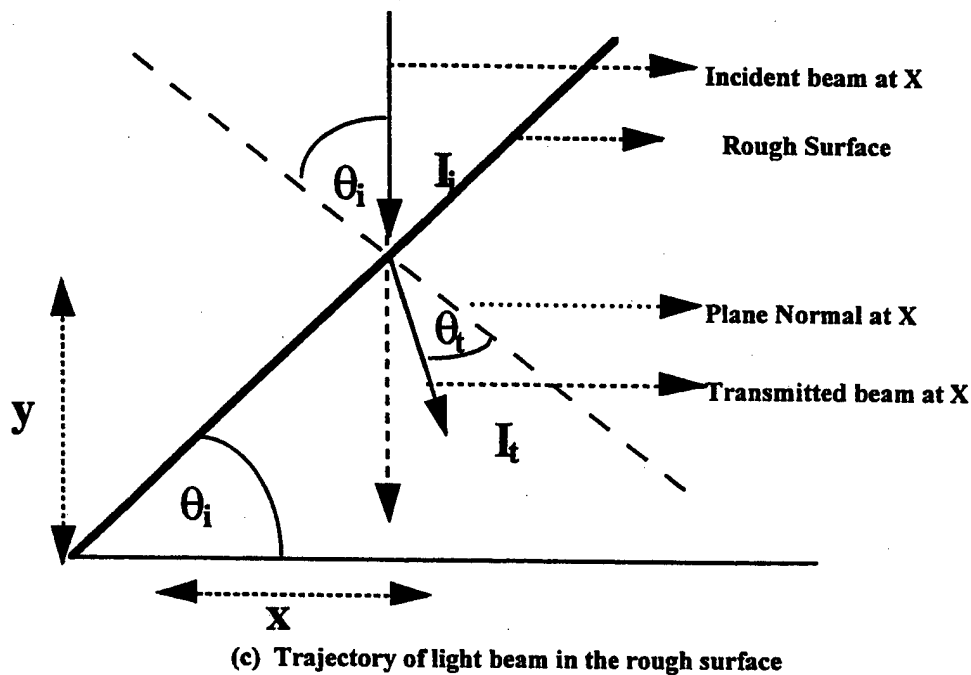
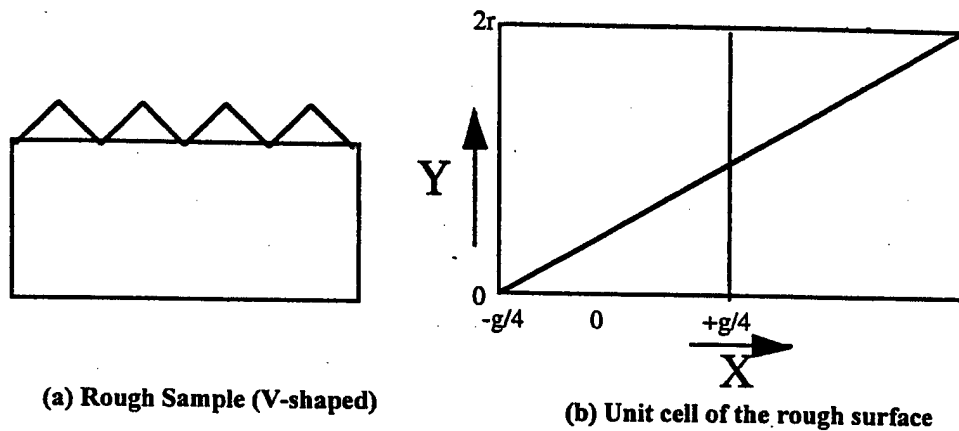


Fig. 10. Schematic diagram of the V-shaped model (a) rough sample, (b) unit cell of the rough sample, and (c) trajectory of the light beam in the rough surface.

PLZT sample respectively, the transmittance (T) is given by:

$$T = \frac{I_t \cos \theta_t}{I_i \cos \theta_i} = \left[\frac{n_t \cos \theta_t}{n_i \cos \theta_i} \right]^2 t^2 \quad (18)$$

The transmitted light intensity (I_t) will then be:

$$I_t = I_i T = I_i n_i t^2 \quad (19)$$

This intensity will further decrease due to absorption. If the sample thickness is greater than the penetration depth ($1/\alpha$), the average intensity (I_o) reaching the sample below the rough surface will be:

$$I_o = \left(\frac{2}{g} \right) x \int_0^{\frac{g}{4}} I_t(x) \exp(-\alpha z) dz dx - \frac{g}{4} \int_0^{\infty} I_t(x) \exp(-\alpha z) dz dx \quad (20)$$

where, z is the sample thickness.

This average intensity (I_o) can be substituted in the sample thickness model which has been reported earlier [11] to examine the influence of surface roughness on photocurrent. The normalized photocurrent (i_m) computed using above formula, is plotted in Fig. 11 as a function of surface roughness for the two chosen surface profiles. The experimental results are also plotted. A wavelength of

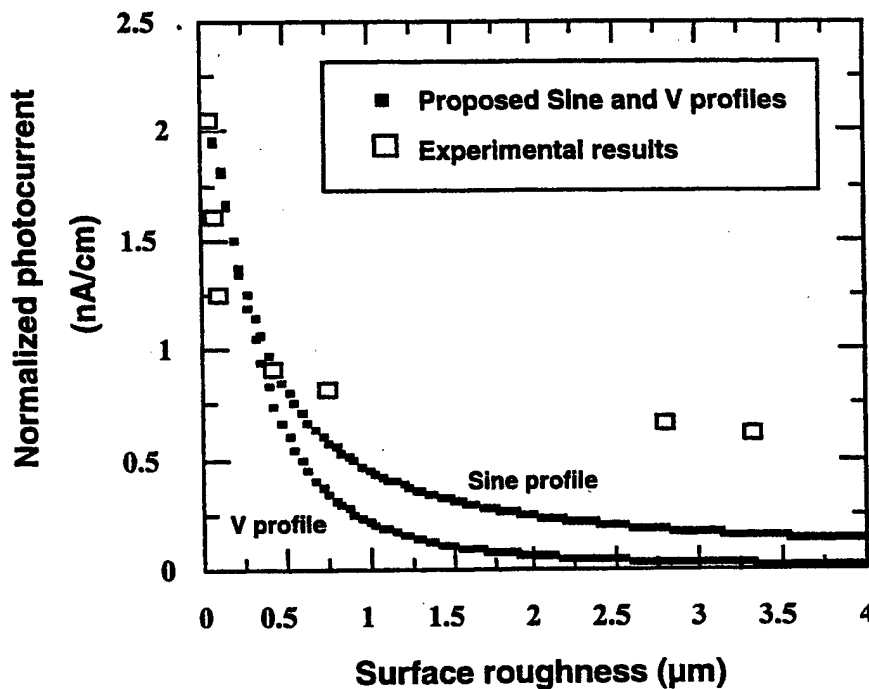


Fig. 11. Comparison of the normalized computed photocurrent in 0.5 at.% WO_3 doped PLZT (3/52/48) ceramics obtained from the two profiles with the experimental results.

roughness at 1 μm gave the best fit of the experimental results which is close to the size of the grain size of the sample.

4. Potential applications based on photovoltaic and photostrictive effects

The direct conversion of photonic to mechanical motion by the photostrictive effect can lead to two broad classes of applications — microactuation and microsensing. Potential applications for microactuation include [12]:

- an alternative mechanism for converting solar energy directly into mechanical motion for planetary exploration
- direct corrective control in adaptive optics/interferometer
- optical micropositioning
- solar tracking actuator/shutter for self alignment of the spacecraft to the sun for optimal power generation using solar sails
- optically controlled valves for space applications
- optically controlled microrobots
- photophones.

The potential microsensing applications include:

- a variety of tunable sensors for incident radiation (UV, visible etc.) based on the deflection as a function of incident radiation intensity
- indirect microsensors based on the photodeflection when the device is loaded with condensing moisture (microhygrometer) or incident interstellar dust (microbalance).

We have successfully demonstrated the application of photoactuation in PLZT ceramic wafers as a photo-driven relay [9] and a photo-driven micro walking machine [13]. These devices are designed to use incident light and have no lead wires or electric circuits.

Fig. 12 illustrates a photodriven relay device using a PLZT bimorph as the driver which consists of two ceramic plates bonded together with their polarization directions opposing each other. A dummy PLZT plate was positioned adjacent to the bimorph to cancel the photovoltage generated in the bimorph. Utilizing the dual beam method, switching was controlled by alternately irradiating the bimorph and the dummy, which can avoid the time delay due to low dark conductivity. The amount of displacement observed at a tip of the bimorph was about 150 μm with the delay time of 1–2 s [9].

Fig. 13 shows a micro-walking machine using photostrictive bimorphs with two ceramic legs fixed on a plastic board. The structure is simple, having only two ceramic legs ($5 \times 20 \times 0.35$ mm). When the two legs were irradiated alternately, the device moved like an inchworm at a speed of several tens of microns per min [13]. The photostrictive bimorph as a whole was caused to bend by ± 150 μm as if it averted the radiation of light. The walking speed can be increased to

approximately 1 mm/min by providing some contrivances such as the use of a foothold having microgrooves fitted to the steps of the legs.

Photomechanical resonance in a PLZT bimorph has been successfully demonstrated using chopped UV irradiation having neither electrical lead wire or circuits. A thin cover glass was attached on the photostrictive bimorph structure to decrease the resonance frequency so as to easily observe the photo-induced resonance. The dual beam method was used to irradiate the two sides of the bimorph alternately, intermittently with a 180° phase difference. The mechanical resonance was determined by changing the chopper frequency. The resonance frequency was about 75 Hz, which is smaller than the audible frequency range [4]. However the achievement of photo-induced mechanical resonance in the audible frequency range suggests the possibility of photostrictive PLZT bimorph-type devices as photoacoustic components for the next communication age.

Recently, a new application of highly efficient, photostrictive PLZT films on flexible substrates has been conceived for usage in the new class of small vehicles for future space missions [14].

In addition some promising devices, which can be fabricated based on tailoring photostrictive films on the flexible substrate in a unimorph structure, are the micro walking device and the light chasing device.

The micro walking device can be designed into arch-shaped photoactuating composite films (Fig. 14 (a)) with a triangular top (Fig. 14 (b)). Photoactuating films may be fabricated from PLZT solutions and coated on one side of a suitable flexible substrate which will then be designed to have a curvature of 1 cm^{-1} . A slight difference in length between the right and left legs could be designed in order to provide a slight difference between their resonance frequencies. This would facilitate in controlling this device in both clockwise and counterclockwise rotations. A light chopper operating at a frequency close to resonance could be used to illuminate the device, in order to maximize the vibration of the bimorph which will then provide the capability to turn by applying different resonance frequencies of two legs.

In order to maximize the photostrictive properties of the sample, the sample geometry could be determined from the proposed model in Section 3.1. After coating a suitable UV transparent electrode, the film could then be poled along the thickness. Under uniform illumination on the upper side of the device, the PLZT film on that side would contract. Since the PLZT film is bonded onto the substrate, the whole device would then decrease the curvature and move.

A 'sunflower' device for chasing the light source may be designed using photoactuating film composites. By tailoring the absorption edge of PLZT ceramics through impurity doping, the device can be utilized for tracking solar radiation. Fig. 15 shows the principle of this 'light source chasing' device. Two unimorphs are attached to both sides of a solar panel (Fig. 15 (a)). When the light source positioned equidistantly between the two unimorphs, there is no difference in the strain due to photostrictive effect which results in the stable state of the solar panel (gray line in Fig. 15 (b)). When the light source moves to the right-hand side, for example, the intensity on the B side will be stronger than on the A

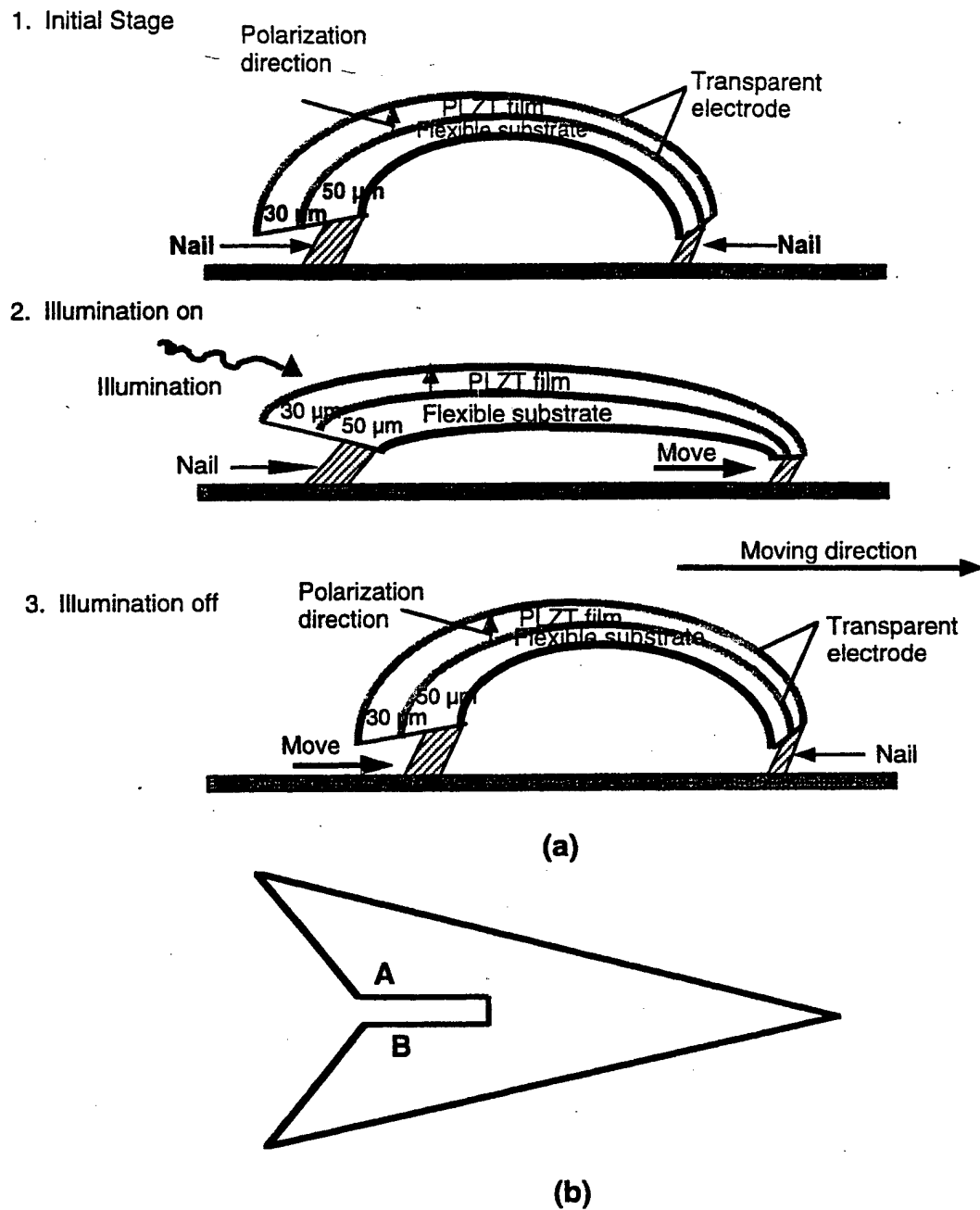


Fig. 14. (a) The schematic diagram of arch-shaped type photoactuating film composites (b) the triangular top shape photoactuating film composites.

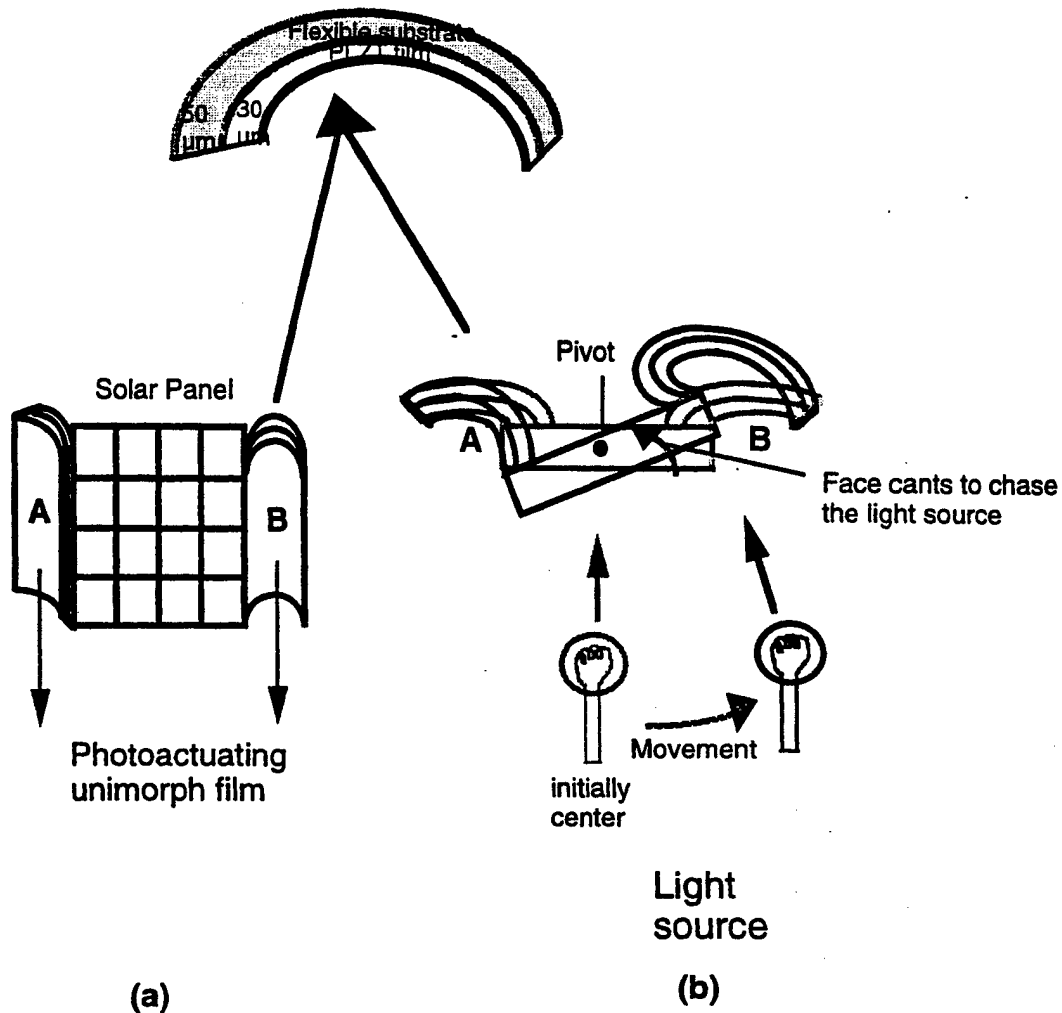


Fig. 15. (a) The light source chasing device based on photoactuating film composites (b) schematic diagram of the movements of device towards the light source.

side. The photoactuating film on the B side would deflect more than the A side which, leads to the panel canting and moving to track the light source.

5. Summary

Photostrictive actuators are driven only by the irradiation of light without requiring the electrical lead wire connection. Therefore, they can be employed in ultra high vacuum or outer space. The direct conversion of photonic to mechanical motion by photostrictive effect can lead to two broad classes of applications, microactuator and microsensing which will open new vistas in the actuator technology. It is evident that the photovoltaic and photostrictive effects

are strongly dependent on the surface characteristics of the sample. The surface characteristics are, therefore, of extreme importance during the fabrication of high efficiency photostrictive device. It is expected that the sample thickness and roughness which will be crucial in designing thick film bimorphs for enhancements in the efficiency of a micromechanical device. We introduced two new devices, a microwalking and a light chasing device in this article.

References

- [1] Uchino K, Aizawa M. Photostrictive actuators using PLZT ceramics. *Jpn J Appl Phys Suppl* 1985;24:139–41.
- [2] Fridkin VM. Solid-state sciences. In: Cardona E, Fulde P, Queisser H-J, editors. *Photoferroelectrics*, vol. 9. New York: Springer-Verlag, 1979. p. 85–113.
- [3] Uchino K. New applications of photostriction. *Innovations Mater Res* 1996;1(1):11–22.
- [4] Chu SY, Uchino K. Impurity doping effect on photostriction in PLZT ceramics. *J Adv Performance Mater* 1994;1:129–43.
- [5] Tanimura M, Uchino K. Effect of impurity doping on photostrictive in ferroelectrics. *Sensors and Materials* 1988;1:47–56.
- [6] Tonooka K, Poosanaas P, Uchino K. Mechanism of bulk photovoltaic effect in ferroelectrics. In: *Proceedings of Conference on SPIE'98 Smart Structure of Materials*, San Diego, California, March, 1998 (to be published).
- [7] Hecht E with contributions by Alfred Zajac. In: *Optics*, 2nd ed. Massachusetts: Addison-Wesley Publishing, 1987. p. 44–616 with contributions by Alfred Zajac.
- [8] Kittel C. *Introduction to solid states physics*, 7th ed. New York: John Wiley and Sons, Inc, 1996 388 pp.
- [9] Sada T, Inoue M, Uchino K. Photostriction in PLZT ceramics. *J Ceram Soc Jpn Inter Ed* 1987;95:499–504.
- [10] Nonaka K, Akiyama M, Takase A, Baba T, Yamamoto K, Ito H. Nonstoichiometry effects and their additivity on anomalous photovoltaic efficiency in lead lanthanum zirconate titanate ceramics. *Jpn J Appl Phys* 1995;34:5380–3.
- [11] Poosanaas P, Dogan A, Thakoor S, Uchino K. Influence of sample thickness on the performance of photostrictive ceramics. *J Appl Phys* 1998;84(3):1508–12.
- [12] Thakoor S, Poosanaas P, Morookian JM, Yavrovian A, Lowry L, Marzwell N, Nelson J, Neurgaokar R, Uchino K. Optical microactuation in piezoceramics. In: *Proceedings of Conference on SPIE'98 Smart Structure of Materials*, San Diego, California, March, 1998 (to be published).
- [13] Uchino K. Micro walking machine using piezoelectric actuators. *J Rob Mech* 1989;124:44–7.
- [14] Thakoor S, Morookian JM, Cutts JA. The role of piezoceramics microactuation for advanced mobility. In: *Proceedings of 10th Conference on IEEE International Symposium on Applications of Ferroelectrics Transactions*, 1996. 1. p. 205–211.

APPENDIX 65

PHOTOSTRICTIVE ACTUATORS

- New Perspective -

K. UCHINO^a, P. POOSANAAS^b, and K. TONOOKA^c

^a *International Center for Actuators and Transducers, Materials Research Laboratory, The Pennsylvania State University University Park, PA 16802, USA;* ^b *National Metal and Materials Technology Center, Bangkok 10400, Thailand;* ^c *Materials Division, Hokkaido National Industrial Research Institute, Sapporo, Japan*

Photostrictive materials, exhibiting light-induced strains, are of interest for future generation wireless remote control photo-actuators, micro-actuators, and micro-sensors applications. $(\text{Pb}, \text{La})(\text{Zr}, \text{Ti}) \text{O}_3$ (PLZT) ceramics doped with WO_3 exhibit large photostriction under uniform illumination of near-ultraviolet light. Using a bimorph configuration, a photo-driven relay and a micro walking device have been demonstrated. However, for the fabrication of these devices, higher response speed must be achieved. The present paper reviews a new theoretical model for photovoltaic effect first, then enhanced performance through sample thickness and surface characteristics, finally its potential future applications.

Keywords: Photovoltaic effect, Photostriction, Actuator, Surface characteristics, PLZT ceramics

1. INTRODUCTION

The continuing thrust towards greater miniaturization and integration of microrobotics and microelectronics has resulted in significant work towards development of ceramic actuators, utilizing their wavelength-dependent optical actuation mechanisms. In the recent days, *photostrictive actuators* - which directly converts the photonic energy to mechanical motion - have drawn significant attention for their potential usage in microactuation and microsensing applications. Optical actuators are also anticipated to be used as the driving component in optically controlled "electromagnetic-noise free" systems. The photostrictive effect has also recently been used in fabricating a photophonic device, where light was transformed directly

into sound from the mechanical vibration induced by intermittent illumination.

The photostrictive effect has been studied mainly in ferroelectric polycrystalline materials for potential commercial applications. Lanthanum-modified lead zirconate titanate (PLZT) ceramic is one of the most promising photostrictive materials due to its relatively high piezoelectric coefficient and ease of fabrication. However, previous studies have shown that for commercial applications, improvements in photovoltaic efficiency and response speed of the PLZT ceramics are essential. The improvement in photostrictive properties require consideration of several parameters, such as material parameters, processing condition and microstructure, and sample configuration and performance testing conditions.

This paper reviews a new model for explaining the photovoltaic effect first, then the influence of sample geometry, and finally describes some of the potential applications.

2. PHOTOSTRICTIVE EFFECT

In principle, photostrictive effect arises from a superposition of the photovoltaic effect, i.e. generation of large voltage from the irradiation of light, and the converse-piezoelectric effect, i.e. expansion or contraction under the voltage applied [1].

The photostrictive phenomenon has been observed in certain ferroelectric materials. The figure of merit of photostriction is generally expressed as the product of photovoltage, E_{ph} , and the piezoelectric constant, d_{33} . Therefore, for application purposes, enhancement and/or optimization of photostrictive properties requires consideration of both the terms in the figure of merit. Recently, PLZT ceramics have gained considerable attention due to their excellent photovoltaic properties, high d_{33} and ease of fabrication.

When a non-centrosymmetric ferroelectric material is illuminated with uniform light having a wavelength corresponding to the absorption edge of the material, a steady photovoltage/photocurrent is generated [2]. In some materials, the photovoltage generated is greater than the band-gap energy, and can be of the order of several kV/cm. This phenomenon, referred to as the anomalous photovoltaic effect (APV), is different from the corresponding phenomenon in the p-n junction of semiconductors (e.g. solar battery) [3, 4]. The APV effect is observed only in the direction of the spontaneous polarization (P_s) in the ferroelectric material. The

generated photovoltage is proportional to the sample length along the P_z direction.

The origin of photovoltaic effect is not yet clear, even though several models have been proposed on the mechanism of photovoltaic effect. The key issues in understanding the APV mechanism are both, impurity doping and crystal asymmetry. We proposed previously one of the current source models, based on the electron energy band model for PLZT ceramics [5]. The donor impurity levels induced in accordance with La doping are present slightly above the valence band. The transition from these levels with an asymmetric potential due to the crystallographic anisotropy may provide the preferred momentum to the electron. The asymmetric crystal exhibiting a photovoltaic response is also piezoelectric in principle, and therefore, a photostriction effect is expected as a coupling of the bulk photovoltaic voltage with the piezoelectric constant.

Recently another model of APV has also been proposed based on the voltage source mechanism [6], which will be described below.

2.1 Voltage Source Model

The photovoltaic properties are attributed to the photocarriers and internal electric fields generated by near-UV illumination. The optical nonlinearity of the second order, which is popularly introduced in ferroelectrics, has been proposed as the origin of photo-induced dc field generation [6]. The expression for the polarization of dielectrics, considering the non-linear effect up to the second order is given by [7]:

$$P = \epsilon_0(\chi_1 E_{op} + \chi_2 E_{op}^2), \quad (1)$$

where ϵ_0 is the permittivity of vacuum, χ_1 is the linear susceptibility, χ_2 is the nonlinear susceptibility of the second order, and E_{op} is the electric field at an optical frequency (THz).

In dielectrics, the value of the local electric field is different from the value of the external electric field. For simplicity, the local field in dielectrics has been approximated using the Lorentz relation for a ferroelectric material as [8]:

$$E_{local} = E + \frac{\gamma P}{3\epsilon_0} \quad (2)$$

where E is the external electric field and γ is the Lorentz factor.

When an alternating electric field at an optical frequency is applied (i.e., light illumination), the average of the local electric field E_{local} is not zero, but can be calculated as:

$$\overline{E_{local}} = \frac{1}{6} \gamma \chi_2 E_{op}^2 \quad (3)$$

It must be noted that Eq. (3) has been derived for a coherent propagation of the light wave at a single frequency. However, the condition of coherent illumination may not be satisfied in our experimental conditions, where a mercury lamp is used as a light source. The nonlinear effect will be affected by the degree of coherence. Therefore, considering the depression of nonlinear effect due to the incoherency, the expression for the effective dc field induced by incoherent light source may be modified as:

$$\overline{E_{local}} = c_1 \gamma \chi_2 (E_{op}^2)^\beta \quad (4)$$

where c_1 is a constant and β is a parameter expressing the depression effect. The value of parameter β is expected to lie between 0 and 1. Replacing the variable E_{op}^2 with the intensity (I_{op}) [7], the following expression for the average induced (dc) field due to the incoherent light can be obtained:

$$E_{dc} = \overline{E_{local}} = c_2 \gamma \chi_2 (I_{op})^\beta \quad (5)$$

where c_2 is a constant and E_{dc} is the effective dc field for photoinduced carriers. Note that the induced field, E_{dc} , is proportional to the nonlinear susceptibility as well as the Lorentz factor, γ .

The photoconductivity can be obtained as a function of light intensity, I_{op} ,

$$\sigma_{op} = c_3 q \mu \sqrt{\frac{I_{op}}{R}} \quad (6)$$

where q is the charge of the photocarrier, μ , the carrier mobility, R , the recombination rate of the carrier, and c_3 is a constant. Since the photocurrent is provided by the product of the photoconductivity and the photoinduced dc field ($J_{ph} = \sigma_{op} E_{dc}$), we finally obtain

$$J_{ph} = c_4 q \mu \gamma \chi_2 \sqrt{\frac{1}{R}} (I_{op})^{\beta + \frac{1}{2}} \quad (7)$$

where, c_4 is another constant. The Eqs. (6) and (7) provide a correlation for the photovoltaic response of ferroelectrics on the basis of optical nonlinearity.

2.2 Model Validation and Analysis

The predictions for the proposed model were validated against experimental measurements of photoconductivity and photocurrent.

PLZT (3/52/48) ceramics samples were cut into the standard sizes of 5x5 mm² and polished to 1 mm thickness. The samples were

poled along the length (5 mm) under a field of 2 kV/mm at 120 °C for 10 min. A short arc mercury lamp (Ushio Electric USH-500D) was used as a light source. The original lamp radiation was passed through an Infrared (IR) blocking filter and Ultraviolet (UV) bandpass filter to obtain a monochromatic beam with a maximum strength around 366 nm wavelength [9, 10]. Photovoltaic measurements were done using a high-input-impedance electrometer (Keithley 617).

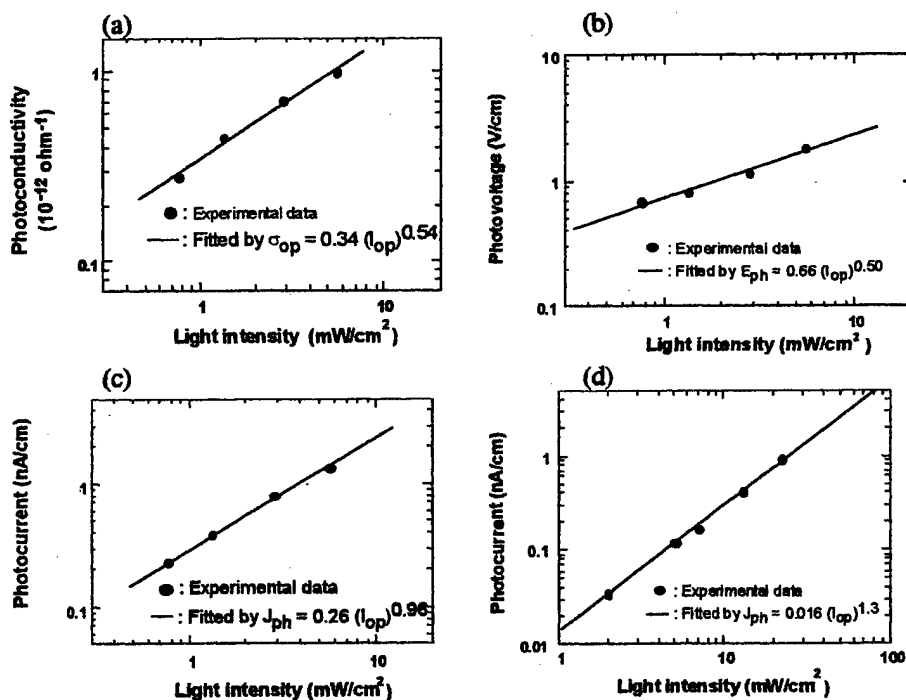


Fig. 1. Dependence of photoconductivity (a), photovoltage (b), and photocurrent (c) on illumination intensity in a PLZT 3/52/48 sample with 1 mm in thickness; (d) the result for a sample with 140 μ m in thickness.

Figure 1(a) shows the plot of photoconductivity (σ_{op}) as a function of light intensity (I_{op}). The exponent relating the photoconductivity and the light intensity was calculated to be 0.54. This is in good agreement with the value of 0.5 derived for the recombination process of the carriers [Eq. (6)]. Figure 1(b) shows the experimental results of the open-circuit photovoltage (E_{ph}) as a function of light intensity. The photovoltage was found to be proportional to the square root of the light intensity, leading to $\beta = 0.5$ [Eq. (5)]. Figure 1(c) shows the experimental results of short-circuit photocurrent (J_{ph}) as a function of light intensity. The parameter β based on Eq. (7) was

calculated to be 0.46, which is very close to the above β value. The depression in β value can be attributed to the incoherent illumination of the mercury lamp.

The experimental data was further analyzed to investigate the effects of incoherent illumination. Since a partial coherence of illuminating light can be achieved in a very small area, an increase in β value is expected in thinner photovoltaic samples. In order to reconfirm this effect, the photocurrent was measured as a function of light intensity in a very thin (140 μm) PLZT sample [Fig. 1(d)]. The parameter β based on Eq. (7) was recalculated and was found to be 0.80, which is higher than β value of 0.46 in the thicker sample (1 mm thickness). These results suggest that the parameter β increases with a decrease in the thickness of photovoltaic sample, due to higher coherency of illumination in thinner samples. This suggests that an enhancement in the photovoltaic properties may be achieved in a very thin sample or by using coherent illumination.

3. SURFACE GEOMETRY DEPENDENCE

Since the photostrictive effect is excited by the absorption of illumination in the surface layer of ceramics, it is apparent that the surface geometry of the photostrictive material will have a strong bearing on the generation of photocurrent and photovoltage. Using a sample thickness closer to the penetration depth will ensure that the entire film will be active and efficiently utilized. Therefore, investigation of photovoltaic response as a function of sample thickness is desired in determining the optimal thickness range with maximum photovoltaic effect. In addition, studying the effect of surface roughness will provide an insight on the absorption dependence of photostriction.

3.1 Thickness Dependence

In order to determine the optimum sample thickness, dependence of photovoltaic effect on sample thickness of PLZT (3/52/48) ceramics doped with 0.5 at.% WO_3 was examined. Photovoltaic response was found to increase with a decrease in sample thickness in PLZT ceramics (see Fig. 2).

A model has been proposed to explain and quantify the observed influence of sample thickness on photovoltaic response [11], where the absorption coefficient is assumed to be independent of light intensity and the photocurrent density is taken to be proportional to

light intensity. The sample is assumed to comprise of thin slices along the thickness direction of the sample.

Figure 2 shows the plot between the normalized photocurrent (i_m) and sample thickness calculated for the external resistance ($R_m = 200 \text{ T}\Omega$). The computed results shows good agreement with the experimental data. With increasing in sample thickness, i_m increases, reaches a maxima, and subsequently it decreases with the sample thickness. The decrease in i_m can mainly be attributed to the dark conductivity (σ_d). The optimum thickness (for the present set of samples) which yields maximum photocurrent is found at $33 \text{ }\mu\text{m}$, which is close to the light (366 nm) penetration depth of the PLZT. The relatively low value of optimum thickness implies that the lower sample thickness will be expected to give better photovoltaic response.

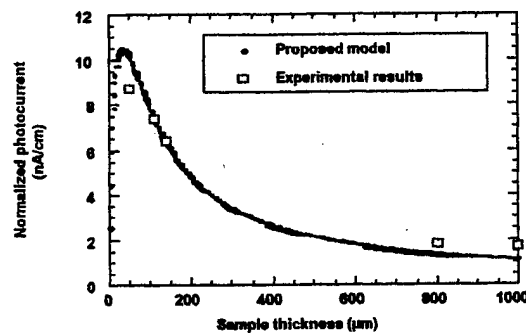


Fig. 2 Sample thickness dependence of the photo-induced current in PLZT 3/52/48 with 0.5 at% of WO_3 .

3.2 Surface Roughness Dependence

The effect of surface roughness on photovoltaic and photostrictive properties was examined in the PLZT sample as used in section 3.1, with different surface roughness obtained by polishing to different surface finishes. The surface roughness was measured by a profilometer (Tencor, Alpha-Step 200) and the average surface roughness was determined using the graphical center line method.

The variation of photovoltaic current with surface roughness is plotted in Fig. 3. The photocurrent increases exponentially with decreasing surface roughness. This is due to the fact that with an increase in surface roughness, the penetration depth of the illumination decreases, while contributions from multiple reflections increase.

A model based on the effect of multireflection has not been proposed for two different shapes, a *sine* profile and a *V* profile roughness. In both these shapes, half of the up-down amplitude was taken as a roughness (r) and the cyclic distance period as a roughness pitch (g). The normalized photo-currents (i_m) computed for the above two surface profiles are plotted also in Fig. 3 as a function of surface roughness. A distance pitch (wavelength) of roughness at $1\text{ }\mu\text{m}$ gave the best fit of the experimental results, which is close to the size of the grain of this PLZT sample.

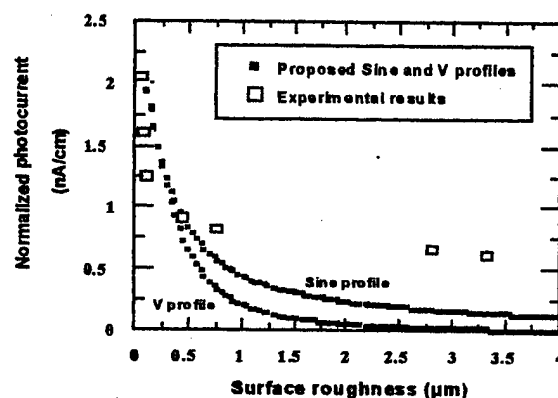


Fig. 3 Variation of photocurrent with surface roughness in the 0.5 at% WO_3 doped PLZT. Comparison with the normalized computed photo-current for the two surface profiles is also made.

4. POTENTIAL APPLICATIONS

We have previously demonstrated the application of photoactuation in PLZT ceramic wafers as photo-driven relay [9] and photo-driven micro walking machine [12]. These devices are designed to use incident light and have neither lead wires nor electric circuits.

Recently, a new application of highly efficient, photostrictive PLZT films on flexible substrates has been conceived for usage in the new class of small vehicles for future space missions [13]. Micro walking device can be designed into arch-shaped photoactuating composite films (unimorph type) with a triangular top (Fig. 4). In order to maximize the photostrictive properties of the sample, the sample thickness can be determined from the proposed model in section 3.1.

This device is driven at their resonance mode under an intermittent illumination. Photo-mechanical resonance in a PLZT

bimorph has been successfully demonstrated [4]. Photo-actuating films may be fabricated from PLZT solutions and coated on one side of a suitable flexible substrate which will then be designed to have a curvature of 1 cm^{-1} . A slight difference in length between the right and left legs is designed in order to provide a slight difference between their resonance frequencies. This facilitates in controlling the device in both clockwise and counterclockwise rotations. A light chopper operating at a frequency close to resonance can be used to illuminate the device, in order to maximize the vibration of the bimorph which will then provide the capability to turn by applying different resonance frequencies of two legs.

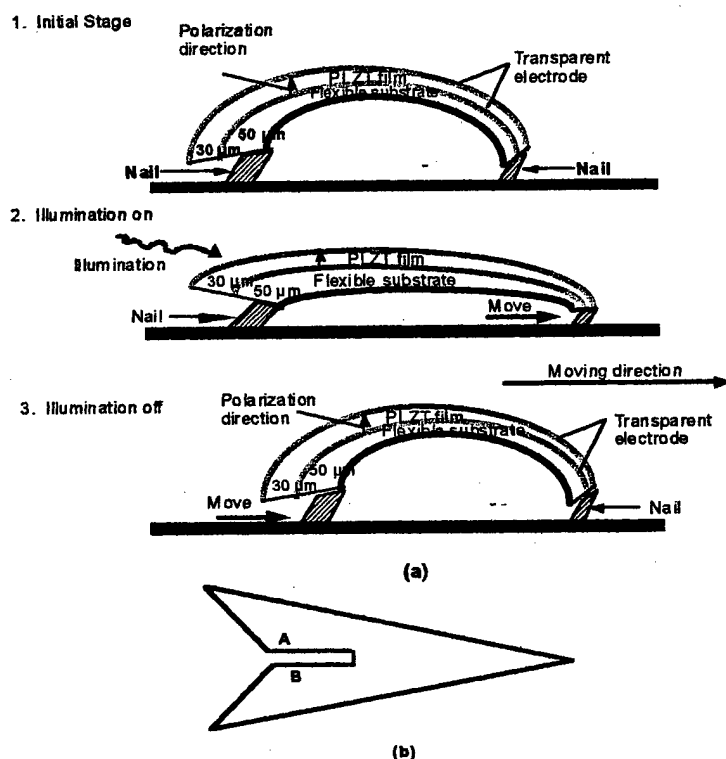


Fig. 4 (a) Schematic diagram of an arch-shaped photoactuating film device, and (b) its triangular top shape.

In conclusion, photostrictive actuators are promising devices in the 21st century because of their remote control capability without interfered by electromagnetic noise. Thin/thick PLZT film approaches seem to be most efficient for these photo-actuation devices.

References

1. Uchino, K. and M. Aizawa, "Photostrictive Actuators Using PLZT Ceramics", Jpn. J. Appl. Phys. Suppl., **24**, 139-141 (1985).
2. Fridkin, V.M., in *Photoferroelectrics*, edited by M. Cardona, P. Fulde, and H.-J. Queisser, Solid-State Sciences 9, (Springer-Verlag, New York), pp. 85-113 (1979).
3. Uchino, K., "New Applications of Photostriction", *Innovations Mater. Res.*, **1**(1), 11-22 (1996).
4. Chu, S.Y. and K. Uchino, "Impurity Doping effect on Photostriction in PLZT Ceramics" *J. Adv. Performance Mater.*, **1**, 129-143 (1994).
5. Tanimura, M. and K. Uchino, "Effect of Impurity Doping on Photostrictive in Ferroelectrics", *Sensors and Materials*, **1**, 47-56 (1988).
6. Poosanaas, P., K. Tonooka, and K. Uchino, "Photostrictive Actuators", *Mechatronics* **10**, 467-487 (2000).
7. Hecht, E., in *Optics*, with contributions by Alfred Zajac, 2nd ed., (Addison-Wesley Publishing, Massachusetts), pp. 44, 81-104, 610-616 (1987).
8. Kittel, C., in *Introduction to Solid States Physics*, 7th ed., (John Wiley & Sons, Inc., New York), p388 (1996).
9. Sada, T., M. Inoue, and K. Uchino, "Photostriction in PLZT Ceramics", *J. Ceram. Soc. Jpn. Inter. Ed.*, **95**, 499-504 (1987).
10. Nonaka, K., M. Akiyama, A. Takase, T. Baba, K. Yamamoto, and H. Ito, "Nonstoichiometry Effects and Their Additivity on Anomalous Photovoltaic Efficiency in Lead Lanthanum Zirconate Titanate Ceramics", *Jpn. J. Appl. Phys.*, **34**, 5380-5383 (1995).
11. Poosanaas, P., A. Dogan, S. Thakoor, and K. Uchino, "Influence of Sample Thickness on the Performance of Photostrictive Ceramics", *J. Appl. Phys.*, **84** (3), 1508-1512 (1998).
12. Uchino, K., "Micro Walking Machine Using Piezoelectric Actuators", *J. Rob. Mech.*, **124**, 44-47 (1989).
13. Thakoor, S., J.M. Morookian, and J.A. Cutts, "The Role of Piezoceramics Microactuation for Advanced Mobility", *Conf. Proc. 10th IEEE Int'l Symp. on Appl. Ferroelectrics*, **1**, 205-211 (1996).

APPENDIX 66

PHOTOSTRICTIVE ACTUATORS

- New Perspective -

K. UCHINO^a, P. POOSANAAS^b, and K. TONOOKA^c

^a *International Center for Actuators and Transducers, Materials Research Laboratory, The Pennsylvania State University University Park, PA 16802, USA;* ^b *National Metal and Materials Technology Center, Bangkok 10400, Thailand;* ^c *Materials Division, Hokkaido National Industrial Research Institute, Sapporo, Japan*

Photostrictive materials, exhibiting light-induced strains, are of interest for future generation wireless remote control photo-actuators, micro-actuators, and micro-sensors applications. (Pb, La)(Zr, Ti) O₃ (PLZT) ceramics doped with WO₃ exhibit large photostriction under uniform illumination of near-ultraviolet light. Using a bimorph configuration, a photo-driven relay and a micro walking device have been demonstrated. However, for the fabrication of these devices, higher response speed must be achieved. The present paper reviews some theoretical models for the photovoltaic effect first, then enhanced performance through sample thickness and surface characteristics, finally its potential future applications.

Keywords: Photovoltaic effect, Photostriction, Actuator, Surface characteristics, PLZT ceramics

1. INTRODUCTION

The continuing thrust towards greater miniaturization and integration of microrobotics and microelectronics has resulted in significant work towards development of ceramic actuators, utilizing their wavelength-dependent optical actuation mechanisms. In the recent days, *photostrictive actuators* - which directly converts the photonic energy to mechanical motion - have drawn significant attention for their potential usage in microactuation and microsensing applications. Optical actuators are also anticipated to be used as the driving component in optically controlled "electromagnetic-noise free" systems. The photostrictive effect has also recently been used in fabricating a photophonic device, where light was transformed directly

into sound from the mechanical vibration induced by intermittent illumination.

The photostrictive effect has been studied mainly in ferroelectric polycrystalline materials for potential commercial applications. Lanthanum-modified lead zirconate titanate (PLZT) ceramic is one of the most promising photostrictive materials due to its relatively high piezoelectric coefficient and ease of fabrication. However, previous studies have shown that for commercial applications, improvements in photovoltaic efficiency and response speed of the PLZT ceramics are essential. The improvement in photostrictive properties require consideration of several parameters, such as material parameters, processing condition and microstructure, and sample configuration and performance testing conditions.

This paper reviews some models for explaining the photovoltaic effect first, then the influence of sample geometry, and finally describes the potential applications.

2. PHOTOSTRICTIVE EFFECT

In principle, photostrictive effect arises from a superposition of the photovoltaic effect, i.e. generation of large voltage from the irradiation of light, and the converse-piezoelectric effect, i.e. expansion or contraction under the voltage applied [1].

The photostrictive phenomenon has been observed in certain ferroelectric materials. The figure of merit of photostriction is generally expressed as the product of photovoltage, E_{ph} , and the piezoelectric constant, d_{33} . Therefore, for application purposes, enhancement and/or optimization of photostrictive properties requires consideration of both the terms in the figure of merit. Recently, PLZT ceramics have gained considerable attention due to their excellent photovoltaic properties, high d_{33} and ease of fabrication.

When a non-centrosymmetric ferroelectric material is illuminated with uniform light having a wavelength corresponding to the absorption edge of the material, a steady photovoltage/photocurrent is generated [2]. In some materials, the photovoltage generated is greater than the band-gap energy, and can be of the order of several kV/cm. This phenomenon, referred to as the anomalous photovoltaic effect (APV), is different from the phenomenon in the p-n junction of semiconductors (e.g. solar battery) [3, 4].

The origin of photovoltaic effect is not yet clear, even though several models have been proposed on the mechanism of photovoltaic

effect. The key issues in understanding the APV mechanism are both, impurity doping and crystal asymmetry. We proposed previously one of the current source models, based on the electron energy band model for PLZT ceramics [5]. The donor impurity levels induced in accordance with La doping are present slightly above the valence band. The transition from these levels with an asymmetric potential due to the crystallographic anisotropy may provide the *preferred* momentum to the electron. The asymmetric crystal exhibiting a photovoltaic response is also piezoelectric in principle, and therefore, a photostriction effect is expected as a coupling of the bulk photovoltaic voltage with the piezoelectric constant.

Recently another model of APV has also been proposed based on the voltage source mechanism [6]. The photovoltaic properties are attributed to the photocarriers and internal electric fields generated by near-UV illumination. The optical nonlinearity of the second order, which is popularly introduced in ferroelectrics, has been proposed as the origin of photo-induced dc field generation [6]. When an alternating electric field at an optical frequency is applied (i.e., light illumination), the average of the local electric field E_{local} is not zero, but can be calculated as:

$$\overline{E_{local}} = \frac{1}{6} \gamma \chi_2 E_{op}^2 \quad (1)$$

where γ is the Lorenz factor of this crystal, χ_2 is the nonlinear susceptibility of the second order, and E_{op} is the electric field at an optical frequency (THz) [7]. Because the nonlinear effect is affected by the degree of coherence, considering the depression of nonlinear effect due to the incoherency, the expression for the effective dc field induced by incoherent light source may be modified as:

$$\overline{E_{local}} = c_1 \gamma \chi_2 (E_{op}^2)^\beta \quad (2)$$

where c_1 is a constant and β is a parameter expressing the depression effect. The value of parameter β is expected to lie between 0 and 1. Replacing the variable E_{op}^2 with the intensity (I_{op}), the following expression for the average induced (dc) field due to the incoherent light can be obtained:

$$E_{dc} = \overline{E_{local}} = c_2 \gamma \chi_2 (I_{op})^\beta \quad (3)$$

where c_2 is a constant and E_{dc} is the effective dc field for photoinduced carriers. Note that the induced field, E_{dc} , is proportional to the nonlinear susceptibility as well as the Lorentz factor, γ .

3. SURFACE GEOMETRY DEPENDENCE

Since the photostrictive effect is excited by the absorption of illumination in the surface layer of ceramics, it is apparent that the surface geometry of the photostrictive material will have a strong bearing on the generation of photocurrent and photovoltage. Using a sample thickness closer to the penetration depth will ensure that the entire film will be active and efficiently utilized. Therefore, investigation of photovoltaic response as a function of sample thickness is desired in determining the optimal thickness range with maximum photovoltaic effect. In addition, studying the effect of surface roughness will provide an insight on the absorption dependence of photostriction.

In order to determine the optimum sample thickness, dependence of photovoltaic effect on sample thickness of PLZT (3/52/48) ceramics doped with 0.5 at.% WO_3 was examined. Photovoltaic response was found to increase with a decrease in sample thickness in PLZT ceramics (see Fig. 1).

A model has been proposed to explain and quantify the observed influence of sample thickness on photovoltaic response [8], where the absorption coefficient is assumed to be independent of light intensity and the photocurrent density is taken to be proportional to light intensity. The sample is assumed to comprise of thin slices along the thickness direction of the sample.

Figure 1 shows the plot between the normalized photocurrent (i_m) and sample thickness calculated for the external resistance ($R_m = 200 \text{ T}\Omega$). The computed result shows good agreement with the experimental data. With increasing in sample thickness, i_m increases, reaches a maximum, and subsequently it decreases with the sample thickness. The decrease in i_m can mainly be attributed to the dark conductivity (σ_d). The optimum thickness (for the present set of samples) which yields maximum photocurrent is found at $33 \mu\text{m}$, which is close to the light (366 nm) penetration depth of the PLZT. The relatively low value of optimum thickness implies that the lower sample thickness will be expected to give better photovoltaic response.

The variation of photovoltaic current with surface roughness is plotted in Fig. 2. The photocurrent increases exponentially with decreasing surface roughness. This is due to the fact that with an increase in surface roughness, the penetration depth of the illumination decreases, while contributions from multiple reflections increase.

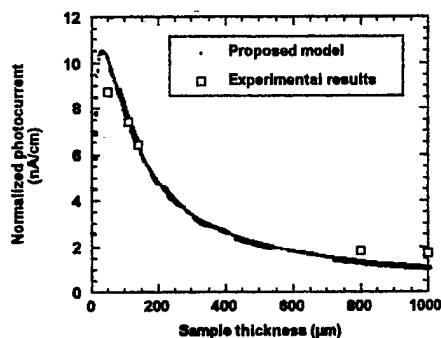


Fig. 1 Sample thickness dependence of the photo-induced current in PLZT 3/52/48 with 0.5 at% of WO_3 .

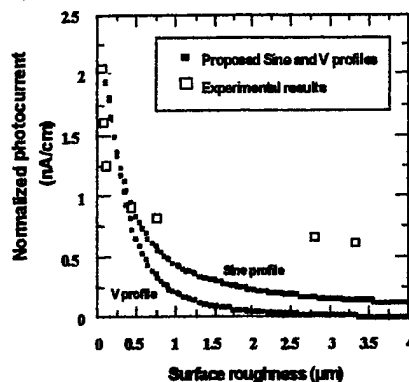


Fig. 2 Surface roughness dependence of the photo-induced current in PLZT.

4. POTENTIAL APPLICATIONS

We have previously demonstrated the application of photoactuation in PLZT ceramic wafers as photo-driven relay [9] and photo-driven micro walking machine [10]. These devices are designed to use incident light and have neither lead wires nor electric circuits.

Recently, a new application of highly efficient, photostrictive PLZT films on flexible substrates has been conceived for usage in the new class of small vehicles for future space missions [11]. Micro walking device can be designed into arch-shaped photoactuating composite films (unimorph type) with a triangular top (Fig. 3). In order to maximize the photostrictive properties of the sample, the sample thickness can be chosen around $33 \mu\text{m}$.

This device is driven at their resonance mode under an intermittent illumination. Photo-mechanical resonance in a PLZT bimorph has been successfully demonstrated [4]. Photo-actuating films may be fabricated from PLZT solutions and coated on one side of a suitable flexible substrate which will then be designed to have a curvature of 1 cm^{-1} . A slight difference in length between the right and left legs is designed in order to provide a slight difference between their resonance frequencies. This facilitates in controlling the device in both clockwise and counterclockwise rotations. A light chopper operating at a frequency close to resonance can be used to illuminate the device, in order to maximize the vibration of the bimorph which will then provide the capability to turn by applying different resonance frequencies of two legs.

In conclusion, photostrictive actuators are promising devices in the 21st century because of their remote control capability without interfered by electromagnetic noise. Thin/thick PLZT film approaches seem to be most efficient for these photo-actuation devices.

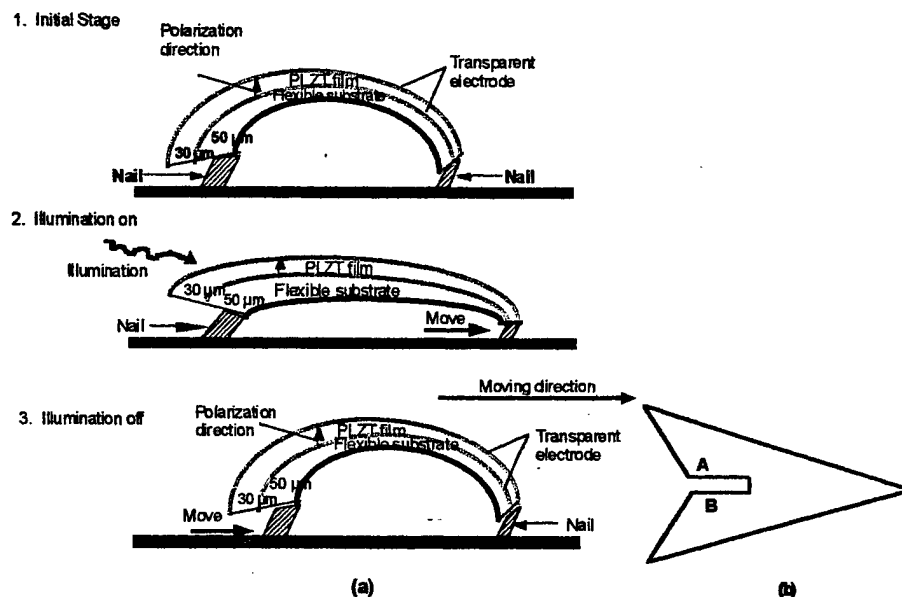


Fig. 3 (a) Schematic diagram of an arch-shaped photoactuating film device, and (b) its triangular top shape.

References

1. Uchino, K. and M. Aizawa, *Jpn.J.Appl.Phys. Suppl.*, **24**, 139-141 (1985).
2. Fridkin, V.M., in *Photoferroelectrics*, edited by Cardona, Fulde, and Queisser, *Solid-State Sci.* **9**, (Springer-Verlag, NY), pp. 85-113 (1979).
3. Uchino, K., *Innovations Mater. Res.*, **1**(1), 11-22 (1996).
4. Chu, S.Y. and K. Uchino, *J.Adv.Performance Mater.*, **1**, 129-143 (1994).
5. Tanimura, M. and K. Uchino, *Sensors and Materials*, **1**, 47-56 (1988).
6. Poosanaas, P., K. Tonooka, and K. Uchino, *Mechatronics* **10**, 467-487 (2000).
7. Hecht, E., in *Optics*, by Alfred Zajac, 2nd ed., (Addison-Wesley Publishing, Massachusetts), pp. 44, 81-104, 610-616 (1987).
8. Poosanaas, P., A. Dogan, S. Thakoor, and K. Uchino, *J. Appl. Phys.*, **84** (3), 1508-1512 (1998).
9. Sada, T., M. Inoue, and K. Uchino, *J. Ceram. Soc. Jpn. Inter. Ed.*, **95**, 499-504 (1987).
10. Uchino, K., *J. Rob. Mech.*, **124**, 44-47 (1989).
11. Thakoor, S., J.M. Morookian, and J.A. Cutts, *Conf. Proc. 10th IEEE Int'l Symp. on Appl. Ferroelectrics*, **1**, 205-211 (1996).

APPENDIX 67

Influence of Composition and Dopant on Photostriction in Lanthanum-Modified Lead Zirconate Titanate Ceramics

¹P. POOSANAAS, ²K. TONOOKA, ³I. R. ABOTHU, ¹S. KOMARNENI, AND ¹K. UCHINO*

¹International Center for Actuators and Transducers, Materials Research Laboratory, The Pennsylvania State University, University Park, PA 16802; ²Materials Division, Hokkaido National Industrial Research Institute, Sapporo, Japan;

³Institute of Materials Research and Engineering (IMRE), Singapore, 119260

ABSTRACT: The anomalous photovoltaic effect, i.e., substantial voltage generation exceeding band gap energies, by homogeneous illumination in the non-centrosymmetric materials is a well-known phenomenon. This mechanism is fundamentally different from those observed in heterojunctions/homojunctions (i.e., solar cells) based on semiconductor materials with a symmetric crystal structure. Recently, light induced strain termed as Photostriction, has been demonstrated in non-centrosymmetric perovskite ferroelectrics as lanthanum-modified lead zirconate titanate (PLZT) ceramics. PLZT ceramics have gained considerable attention due to their large photostrictive responses. When a light is illuminated on a polarized photostrictive bimorph, a large photovoltage of the order of kV/mm is generated across its length in the spontaneous polarization direction which results in strain generation by converse-piezoelectric effect and caused the bimorph to deflect in the direction away from the illumination. The photoactuation has been demonstrated in PLZT ceramic wafers as two different kinds of actuators, (i) photo-driven relay and (ii) photo-driven micro walking machine. These materials are also promising for the photo-acoustic device (e.g., Photophone) of the optical communication system. However, photostriction being a recently observed phenomenon, is far from optimum condition. It is expected that the optimization with respect to materials and microstructural characteristics will lead to a substantial enhancement in the photoactuation efficiency. Increasing the photoactuation efficiency will eliminate the need for electrical energy, and will open up numerous possibilities of contactless actuators. In this paper the influence of composition dependence and impurity doping effects on microstructure and photostrictive responses of PLZT ceramics have been investigated.

INTRODUCTION

MATERIALS exhibiting the photostrictive effect have been focus of attention for their potential usage as wireless photodriven actuators, relays, and microrobots. (Pb, La)(Zr, Ti) O₃ (PLZT) ceramics doped with WO₃ exhibit large photostriction under uniform illumination of near-ultraviolet light [Tanimura and Uchino (1988), Chu and Uchino (1994), and Nonaka et al. (1996)]. These materials are also promising candidates for use in photoacoustic devices such as photophones in optical communication systems [Chu and Uchino (1994)]. The photostrictive properties of PLZT ceramics are influenced by material parameters (e.g., composition and stoichiometry, dopant type and concentration), processing conditions (e.g., processing route and parameters), and performance testing conditions (e.g., surface characteristics and illumination).

In order to utilize the photostrictive materials for commercial applications, their performance and efficiency need to be further improved. Increasing the performance of photostrictive materials will also open up numerous applications

as contactless actuators. The present research was aimed towards improving the performance of photostrictive materials by optimizing the material parameters (composition and dopant type and concentration) of lanthanum-modified lead zirconate titanate (PLZT) ceramics.

EXPERIMENTAL PROCEDURE

PLZT compositions are given in the form of Pb_{1-x}La_x(Zr_yTi_{1-y})_{1-x/4}O₃ (abbreviated as PLZT X/Y/Z, X = 100x; Y = 100y; and Z = 100(1-y)). PLZT ceramics with concentration of La varying from 2–5 at%, Zr/Ti ratio varying from 48/52 to 54/46 were prepared by the conventional oxide mixing process. These series of compositions are located in the area around the morphotropic phase boundary (MPB), including the particular composition 3/52/48 which was reported to exhibit the maximum photovoltaic effect in the previous studies [Uchino and Aizawa (1985), Chu and Uchino (1995)]. In order to study the effects of impurity doping on photostriction of PLZT ceramics. PLZT (3/52/48) doped with Nb⁵⁺, Mo⁶⁺, and Gd³⁺ were also prepared by the conventional oxide mixing process. The details of the conventional oxide mixing process was reported in an earlier publication [Poosanaas et al. (1997)].

*Author to whom correspondence should be addressed. E-mail address kenji-uchino@alpha.mrl.psu.edu

Phase identification was performed using X-ray diffraction (Scintag diffractometer, Vax 3100 System). All samples exhibited perovskite structures. Microstructure and grain size of the samples were observed by scanning electron microscopy (ISI-DS 130). Dielectric properties of PLZT samples were measured with an impedance analyzer (HP-4284A). Samples for dielectric measurements were polished to about 10 mm in diameter and 1 mm in thickness, then electroded with platinum (Pt) by sputtering. Piezoelectric properties of all the samples were measured by using a Berlincourt d_{33} meter (Channel Products, Inc.) at 100 Hz. Samples for piezoelectric measurement were of the same configuration as for dielectric measurements. They were poled in silicone oil at 120 °C under a 2 kV/mm electric field for 10 min.

Photovoltaic measurements were done using a high-input-impedance electrometer (Keithley 617), while the photostriction was measured by a displacement sensor (LVDT, Millitron model 1301). These measurements were done by radiating the light perpendicular to the polarization direction. The samples of $5 \times 5 \times 1$ mm³ were cut and polished for these measurements. The 5×1 mm² surfaces were platinum electroded and poled. A high pressure mercury lamp (Ushio Electric USH-500D) was used as a light source for the measurement. The white radiation was passed through an IR blocking filter and an UV bandpass filter to obtain a beam with a maximum strength around 366 nm and an intensity of 3.25 mW/cm², before illuminating the samples (5×5 mm² polished surface).

RESULTS AND DISCUSSION

Photostrictive Effect Near the Morphotropic Phase Boundary

THE EFFECT OF COMPOSITION ON THE GRAIN SIZE

The photovoltaic and piezoelectric effects are reported to depend on the grain size [Sada, Inoue, and Uchino (1987)]. PLZT ceramic samples were polished, thermally etched and observed under an SEM in order to study the effect of composition on the grain size. The average grain sizes, determined by the intercept method, were in the range of 1 to 5 μ m. Figure 1 shows the variation of average grain size as a function of Zr/Ti ratio and La content. The average grain size decreases with La addition. As Zr/Ti ratio increases and approaches the MPB region, the average grain size increases [Poosanaas and Uchino (1998)]. This behavior agrees well with the previous study reported by Haertling and Land (1971) and Akbas, Reaney, and Lee (1996). However, the grain size distribution does not seem to reflect directly on the photovoltaic property contour discussed below.

PIEZOELECTRIC PROPERTIES

The piezoelectric constant (d_{33}) contour map for the PLZT system is plotted in Figure 2. The maximum d_{33} was also found at the MPB, which increased with increasing Zr/Ti ratio [Poosanaas and Uchino (1998)].

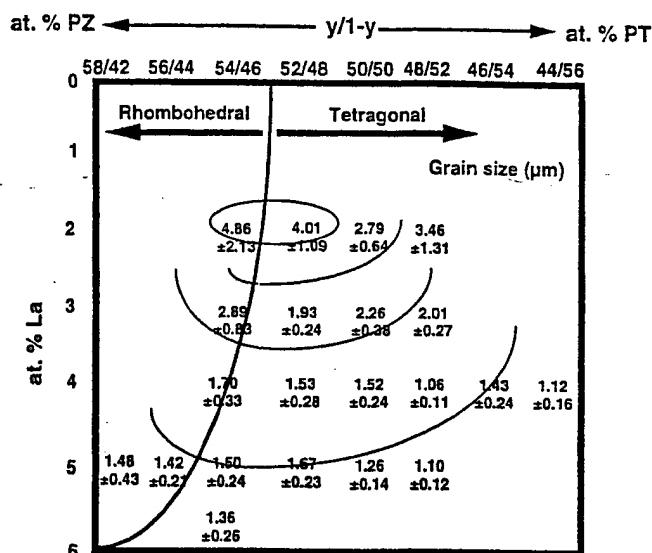


Figure 1. The contour map of the average grain size in PLZT ceramics. Larger grain sizes were found along the MPB of PLZT system.

PHOTOVOLTAIC PROPERTIES

In an earlier investigation [Sada, Inoue, and Uchino (1987)], the highest photovoltaic responses in the PLZT system were observed in the composition PLZT 3/52/48. However, due to the large composition interval used in this study, it may be possible that the optimal composition was only approximately identified. This would be of importance especially around the MPB where small composition changes significantly influence the photovoltaic properties. The contour maps of the photocurrent and photovoltage in the PLZT phase diagram are shown in Figures 3 and 4, respectively. In these two figures, the solid circles indicate the location of PLZT 3/52/48, which correspond to the earlier reported maximum photocurrent and photovoltage.

In the present work, with measurements made for much smaller compositional intervals, the maximum photocurrent and photovoltage were observed at different compositions of

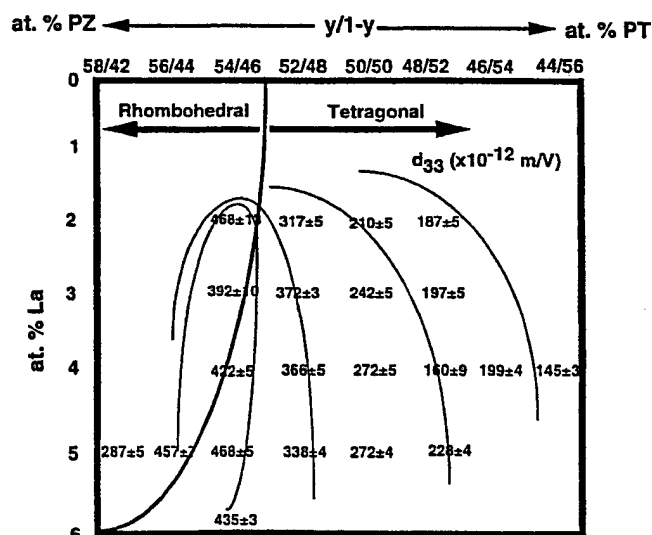


Figure 2. Variation of piezoelectric constant (d_{33}) in the PLZT system. The maxima of d_{33} have been found along the MPB.

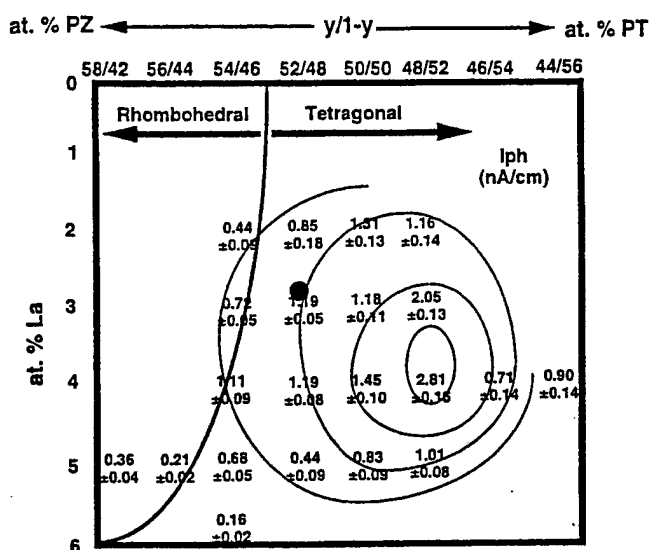


Figure 3. The contour map of photocurrent in PLZT ceramics. The maximum photocurrent was found at PLZT 4/48/52 having tetragonal phase. ● represented the maximum photocurrent composition reported earlier.

PLZT ceramics. The maximum photocurrent was observed in PLZT 4/48/52, which corresponds to the tetragonal phase. The maximum photovoltage was observed in PLZT 5/54/46, which is along the MPB. The magnitudes of photocurrent and photovoltage were enhanced by a factor of 2 or more for these new compositions [Poosanaas and Uchino (1998)].

It must be noted that the maximum photocurrent and photovoltage are obtained at different compositions. Although, the addition of La content increases the impurity level and thereby photocurrent, the increase in La content and Zr/Ti ratio also promotes the stability of higher symmetry cubic phase resulting in a decrease in photocurrent at much higher La contents (e.g., 5 at% La content). This provides the maximum point of the photocurrent at PLZT 4/48/52.

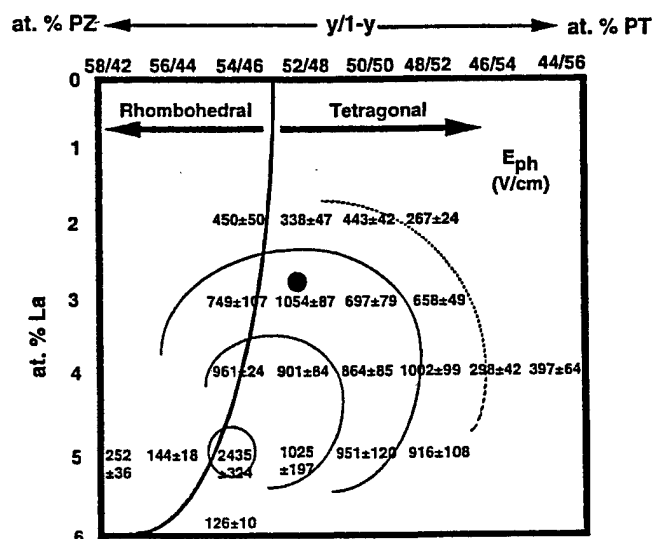


Figure 4. The contour map of photovoltage in PLZT ceramics. Photovoltage was found to be maximum at PLZT 5/54/46 and along the MPB of PLZT system. ● represented the composition with maximum photovoltage reported earlier.

The contour map of photoconductance in the PLZT phase diagram is shown in Figure 5. It can be noted that the photoconductance is low along the MPB. The minimum photoconductance corresponds to the composition PLZT 5/54/46, where a maximum in photovoltage was observed.

Since the maximum photocurrent, which governs the response speed, and maximum photovoltage, which governs the magnitude of strain, are located at different compositions of PLZT ceramics, new figures of merit for photostriction considering both these terms are required. These new figures of merit for photostriction can be derived as follows:

The photoinduced strain as a function of time, t , is given by:

$$x_{ph} = d_{33}E_{ph}\left(1 - \exp\left(\frac{-t}{RC}\right)\right) \quad (1)$$

For $t \ll RC$, the above equation reduces to:

$$x_{ph} = d_{33}E_{ph}\left(\frac{t}{RC}\right) \quad (2)$$

thus the figure of merit for speed is defined as $d_{33}I_{ph}/C$, because the sample resistance, R , is provided by E_{ph}/I_{ph} .

For $t \gg RC$, the equation reduces to the figure of merit for the saturated strain:

$$x_{ph} = d_{33}E_{ph} \quad (3)$$

where x_{ph} is the photo-induced strain, d_{33} , the piezoelectric constant of the materials, E_{ph} , photovoltage, I_{ph} , photocurrent, and C is the capacitance of the material, respectively.

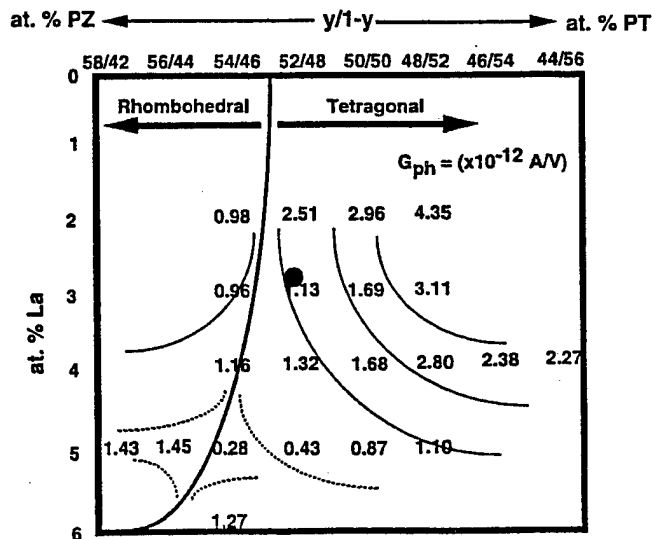


Figure 5. The contour map of photoconductance in PLZT system. Photoconductance is minimum along the MPB. The minimum photoconductance was found at PLZT 5/54/46 where it also exhibits the maximum photovoltage.

In order to obtain a high photo-induced strain, materials with high d_{33} and E_{ph} are needed. On the contrary, for high response speed, materials with high d_{33} , I_{ph} and low dielectric constant are required.

Impurity Doping Effects

Additions of small quantities of impurity atoms to PLZT ceramics have made dramatic effects on microstructure and photovoltaic and photostrictive properties of PLZT ceramics. So far, only the influence of two B-sites donor dopants, W^{6+} and Ta^{5+} , have been intensively examined and reported in the literature [Chu and Uchino (1994, 1995), Sada, Inoue, and Uchino (1987), and Nonaka et al. (1995)]. Therefore, it will be of great interest to study the photovoltaic and photostrictive effects of the dopants Nb^{5+} and Mo^{6+} , which are in the same column of periodic table as Ta^{5+} and W^{6+} .

The rare earth metal dopants have also been observed to profoundly affect the photoluminescence of PLZT ceramics. It is therefore, expected that they will influence the photovoltaic properties of PLZT ceramics. Substantial work has been carried out on lanthanum modified PZT ceramics with enhancement in performance. Lanthanum substitution for Pb^{2+} reduces the distortion (anisotropy) of the oxygen octahedral (ABO_3) unit cell and thereby reduces the light scattering. It also produces a significant number of lattice vacancies which improves densification, and results in highly uniform microstructure with reduced tendency of grain growth. However, little work has been reported on the PLZT doped by other lanthanides such as Gd^{3+} which has the same trivalent state and an ionic radius close to the A-site cations ($Pb^{2+} = 1.20$ Å, $La^{3+} = 1.016$ Å, and $Gd^{3+} = 0.938$ Å) [Weast et al. (1969)]. Similar to La^{3+} , the Gd^{3+} dopant is also expected to substitute in the Pb^{2+} site, main-

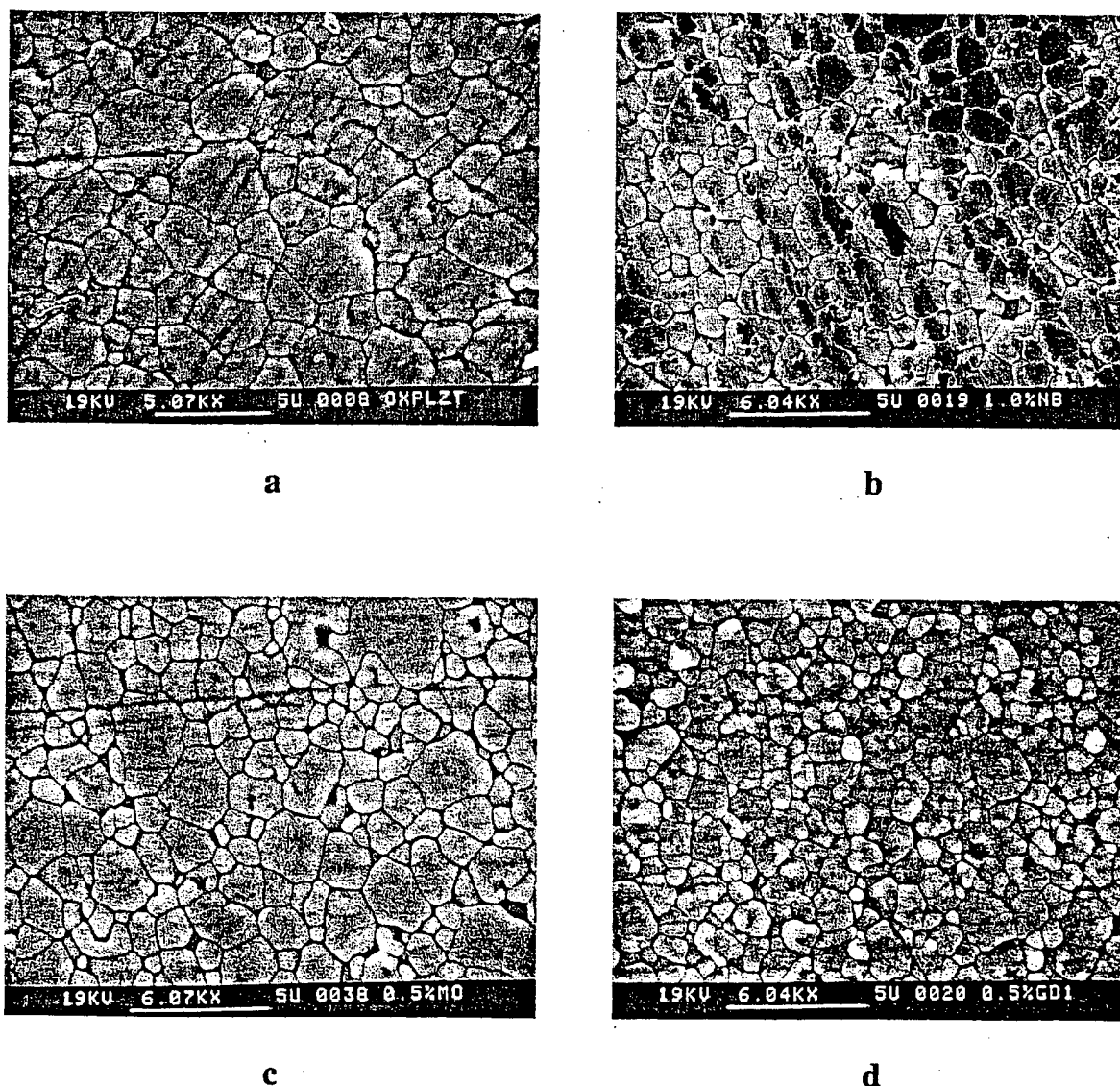


Figure 6. SEM micrographs of PLZT (3/52/48) ceramics (a) undoped; (b) doped with 1 at % Nb_2O_5 ; (c) doped with 0.5 at% MoO_3 ; and (d) doped with 0.5 at% Gd_2O_3 .

tain the stoichiometry and enhance the PZT properties. In this paper, the photovoltaic and photostrictive effects of Nb^{5+} , Mo^{6+} , and Gd^{3+} doped PLZT (3/52/48) ceramics fabricated by the conventional oxide mixing method have been investigated.

MICROSTRUCTURE ANALYSIS

SEM micrographs of the thermally etched surfaces of the undoped PLZT and selected micrographs of Nb^{5+} , Mo^{6+} , and Gd^{3+} doped PLZT ceramics samples are shown in Figure 6 (a)–(d). The mean grain sizes, determined from the intercept method, are plotted in Figure 7 as a function of dopant concentration. Figure 7 indicates that doping with Nb^{5+} is effective in suppressing the grain growth of PLZT ceramics for all concentrations. In the case of Gd^{3+} doped PLZT ceramics, anomalous grain growth was observed with the addition of a small amount (0.3 at%) of Gd_2O_3 as shown in Figure 8. However, with larger additions of Gd^{3+} , grain growth is suppressed, resulting in a minimum grain size corresponding to 0.5 at% Gd_2O_3 content.

In the PLZT ceramics doped with Mo^{6+} , the grain size decreases with dopant concentration. The minimum grain size was found at a concentration of 0.5 at% MoO_3 . The decrease in grain size with dopant addition is attributed to the association of charged vacancies (formed by donor dopants) and impurity ions, which decreases the grain boundary mobility. In this study, addition of 0.5 at% Gd_2O_3 was found to be the most effective and resulted in a grain size decrease of PLZT ceramics by more than 100%.

DIELECTRIC AND PIEZOELECTRIC PROPERTIES

Figure 9 shows the variation of room temperature dielectric constant (ϵ_{RT}) as a function of MoO_3 , Nb_2O_5 , and Gd_2O_3 concentration measured at 1 kHz. The room temperature dielectric constant was found to decrease with increasing MoO_3 content. This was partially due to the lower grain size observed in the Mo^{6+} doped PLZT ceramics. In the case of Gd^{3+} doped PLZT ceramics, the ϵ_{RT} decreased with a small increase in Gd_2O_3 content and then increased. The ϵ_{RT} showed the minimum at 0.5 at% Gd_2O_3 content, which also corresponds to the minimum grain size. However, Nb^{5+} was found to increase the ϵ_{RT} which is generally explained on the basis of the charge compensation due to the Pb evaporation during sintering by creating donor impurities of Nb^{5+} [Murty et al. (1992) and Yoon et al. (1998)].

Figure 10 shows the piezoelectric constant (d_{33}) as a function of MoO_3 , Nb_2O_5 , and Gd_2O_3 concentration. It can be observed that all dopants cause a decrease in the parameter d_{33} . This is mainly due to the dopant-influenced decrease in grain size, which reduces the domain wall contribution to the piezoelectric properties and piezoelectric constant. Nb -doped PLZT almost sustains similar magnitude of d_{33} , probably due to the easy domain wall mobility as discussed above.

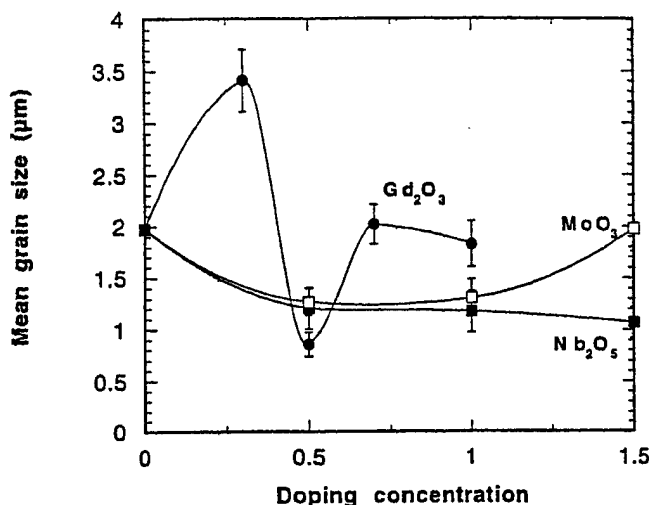


Figure 7. Variation of mean grain size as a function of doping concentration in PLZT (3/52/48) ceramics fabricated by oxide mixing method.

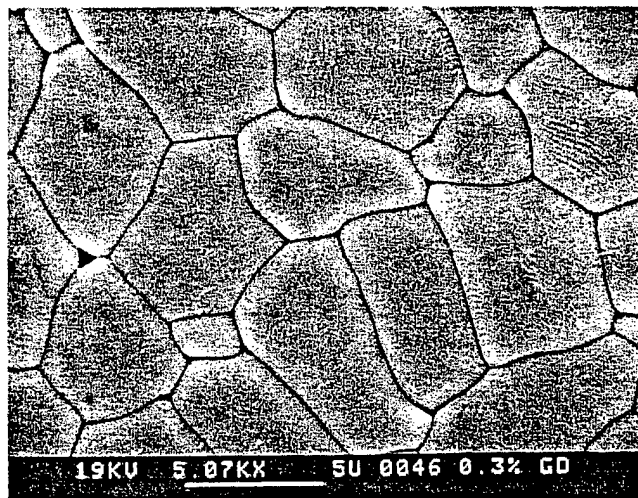


Figure 8. SEM micrograph of 0.3 at% Gd_2O_3 doped PLZT (3/52/48) ceramic. The anomalous grain growth was observed.

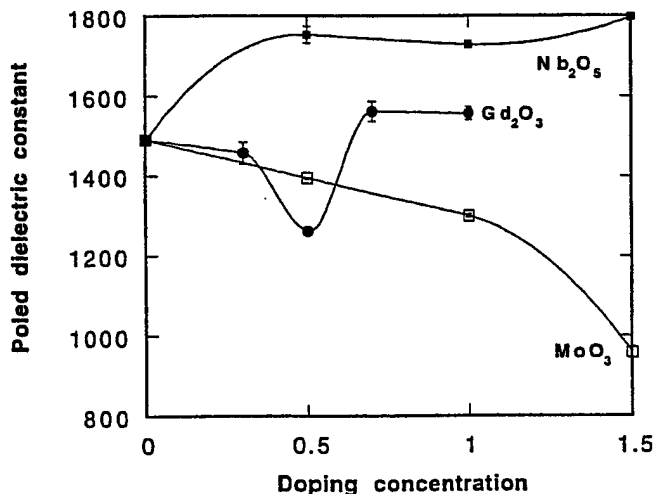


Figure 9. Variation of room temperature dielectric constant with doping concentration in PLZT (3/52/48) ceramics.

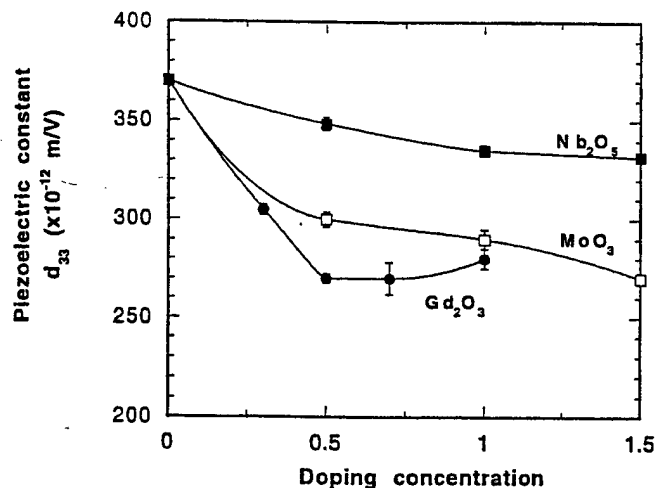


Figure 10. The piezoelectric constant as a function of doping concentration in PLZT (3/52/48) ceramics.

PHOTOVOLTAIC AND PHOTOSTRICTIVE PROPERTIES

Figures 11 and 12 show the variation of photovoltage and photocurrent with MoO_3 , Nb_2O_5 , and Gd_2O_3 concentration under an illumination intensity of 3.25 mW/cm^2 . The maximum values of photovoltage and photocurrent were obtained at 0.5 at% of MoO_3 , 1 at% Nb_2O_5 , and at 0.5 at% Gd_2O_3 concentrations. The maximum induced photocurrent was of the order of nA/cm, whereas, the maximum photovoltage was more than 1 kV/cm. A modified value of photocurrent density (nA/cm) was used in this paper by integrating the current with respect to the light penetration depth since light is almost absorbed on the surface region of the sample. The higher magnitudes of photovoltage achieved in smaller grain size samples (0.5 at% Gd_2O_3 and 0.5 at% MoO_3) suggests that photovoltage increases with decreasing grain size. This is consistent with earlier reported work, where the photovoltage was found to increase with the number of grain boundaries [Brody (1975)]. The

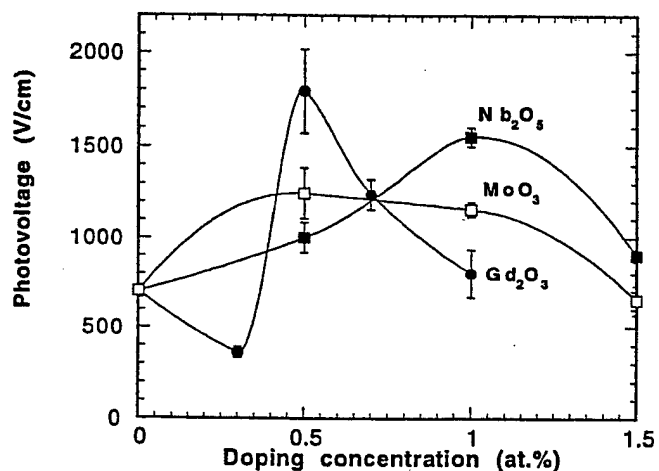


Figure 11. Photovoltage as a function of doping concentration in PLZT (3/52/48) ceramics.

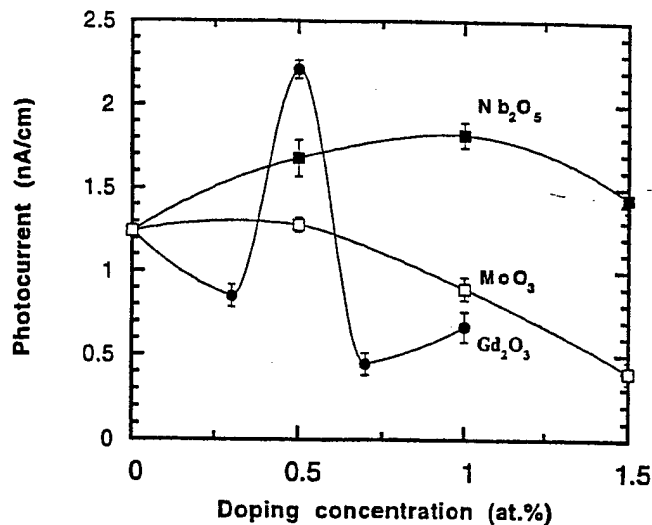


Figure 12. Photocurrent as a function of doping concentration in PLZT (3/52/48) ceramics.

PLZT ceramic samples doped with 0.5 at% Gd_2O_3 concentration, resulted in smallest grain size as well as the maximum photocurrent and photovoltage values. The lowest photovoltage among all the samples was observed in the composition with 0.3 at% Gd_2O_3 concentration, which can be attributed to the anomalous grain growth observed in this sample.

Figure 13 shows the photoinduced strain as a function of dopant type and concentration. The maximum photostriction among all the samples was found in PLZT ceramics doped with 0.5 at% Gd_2O_3 . Similarly, the maximum photostriction was observed at 0.5 at% MoO_3 and 1.0 at% Nb_2O_5 concentrations in PLZT ceramics doped with Nb^{5+} and Mo^{6+} dopants. Since all the dopants decreased the d_{33} of PLZT based ceramics, the photo-induced strain is solely governed by the photovoltage effect.

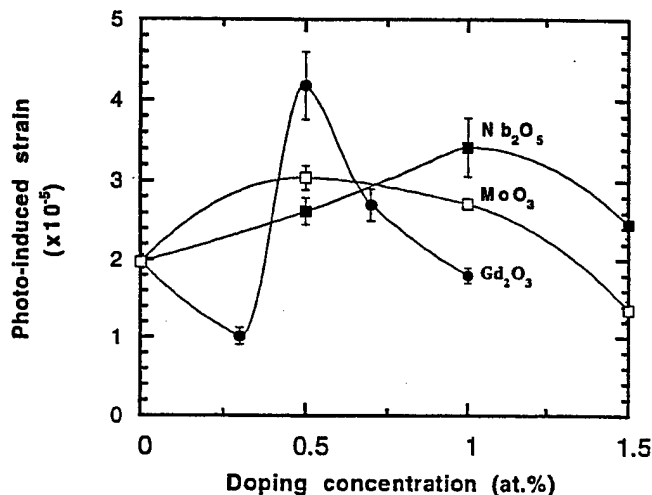


Figure 13. Photo-induced strain as a function of doping concentration in PLZT (3/52/48) ceramics.

CONCLUSION

A rigorous investigation of the composition dependence, especially near the morphotropic boundary, on photovoltaic properties in PLZT ceramics was carried out in order to examine compositions for the maximum photovoltaic properties. The maximum photocurrent was found at PLZT 4/48/52 which is in the tetragonal phase while the maximum photovoltage was found at PLZT 5/54/46 which is around the MPB of the PLZT phase diagram. The photocurrent and photovoltage were improved more than twice higher for the new compositions of PLZT.

Nb^{5+} , Mo^{6+} , and Gd^{3+} dopants were found to be effective in suppressing the grain growth of PLZT ceramics. Nb^{5+} has been found to enhance the photovoltaic and photostrictive properties in all concentrations. However, the Mo^{6+} and Gd^{3+} dopants exhibited anomalous variations in grain sizes. Doping PLZT ceramics with 0.5 at% Gd_2O_3 concentration was found to be the most effective in reducing the grain size and enhancing the photovoltaic and photostrictive properties of PLZT ceramics.

The high performance photostrictive materials can be tailored using these new compositions and these promising dopants.

ACKNOWLEDGMENTS

One of the authors (P. Poosanaas) would like to acknowledge the Royal Thai Government and Dr. Harit Sutabutr from the National Metal and Materials Technology Center (Thailand) for granting MOSTE fellowship.

REFERENCES

- Akbas, M. A., I. M. Reaney, and W. E. Lee, 1996, "Domain Structure-Property Relation in Lead Lanthanum Zirconate Titanate Ceramics," *J. Mater. Res.*, 11, 2293-2301.
- Brody, P. S., 1975, "High Voltage Photovoltaic Effect in Barium Titanate and Lead Titanate-Lead Zirconate Ceramics," *J. Solid State Chem.*, 12, 193-200.
- Chu, S. Y. and K. Uchino, 1994, "Impurity Doping effect on Photostriction in PLZT Ceramics," *J. Adv. Performance Mater.*, 1, 129-143.
- Chu, S. Y. and K. Uchino, 1995, "Photostrictive effect in PLZT Based Ceramics and Its Applications," *Ferroelectrics*, 174, 185-196.
- Haertling, G. and C. Land, 1971, "Hot Pressed (Pb, La) (Zr, Ti) O₃ Ferroelectric Ceramics for electrooptic Applications," *J. Amer. Ceram. Soc.*, 54, 1-11.
- Murty, K. V. R., K. Umakantham, S. N. Murty, K. C. Mouli, and A. Bhanumathi, 1992, "Hysteresis Behavior and Piezoelectric properties of Nb Doped PLZT Ceramics," *Proc. 8th IEEE Int'l Symposium on Applications of Ferroelectrics Transactions*, 500-503.
- Nonaka, K., M. Akiyama, A. Takase, T. Baba, K. Yamamoto, and H. Ito, 1995, "Nonstoichiometry effects and Their Additivity on Anomalous Photovoltaic Efficiency in Lead Lanthanum Zirconate Titanate Ceramics," *Jpn. J. Appl. Phys.*, 34, 5380-5383.
- Nonaka, K., M. Akiyama, A. Takase, T. Baba, K. Yamamoto, and H. Ito, 1996, "Photovoltaic Response map in PLZT Ceramics Doped with Various Impurity Elements," *J. Mater. Sci. Lett.*, 15, 2096-2098.
- Poosanaas, P., A. Dogan, A. V. Prasadara, S. Komarneni, and K. Uchino, 1997, "Photostriction of Sol-gel Processed PLZT Ceramics," *J. Electroceramics*, 1(1), 105-111.
- Poosanaas, P., and K. Uchino, 1998, "Photostrictive Effect in Lanthanum-Modified Lead Zirconate Titanate Ceramics Near The Morphotropic Phase Boundary," submitted to the special issue of *J. Mater., Chem., Phys.*
- Sada, T., M. Inoue, and K. Uchino, 1987, "Photostriction in PLZT Ceramics," *J. Ceram. Soc. Jpn. Inter. Ed.*, 95, 499-504.
- Tanimura, M. and K. Uchino, 1988, "Effect of Impurity Doping on Photostrictive in Ferroelectrics," *Sensors and Materials*, 1, 47-56.
- Uchino, K. and M. Aizawa, 1985, "Photostrictive Actuators Using PLZT Ceramics," *Jpn. J. Appl. Phys. Suppl.*, 24, 139-141.
- Weast, R. C., G. L. Tuve, S. M. Selby, and I. Sunshine, in *Handbook of Chemistry and Physics*, 50th edition, (The Chemical Rubber Co., Ohio, 1969), B-2 and F-152.
- Yoon, K. H., Y. W. Kim, and D. H. Kang, 1998, "Donor Substitution effect on Dielectric and Electrostrictive Properties of (Pb_{0.73}, La_{0.27}) (Zr_{0.75}Ti_{0.25}) O₃ Ceramics," *J. Mater. Sci. Lett.*, 17, 159-162.

APPENDIX 68



Effect of Ceramic Processing Methods on Photostrictive Ceramics

P. POOSANAAS

*International Center for Actuators and Transducers, Materials Research Laboratory,
The Pennsylvania State University, University Park, PA 16802*

A. DOGAN

Ceramic Engineering Department, Anadolu University, Eskisehir, Turkiye

A.V. PRASADARAO

Department of Inorganic & Analytical Chemistry, Andhra University, India

S. KOMARNENI AND K. UCHINO

*International Center for Actuators and Transducers, Materials Research Laboratory,
The Pennsylvania State University, University Park, PA 16802*

Abstract. Lanthanum-modified lead zirconate titanate (PLZT) ceramics (3/52/48) doped with 0.5 at.% WO_3 were prepared by three different processing methods, coprecipitation, sol-gel and conventional oxide mixing techniques, to investigate the effect of processing route on photovoltaic and photostrictive properties. The piezoelectric constant (d_{33}) was observed to be independent of processing technique. Photovoltaic and photo-induced strain were found to get enhanced with decreasing grain size and increasing relative density. PLZT ceramics prepared by the coprecipitation route possess unique combination of favorable properties namely: high purity, higher degree of homogeneity, uniform distribution of doping, stoichiometric compositions, finer grain size and highest density. This resulted into enhanced photostrictive properties in coprecipitated PLZT ceramics.

Keywords: coprecipitation technique, photostriction, photovoltaic effect, PLZT ceramic, sol-gel technique, tungsten

Introduction

Photostriction is the light induced strain in a material, which can also be regarded as the superposition of photovoltaic and converse-piezoelectric effects [1]. Materials exhibiting photostrictive effect are of interest for their potential usage in new types of actuators such as wireless remote control photo-actuators. The possibility of directly producing strain by light illumination without any electrical lead wire connection makes them very attractive for micro-actuator and micro-sensor applications. Flexible microactuators based on tailored films of photostrictive PLZT with respect to the sample thickness and surface characteristics on flexible substrate have high potential for a substantial enhancement in the photoactuation efficiency. This flexible actuators can be used in bio-morphic explorers for future space missions as proposed by Thakoor et al. [2]. Additionally they would also be useful for a variety of applications including photostrictive motor, transformers, transducers, advanced

mobility, shape control, and microvalves [2, 3]. Adaptive space structures which can be controlled by the illumination are some of the possible and intriguing applications. These materials are also promising for the photo-acoustic device of the optical communication system, such as photophone [4].

Lanthanum-modified lead zirconate titanate (PLZT) ceramics are one of the proven photostrictive material. It has been observed that doping WO_3 , donor in the B-site, into the PLZT ceramic results in significant enhancement in this property [5–7]. Besides the effect of doping, fabrication and processing methods have been reported to profoundly affect the photovoltaic properties and the strain response. This effect comes through the influence of processing methods on the microstructure, and other physical properties such as density, porosity, and chemical composition. Ceramic materials with high density, low porosity, better homogeneity and a good control of stoichiometry are desired for enhanced photovoltaic and photostrictive properties. Investigation of the microstructure and properties of PLZT ceramics fabricated by different routes are of interest for finding the technique with best photostrictive properties.

It has been observed that the conventional solid-state reaction of the metal oxides and carbonates often results in PLZT products with moderate photovoltaic and photostrictive properties due to the compositional and structural inhomogeneities, characteristic of this fabrication route [8, 9]. Coprecipitation and sol-gel techniques are two of the chemical routes which has the inherent advantage in producing high density homogeneous ceramics with a greater control of stoichiometry [10–12]. Therefore, process for preparation of PLZT via chemical routes with suitable non-oxide precursors is attractive. Among various non-oxide routes, the hydroxide coprecipitation method has also been widely used for the preparation of PLZT powders [11–14]. Fine powders prepared by this route are more homogeneous and more reactive than those prepared by conventional oxide mixing process. In addition, the lower processing temperature also minimizes the loss of PbO evaporation.

In order to investigate the influence of processing techniques on photostrictive property, ceramics of PLZT (3/52/48) doped with 0.5 at.% WO_3 were prepared by three different methods, (i) conventional oxide mixing process, (ii) sol-gel technique using lead(II) acetate trihydrate, lanthanum(III) acetylacetonate hydrate, Zr, Ti and W alkoxides, and (iii) hydroxide coprecipitation routes using nitrate and chloride precursors. The photostrictive effect of these materials were characterized and correlated to the fabrication method.

Experimental procedure

PLZT (3/52/48) ceramic with a composition of 3 at.% La, Zr/Ti ratio of 52/48 and doped with WO_3 was selected due to its proven high photovoltaic effect [5]. PLZT ceramics doped with 0.5 at.% WO_3 were prepared by the conventional oxide mixing process and by the chemical synthesis (sol-gel and coprecipitation) techniques. Figure 1 illustrates a flow chart for the sample preparation by the conventional oxide mixing process. The flow chart for the sample preparation by the sol-gel technique using lead(II) acetate trihydrate, lanthanum(III) acetylacetonate hydrate, Zr, Ti, and W alkoxides, is shown in figure 2. The details of these two preparation techniques were reported in an earlier communication [9]. The details of the processing technique for hydroxide coprecipitation is shown in figure 3.

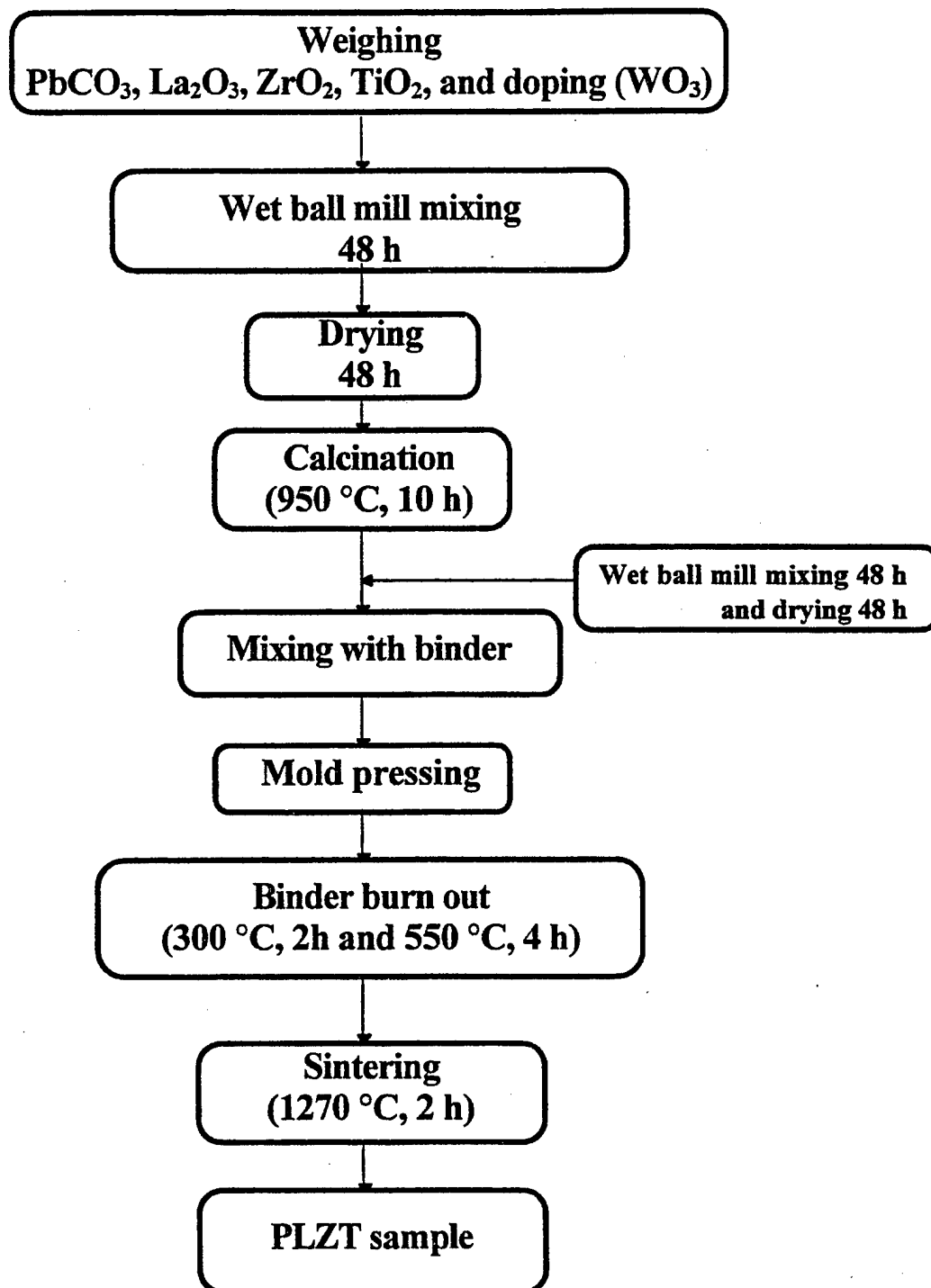


Figure 1. Flow diagram of sample preparation by conventional oxide mixing process.

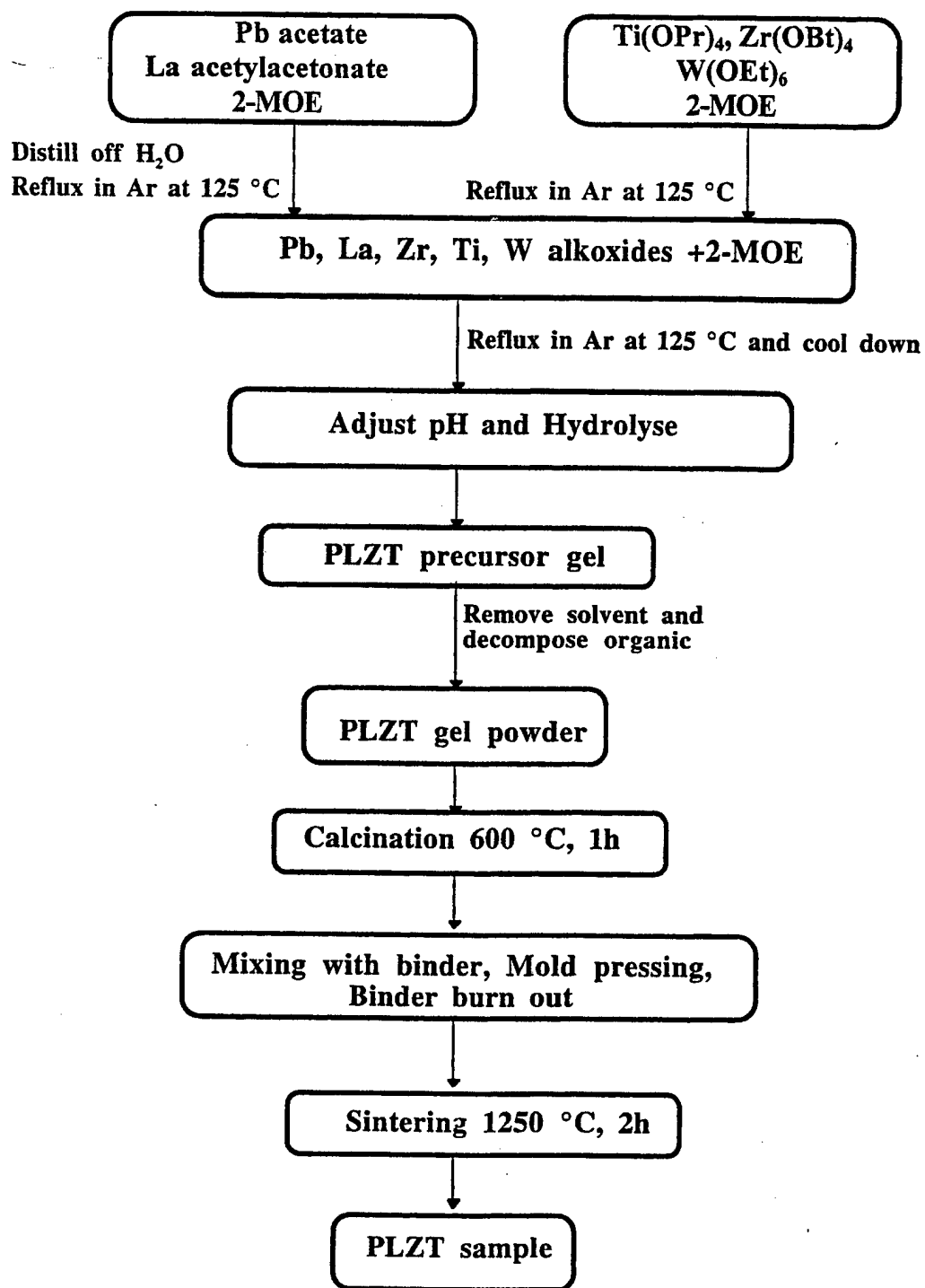


Figure 2. Flow diagram of sample preparation by sol-gel technique: 2-MOE: 2-methoxyethanol; Ti(OPr)₄: Titanium(IV) isopropoxide; Zr(OBt)₄: Zirconium(IV) butoxide; W(OEt)₆: Tungsten(VI) ethoxide.

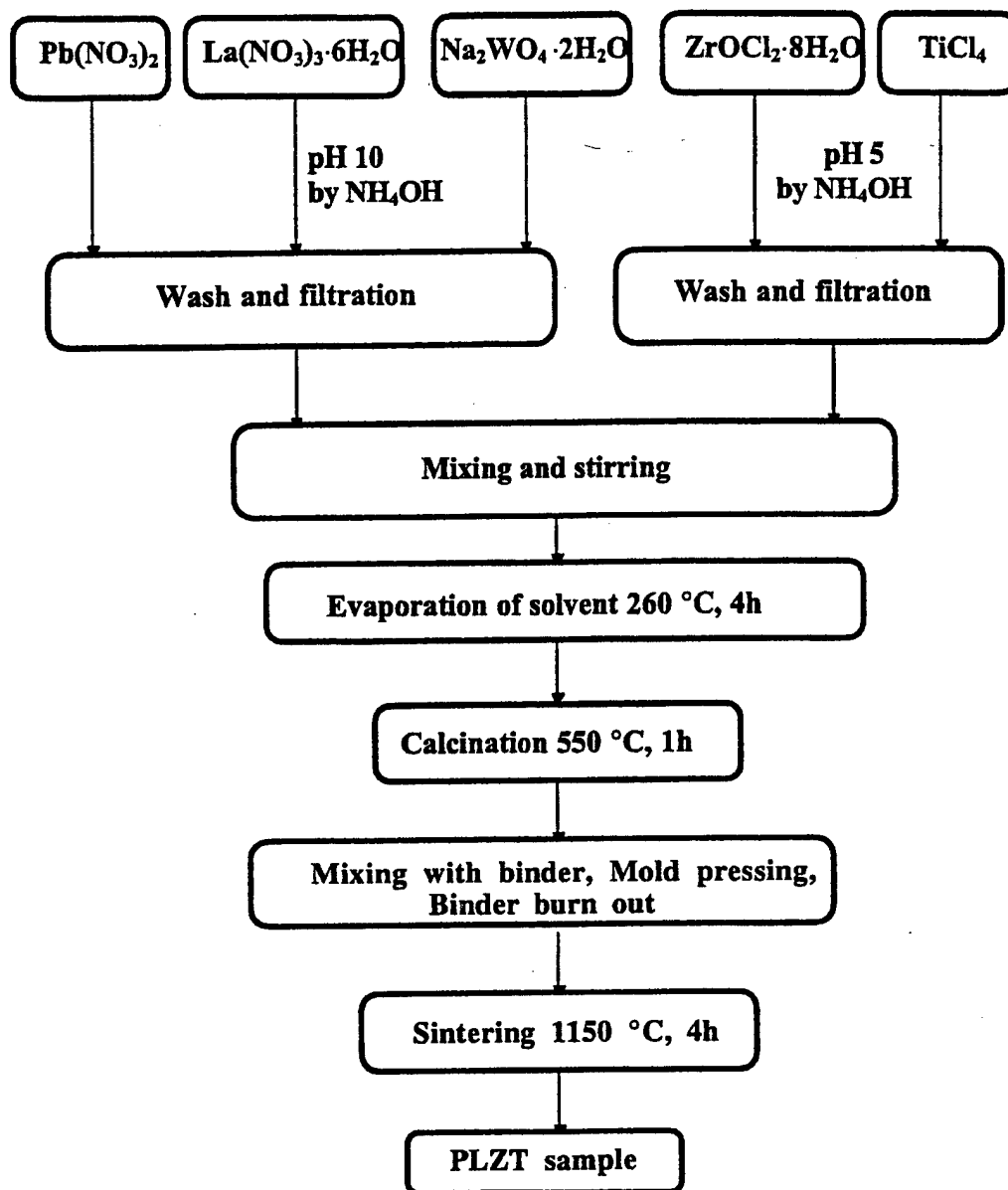


Figure 3. Flow diagram of sample preparation by coprecipitation technique: $\text{Pb}(\text{NO}_3)_2$: Lead nitrate; $\text{La}(\text{NO}_3)_3 \cdot 6\text{H}_2\text{O}$: lanthanum nitrate; $\text{ZrOCl}_2 \cdot 8\text{H}_2\text{O}$: Zirconium oxychloride; TiCl_4 : Titanium tetrachloride; $\text{Na}_2\text{WO}_4 \cdot 2\text{H}_2\text{O}$: Sodium tungstate.

In order to achieve a product with desired stoichiometry and homogeneity, the optimum coprecipitation conditions for metal hydroxide precursors were determined on the basis of solubility limit for aqueous solutions [13]. The starting reagents were high purity lead nitrate $\text{Pb}(\text{NO}_3)_2$, lanthanum nitrate $\text{La}(\text{NO}_3)_3 \cdot 6\text{H}_2\text{O}$, zirconium oxychloride $\text{ZrOCl}_2 \cdot 8\text{H}_2\text{O}$, and titanium tetrachloride TiCl_4 . Sodium tungstate $\text{Na}_2\text{WO}_4 \cdot 2\text{H}_2\text{O}$ was added for the doping. The precursor site A comprising of $\text{Pb}(\text{NO}_3)_2$, $\text{La}(\text{NO}_3)_3 \cdot 6\text{H}_2\text{O}$, and $\text{Na}_2\text{WO}_4 \cdot 2\text{H}_2\text{O}$ was dissolved together in deionized (DI) water to form an aqueous solution. On the other hand precursor site B with $\text{ZrOCl}_2 \cdot 8\text{H}_2\text{O}$, TiCl_4 , was also dissolved in DI water. The

coprecipitation was achieved in these precursors by adding aqueous NH_4OH solution. In the precursor site A, aqueous NH_4OH solution was slowly added and stirred to precipitate A-site powders. The solution pH in A and B precursor sites was adjusted and maintained at pH 10 and 5 respectively. The precipitates of A and B sites were then washed with DI water (pH 10 and 5 respectively) to remove the residual, NO_3^- , Na^+ , and Cl^- ion. Both A and B site precipitates were filtered, mixed and rinsed thoroughly using reagent alcohol, followed by overnight drying at 80°C . The dry cake was crushed and ground using porcelain mortar and pestle. In order to evaporate the absorbed water, thermal treatment was given on the as-dried powder. Thermogravimetric, differential thermal analysis (TGA 7, DTA 1700, Perkin Elmer), and X-ray diffraction (Scintag diffractometer, Vax 3100 System) were performed to characterize the precipitated powders. Subsequently, the powder was calcined and sintered.

The comparison of the properties of ceramics derived from the three different methods were made. The density of the sintered samples was determined by the Archimedes method while microstructure and grain size of the samples were observed by scanning electron microscopy (ISI DS-130). Dielectric properties of PLZT samples were measured with an impedance analyzer (HP-4274A). Samples for dielectric measurement were polished to about 10 mm in diameter and 1 mm in thickness, then electroded with platinum (Pt) by sputtering. Piezoelectric properties of all the samples were measured by using a Berlincourt d_{33} meter (Channel Products, Inc.) at 100 Hz. Samples for piezoelectric measurement were of the same dimension as for dielectric measurements, except they were poled in silicone oil at 120°C under a 2 kV/mm electric field for 10 min.

Photovoltaic measurements were done using a high-input-impedance electrometer (Keithley 617), while the photostriction was measured by a displacement sensor (LVDT, Millitron model 1301). Figure 4 shows the experimental setup for these measurements [9]. These measurements were done by radiating the light perpendicular to the polarization direction. The samples of $5 \times 5 \times 1 \text{ mm}^3$ were cut and polished for these measurements. The $5 \times 1 \text{ mm}^2$ surfaces were silver electroded. Poling was performed by applying 2 kV/mm electric field for 10 min in silicone oil at 120°C . A high pressure mercury lamp (Ushio

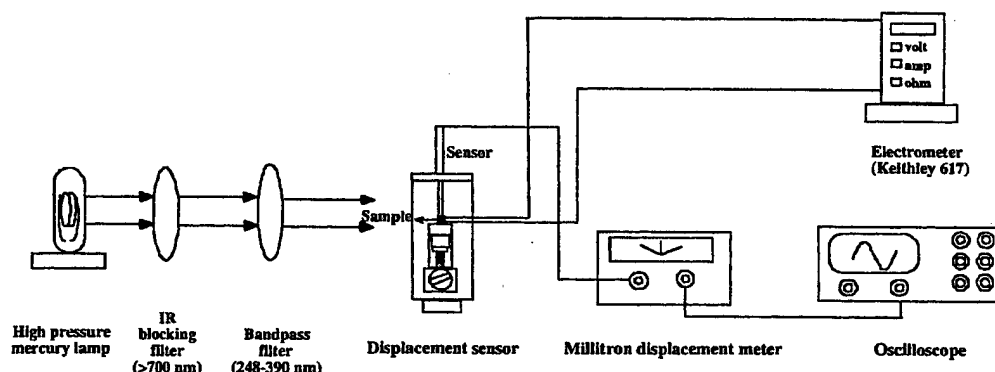


Figure 4. Experimental set up for photovoltaic and photostrictive measurement. Illumination: High pressure mercury lamp; without polarizer; filter (IR blocking filter/bandpass filter); wavelength = 366 nm; intensity = 3.25 mW/cm^2 .

Electric USH-500D) was used as a light source for the measurement. The white radiation was passed through an IR blocking filter and an UV bandpass filter to obtain a beam with a maximum strength around 366 nm and an intensity of 3.25 mW/cm², before illuminating the samples (5 × 5 mm² polished surface).

Results and discussion

Characterization of powder derived from coprecipitation technique

The as-dried powder from coprecipitation technique was examined using TGA-DTA, and X-ray diffractometer. The physico-chemical change of the precipitate with temperature was investigated with a TGA-DTA apparatus, in the temperature range of 50–1050°C at a heating rate of 10°C/min under an air atmosphere and by a powder X-ray diffraction with CuK α radiation. Figure 5 shows TGA and DTA curves for the as-dried precipitate. The initial weight loss in the temperature range of 55–250°C may be attributed to the liberation of surface absorbed water and/or occluded solvent (water, ethanol), and is accompanied by an endothermic DTA peak. Dehydration of the powder resulted in the endothermic peak observed at about 150°C. The weight loss at 330–500°C is due to the decomposition of hydroxyl group. The final weight loss above 600°C can be attributed to the strongly bonded

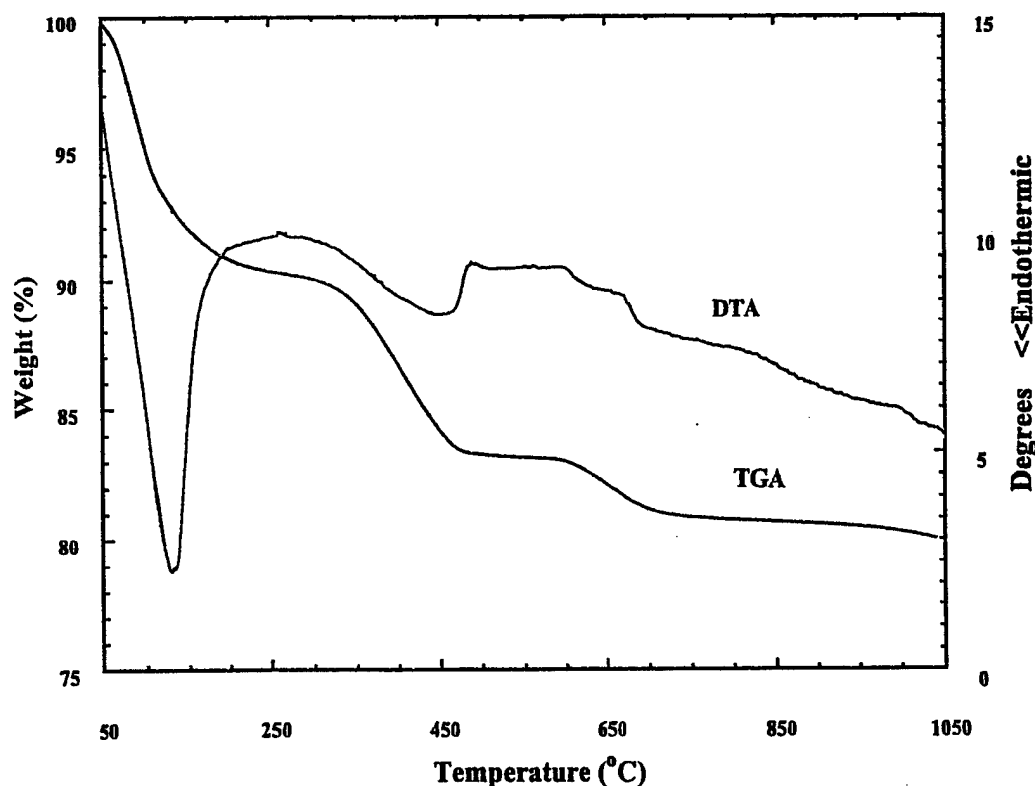


Figure 5. TGA-DTA curves for the as-dried precipitate of PLZT.

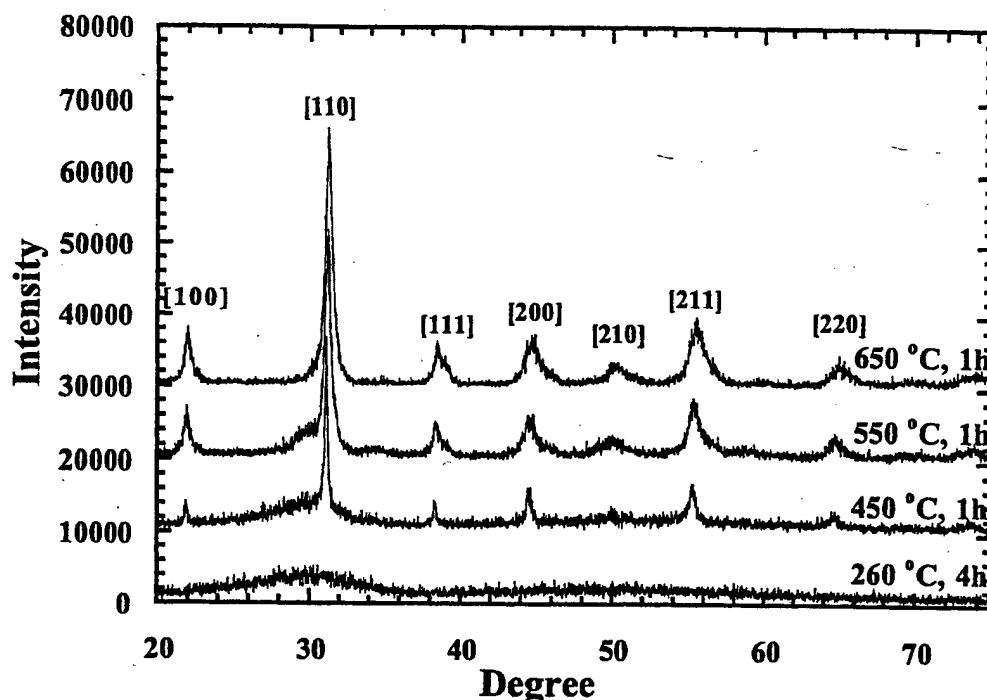


Figure 6. X-ray diffraction patterns of PLZT derived from coprecipitation technique.

hydroxyl group.

Figure 6 shows a series of X-ray diffraction patterns of the as-dried powder at different temperatures. Crystallization of the perovskite phases during thermal treatment can be observed. The precipitate was found to be amorphous up to 450°C for 1 h. The crystalline perovskite phase of PLZT appears after 450°C for 1 h. The complete perovskite phase of PLZT was formed at 550°C for 1 h. Based on these results the calcination temperature was selected to be 550°C for 1 h.

Comparison of ceramics derived from three different processing techniques

Physical properties of ceramics produced from three different processing methods are listed in Table 1. As can be seen from this table, depending on the processing technique, the samples with the same composition exhibit different results.

Figure 7 shows the relative sintered density of 0.5 at.% WO_3 doped PLZT ceramics prepared through three different methods as a function of sintering temperature after 2 h sintering time. A relative density of 98% was achieved for PLZT oxide samples sintered at 1200°C. The sintered density saturated and remained constant as the sintering temperature increases to 1300°C. On the other hand, in the sol-gel PLZT a maximum density of 93% was observed at a sintering temperature of 1250°C. The sintered density decreased as the sintering temperature was further increased. This was probably due to the evaporation of PbO during sintering. A relative density of 97% was achieved for coprecipitated PLZT ceramics sintered at 1150°C. However the relative density of coprecipitated ceramics was

Table 1. Comparison of ceramics derived from three different processing techniques.

Conditions/properties	Conventional oxide mixing process	Sol-gel technique	Coprecipitation technique
Calcination	950°C, 10 h	600°C, 1 h	550°C, 1 h
Sintering	1270°C, 2 h	1250°C, 2 h	1150°C, 4 h
Maximum relative density (%)	98%	93%	99%
Average grain size (μm)	1.87 ± 0.08	1.72 ± 0.06	1.12 ± 0.05
Piezoelectric constant d_{33} ($\times 10^{-12}$ m/V)	320	315	310
Curie temperature ($^{\circ}\text{C}$)	300	299	299
Maximum dielectric constant	15200 ± 200	12700 ± 100	10000 ± 100
Room temperature dielectric constant	1600 ± 30	1235 ± 20	1220 ± 20
Photovoltage, E_{ph} , ^a (V/cm)	1500	1650	2010
Photocurrent (nA/cm) ^a	1.7	2.48	2.50
Photoinduced strain ^a ($\times 10^{-5}$)	4.50	4.94	6.10
Calculated ($d_{33} \times E_{\text{ph}}$)	4.80	5.20	6.23

^aFor the illumination intensity 3.25 mW/cm^2 .

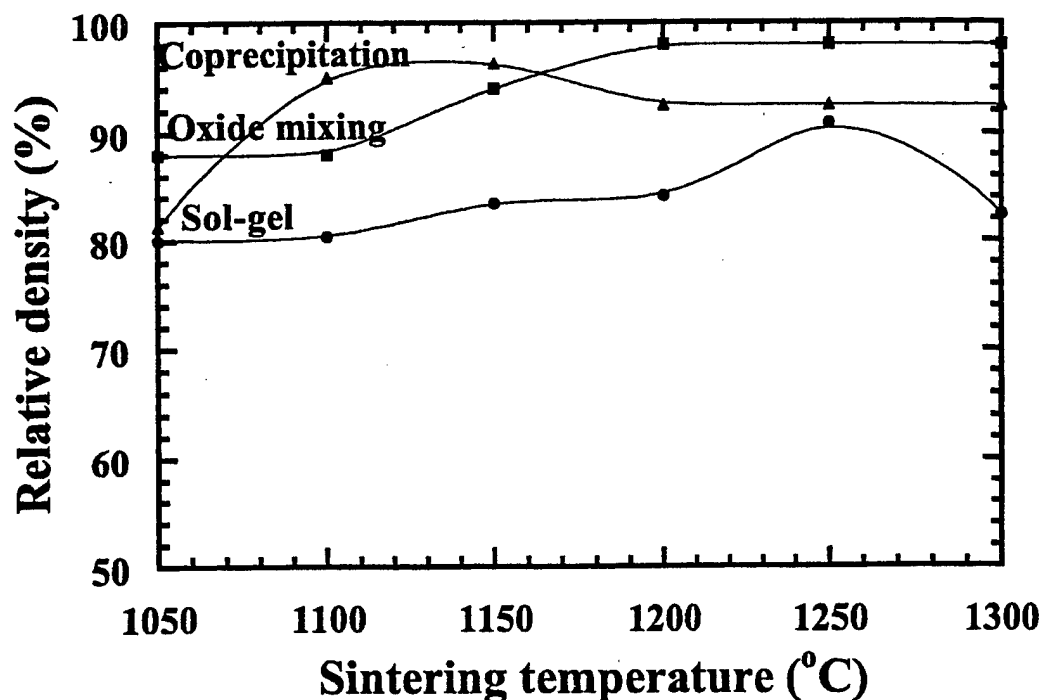


Figure 7. Relative density as a function of sintering temperature after 2 h sintering time.

enhanced to 99% after 4 h of sintering at the same temperature as shown in figure 8. As evident from figure 7, the sol-gel PLZT exhibits lower density as compared to the oxide PLZT at all the sintering temperatures. This lower density was probably due to finer and agglomerated particles. The high density in PLZT oxide samples is due to higher

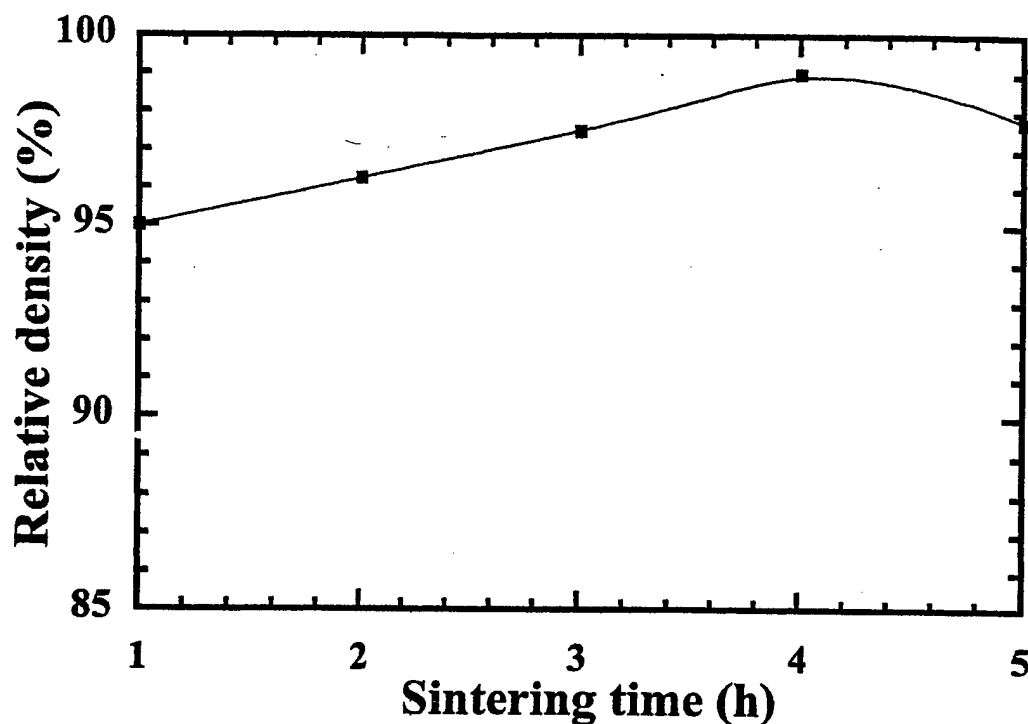


Figure 8. Relative density of coprecipitated PLZT ceramics as a function of sintering time (at 1150°C).

packing density without agglomeration as compared to sol-gel ceramics. Coprecipitated PLZT ceramics possessed the highest density at the lowest sintering temperature among all ceramics due to no agglomeration associated with this route.

Figure 9 shows the SEM micrographs of the sintered ceramics. The average grain size of samples were determined. The average grain sizes for oxide mixing, sol-gel, and coprecipitated samples were 1.87, 1.72, and 1.12 μm , respectively. The grain size was smallest for the coprecipitated ceramics among all the samples. In general average grain size of ceramics prepared by chemical synthesis is smaller as compared to solid state reaction due to more reactive powder obtained through chemical routes which resulted in lower sintering temperature.

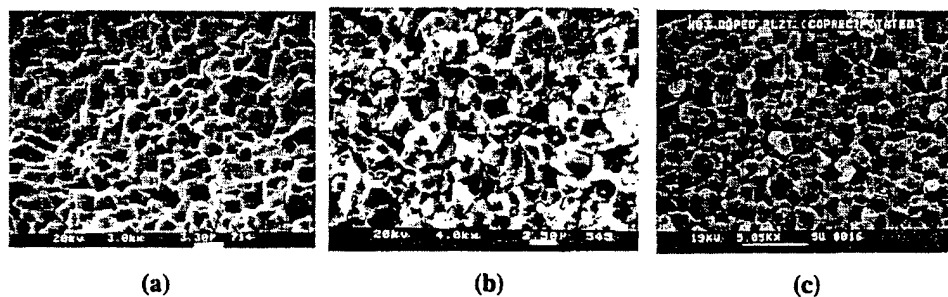


Figure 9. SEM micrographs of 0.5 at.% WO_3 doped PLZT ceramics prepared by (a) conventional oxide mixing process (b) sol-gel technique and (c) coprecipitation technique.

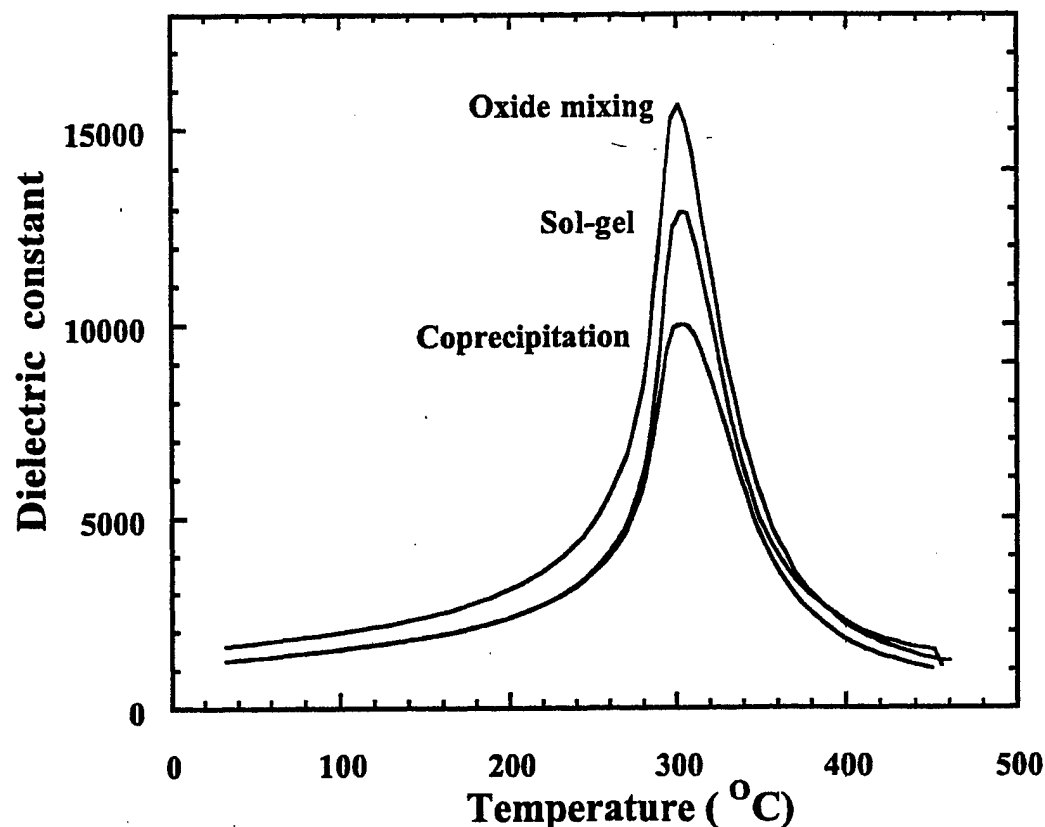


Figure 10. Dielectric constant as a function of temperature at 1 kHz.

The dielectric constants of the ceramics derived from three different processing techniques are shown in figure 10. There was no difference in the Curie temperature among three samples. PLZT ceramics from sol-gel and coprecipitation techniques exhibited lower dielectric constant compared to the oxide PLZT due to the smaller grain size observed in these ceramics. The piezoelectric constant d_{33} showed a similar tendency for the ceramics prepared by three different methods with the minimum for the coprecipitated sample. However photovoltaic and photostrictive properties vary greatly with the processing techniques. The photo-induced electric field reached more than 1 kV/cm and the photocurrent density was of the order of nA/cm under the illumination intensity of 3.25 mW/cm² for 366 nm wavelength. Coprecipitated PLZT ceramic showed the highest in both the photo-induced electric field and strain among all samples, followed by sol-gel PLZT and oxide mixing PLZT, due to the smaller grain size observed in this ceramic. Coprecipitated sample exhibited photocurrent similar to sol-gel PLZT, which are higher than oxide mixing PLZT. Table 1 listed the calculated product values of piezoelectric constant d_{33} , and photo-induced electric field E_{ph} , which are in good agreement with the experimental data.

Difference between samples prepared by solid-state reaction as in oxide mixing process and chemical synthesis routes as in sol-gel and coprecipitated methods arises due to the difference in a couple of factors. Ceramics prepared by solid state reaction have compositional variation and inhomogeneous distribution of impurities whereas the ceramics prepared by chemical synthesis exhibit high purity and preferable properties such as higher

degree of homogeneity, uniform distribution of doping and stoichiometric compositions. The atomic level interaction and mixing in chemical synthesis resulted in smaller grain size and lower sintering temperature. As a result the ceramics prepared by sol-gel and coprecipitated techniques exhibit better photovoltaic and photostrictive properties as compared to the oxide mixing process. Photovoltage increases with decreasing grain size as the photovoltage is effected by the number of grain boundaries [8, 15]. Increasing the number of grains by decreasing the grain size may increase the photovoltage of the samples as observed in coprecipitated and sol-gel ceramics. Enhancement in photo-induced strain for the coprecipitated sample is due to increase in photovoltage, as the piezoelectric constant of the three samples are similar. The coprecipitated ceramics exhibited the highest photovoltage and photo-induced strain, as it possesses favorable combination of smallest grain size and highest relative density. The lower relative density of ceramics prepared by sol-gel route is a major limitation of this technique.

Potential application

The direct conversion of photonic to mechanical motion by photostrictive effect can lead to two broad classes of applications, microactuator and microsensing. Tailored films of photostrictive PLZT on flexible substrate with higher efficiency will pave the way for newer technologies required in the new class of small vehicles for future space missions. A unique combination of direct/driven, electrically/photonicallly stimulated, strong and flexible actuators will lead to ultra-low mass and compact volume packaging, offering a possibility of providing multiple explorers at low cost with tailored tentacles to communicate with extremely high specificity. This will open new vistas in the actuator technology. A contactless optical energy for rover propulsion will be another potential application. In addition, the tetherless optical control of flexible microactuators would also be useful for high precision surgery or minimally invasive medical diagnostics, optical micropositioning, optically controlled microrobots, solar tracking actuator/shutter, photostrictive motor, transducers and photophones.

Acknowledgments

One of the authors (P. Poosanaas) would like to acknowledge the Royal Thai Government and Dr. Harit Sutabutr from the National Metal and Materials Technology Center (Thailand) for granting MOSTE fellowship.

References

1. K. Uchino and M. Aizawa, *Jpn. J. Appl. Phys.* **24**, 139 (1985).
2. S. Thakoor, J.M. Morookian, and J.A. Cutts, *Proceedings of the Tenth IEEE International Symposium on Applications of Ferroelectrics Transactions* (1996), vol. 1, p. 205.
3. M. Sayer, M. Lukacs, and T. Olding, *Integrated Ferroelectrics* **17**, 1 (1997).
4. K. Uchino, *Innovations Mater. Res.* **1**(1), 11 (1996).
5. S.Y. Chu and K. Uchino, *J. Adv. Performance Mater.* **1**, 129 (1994).

6. M. Taminura and K. Uchino, *Sensors and Materials* **1**, 47 (1988).
7. K. Nonaka, M. Akiyama, A. Takase, T. Baba, K. Yamamoto, and H. Ito, *J. Mater. Sci. Lett.* **15**, 2096 (1996).
8. T. Sada, M. Inoue, and K. Uchino, *J. Ceram. Soc. Jpn. Inter. Ed.* **95**, 499 (1987).
9. P. Poosanaas, A. Dogan, A.V. Prasadaraao, S. Komarneni, and K. Uchino, *J. Electroceramics* **1**(1), 111 (1997).
10. B.S. Chiou, J.N. Kno, and H.T. Dai, *J. Elec. Mater.* **19**(4), 393 (1990).
11. Y. Yoshikawa, K. Tsuzuki, T. Kobayashi, and A. Takagi, *J. Mater. Sci.* **23**, 2729 (1988).
12. J. Thomson, *Ceram. Bull.* **53**(5), 421 (1974).
13. J.H. Choy, Y.S. Han, and J.T. Kim, *J. Mater. Chem.* **5**(1), 65 (1995).
14. M. Murata, K. Wakino, K. Tanaka, and Y. Hamakawa, *Mat. Res. Bull.* **11**, 323 (1976).
15. P.S. Brody and B.J. Rod, *Integrated Ferroelectrics* **2**, 1 (1992).